TESIS DE LA UNIVERSIDAD
DE ZARAGOZA

2013

26

Cristina Sáenz de Pipaón Soba

Contributions to Molecular Magnetism: Chiral Magnets and Networked SMMs

Departamento

Física de la Materia Condensada

Director/es

Palacio Parada, Fernando
Campo Ruiz, Jesús Javier

ISSN 2254-7606

Prensas de la Universidad
Universidad Zaragoza

Tesis Doctoral

CONTRIBUTIONS TO MOLECULAR MAGNETISM: CHIRAL MAGNETS AND NETWORKED SMMS

Autor

Cristina Sáenz de Pipaón Soba

Director/es

Palacio Parada, Fernando
Campo Ruiz, Jesús Javier

UNIVERSIDAD DE ZARAGOZA
Física de la Materia Condensada

2013

icma
Instituto de Ciencia
de Materiales de Aragón

CSIC
Consejo Superior de Investigaciones Científicas

Universidad
Zaragoza
1542

Contributions to Molecular Magnetism: Chiral Magnets and Networked SMMs.

Cristina Sáenz de Pipaón Soba

Zaragoza, Enero 2013

THESIS SUPERVISORS:

Javier Campo Ruiz
Fernando Palacio Parada

A mis padres, Juani y Jesús.
A mis hermanos, Ana y Miguel.

Aprender sin pensar es inútil.
Pensar sin aprender es peligroso.

Contents

Resumen

Los compuestos moleculares pueden combinar las propiedades intrínsecas de su naturaleza molecular (tamaño nanoscópico, bajo peso específico, gran versatilidad sintética, transparencia, plasticidad, procesabilidad, biocompatibilidad,...etc..) con una o más propiedades físicas de interés. De entre todos ellos, los materiales moleculares magnéticos despiertan un interés creciente debido en parte a las posibilidades tecnológicas que ofrecen [1]. Eligiendo apropiadamente los bloques que forman estos compuestos (moléculas puramente orgánicas o bien con fragmentos inorgánicos) y su conectividad (clústeres, cadenas, planos o estructuras tridimensionales), se puede ejercer cierto control sobre las propiedades magnéticas del material para obtener ferromagnetos, antiferromagnetos, Single Molecule Magnets, Single Chain Magnets, imanes quirales, etc. Además se pueden lograr materiales moleculares magnéticos multifuncionales que combinan el magnetismo y una o más propiedades físicas de interés práctico (fotomagnetismo, magnetoóptica, magnetoconductividad, etc.). Al contener los bloques moleculares un número limitado de átomos magnéticos, los materiales moleculares magnéticos también resultan excelentes sistemas donde estudiar conceptos básicos de física como el canje magnético, el efecto túnel, la transferencia electrónica, la anisotropía magnética, la coexistencia de quiralidad nuclear y magnética [2], entre otros fenómenos.

Dentro de los materiales moleculares magnéticos multifuncionales, pueden encontrarse compuestos moleculares donde coexisten quiralidad nuclear y magnética. La palabra quiralidad proviene del griego $\chi\varepsilon\iota\rho$ que significa mano, y se refiere a la propiedad de los objetos o entes que se dicen no superponibles con su imagen especular. En el caso de moléculas aisladas o formando cristales, la definición implica, matemáticamente hablando, que su grupo de simetría no posee operaciones impropias. Esta ruptura de la simetría espacial en compuestos que presentan quiralidad nuclear permite la existencia de propiedades como piezoelectricidad, actividad óptica natural, piroelectricidad o generación de segundos harmónicos en la emisión de luz. Si además de una estructura nuclear quiral la estructura magnética es también quiral, en cierta manera, las simetrías espacial y temporal se rompen simultáneamente (teniendo en cuenta que el momento magnético es un vector axial), provocando la aparición de nuevos fenómenos físicos, tales como el dicroísmo magnetoquiral [3].

Entre las múltiples posibilidades tecnológicas que ofrecen los materiales magnéticos moleculares, una de las que despiertan mayor interés es la posibilidad de aumentar la capacidad de almacenamiento de datos, reduciendo hasta niveles moleculares la unidad mínima de información. Los imanes monomoleculares (Single Molecule Magnets) representan una parte importante de la investigación en materiales moleculares magnéticos [4]. Son compuestos moleculares paramagnéticos que, por debajo de su temperatura de bloqueo, presentan un comportamiento superparamagnético. Su interés radica especialmente en sus aplicaciones en el campo de almacenamiento de la información, y en las oportunidades que ofrecen para estudiar el canje magnético, el efecto túnel de la magnetización y las interaciones dipolares, entre otros fenómenos. También es posible con sistemas quirales magnéticos polarizar una corriente de espín controlando la dirección de los momentos magnéticos externamente, lo que favorece el desarrollo de la espintrónica [5].

El objetivo general del trabajo desarrollado en esta tesis es doble: por un lado, el estudio de la estructura nuclear y magnética de materiales moleculares magnéticos donde quiralidad nuclear y magnética coexisten (línea A); y por otro lado, el estudio y caracterización magnética de imanes orgánicos monomoleculares (SMMs) organizados en redes (línea B). A continuación, ambas líneas son detalladas.

Línea A

En esta tesis se realiza una revisión del concepto de quiralidad magnética, que puede resultar confuso debido a la variedad de definiciones existentes. Asimismo se propone una definición global para sistemas quirales magnéticos. Se quiere verificar la existencia de quiralidad magnética en compuestos quirales que presentan orden magnético y donde la simetría favorece la presencia de quiralidad magnética. En compuestos de este tipo donde quiralidad nuclear y magnética coexisten en una fase ordenada magnéticamente, todavía no ha sido observado el dicroismo magnetoquiral ya conocido en sistemas enantiopuros paramagnéticos, diamagnéticos y ferromagnéticos.

El estudio está centrado en dos compuestos quirales con una estructura parecida $[Mn(CN)_6][Mn(S)pnH(H_2O)]{\cdot}2H_2O$ [6] (donde (S)-pn equivale a (S)-1,2-diaminopropano), y $[Cr(CN)_6][Mn(R){-}pnH(DMF)]{\cdot}2H_2O$ [7] (donde DMF significa N,N-dimetilformamida=$(CH_3)_2$-N-CHO) y un compuesto racémico de uno de ellos $[Cr(CN)_6][Mn(rac) - pnH(DMF)]{\cdot}2H_2O$. El primer compuesto, denotado como GN-MnMn, se ordena magnéticamente a 28K y los dos siguientes, GN-DMF(R) y GN-DMF(rac) respectivamente, se ordenan a 33K. Estos compuestos son similares al llamado Green Needle y denotado como GN, $[Cr(CN)_6][Mn(S)pnH(H_2O)]\cdot 2H_2O$ [8], ya estudiado previamente por este grupo de investigación. Para poder verificar la existencia de quiralidad magnética en las muestras anteriormente citadas, es necesario determinar su estructura magnética. Por esta razón, se han realizado experimentos de difracción de neutrones en el Institute Laue Langvenin (ILL), empleando el difractómetro de cuatro círculos D15 y el difractómetro Laue VIVALDI.

A partir de los datos de difracción de neutrones obtenidos, con la ayuda de la teoría de representaciones irreducibles y el programa FULLPROF [9], se han resuelto las estructuras magnéticas de los tres compuestos. Basándonos en la definición de quiralidad magnética propuesta y desarrollada en el capítulo 2 de esta tesis, se ha encontrado que en las muestras GN-MnMn y GN-DMF(R) coexisten quiralidad nuclear y magnt́ica. Este hecho convierte estos compuestos en excelentes candidatos para realizar experimentos de dicroismo magnetoquiral y observar si existe alguna diferencia entre la señal en fase paramagnética y en fase ordenada. El compuesto GN-DMF(rac) no presenta quiralidad magnética debido a la simetría de la estructura.

Línea B

Estudios anteriores han observado que algunos cubanos de Co(II) presentan un comportamiento de SMM en torno a 5K [10]. Pequeñas diferencias en la estructura nuclear del cluster generan variaciones en las interacciones magnéticas entre iones Co(II), provocando cambios en la barrera energética o en el estado fundamental, influyendo por tanto en su magnetismo. Incluso pueden encontrarse situaciones en las que existe orden magnético a largo alcance por interacciones de canje [11, 12] o dipolares [13]. Nuestro objetivo en esta parte de la tesis es doble, por un lado queremos caracterizar cómo ligeras modificaciones en la simetría del cubano de Co(II) influyen en sus propiedades magnéticas. Por otro lado, se quiere estudiar si estos SMMs cuando están ordenados en redes, conservan sus características puntuales de clústeres discretos y cómo el entorno puede influir en su magnetismo, pudiendo darse el caso de la existencia de orden magnético de largo alcance.

Para llevar a cabo estas investigaciones, se han caracterizado magnéticamente cubanos de Cobalto (II) aislados o dispuestos en redes de diferente dimensionalidad, sintetizados por miembros del grupo consolidado M4 y que forman parte de la tesis de la Lcda. Elena Forcén. Entre ellos se dispone de un compuesto $\mathrm{Co_4(citr)_4[Co(H_2O)_4]_4}$ (donde citr=citrato) que presenta tres fases cristalinas interconvertibles en estado sólido, en las que los clusters se encuentran aislados, formando una estructura nuclear modulada o constituyendo un polímero lineal. También se han estudiado redes bidimensionales cuadradas del tipo $A_4[Co_4cit_4\{Co(OHCH_2CH_2OH)(H_2O)_2\}_2]\cdot nH_20$ (A=K, Rb, Cs) [14, 15] y rómbicas $Cs_4[Co_4cit_4\{Co(H_2O)_4\}_2]\cdot 11H_2O$ formadas por

cubanos de Co(II) en su nodos y cobaltos que actúan como nexos entre ellos. Incrementando la dimensionalidad de la red, se ha estudiado en esta tesis una red tridimensional de tipo diamante $(K_4Co_4(cit[\mu - Co(H_2O)_4]_2{\cdot}8H_2O)_n$ con cubanos en los nodos que presenta una estructura MOF (Metal Organic Framework), lo que puede dar lugar a interesantes aplicaciones. El estudio magnético y calorimétrico de estos compuestos se ha realizado en varios equipos comerciales de Quantum Design (PPMS y MPMS). También se ha empleado, gracias a la colaboración con el Dr. F. Luis del ICMA, un refrigerador de dilución dotado con un SQUID para los estudios magnéticos a muy baja temperatura.

La caracterización magnética de estos compuestos ha permitido observar la coexistencia de diferentes procesos de bloqueo y orden magnético en la misma muestra. Asimismo se ha observado como modificaciones estructurales influyen en la respuesta magnética.

Acronyms

CsCo$_4$/R	$Cs_4\{[Co(C_6H_4O_7)]_4\mu(Co(H_2O)_4)_2]\cdot 16H_2O$
CsCo$_4$/S	$(C_{28}H_{36}Co_6O_{36}Cs_4)_n{\cdot}4.5nH_2O{\cdot}2.5n(C_2H_6O_2)$
CsCo$_4$+1	$Cs_2[Co(H_2O)_6][Co_6(C_6H_4O_7)_4(H_2O)_8]\cdot 12H_2O_n$
DM	Dzyaloshinskii-Moriya
DMF	Dimethylformamide
ETG	Ethylene glicol
FT	Fourier Transform
GN	$[Cr(CN)_6][Mn(S)-pnH(H_2O)]{\cdot}2H_2O$
GN-MnMn	$[Mn(CN)_6][Mn(S)-pnH(H_2O)]\cdot 2H_2O$
GN-DMF(R)	$[Cr(CN)_6][Mn(R)-pnH(DMF)]{\cdot}H_2O$
GN-DMF(rac)	$[Cr(CN)_6][Mn(rac)-pnH(DMF)]{\cdot}H_2O$
ILL	Institute Laue Langvenin
IR	Irreducible representation
KCo$_4$/S	$(C_{28}H_{36}Co_6O_{36}K_4)_n{\cdot}XH_2O{\cdot}Yn(C_2H_6O_2)$
RbCo$_4$/S	$(C_{28}H_{36}Co_6O_{36}Rb_4)_n\cdot 9.5\cdot n(H_2O)\cdot 2n(C_2H_6O_2)$
SSM	Single Molecular Magnets
YN	$K_{0.4}[Cr(CN)_6][Mn(S)-pn](S)-pnH_{0.6}$

Introduction

Magnetism is a really broad branch of physics, and magnetic compounds are used for a wide variety of technical applications. Reducing the size of the magnetic units until a molecular level, we reach the area of molecular magnetism, where magnetism is combined with some of the intrinsic properties of molecular solids (nanoscopic size, low density, synthetic versatility, optical transparency, and so on). An interested reader could easily find excellent books devoted to it (*i. e.* see references [16, 17]). A smart synthesis chooses the molecular blocks (only organic molecules or organic molecules combined with inorganic fragments) and their connectivity (clusters, chains, plains or three-dimensional structures) to exert some control in the magnetic properties of the material. Moreover, multifunctional molecular magnetic materials combine magnetism and one or more physical properties (fotomagnetism, magnetooptic, magnetoconductivity, etc.). Due to the limited amount of magnetic atoms of molecular materials, they are excellent systems to study fundamental concepts of physic as magnetic exchange, tunnel effect of magnetization, electronic transfer, magnetic anisotropy, coexistence of nuclear and magnetic chirality, etc.

Molecular magnetism has achieved important goals in the past two decades providing examples of novel phenomena and potential applications. It went under a revolution when the first molecular ferromagnet of organic-metalorganic nature was synthesized in 1985, the salt $[FeIII(Cp)*_2]^+[TCNE]^-$ that present spontaneous magnetization and magnetic order below 4.5K [18]. Since then, other molecular materials of different nature: purely organic, inorganic or metalorganic, have been discover to order magnetically at different temperatures. Through the development of new Prussian Blue Analogues (PBA) [19], a very important step was reached when molecule-based long-range magnetically ordered (LRMO) materials with Curie temperatures above room temperature (RT) were obtained. One paradigmatic example of the continuous evolution of molecular magnetism can be found in the organic magnets: the first organic ferromagnet, $p-NPNN$, appeared in 1991 and has an order temperature of 0.67K [20]. From there, in just five years, the ordering temperature reached 36K at normal pressure and 76K at 20Kbar, which is in the temperature region of the liquid nitrogen, for the phase β of the organic radical $p - NC - C_6F_4 - CNSSN$ [21, 22]. It has been a synergy between a rational approach of the exchange interaction and coordination chemistry which has allowed molecule-based magnets to reach high ordering temperatures. But there have been others milestones in the development of molecular magnetism, like the magnetic hysteresis at molecular level, the discover of photoswichtable magnetic materials, and materials combining conduction and bulk ferromagnetism [23, 24]. This thesis is devoted to multifunctional molecular materials where nuclear and magnetic chirality coexist and Single Molecule Magnets (SMM).

Historically, chirality was mainly studied in biology due to the important role that it plays in life, *i. e.* biological molecules use only left-handed amino acids and only right-handed sugars. But chirality can confer unique properties to compounds, arising interest progressively into much fields of chemistry, as organometallic and coordination compounds, metal nanoparticles and molecular materials [25]. A chiral nuclear structure may confer to the compound piezoelectricity, Natural Optical Activity (NOA), Pyroelectricity or Second Harmonic Generation [26], properties that can be relevant in the design of new molecular devices. Especially, because molecule-based materials are transparent for the light, their optical properties have attracted much attention. Moreover, if magnetic chirality coexists with nuclear chirality, spatial and temporal symmetries are simultaneously broken, and a new effect called magnetochiral anisotropy (MChA) will appear. This effect was observed in 1997 by Rikken and Raupach [27] for a paramagnetic enantiopure system. The phenomenon is enhanced in enantiopure chiral ferromagnets and the bistability of a magnetically ordered state open the possibility to employ such materials for data storage with a detections based in MChD instead of magnetic circular dichroism [28]. Moreover, ferromagnetic chiral media are magneto-electric, so it is possible electrical reading/writing of the magnetic state of the medium [29] [30]. Materials of this category are very interesting for their potential applications, and in addition, they allow to explore new fields for physics. The first compound where the coexistence of nuclear and magnetic chirality has been demostrated is $[Cr(CN)_6][Mn(S)pnH(H_2O)]{\cdot}2H_2O$ [8]. It orders magnetically and the resultant magnetic structure, determined by our working group [31], is chiral according to the definition given in section 2.5. The existence of a soliton at the magnetic phase transition temperature for this compound was first postulated [32] and then demonstrated [33]. The experiments performed with this compound reveal the role that magnetic chirality plays in dynamical properties, the chirality can strongly influence the generation, mobility and relaxation of spin-wave excitations. Very similar to GN are two chiral nuclear compounds studied in this thesis $[Mn(CN)_6][Mn(S)pnH(H_2O)] \cdot 2H_2O$ [6], denoted as

GN-MnMn, and $[Cr(CN)_6][Mn(R)-pnH(DMF)]{\cdot}H_2O$ [7], denoted as GN-DMF(R); and a racemic compound $[Cr(CN)_6][Mn(rac)-pnH(DMF)]{\cdot}H_2O$ [6], denoted as GN-DMF(rac). One of the objectives of this thesis is the study of the coexistence of nuclear and magnetic chirality in the nuclear chiral compounds below their T_C. In order to do that, it has been necessary to settle down a global definition for magnetic chirality that clarify this concept and to determine their magnetic structures. The magnetic structures found from neutron diffraction data reveals that the magnetic structures of GN-MnMn and GN-DMF(R) are chiral. The coexistence of nuclear and magnetic chirality makes this compound excellent system to study the influence of magnetic chirality in several physical properties, as the existence of enhanced magnetochiral dichroism. The GN-DMF(rac) has an achiral magnetic structure as it was expected.

From the first single molecule magnet synthesized in 1980, $Mn_{12}ac$, $[Mn_{12}O_{12}(CH_3COO)_16(H_2O_4)]\cdot 4H_2O\cdot CH_3COOH$ [34], which is still one of the most studied SMM, this field has gone under a great development. SMMs are metalorganic compounds that, below a blocking temperature, show superparamagnetic behavior and exhibit magnetic hysteresis of purely molecular origin. An isolated high spin ground state and a high magnetic Ising-anisotropy generate an energy barrier(Δ). Below the blocking temperature (T_B), the energy barrier denies the reversal of the magnetization by thermal activation, the system is said to be blocked and the magnetization decays exponentially with the time in a classical framework. But SMMs are in the limit between classical and quantum physics, and they can also relax through quantum tunneling mechanisms [35] and show quantic coherence phenomenons. SMMs are materials that have incredible potential applications not only in the field of data storage, but also exists the possibility to integrate them as building blocks in quantum computers [36], giving rise to the development of the spintronics [5] [37]. In addition, the finite number of atoms in SMMs and their uniform size the are excellent probes to test quantum theories and to study the exchange interactions, anisotropy effects, long range order by dipolar forces [13]), spin-glass-like-dynamics or competition between single-particle blocking and collective blocking. In addition they can be seen as functional building blocks for high dimensional frameworks, and constitute a new branch for the bottom-up methods. In this theses, we have studied different compounds with cubanes of Co(II) isolated or arranged in networks of different dimensionality. Several Co(II) cubanes have been reported to behave as SMM with a blocking temperature below 5K.

The objective is to remark how structural differences can influence in the energy barrier and observe the competition between individual and collective phenomena.

Part I

Neutron diffraction study of chiral compounds

Chapter 1

Introduction and objectives

1.1 Introduction

This part of the thesis refers to the study of chiral molecular magnets. The term "chiral magnet" is sometimes confusing, because the adjective chiral can refer to nuclear chirality or magnetic chirality. For this reason, we feel that these concepts must be clarified before going deep in any study. From the chemistry point of view, the *structural chirality* may be defined as a particular arrangement of atoms that excludes any improper symmetry element. From the magnetic point of view, the considered objects are the magnetic moments instead of the atoms. Some typical examples of magnetic chirality are frustrated antiferromagnetic triangular lattices or helicoidal arrangements of spins. In this last situation, the antisymmetric Dzyaloshinskii-Moriya (DM) interaction can play a very important role.

In the section 1.2, the concept of nuclear chirality is clarified and the up-to-date concept of magnetic chirality is summarized. The DM interaction is explained and its importance is outlined. In order to remark the importance of chiral molecular magnets, their main features, properties and some synthesis strategies are presented in section 1.3. Special attention is devoted to chiral ciano-based molecular magnets previously studied by our working group that are related to the compounds studied in this thesis. The objectives of the thesis can be found at the end of this chapter.

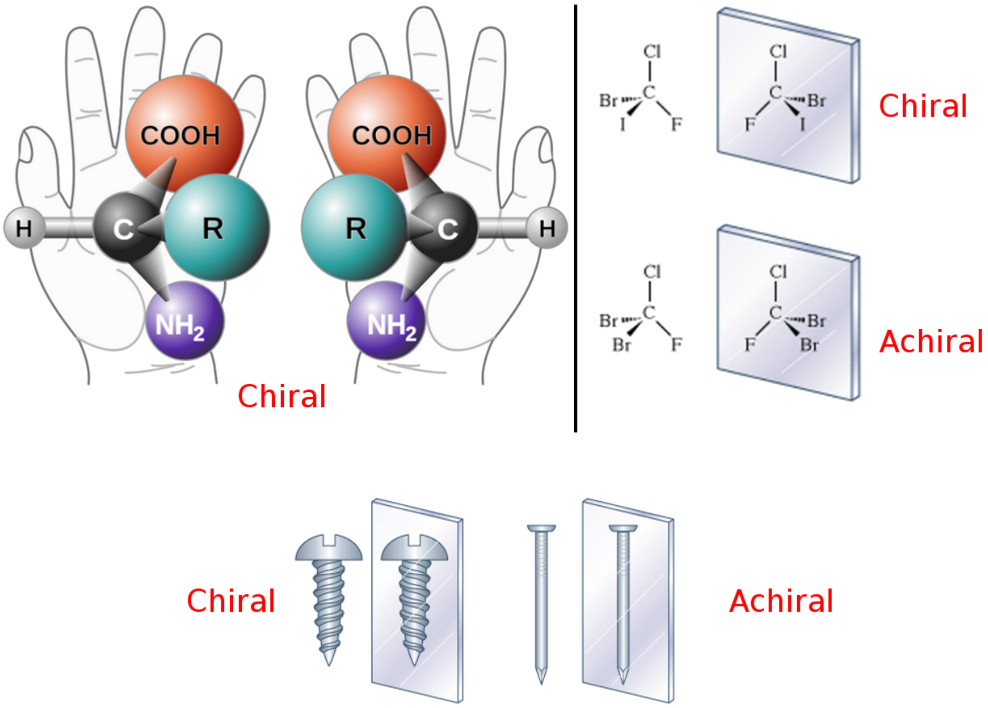

Figure 1.1: Examples of chirality. If an object is not superimposable with its specular image, it is said to be chiral

1.2 Chirality

The term chirality is derived from the Greek word $\chi\varepsilon\iota\rho$ (cheir) for hand, and it is related to the concept of "handedness".

Chirality is a concept that appears in several branches of science, but it is always related to the absence of a symmetry operation. For example, we can use the term chiral referred to a property of elemental particles (i. e. spin), a physical phenomenon (i. e. electromagnetic wave propagation) or a spatial symmetry. In each definition, the common nexus is that the hamiltonian is invariant or not under some symmetry operations. We are concerned with spatial chirality and the next sections are devoted to the concept of nuclear and magnetic chirality. Human hands are perhaps the most universally recognized example of spatial chirality. The left hand is a non-superposable mirror image of the right hand; no matter how the two hands are oriented, it is impossible for all the major features of both hands to coincide as can be seen in figure 1.1.

1.2.1 Non-magnetic chirality

The term chirality, in a nuclear sense, refers to the symmetry restriction of the absence of improper symmetry operations in a molecule or a crystal. There is a punctual definition, called chemical, which is used referred to molecules and another definition more general, which is applied to whole crystal structures. This last one takes into account also the way the molecules are distributed in the crystal structure.

Molecular chirality

In chemistry, chirality usually refers to molecules, being a local concept. According to IUPAC (The International Union of Pure and Applied Chemistry) [38], chirality is the geometric property of a rigid object (or spatial arrangement of points or atoms) of being non-superposable on its mirror image; such an object has no symmetry elements of the second kind, i. e, improper elements (a mirror plane, a center of inversion, a rotoreflection axes).

A molecule non-superposable on its mirror image is called a chiral molecule, and its two mirror images are called enantiomers or optical isomers. In a racemic compound the molecules are chiral, but a mix of both chiralities makes the compound achiral. The word "racemic" is derived from the Latin word "racemus" for "bunch of grapes"; the term having its origins in the work of Louis Pasteur who isolated racemic tartaric acid from wine [39]

There are several nomenclatures to refer to a pair of enantiomers. The more general one designate them as "right-" (R) and "left-handed" (S). Each chiral center is labeled R or S according to a system that assigns a priority to the ligands of the chiral center according to the Cahn-Ingold-Prelog priority rules (CIP) based on atomic numbers [40, 41]. If the center is oriented so that the lowest-priority of the ligands is pointed away from a viewer, the viewer see two possibilities: if the priority of the remaining substituents decreases in clockwise direction, it is labeled R, if it decreases in counterclockwise direction, it is S. This system labels each chiral center in a molecule (and also has an extension to chiral molecules not involving chiral centers) and can label, for example, an (R,R) isomer versus an (R,S), so it is useful for naming molecules with more than one stereocenter or chiral center.

Pairs of enantiomers can also be named according to their optical activity. If it rotates the light clockwise (as seen by a viewer towards whom the light is traveling), the enantiomer is labeled dextrorotatory (+); it mirror imagine rotates light anticlockwise and is labeled levorotatory (-).

In biology, there are a great number of chiral molecules and they are designated L or D relating the spatial configuration of the molecule atoms to glyceraldehyde, which is chiral itself . Most aminoacids are L and sugars are D. Proteins are named left-handed or right-handed depending on which aminoacid they proceed from. Enzymes are also chiral and distinguish between two enantiomers of a chiral substrate.

The (+) or (-) and L or D nomenclatures are confusing if we have more than one chiral center, the only nomenclature useful in this case is the R or S classification.

Most commonly, chiral molecules have point chirality, centered around a single atom, which has different substituent ligands and it is chiral. However in rare cases, two of the ligands differ from each other by being mirror images of each other. When this happens, the mirror image of the molecule is identical to the original, and the molecule is achiral. This is called pseudochirality. A molecule can have multiple chiral centers without being chiral overall if there is a symmetry between the two (or more) chiral centers themselves. Such a molecule is called a meso-compound (see example in figure 1.2a). It is also possible for a molecule to be chiral without having actual point chirality. Common examples include 1,1'-bi-2-naphthol (BINOL) (figure 1.2c), 1,3-dichloro-allene, and BINAP, which have axial chirality; (E)-cyclooctene (figure 1.2b) which has planar chirality; and certain calixarenes and fullerenes which have inherent chirality. As molecules have considerable flexibility, they can adopt a variety of different conformations. These various conformations can be chiral, so it is also possible for a molecule to be chiral without having actual point chirality. When assessing chirality, a time-averaged structure is considered and for routine compounds, one should refer to the most symmetric possible conformation.

Nuclear chirality

In order to understand chirality in a physical context, we use the concept of congruence. Two objects, A and B, are said to be congruent if to each point of A corresponds a point of B; and the distance between two points of A is equal to the distance between the corresponding points in B. Consequently, the angles will be equal in A and B in absolute value. Such correspondence is an isomerism. The congruence can be direct or opposite (positive or negative), according to whether the corresponding angles have the same or opposite angles. An object will be said enantiomorphous or enantiomer with respect to another if they are congruent and the congruence is opposite [42].

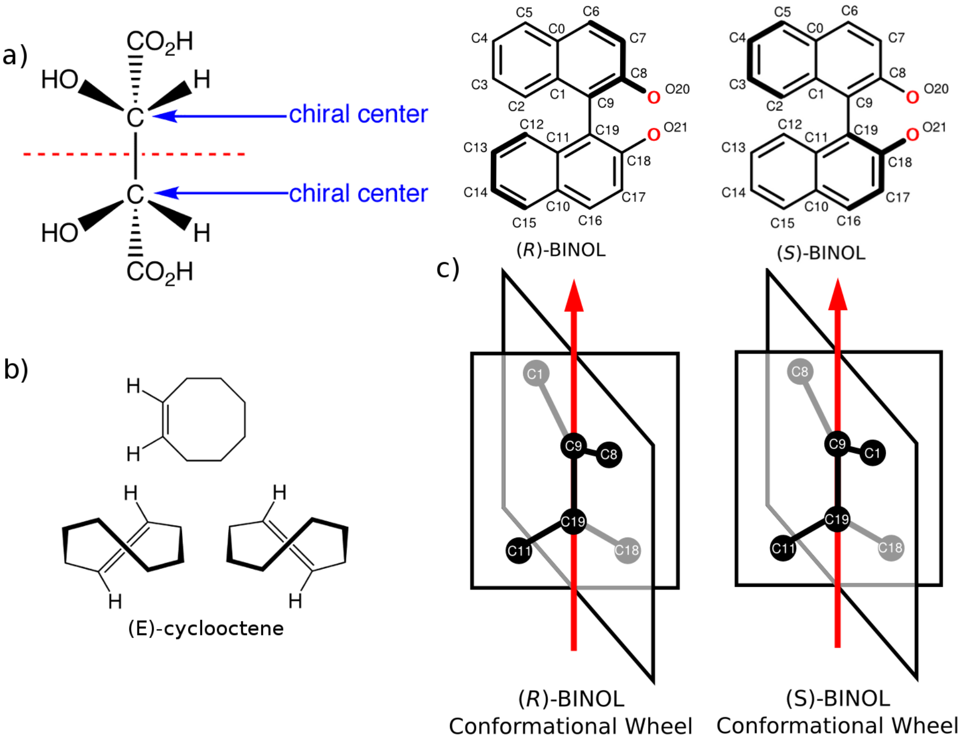

Figure 1.2: a) Schematic drawing of an example for a mesocompound. b)(E)-cyclooctene, which shows planar chirality. c)1,1'-bi-2-naphthol (BINOL), which presents axial chirality

If the congruence is direct, the objects can be bought to coincidence by symmetry operations whose determinant is equal to +1, called proper operations, which are translations, rotations and screws axis. If the congruence is opposite, one object will be said to be enantiomorphous with respect to the other one and the two objects can be bought to coincidence by symmetry operations whose determinant is equal to -1. This symmetry operations, called improper operations, are reflections, inversions, glide planes, rotoinversions and rotoreflections. Screws, glide planes, rotoinversions and rotoreflections can be decomposed as a product of symmetry operations.

Crystals can present different symmetry operations. When translations and symmetry operations involving them are not taking into account, 32 point groups can be constructed by combining symmetry operations in a three-dimensional space. These crystal point groups, also called crystal classes, can be seen in table 1.1. The 32 point groups can be split in 21 non-centrosymmetric point groups and 11 centrosymmetric point groups. In a centrosymmetric group for every point (x, y, x) there is an indistinguishable point (-x, -y,-z).

The 21 non-centrosymmetric groups can be divided in 10 polar groups and 11 enantiomorphic groups. Polar groups presents a polar direction which is not symmetry equivalent to its opposite direction. Enantiomorphic groups only allow proper symmetry operations.

The compatibility of the crystal structure with rotation or inversion axes of order 1, 2, 3, 4, 6 impose some restrictions on the geometry of the lattice. Seven crystal systems can be distinguished: triclinic, monoclinic, orthorhombic, tetragonal, trigonal, hexagonal and cubic. These crystal systems can also be combined with one of the following lattice centering: primitive centering (P), body centered (I), face centered (F) and centered on a single face (A, B, C). There are 14 possible combinations of lattice centering and crystal systems, which are the 14 Bravais lattices. If we combine the 14 Bravais lattices with the 32 point groups, we obtained 73 symmorphic groups. In a symmorphic group, all generating symmetry operations leave one common point fixed. If we introduce translations, 230 space groups are found.

In the 230 space groups [26], there are 65 enantiomorphic or chiral groups, which arise from the 11 enantiomorphic point groups where only proper symmetry operations are allowed and the congruence between their objects is direct. Thus, a chiral space group contains only pure rotations, pure translations and screw rotations, which are proper symmetry elements with determinant +1. Some chiral space groups are also polar. Enantiomorphic crystals can be build by chiral or achiral molecules or atom groups. In the last cases, the achiral molecules or atom groups form chiral configurations in the structure.

Table 1.1: Laue Classes, centrosymmetric/non-centrosymmetric crystal classes (CS/NCS), enantiomorphic or polar group (E/P), and the occurrence (✓) or not of natural optical activity (N), pyroelectricity and piezoelectricity (Pe) and Second Harmonic Generation (S)

Crystal System	Laue Class	CS	NCS	E	N	Pe	S
Triclinic	-1		1	E	✓	✓	✓
		-1					
Monoclinic	2/m		2	E	✓	✓	✓
			m	P	✓	✓	✓
		2/m					
Orthorhombic	2/m 2/m 2/m		222	E	✓		✓
			mm2	P	✓	✓	✓
		2/m 2/m 2/m					
Tetragonal	4/m		4	E	✓	✓	✓
			-4	P	✓		✓
		4/m					
	4/m 2/m 2/m		422	E	✓		✓
			4mm	P		✓	✓
			-42m	P	✓		✓
		4/m 2/m 2/m					
Trigonal	-3		3	E	✓	✓	✓
		-3					
	-3 2/m		32	E	✓		✓
			3m	P		✓	✓
		-3 2/m					
Hexagonal	6/m		6	E	✓	✓	✓
			-6	P			✓
		6/m					
	6/m 2/m 2/m		622	E	✓		✓
			6mm	P		✓	✓
			-62m	P			✓
		6/m 2/m 2/m					
Cubic	2/m -3		23	E	✓		✓
		2/m -3					
	-4/m -3 2/m		432	E	✓		
			-43m	P			✓
		-4/m -3 2/m					

1.2.2 Previous definitions of magnetic chirality

The concept of magnetic chirality has been widely discussed and several local definitions have been given, but there is not an universal and global definition for magnetic chirality as it varies from one author to another [43–47]. It does not seem to be very clear, and it is often mixed with the concept of nuclear or crystallographic chirality. Nuclear and magnetic chirality are separated concepts: a chiral nuclear structure may be magnetically chiral or not, and a chiral magnetic structure may be chiral nuclear or not. Part of the confusion in the definition of magnetic chirality also arises from the different phenomena related to it. Most part of the studies about magnetic chirality are done to describe magnetic phase diagrams, new critical exponents, chiral critical fluctuations, etc. We are interested in magnetic chirality referred to magnetic structures.

Blume [48] and Malayev [49] were the first authors interested in describing a magnetically chiral structure. Blume tried to explain that the magnetization density in different regions of the unit cell may not be collinear with the net magnetization. In this section, we give a brief glimpse of the different definitions for magnetic chirality that have been employed more or less frequently, and remark the need of a global definition. In the chapter 2, in the section 2.5, we explain the definition we propose and adopt for magnetic chirality. The magnetic chirality may arise due to the antisymmetric magnetic interactions and/or the single-ion anisotropy through the spin-orbital interactions. The most important antisymmetric magnetic interaction in this context is the Dzyaloshinskii-Moriya (DM) interaction that violates the inversion symmetry in the spin space. DM interaction is explained in this section.

Local definitions for magnetic chirality

When the first studies of canted or non-collinear magnets appeared, with the discovery of rare-earth helimagnets such as Ho, Dy and Tb, several studies where performed to described the geometry of the arrangement of the spins. Villain [43] tried to describe the behavior of a frustrated lattice, which is a lattice in which all interactions between pair of spins can not be simultaneously satisfied. He focused on sets of four classical, two dimensional spins and stated two types of ground states that can be seen in figure 1.3:

- If there is an even number (0, 2 or 4) of antiferromagnetic bonds, all spins are in the same direction, and the set of four spins is a non-frustrated plaquette.
- If there is an odd number (1 or 3) of antiferromagnetic bonds, the ground state is canted, and the plaquette is frustrated. The system has an extra

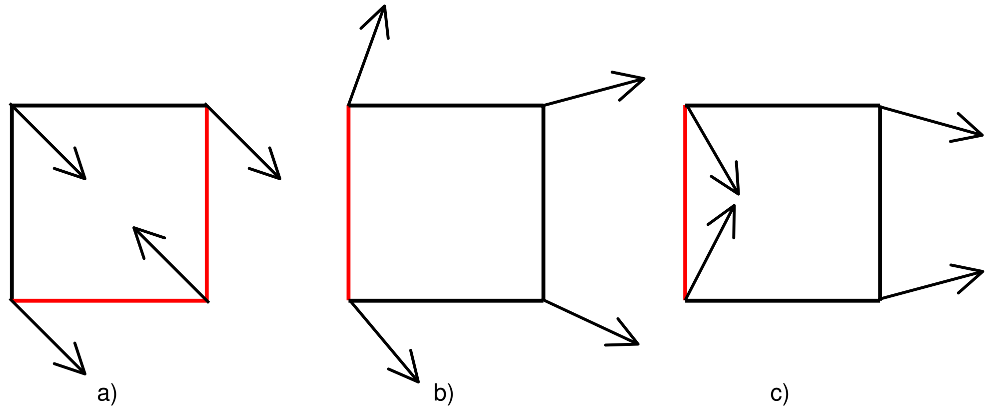

Figure 1.3: Plaquette where black bonds are ferromagnetic and red bonds are antiferromagnetic. a) Non-frustrated plaquette; b) Frustrated plaquette, spins rotate clockwise; c) Frustrated spins rotate counterclockwise

> degeneracy, characterized by τ, that indicates whether the spins rotate clockwise ($\tau = 1$) or counter-clockwise ($\tau = -1$) during a clockwise trip around the plaquette. Both states have the same energy.

Villain gave a local definition of chirality based in the sign of τ, which only involved the atoms in a close trip around the plaquette.

Another example of frustration is the organization of spins in antiferromagnetic materials when the spins are located at the vertices of a triangular lattice. Miyashita and Shiba [44] applied Villain's discovery to the case of a triangular lattice where frustration led to the non-collinear or canted ordered state. They introduced a scalar quantity, chirality, defined by equation 1.1. In this equation the summation runs over the three directed bonds surrounding a plaquette and k_p gives ± 1 for the two degenerated spin configurations depicted in figure 1.4. In this case, chirality is a pseudoscalar which is invariant under global spin rotation but it changes sign under global spin reflection.

$$k_p = \frac{2}{3\sqrt{3}} \sum_{<ij>}^{p} [\mathbf{S}_i \times \mathbf{S}_j]_z \tag{1.1}$$

Kawamura and Miyashita [45] extended this definition of chirality to a two-dimensional Heisenberg antiferromagnet on a triangular lattice, for which they redefined chirality as a vector given in equation 1.2.

$$\mathbf{k}_p = \mathbf{S}_1 \times \mathbf{S}_2 + \mathbf{S}_2 \times \mathbf{S}_3 + \mathbf{S}_3 \times \mathbf{S}_1 \tag{1.2}$$

Similar chiral degeneracy is also found in other types of canted magnets, such as helimagnets (spiral magnets, see figure 1.5) in which right- and left-

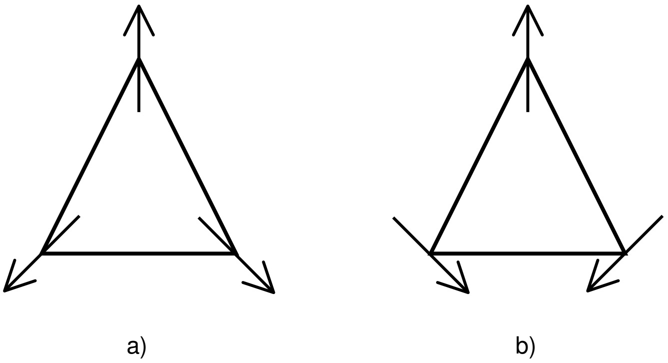

Figure 1.4: Plaquette where bonds are antiferromagnetic. a) *(+)* chirality b) *(-)* chirality

handed helices are energetically degenerated [46][50].

Another kind of chirality can be observed in many antiferromagnetic pyrochlores [51], where a high degree of geometrical frustration exists. Theoretical studies predict that the magnetic ground state is continuously disordered and susceptibility measurements show that they often behave as conventional spin glasses. As a consequence of frustration, non coplanar ordered phases, are stabilized and the anomalous Hall effect (AHE) can appear due to spin chirality. Three non-coplanar spins $\mathbf{S}_1$, $\mathbf{S}_1$, and $\mathbf{S}_1$ contribute to the AHE with a term which is proportional to the so-defined scalar chirality [52] shown in equation 1.3. Of course, in disordered configurations chirality is locally non-zero, but its average generally vanishes and this contribution can only be observed in systems with long range chiral ordering.

$$\chi_{123} = \mathbf{S}_1 \cdot (\mathbf{S}_2 \times \mathbf{S}_3) \tag{1.3}$$

All this definitions are local, and we are looking for more general definition of magnetic chirality or chirality of a magnetic structure.

Blume-Malayev equation

Blume [48] and Maleyev [49] formulated that the scattered intensity of a polarized neutron beam can be written as in equation 1.4:

$$I = C(|F_N|^2 + \mathbf{F_{M\perp}} \cdot (\mathbf{F_{M\perp}})^* + \mathbf{P} \cdot \mathbf{F_{M\perp}} F_N^* + \mathbf{P} \cdot (\mathbf{F_{M\perp}})^* F_N + \mathbf{P} \cdot (\mathbf{F_{M\perp}} \times (\mathbf{F_{M\perp}})^*) \tag{1.4}$$

In equation 1.4, I is the scattered intensity, F_N is the nuclear structure factor, $\mathbf{F}_{M\perp}$ is the component of the magnetic structure factor which is perpendicular to the scattering vector $\mathbf{q}$ and $\mathbf{P}$ is the polarization of the neutron beam. In

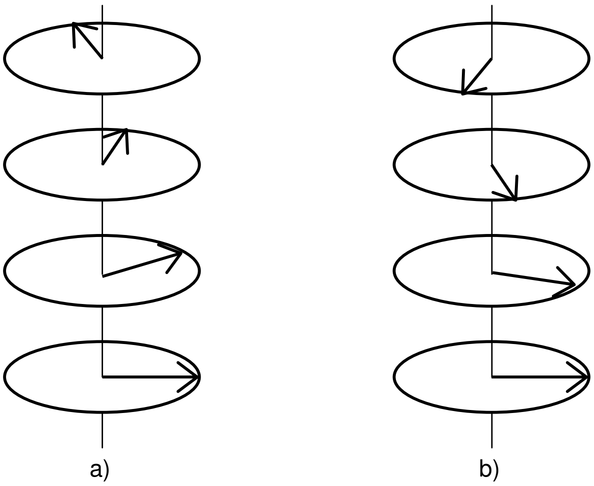

Figure 1.5: Chiral degeneracy in the ordered state of a XY helimagnet.

the cases we have studied, $\mathbf{P}$ is zero as the neutron beam was not polarized. $\mathbf{F}_{M\perp}$ is also called the magnetic interaction vector and is defined as $\mathbf{F}_{\mathbf{M}\perp}(\mathbf{q}) = \mathbf{e} \times \mathbf{F}_{\mathbf{M}}(\mathbf{q}) \times \mathbf{e}$, where $\mathbf{e}$ is a unitary vector in the direction of $\mathbf{q}$. Both the magnetic structure factor and the interaction vector are in general complex vectors. The neutron scattering theory is briefly explained in appendix A.

The term $\mathbf{F}_{\mathbf{M}\perp} \times \mathbf{F}_{\mathbf{M}\perp}{}^*$ is the so-called chiral term. Dra. Clara González adopted in her thesis [31] a definition for chirality based on this term. We will modify this definition in section 2.5 to adopt a global definition for magnetic chirality.

The DM interaction.

A general spin Hamiltonian including the Zeeman term and describing the low-lying states for any pair of interacting magnetic centers A and B, may be written as follows (i. e. see ref. [53]):

$$H = J\mathbf{S}_A{\cdot}\mathbf{S}_B + \mathbf{S}_A\bar{D}\mathbf{S}_B + \mathbf{d}{\cdot}(\mathbf{S}_A \times \mathbf{S}_B) + \beta(\mathbf{S}_A{\cdot}\mathbf{g}_A + \mathbf{S}_B{\cdot}\mathbf{g}_B)\mathbf{H} \qquad (1.5)$$

In equation 1.5, there are several terms:

- The first term refers to the isotropic exchange interaction, which lines up the spins of the magnetic atoms. This term is characterized by the exchange constant J, which gives the strength of the magnetic interaction, and can be either positive or negative depending on the nature of the interaction. If the interaction is ferromagnetic J is positive, while for antiferromagnetic couplings J will take negative values.

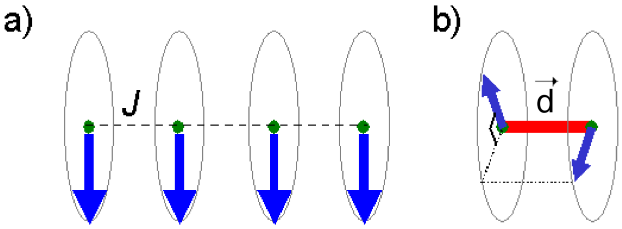

Figure 1.6: a) Example of a ferromagnetic interaction b) Example of DM interaction

- The second term describes both the dipolar and the anisotropic interaction, characterized by the tensor $\bar{D}$. The dipolar interaction arises from the influence of the magnetic field created by one of the magnetic ions on the magnetic moment due to the other. The anisotropic interaction results from the combined effects of the local spin-orbit coupling and the interaction between the magnetic center.

- The third term refers to the antisymmetric interaction called the Dzyaloshinski-Moriya interaction (DM) that will be further explained in this section.

- The last term refers to the Zeeman term, which describes the splitting of the spectral lines of an atom in the presence of a strong magnetic field. This effect is due to the distortion of the electron orbitals in the presence of a magnetic field.

We are specially interested in the term referred to the DM interaction. This interaction results from the anisotropic exchange interaction which is a combined effect of the spin-orbit coupling and the exchange interaction. It was first proposed by Dzyaloshinsky [54] using symmetry arguments, and then analyzed by Moriya [55, 56].

According to the DM term in equation 1.5, the energy due to this term is minimized when the cross product of spins is as big as possible and its sign is opposite to **d**. This can be reached by spins 90^o apart and lying in a plane perpendicular to **d**. To minimize the DM interaction, spins tend to form non collinear spin structures. Therefore, as can be seen in figure 1.6, DM compete with the isotropic exchange interaction that tends to form collinear magnetic structures. DM interaction is responsible for weak ferromagnetism, as it favors a canted spin arrangement instead of a collinear one.

In a crystal, the DM interaction depends on the sites in which the magnetic atoms are, i.e. it depends on the crystal symmetries. The vector **d** is determined by the fact that the energy of the system must remain invariant to the symmetry transformations of the crystal. Moriya [55] published the symmetry rules which control **d**. Calling AB the line joining two atoms i j, and C its midpoint, the following rules applied to **d**:

- $\mathbf{d} = \mathbf{0}$ if a center of inversion was located at C.
- $\mathbf{d} \perp AB$ if a mirror plane perpendicular to AB passed through C.
- $\mathbf{d}\perp$ to a mirror plane if the mirror plane included AB.
- $\mathbf{d}\perp$ to a two-fold axis if the two-fold rotation axis was perpendicular to AB at C.
- $\mathbf{d} \parallel AB$ if AB was an n-fold rotation axis for $n \geqslant 2$.

However, these rules do not include all the cases, and then theoretical calculations are needed.

As it will be see in section 2.5, no-collinearity is a requisite for magnetic chirality. The DM interaction could cause a canting in the magnetic moments, which could produce a magnetic chiral structure (see section 2.5). All the compounds shown in this thesis have nuclear chirality, and they do not present an inversion centre between the magnetic atoms, so DM may exist.

1.3 Chiral Molecular Magnets

Historically, the interest in looking for chiral compounds was centered on organic molecules and drugs, for the important role that chirality plays in life, e. g., biological molecules use only left-handed amino acids and only right-handed sugars. Progressively, interest has spread towards new fields of chemistry like organometallic and coordination compounds [57–59], metal nanoparticles [60] and molecular materials [25]. One reason for the increasing interest in chiral compounds lies on their unique properties. The non-centrosymmetric (polar or enantiomorphous) nuclear structure of a compound will determine some of their possible properties, such as [26]:

- Piezoelectric effect. Ability to generate an electric potential in response to applied mechanical stress
- Natural Optical Activity (NOA).Rotation in the polarization of transmitted light due to the spatial symmetry breaking.
- Pyroelectricity. Ability to generate an electric potential when the material is cooled or heated.

- Second Harmonic Generation. Induction of light waves of twice the frequency due to the nonlinear optical susceptibility, just by making the light pass through a chiral material.

In table 1.1, the occurrence of these phenomenons in non-centrosymmetric crystal classes can be seen.

Especially, because most of the molecule-based materials are transparent to the light, in recent years optical properties of them have attracted much attention. As it has been said before, a compound crystallized in a non-centrosymmetric group can present NOA. According to the table 1.1, the 11 enantiomorphous group and 4 polar groups show this effect. Due to the spatial symmetry breaking, there is a difference between the refractive indexes for left circularly polarized light and right circularly polarized light (n_L and n_R). This difference causes a levo- or dextro- rotation in a beam of linearly polarized light that passes through a medium that exhibits NOA.

Another phenomenon that appears in all the material (chiral or achiral) under an applied magnetic field is the magnetic optical activity (MOA). Due to the time reversal symmetry breaking, the material presents different absorption and reflection coefficients depending on if the wave vector of the light is parallel or antiparallel to the magnetic field applied. This effect was first observed by Faraday [61].

If we break both symmetries (spatial and temporal) simultaneously, a new effect called magnetochiral anisotropy (MChA) will appear even when the medium interacts with non-polarized light. This effect was predicted 20 years ago [62, 63], but wasn't observed until 1997 by Rikken and Raupach [27]. They observed that a static magnetic field parallel to the propagation direction of an incident beam could produce a small shift in the value of the absorption coefficient of a chiral molecule. The sign of the shift changes for light propagating parallel or antiparallel to the magnetic field direction or by replacing the chiral molecule by its enantiomer. The effect is called magnetochiral dichroism (MChD) in absorption or transmission and magneto-chiral birefringence in refraction. The MChA can be explained by an additional term $\mathbf{k} \cdot \mathbf{B}$, where $\mathbf{k}$ is the wave propagation vector, in the dielectric tensor of chiral media subject to a magnetic field. The essential features of MChA are its dependence on the relative orientations of $\mathbf{k}$ and $\mathbf{B}$, the dependence on the handedness of the chiral medium (enantioselectivity) and its independence on the polarization state of light (dextro or levo).

The phenomenon of MChA has been observed in paramagnetic [3, 27, 64] and diamagnetic [65] enantiopure systems, but it is enhanced in enantiopure chiral ferromagnets. The MChA in the magnetically ordered phase for the com-

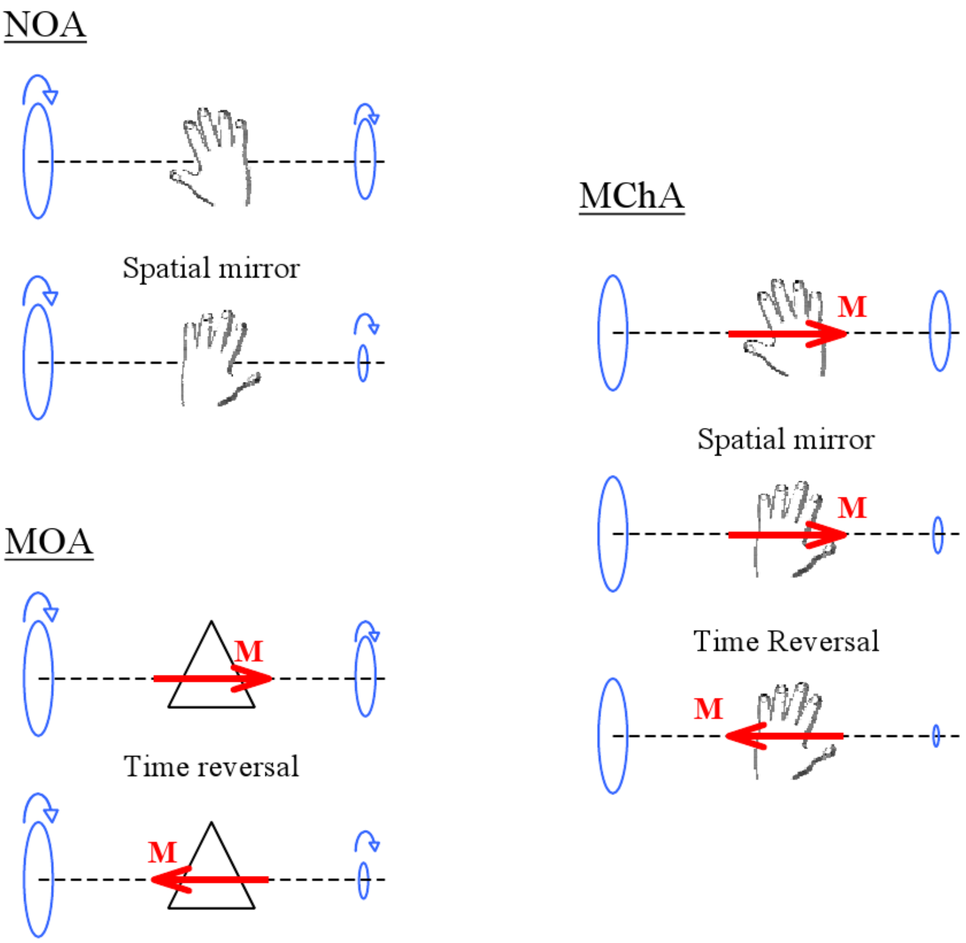

Figure 1.7: Schematic representation of NOA in an enantiopure medium using circularly polarized light , of MOA in a magnetic medium using circularly polarized light and of MChA in an enantiopure magnetic medium using unpolarized light.

pound $[N(CH_3)(n-C_3H_7)_2(s-C_4H_9)][MnCr(ox)_3]$, is a factor of 17 bigger than in the paramagnetic phase [28]. The bistability inherent to the existence of a magnetically ordered state opens the possibility to employ such materials for data storage with a detection based in MChD instead of magnetic circular dichroism. Moreover, as ferromagnetic chiral media are magneto-electric, it is possible electrical reading/writing of the magnetic state of the medium [29, 30]. These compounds will certainly bring new physics into sight, like new universality classes with new critical exponents. Materials of this category are not only interesting from a scientific point of view but the may also open an area for new applications [28].

We are going to focus our efforts in studying chiral molecular magnets, which present not only a chiral nuclear structure, but also a magnetic chiral structure. The coexistence of both chiralities in a magnetic ordered phase can make appear interesting properties, as an increased MChD, or open new horizons.

1.3.1 Synthesis Strategies

Despite a large amount of interest, until now not many molecular candidates likely to exhibit both chiralities have been synthesized, due to the difficulty to control the chirality, not only in the molecular structure, but also in the entire crystal structure. To obtain nuclear chiral compounds, several strategies can be followed [2]:

- Rely on spontaneous resolution process starting from achiral building blocks. This approach can hardly be considered a rational strategy. Nevertheless, some families have been synthesized in this way [66, 67].

- Use chiral ligands bearing unpaired electrons (chiral radicals) to build chiral molecule-based magnets through the metal-radical approach. This strategy presents the advantage that the synthesis of the enantiopure organic molecules acting as radicals is well documented. The main problem of this approach is that is has essentially led to 1D crystallographic structures [68, 69].

- Use chiral bridging ligands from the chiral pool. Using an available enantiopure molecule facilitates the synthesis and may allow to increase the dimensionality. This technique has lead to the synthesis of extended 2D and 3D coordination networks, e. g., (L)-mal ion [70], (L)-tartrate ion [71]. It has the inconvenience that if homometallic networks are synthesized, the antiferromagnetic exchange interaction is favored.

- Associate the chiral coligand with achiral connectors to build chiral extended networks. In order to increase the dimensionality of networks and have interesting magnetic properties, bridging ligands that transmit the exchange interaction are desirable. This technique has been used to synthesized the compounds studied in this thesis, that are described in the next section.

- Master the configuration of intrinsically chiral networks by enantioselective self-assembly. Although this method can not be considered a rational strategy because the absolute configuration of the coordinated metal ions can not be controlled a priori, a clear successful example is the oxalate family [72–74].

In order to obtain chirality not only in the nuclear structure, but also in the magnetic structure, some other considerations have to be taken into account in the synthesis process. If the magnetic structure is collinear the left-handed and right-handed chiral magnetic structures are degenerate and the magnetic structure inevitably becomes achiral. Bearing this in mind, it is apparent that the crystallographic chirality is not always accompanied by the magnetic chirality. In order to obtain molecular magnets where crystallographic and magnetic chirality coexists, we need to control the crystallographic chirality via chemical synthesis, and then manipulate resultant asymmetric exchange interactions (DM interaction or high Jahn-Teller effect). Bearing this in mind, we have pointed our attention towards CN compounds described in the next subsection.

1.3.2 CN based chiral compounds

In order to obtain molecular compounds with a chiral nuclear and magnetic structure that order magnetically, extended multidimensional arrays of paramagnetic metal ions with chiral bridging ligands have been synthesized. Cyanide-bridged Prussian-blue systems are well known for their magnetic ordering at rather high temperatures, because the bridging ligand favors the formation of 2D or 3D networks and transmits well the exchange interaction. A chiral coligand in an enantiopure form is the responsible of transferring its chirality to the metal centre, therefore the crystallographic chirality could be controlled.

The cyanide groups $C \equiv N^-$ are used to bridge two metal ions, as this group has a pair of empty antibonding orbitals. In a Prussian Blue compound, the *M* and *M'* centers are octahedral and connected together by nearly linear $MN \equiv CM'$ cyanide bridges as can be seen in figure 1.9. The different atoms at each end of the cyanide ion have different bonding affinities to metal ions, helping to construct coordination compounds. The *M'* atom, which is

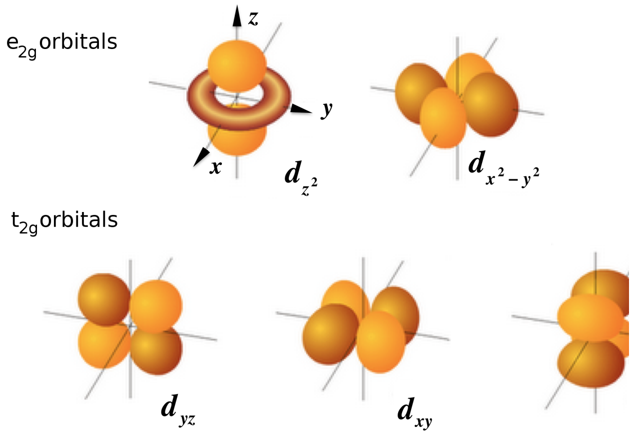

Figure 1.8: Splitting of the energies of the d-orbitals by octahedral crystal fields.

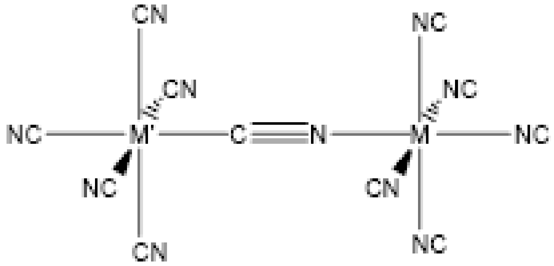

Figure 1.9: Schematic view of two metal centres connected by a cyanide linkage.

surrounded by the carbon atoms of six cyanide ligands, is in a large ligand field. As a result, all known $[M'(CN)_6]$ units are invariably low spin and have electrons only in the t_{2g} orbitals [75]. In contrast, the M atom, which is surrounded by nitrogen atoms of cyanide ligands or oxygen from water molecules, is in a weak ligand field and is almost always high-spin. For the M atoms, it is possible for unpaired electrons to be present only in the t_{2g} orbitals (for d^2 or d^3 ions), only in the e_g orbitals (for d^8 and d^9 ions), or in both the t_{2g} and e_g orbitals (for d^4 through d^7 ions). In figure 1.8 the splitting of the d-orbitals by octahedral crystal fields can be seen.

As magnetic exchange is a short-range phenomenon, in a first order of approximation, we can neglect interactions with second nearest neighbors (which are more than 10Å away) and with more distant magnetic centers. Thus, the analysis reduces to a consideration of the exchange interactions present between two metal centers connected by a cyanide linkage. The nature of the interaction between the two metal center *M* and *M'* (ferromagnetic or antiferromagnetic) arises from the orthogonality of the orbitals of unpaired electrons: mutually orthogonal magnetic orbitals will contribute to the ferromagnetic exchange term, whereas non-orthogonal magnetic orbitals will contribute to the antiferromagnetic term. The net interaction is simply the sum of all the ferromagnetic and antiferromagnetic contributions. One of the most important characteristics of the cyanide compounds is that their magnetic behavior can be predicted. It is therefore possible to tune the material changing the metal ion, its oxidation state and therefore the number of unpaired electrons per site. This is explained by the Goodeneough-Kanamori rules [76]. According to these rules, the exchange interaction between an M and a *M'* metal sites through a linear $M - NC - M'$ fragment can present three situations[75]:

1. If the unpaired electrons of M occupy e_g orbitals, all the exchange interactions with the t_{2g} magnetic orbitals present on $[M'(CN)_6]$ will be ferromagnetic. Thus, if a Prussian Blue is prepared by adding a d^8 or d^9 M cation to a paramagnetic $[M'(CN)_6]$ anion, a ferromagnet should result.
2. If all the unpaired electrons of M occupy t_{2g} type orbitals, all the exchange interactions with the t_{2g} magnetic orbitals present on $[M'(CN)_6]$ will be antiferromagnetic. In this case, if the Prussian Blue is prepared by adding a d^2 or d^3 cation to a paramagnetic $[M'(CN)_6]$ anion, a ferrimagnet should result.
3. If the unpaired electrons of M lie in both t_{2g} and e_g orbitals, ferromagnetic and antiferromagnetic interactions with the t_{2g} magnetic orbitals on $[M'(CN)_6]$ coexist and compete. Here, the overall nature of the interaction is not so simple to predict. Usually, the antiferromagnetic interactions dominate and the solid orders ferrimagnetically.

The compounds belonging to this family are extensively used as pigments and as electrochromic and electrocatalyst materials, and they have shown the capability to exhibit photo-induced properties.

All these characteristics of cyanide-bridged Prussian-blue systems, make them excellent candidates for a smart design of nuclear and magnetic chiral compounds. To assure the presence of magnetic chirality in these compounds, the group of Prof. K. Inoue from the Hiroshima University has developed two synthetic strategies. The simplest one is to make use of a geometric approach using a chiral crystallographic skeleton, like a spiral, where paramagnetic blocks with high magnetic anisotropy, are joined. This skeleton would by itself allow antisymmetric magnetic interactions of DM type. This strategy has been used in the 3D networks $[Cr(CN)_6][Mn(S)-pn]\{(S)-pnH\}_{0.6}K_{0.4}$ (Yellow Needle, YN) [77] and $[Cr(CN)_6][Mn(NH_2-(ala)]_3 \cdot H_2O$ (Similar to Yellow Needle, SYN) [78], where (S)-pn=(S)-1,2-diaminopropane and

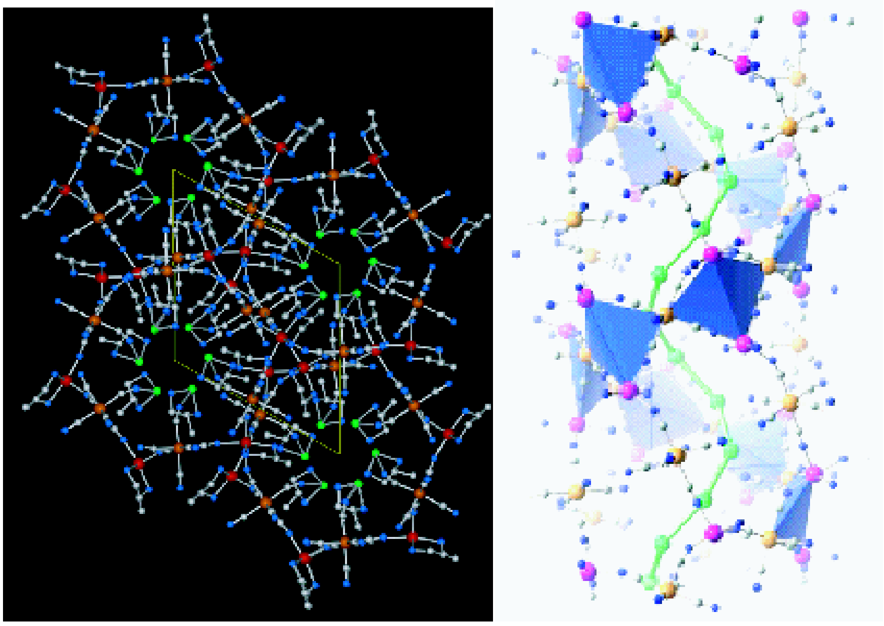

Figure 1.10: A) View of the YN structure along the *c* axis. Some atoms are omitted for clarity. Color scheme: Cr: brown, Mn: red, C: gray, N: blue B) View of the bonding and coordination octahedra of YN. Figure taken from [31]

ala=alanine. The nuclear and magnetic structure for the YN compound can be seen in figures 1.10 and 1.11.

Other possibility used is based on DM interactions along a crystallographic axis in a non-centrosymmetric material, without the need of a chiral skeleton. This second strategy has been followed to form 2D networks as $[Cr(CN)_6][Mn(S)-pnH]$ (denoted as Green Needle, GN, for its shape and colour) [8] and $[W(CN)_8]_4[Cu(S)-pnH_2O]_4[Cu(S)-pn]_2 \cdot 2.5H_2O$ (WCu) [79]. The two chiral compounds studied in this thesis are the result of two modifications in the GN synthesis, $[Mn(CN)_6][Mn(S)pnH(H_2O)]{\cdot}2H_2O$ (GN-MnMn) [6] and $[Cr(CN)_6][Mn(R){-}pnH(DMF)]{\cdot}2H_2O$ (GN-DMF) [7], where DMF stands for N,N-dimethylformamide=$(CH_3)_2N-CHO$. For example, the WCu compound crystallizes in the space group P2_1, being the 2_1 axis parallel to the *b* axis. It is logical to think that the canting of the spins is due to DM vectors induced along the *b* axis.

Both strategies can give rise to materials very different in nature, since in the first one, magnetic chirality arises from the crystallographic geometry, whereas in the second, magnetic chirality is due to the lack of an inversion centre in the material. The nuclear and magnetic structure of some of this compounds (GN, YN and SYN) have been presented and discussed in Dra.

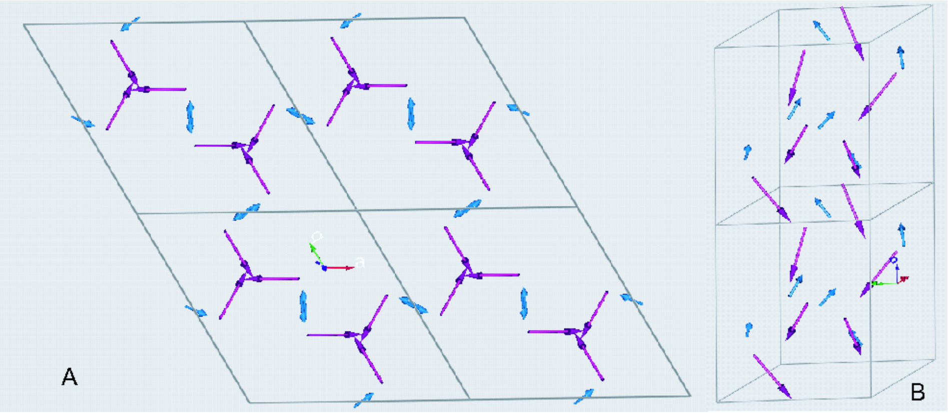

Figure 1.11: A) View along the c axis of YN magnetic structure with Cr atoms in blue and Mn atoms in pink. B) Another view of the structure, with the c axis in vertical to easily see the helixes both types of atoms are displaying. Figure taken from [31]

Clara Gonzalez's thesis [31]. Due to the likeness between GN and the compounds studied in this thesis, a brief summary about the GN nuclear and magnetic structure and properties is provided in the next subsection.

GN

The GN compound has been widely studied [8, 32, 33, 80–83]. It was synthesized in 2003 by Inoue and coworkers [8]. In figure 1.12, an ORTEP drawing of the asymmetric unit of the compound can be seen. Four cyanide groups in the $[Cr(CN)6]^{3-}$ ion are linked to Mn^{II} ions to form a bimetallic network, which is arranged almost perpendicular to the c axis. The compound crystallizes in the space group $P2_12_12_1$ and shows two sublattices, one of Cr^{III} and another of Mn^{II}. It presents three different phases which are interconvertible (a scheme can be seen in figure 1.13). Each phase is magnetic at low temperature, with critical temperatures of T_c=38K, 39K and 73K for the Phases I, II and III, respectively. All the critical temperatures are remarkably high for a metal-organic molecular magnet. The three phases can be transformed into one another, differing mainly in the position of the chiral carbon and also in the water content. Magnetization measurements reveal a ferrimagnetic ordering. Chirality in the magnetic structure was at first suggested by the enhanced magnetic circular dichroism near T_C. AC susceptibility measurements show an unusual behavior between 34K and 38K, as can be seen in figure 1.14 [84].

In Dra. Clara Gonzalez thesis [31], the three phases were studied by single crystal neutron diffraction experiments performed in VIVALDI and D10 at

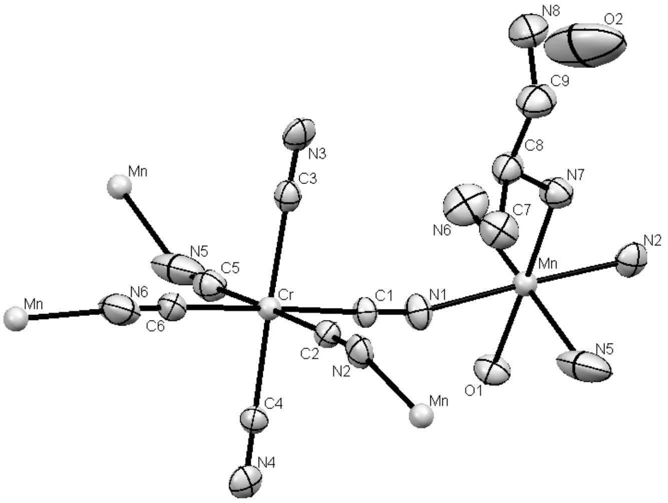

Figure 1.12: ORTEP drawing of the asymmetric unit of the GN compound. Hydrogen atoms are omitted for simplicity.

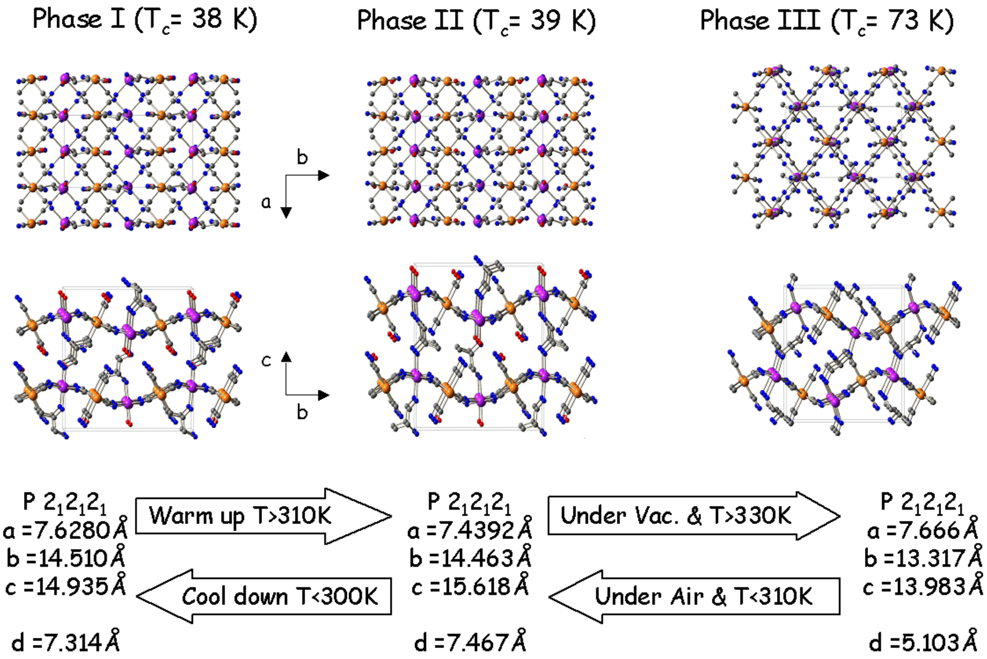

Figure 1.13: Scheme of the transformation of the phases in GN compound. The lattice parameters and the interlayer distance between Cr and Mn are shown. Figure taken from [31]

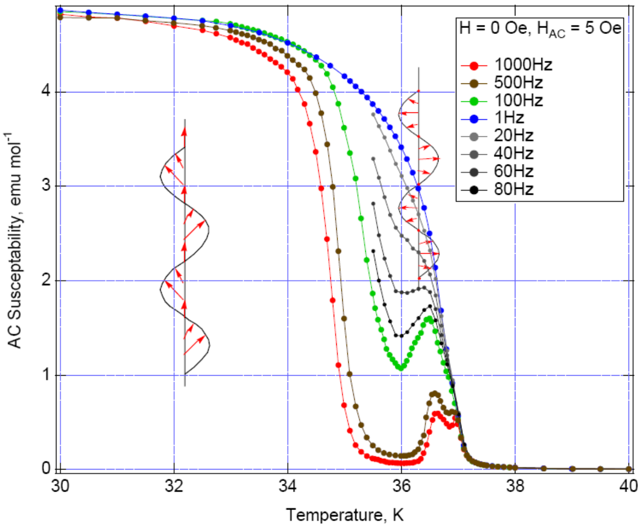

Figure 1.14: Ac susceptibility measurements of GN at frequencies between 1 Hz and 1 kHz and zero applied dc field. Figure taken from [84]

the ILL. The nuclear phases were refined, and the magnetic structures were determined.

Phases I and II consist of planes containing Cr^{III} and Mn^{II} octahedra linked by CN groups, where the Mn^{II} ion is also attached to a water molecule. In contrast, in Phase III there are no water molecules, and the Mn^{II} ion is linked to six CN groups, one of which is also linked to the diaminopropane moiety. As a consequence of the loss of water, the distances between magnetic atoms in the same plane and from one plane to the neighboring plane, which are similar for Phases I and II, they are much smaller for Phase III. Among the three phases, Phase I presents a more similar structure to GN-MnMn and GN-DMF. For this reason, some of its features are described in this section.

As the distortion of the environments of magnetic atoms may be important in order to compare the magnetism of GN with the magnetic behavior of Gn-MnMn and GN-DMF, the distances and angles for Cr^{III} and Mn^{II} octahedra can be found in table 1.2. Another factor that could be important, is the distance between magnetic atoms in the same plane and from one plane to the neighboring one. For Phase I, the distances are listed in table 1.3.

A propagation vector equal to zero was found for the three phases and the magnetic structures agree with the previous magnetic measurements performed in single crystals. The structures for the three magnetic phases all correspond to two sublattices, one of chromium and the other one of manganese disposed ferrimagnetically with respect to each other. For Phases I and II the magnetic structure can be described by the Irreducible Representation Γ_4, which allows

Table 1.2: Bond lengths and angles for Cr^{III} and Mn^{II} octahedra at 43K. Data obtained in D10.

A-X-B	d_{A-X}Å	d_{B-X}Å	$\widehat{AXB}$
C1-Cr-C6	2.126(8)	2.023(8)	177.8(5)
C2-Cr-C5	2.006(7)	2.084(7)	177.0(4)
C3-Cr-C4	2.009(7)	2.033(7)	173.2(4)
N1-Mn-N5	2.125(7)	2.186(7)	178.1(3)
N2-Mn-N6	2.163(7)	2.224(7)	177.2(3)
N7-Mn-O1	2.327(7)	2.239(7)	177.8(4)

A-X-B	$\widehat{AMnB}$	A-Mn-B	$\widehat{AMnB}$
C4-Cr-C5	90.69	O1-Mn-N2	86.13
C4-Cr-C1	87.08	O1-Mn-N5	95.85
C4-Cr-C2	86.48	O1-Mn-N6	92.56
C4-Cr-C6	90.80	O1-Mn-N1	82.23
C3-Cr-C6	95.34	N7-Mn-N3	93.38
C3-Cr-C5	90.83	N7-Mn-N5	86.29
C3-Cr-C1	86.76	N7-Mn-N6	88.02
C3-Cr-C2	91.88	N7-Mn-N1	95.64
C6-Cr-C5	92.23	N1-Mn-N2	90.02
C5-Cr-C1	88.50	N3-Mn-N5	90.11
C1-Cr-C2	90.37	N5-Mn-N6	87.54
C2-Cr-C3	91.88	N6-Mn-N1	92.28

Table 1.3: Shortest distances between magnetic atoms in the same layer (intra) and from different layers (inter). Data obtained in D10 at 43K.

Atoms	d Å
Cr-Mn(Intra)	5.268(2)
Cr-Cr(Inter)	8.041(2)
Mn-Mn(Inter)	8.279(3)
Cr-Mn(Inter)	7.285(2)

a ferromagnetic component along the *a* axis, whereas for magnetic Phase III it is Γ_2, which allows a ferromagnetic component along the *b* axis. In table 1.4 the values of the moments found for each magnetic phase are given. The magnetic structure for Phase I is shown in figure 1.15.

The magnetic moments for Mn^{II} and Cr^{III} are nearly along the easy axis *a* and they are almost contained in the basal plane of their octahedra. The magnetic moment of the Mn^{II} is directed almost in the bisectrix between the bonding directions in the basal planes. The magnetic moment of the Cr^{III} cation is directed almost in the bonding direction C1-Cr-C6, being C1-Cr the largest distance between the Cr and their ligand atoms (2.13Å). The net magnetic moment along the *a* axis of different layers is directed towards the same sense of the *a* axis.

The magnetic moments of Cr and Mn atoms are not collinear, they are tilted as can be seen in figure 1.15. This may be due to several factors. Among them the DM interaction, as there is not a symmetry element rules it out. But it could be also explained because of the tilting of the octahedra and the anisotropy of the ions.

Table 1.4: Magnetic moments for Cr and Mn along each axis and the total magnetic moment for the GN compound.

Cation	M_x μ_B	M_y μ_B	M_z μ_B	M μ_B
Cr^{III}	2.6(5)	-1.7(9)	-1.5(8)	3.4(7)
Mn^{II}	4.8(5)	-1.5(9)	-0.8(8)	5(1)

According to the definition of magnetic chirality adopted in Dra. Clara Gonzalez thesis, the compound was found to be magnetically chiral. Our more general definition explained in 2.5, has corroborated that GN is the first molecular magnet where nuclear chirality and magnetic chirality coexist

Several studies about the GN reveal a dynamical anomaly between 37K and 35K [8, 33, 82, 83]. A transition from a commensurate to an incommensurate magnetic phase has been postulated at the magnetic order temperature, which implies the formation of a chiral spin soliton in the lattice [32]. With the aim to observe if the neutron diffraction experiments could corroborate the existence of this reorientation phase, we performed neutron diffraction experiments in D15 at the ILL. We scanned the reciprocal space near the critical temperature region searching for any anomaly. In appendix B more details about this experiment can be found. Due to the estimated relation between the DM interaction and the symmetric exchange: $|\vec{D}| \sim 0.01J$, the length per turn of the spin helix is on the order of 100 lattice parameters. Unfortunately, the resolution needed to separate the main Bragg peaks and satellite peaks in a magnetic structure with a period of $\sim 100 \cdot 15$Å is out of the experimental possibilities for actual neutron diffractometers.

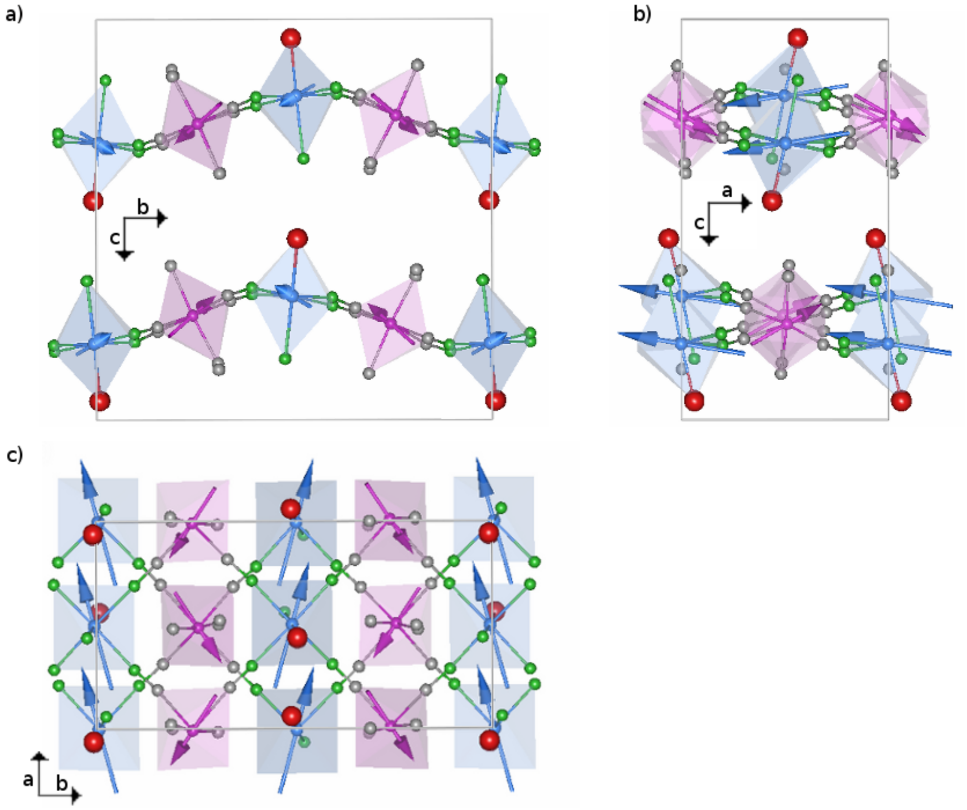

Figure 1.15: Magnetic structure of GN-Phase 1. Views along the a, b and c axes. Mn^{II} atoms are in blue and Cr^{III} atoms are in pink

1.4 Objectives

The general objective of this part of the thesis is to study the coexistence of nuclear and magnetic chirality in new molecular magnets. In particular, we are interested in GN, GN-MnMn and GN-DMF compounds and how structural modifications can influence the magnetic structure, and hence, the magnetic chirality. The main structural difference between GN and GN-MnMn is the substitution of the Cr^{III} cation for the Mn^{III}. We expect that this modification has some influence in the anisotropy and hence in the DM interaction. The substitution of H_2O by a DMF molecule as a ligand of Mn^{II} is the main structural difference between GN and GN-DMF. This modification increases the distance between layers due to the higher volume occupied by the DMF molecule. The separation between layers is expected to have an influence in the magnetic order. The GN-MnMn and GN-DMF compounds are studied in chapters 2 and 3 respectively. Moreover, the racemic form of GN-DMF has been also studied in chapter 3 in order to check if the nuclear chirality may influence the magnetic chirality.

As it has been said in the previous section, some doubts about the existence of a magnetic reorientation phase for the GN were risen from dynamical features. We have also studied the critical temperature region in GN and scaned the reciprocal space searching for an evidence of a magnetic structure with a propagation vector different from zero. The results can be found in appendix B.

In order to perform the magnetic analysis, neutron diffraction experiments have been performed in D15 and VIVALDI at the ILL. From the data acquired the nuclear structures have been refined and, with the help or IR theory, the magnetic structures have been determined. Moreover, due to the lack of a general definition for magnetic chirality, we propose a global definition for chirality and studied in which cases a magnetic structure can present magnetic chirality.

Chapter 2

Neutron study of the $[Mn^{III}(CN)_6][Mn^{II}(S)\text{-}pnH(H_2O)]\cdot 2H_2O$ compound

2.1 Introduction

With the objective of finding nuclear and magnetic chirality in molecular magnets, several compounds belonging to the family of the cyanide-bridged molecular magnets have been studied. This chapter is devoted to the compound $[Mn^{III}(CN)_6][Mn^{II}(S)\text{-}pnH(H_2O)]\cdot 2H_2O$, where (S)-pn=(S)-1,2-diaminopropane, which, for convenience, is denoted as GN-MnMn. This compound is a good candidate to present coexistence of nuclear and magnetic chirality for its similitude with GN compound. It allows us to study the difference between both, GN and GN-MnMn, which lies in the replacement of a Cr^{III} ion for a Mn^{III} ion of different magnetocrystalline anisotropy. In order to refine the nuclear structure and to solve the magnetic one, single-crystal neutron diffraction experiments have been performed in the Laue diffractometer VIVALDI, at the ILL.

The chapter is organized as follows: in section 2.2, the synthesis, the structure solved by X-ray measurements and the magnetization measurements are summarized. Then, in section 2.3, a description of the experiment conducted on the instrument VIVALDI is given. In section 2.4 the results for the nuclear and magnetic structure are shown. Once the magnetic structure is known, in section 2.5, we discuss the existence of magnetic chirality and explain the definition we have adopted for magnetic chirality. Finally, the main conclusions are presented in section 2.6.

2.2 Synthesis, X-ray structure and magnetic characterization

The complex [Mn(CN)$_6$][Mn(S)-pnH(H$_2$O)]·2H$_2$O was synthesized by Prof. M. Ohba and coworkers [6] at the Kyushu University (Japan). Enantiomers of GN-MnMn were obtained as dark-red crystals by the reaction of $MnCl_2{\cdot}4H_2O$, $L \cdot 2HCl$ (where L=S- or R-1,2-diaminopropane), KOH, and $K_3[Mn(CN)_6]$ in the 1:3:5:1 molar ratio. To avoid the oxidation and decomposition of $[Mn(CN)_6]^{3-}$, all the operations for the synthesis were carried out in a deoxygenated aqueous solution with cooling and light shielding. Crystals up to $1mm^3$ in volume were obtained by slow evaporation. The room-temperature crystal data from X-ray structural analysis can be obtained at *www.ccdc.cam.ac.uk/*.

The unit cell is orthorhombic and the space group is $P2_12_12_1$. The lattice parameters at 243K are $a = 7.5145(5)$, $b = 14.261(1)$ and $c = 14.844(1)$. The Mn^{2+} ions are linked to four Mn^{3+} ions by four of the six cyanide groups in the $[Mn(CN)_6]^{3-}$ ion, forming a bimetallic network, which is arranged almost perpendicular to the c axis. The Mn^{2+} ions are also linked to one water molecule and to the amino-acid ligand, which induces the chirality and completes the octahedron. Elemental analysis on samples under vacuum for a few hours at room temperature in order to remove the remaining surface water molecules reveals a number of water which depends on the measurement conditions, but it is at least 1.7 in any cases. This uncertainty in the number of water molecules can be solved with neutron data measurements and was one reasons that motivates our study.

This structure is the same as that of $[Cr(CN)_6][Mn(HL) - (H_2O)] \cdot H_2O$ (GN) except for the number of lattice water molecules [8] and the substitution of Cr^{III} by Mn^{III}. In figure 2.1, an ORTEP drawing of the asymmetric unit of the compound can be seen.

Magnetic behavior of polycrystalline samples have been characterized and published along with the synthesis [6]. At room temperature, the susceptibility value is consistent with the spin-only value expected for magnetically isolated Mn^{II} (S=5/2) and low spin Mn^{III} (S=2/2) ions. A Curie-Weiss plot in the temperature range of 300 -100K gives a Weiss constant of -56 K, which suggests an antiferromagnetic interaction between the adjacent Mn^{II} and Mn^{III} ions through cyanide bridges. Magnetization measurements versus temperature at weak field and plots of the derivative of magnetization with respect to temperature shows a magnetic phase transition temperature of 21.2K, as can be seen in figure 2.2.

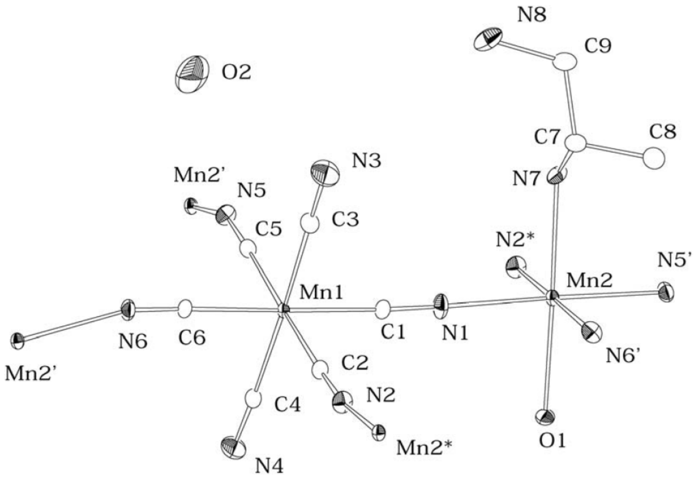

Figure 2.1: ORTEP drawing of the asymmetric unit of the compound $[Mn^{III}(CN)_6][Mn^{II}(S)pnH(H_2O)]{\cdot}2H_2O$. Taken from [6].

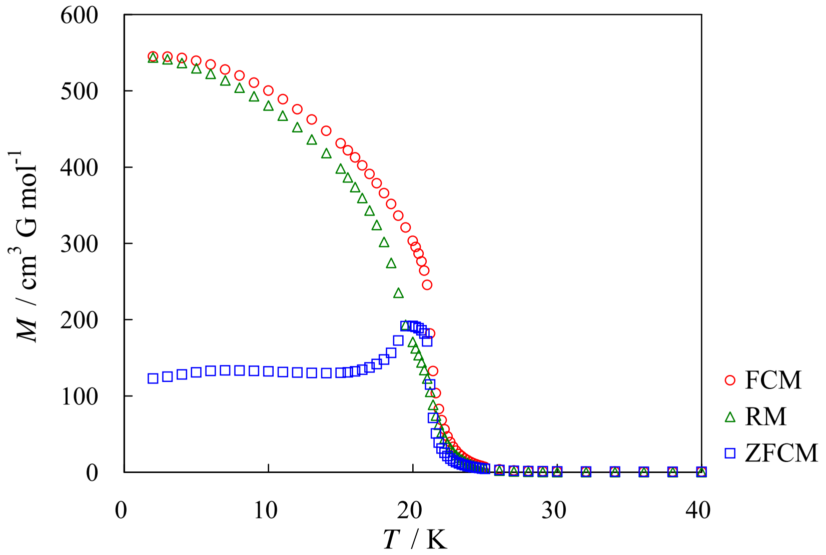

Figure 2.2: Weak field magnetization of GN-MnMn under an applied field of 5G. Adapted from [6].

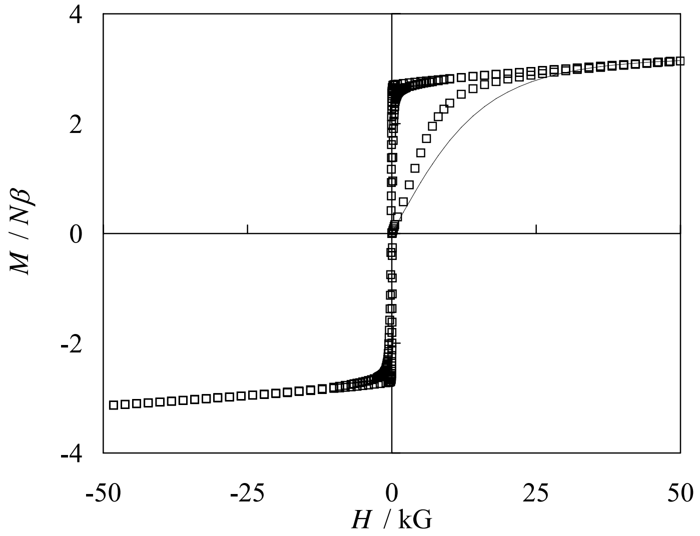

Figure 2.3: Magnetic hysteresis loop for GN-MnMn at 2 K. Solid line expresses Brillouin function for S=3/2 with g=2.14. Adapted from [6]

A magnetic hysteresis loop is given in figure 2.3. The saturation magnetization value per unit formula at 50 kG is around $3.1\mu_B$, which corresponds to the value of S=3/2 expected for antiferromagneticallym coupled Mn^{II} and Mn^{III} with an average g value of 2.12 and 2.14, respectively. Coercive fields has been determined to be 120 G.

Susceptibility measurements in the presence of an AC magnetic field of 3 G show an increase in the in-phase signal and out-of phase signal below 21.2K, as can be seen in figure 2.4. The in-phase signal (χ') presents a peak at 20.8K with a shoulder around 19.6 K which depends of the frequency. The out-phase signal have a frequency-dependent peak at 19.1 K with a shoulder around 20 K at low frequency. The curve shape drastically changes with the increase of frequency. Also a small magnetic anomaly was observed around 8 K in the out-phase signal.

The existence of the second peak in the AC signals and the ZFCM and RM curves can indicate a two-step magnetic phase change. Such behavior has not been observed in the GN, suggesting that they would originate from domain dynamics and spin reorientation which correlates with the magnetic anisotropy of Mn^{III} ion and chiral structure.

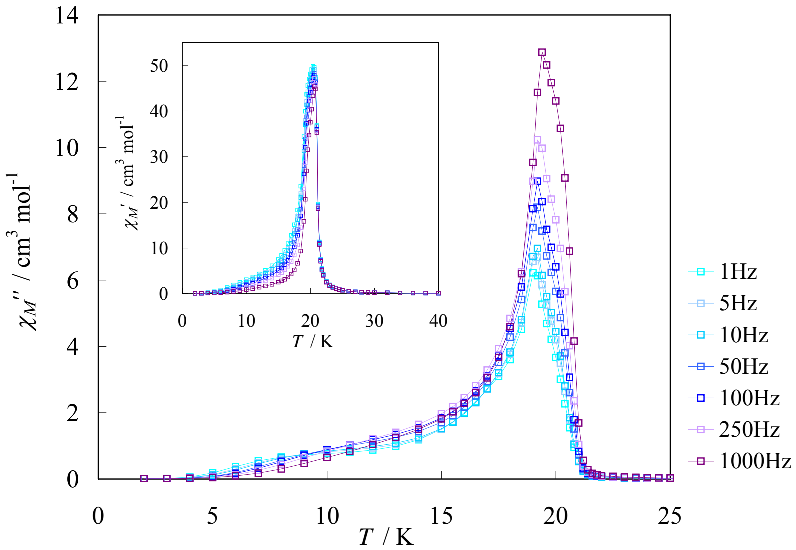

Figure 2.4: Temperature dependence of the AC magnetic susceptibility of GN-MnMn under applied field of AC 3G.

2.3 Neutron Measurements

As it has been previously said, neutron techniques are used to determine the nuclear and magnetic structure of the compounds studied in this thesis. As the scattering length of neutrons is not linearly dependent with Z as happens for photons, neutrons are a very useful tool to determine atomic positions of light elements as hydrogen. This allows us to refine accurately the nuclear structure and to find the positions of hydrogen atoms and water molecules that may affect the magnetic interactions. In fact, the exact number of water molecules presents in GN-MnMn could not have been determined as it depends of the measurement conditions. Neutrons interact not only with atomic nucleus via strong interactions, but also with the magnetic moments of the atoms via dipolar magnetic interactions. For this reason, they can be used to solve the magnetic structure of the compounds (see appendix A for more information about neutron diffraction theory).

Due to the small size of crystals for the GN-MnMn compound, neutron diffractions measurements have been performed only in VIVALDI (see section A.4.2), which can obtain data in a short time for samples up to $1mm^3$. Several patterns have been recorded at 290K and 25K in order to refine the nuclear structure, and some more at 2K to determine the magnetic structure. The experimental procedures followed, the data collection and reduction procedures are described in the next subsection.

2.3.1 VIVALDI. Experimental procedure

A rectangular crystal of 0.8x0.4x0.3mm^3 was attached with vacuum grease to a cylindrical Vanadium pin of 1mm diameter. A standard He-flow ILL "Orange" cryostat, which allows us to reach temperatures between 1.5K and 325K, was used. The final aperture of the neutron incoming beam was chosen to be 3mm in diameter, in order to minimize the ratio of background scattering with respect to the scattering from the crystal.

Patterns were recorder at three temperatures. In order to refine the nuclear structure at room temperature and to find accurately the number of water molecules, data were collected at 295K. The nuclear structure above T_C can be determine from data at 25K, and the magnetic structure has been determined at 2K.

After aligning the crystal and checking the crystal diffraction quality, we cooled down to collect 10 patterns at 25K, at ϕ intervals of 20°, where ϕ stands for the angle of rotation of the crystal around the vertical axis perpendicular to the incident neutron beam. Each pattern was collected for 2 hours. These 10 patterns at 25K allowed us to refine the nuclear structure above T_c. To solve the magnetic structure, the crystal was cooled down the transition temperature. At 2K, 8 patterns were collected for 2 hours each at ϕ intervals of 20°. Finally, to refine the nuclear structure at 290K, seven patterns were recorded, each of them with a exposure time of three hours. The exposition time had to be increased to improve the number of reflections observed at high temperature due to the thermal motion of the atoms.

All the Laue patterns were indexed, as explained in appendix A, using the programm LAUEGEN of the Daesbury Laboratory Laue Suite [85], and the reflections were integrated using a two-dimensional version of the $\sigma(I)/I$ algorithm [86] implemented in the ARGONNE_BOXES program. We didn't correct for absorption due to the small size sample and extinction was considered as negligible. The integrated reflections were normalized to a common incident wavelength, using a curve derived by comparing equivalent reflections and multiple observations, via the programm LAUENORM [87]. The integrated and normalized reflections were used for nuclear structure refinement and magnetic structure determination with SHELX [88] and Fullprof [9] programs.

All relevant experiment details (temperature, exposure times, number of reflections wavelength range,etc...) are summarized in table 2.1.

In figure 2.5 the same pattern collected at 2K and 25K for $\phi = -5^o$ is shown. The crystallinity of the sample was enough to observe clearly the weaker diffraction spots after two hours of exposure, and the patterns show

Table 2.1: Experimental details for GN-MnMn

GN-MnMn VIVALDI			
Chemical Formula	$[Mn^{III}(CN)_6][Mn^{II}(S)pnH(H_2O)]\cdot 2H_2O$		
Lattice, Space	Orthorhombic, $P2_12_12_1$		
a, b, c Å	7.662 14.633 15.003		
Z	4		
Temperature	290K	25K	2K
N^o of patterns	7	10	8
λ_{range} Å	0.92-2.10	0.92-2.10	0.92-2.10
d_{min} Å	0.84	0.62	0.62
Measured reflections	7814	18286	14106
Unique Reflections	1330	2875	2914
$(sin\theta/\lambda)_{max}{}^{-1}$	0.6054	0.8067	0.8235
Resolution Å	0.83	0.62	0.61
θ_{max}	33.8	47.9	49.25
R_{Laue1}	0.218	0.228	0.219
R_{Laue2}	0.204	0.209	0.200
R_{Laue3}	0.157	0.158	0.171
R_σ	0.083	0.104	0.137
hkl range	$0<h<9$	$0<h<11$	$0<h<11$
	$0<l<17$	$0<l<22$	$0<l<22$
	$0<k<17$	$0<k<24$	$0<k<24$

no evidence of twining. The pattern at 2K is indexed, as is shown in the top of figure, with the same lattice parameters as the pattern at 25K, without the presence of any extra peaks or magnetic satellites. This evidences that the magnetic phase has a propagation vector equal to zero.

For the patterns collected at 290K, the exposure time was increased to three hours, due to the thermal motion, which decreases the intensity of the reflections. For this data set, the curve normalization obtained at 25K was used, which allows us to increase the number of accepted reflections to about 600 more. Still, the number of reflections at high temperature, is lower than that at low temperature, which is not due to the number of patterns, because at 2K only one more pattern was recorder, but to a necessary increased in the d_{min} (the minimum distance that can observed, see section A.4.2). In figure 2.6 the normalization curve for 25K is shown. It is easy to see the good quality of the refinement, as the normalization curve is smooth and the number of points where the observed and calculated values coincide on this scale is high,

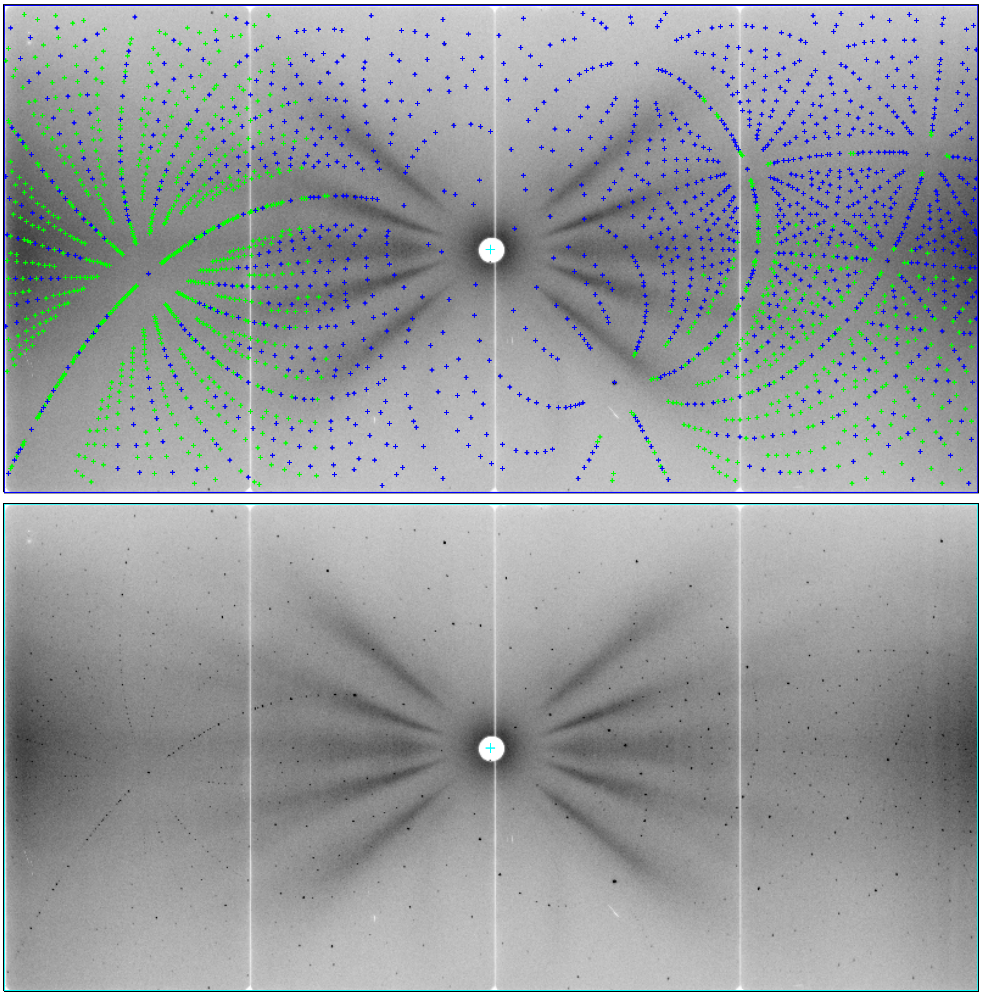

Figure 2.5: Laue patterns for GN-MnMn at T=2K (top) and 25K (bottom) at $\phi = -5^o$. On the top, the pattern at 2K has been indexed with the same lattice parameters as in the paramagnetic phase

and those which do not coincide have close values.

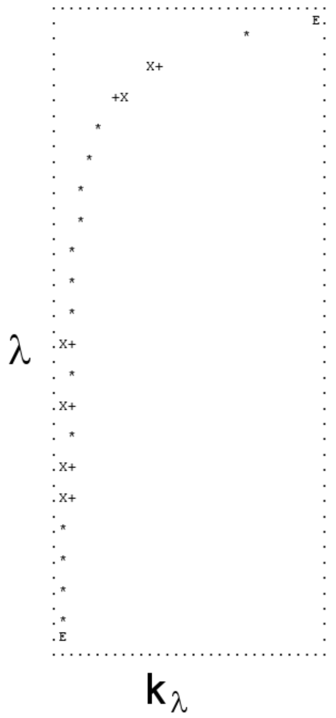

Figure 2.6: Empirical wavelenght normalisation curve for 25K data in VIVALDI. The experimental and theoretical values are shown: E is the extrapolated point on the graph, X the observed point for the curve fitting, + the calculated point from the fitted curve and * are points where the observed and calculated values coincide

2.4 Results

2.4.1 Nuclear phase

The nuclear structure has been refined at 290K and 25K from data collected in VIVALDI. The structure solved at 290K by X-ray measurement [6] was used as starting point for the nuclear refinement. The hydrogen positions were not determined by X-ray and hydrogen atoms were placed in calculated positions. Also, the number of water molecules were not determined. With neutrons, all the atoms have been positioned and thermal parameters refined anisotropically by full-matrix least-squares technique based on F^2 using the programm SHELXL97 [88]. Experimental and refined data from the structural refinements are summarized in table 2.1, and the fractional coordinates and thermal parameters are listed in Appendix C (table C.1 and table C.2).

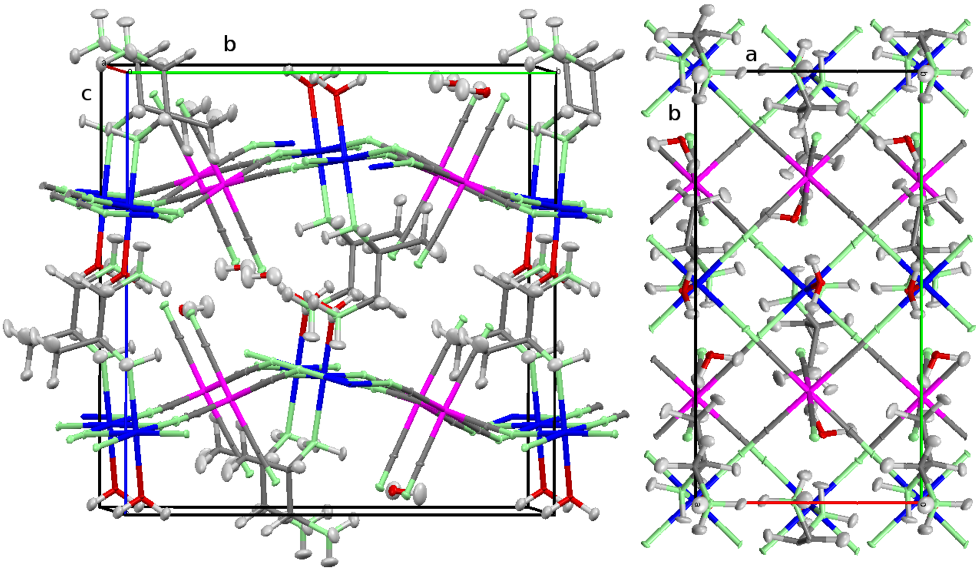

Figure 2.7: View of the nuclear structure of the compound $[Mn(CN)_6][Mn(S)pnH(H_2O)]\cdot 2H_2O$ refined at 25K along the a axis (left) and the c axis (right)

The agreement factors obtained at 290K with SHELX are R=0.0707 for 1103 reflections whose intensity is bigger than 4σ and 0.1009 for all data. At 25K, the agreement factors are R=0.0979 for reflections whose intensity is bigger than 4σ, and 0.1294 for all data. The same factors at 2K for the reflections at $\theta > 30^o$ are R=0.1076 for reflections whose intensity is bigger than 4σ, and 0.1461 for all data. Due to the high-quality of the sample, there is only one restriction in the refinements: the distance between H and O atoms of the water molecule at 290K.

The refined nuclear structure of the compound consists in two bimetallic planes containing Mn^{III} and Mn^{II} atoms in a octahedral environments and linked by cyanide groups. The Mn^{II} atom is also linked to a water molecule. There is one water molecule of crystallization per unit formula, and four per unit cell. The two dimensional networks are arranged almost perpendicularly to the c axis. The nuclear structure refined at 25K can be seen in figure 2.7

At 290K, the reported structure contains and uncertain number of water molecules [6]. Our data analysis shows unambiguously that there is one water molecule per unit formula and four per unit cell. However, the magnitude of the thermal parameters for the water molecule (see table C.2) are indicative of some disorder. We tried to split the atomic positions of the water O and H atoms, but localizations with minimal energy could not be found. The thermal ellipsoids do not present irregular shapes such as cigar or plate shapes. We conclude that disorder is a dynamical disorder because the water molecule has enough space available for motion. There exist several hydrogen bonds between the water molecule and the network (see table 2.2) that justify the water molecule orientation. At high temperature, the dynamical disorder of the water molecule breaks the hydrogen bond $O2 \cdots H2B \cdots N3$, due to the increase in distance between atoms and the misalignment.

At 25K, the thermal parameters of the atoms of the water molecule precludes disorder. All atoms have been refined with anisotropic thermal parameters except Mn^{III}, whose thermal parameter was too low. The hydrogen bonds are also shown in table 2.2.

Table 2.2: Hydrogen bonds for GN-MnMn at 290K, and 25K. The water molecule is constituted by H2A, O2 and H2B atoms. The hydrogen bond $O2 \cdots H2B \cdots N3$ at 290K is broken.

$A \cdots H \cdots B$	T	$d_{A \cdots H}$Å	$d_{H \cdots B}$Å	$\widehat{AHB}$
$N7 \cdots H1 \cdots O2$	295K	1.013(18)	2.13(2)	165.9(15)
	25K	1.047(8)	2.130(9)	162.8(7)
$N8 \cdots H10 \cdots O1$	295K	1.03(3)	1.95(2)	170.4(14)
	25K	1.054(10)	1.902(11)	172.1(8)
$N8 \cdots H11 \cdots O2$	295K	1.03(3)	1.88(3)	170.4(19)
	25K	1.063(10)	1.813(11)	174.2(10)
$O1 \cdots H12 \cdots N3$	295K	0.93(2)	1.790(16)	173.2(17)
	25K	1.003(11)	1.816(10)	175.4(9)
$O1 \cdots H13 \cdots N4$	295K	0.96(2)	1.858(18)	169.8(17)
	25K	1.001(10)	1.844(9)	168.2(9)
$O2 \cdots H2A \cdots N3$	295K	0.89(3)	2.37(2)	152(3)
	25K	0.971(12)	2.299(12)	150.4(11)
$O2 \cdots H2B \cdots N3$	290K	0.918(2)	3.31(4)	127.3(9)
	25K	0.960(13)	2.141(12)	166.1(9)

The Mn^{III} and Mn^{II} are in an octahedral environment. The distortion of their octahedra may be relevant for the magnetic behavior of the compound, so it can be seen in table 2.4. The distance and angles are similar to what has been found in another compounds. We can calculate the distortion of each octahedra by using the equation 2.1. The values obtained are shown in table 2.4.

$$\Delta_d = \frac{1}{6} \cdot \sum_{i=1}^{6} \frac{d_i - \bar{d}^2}{\bar{d}^2} \tag{2.1}$$

Table 2.3: Bond lengths and angles for Mn^{III} and Mn^{II} at 25K.

A-Mn-B	d_{A-Mn}Å	d_{B-Mn}Å	$\widehat{AMnB}$
C1-Mn^{III}-C6	2.021(7)	2.014(7)	178.4(4)
C2-Mn^{III}-C5	2.013(7)	2.024(7)	178.2(4)
C3-Mn^{III}-C4	2.018(7)	2.043(7)	177.1(4)
N1-Mn^{II}-N5	2.238(7)	2.241(7)	177.1(3)
N2-Mn^{II}-N6	2.234(7)	2.250(7)	177.2(3)
N7-Mn^{II}-O1	2.347(7)	2.291(7)	177.8(4)

A-Mn-B	$\widehat{AMnB}$	A-Mn-B	$\widehat{AMnB}$
C4-Mn^{III}-C5	88.87(4)	O1-Mn^{II}-N2	94.78(4)
C4-Mn^{III}-C6	87.87(4)	O1-Mn^{II}-N5	91.76(4)
C4-Mn^{III}-C2	92.93(4)	O1-Mn^{II}-N6	82.53(4)
C4-Mn^{III}-C1	93.66(4)	O1-Mn^{II}-N1	85.31(4)
C3-Mn^{III}-C6	89.48(4)	N7-Mn^{II}-N2	87.16(4)
C3-Mn^{III}-C5	89.97(4)	N7-Mn^{II}-N5	89.45(4)
C3-Mn^{III}-C1	88.98(4)	N7-Mn^{II}-N6	95.54(4)
C3-Mn^{III}-C2	88.23(4)	N7-Mn^{II}-N1	93.49(4)
C6-Mn^{III}-C5	88.90(4)	N1-Mn^{II}-N2	92.21(4)
C5-Mn^{III}-C1	90.55(4)	N2-Mn^{II}-N5	87.73(4)
C1-Mn^{III}-C2	89.47(4)	N5-Mn^{II}-N6	91.64(4)
C2-Mn^{III}-C6	91.04(4)	N6-Mn^{II}-N1	88.28(4)

Table 2.4: Distortion calculated of the octahedral environment for GN and GN-MnMn magnetic atoms at 43K for GN and 25K for GN-MnMn.

Cation	Δ_d
GN Cr^{III}	$4.6{\cdot}10^{-4}$
GN Mn^{II}	$8.4{\cdot}10^{-4}$
GN-MnMn Mn^{III}	$2.5{\cdot}10^{-5}$
GN-MnMn Mn^{II}	$3.2{\cdot}10^{-4}$

If the octahedral environment of Cr^{III} in GN and Mn^{III} in GN-MnMn are compared, we found that the distortion of the Cr^{III} octahedra is one order of magnitude higher. The C-M^{III}-C angles for no opposite C atoms, are in the range 95.3^o-86.5^o for the GN and 93.7-87.9^o for the GN-MnMn. The C-M^{III}-C angles for opposite C atoms are in the range 173.2^o-178.1^o for the GN and 177.1^o-178.4 for the GN-MnMn. The explanation of this difference can not be related to the Jahn-Teller effect. In the case of octahedral coordination, the Jahn-Teller effect is more pronounced when an odd number of electrons occupies the e_g orbitals, as in complexes with the configurations d^9, low-spin d^7 or high-spin d^4 complexes, all of which have doubly degenerate ground states [76]. In such compounds, the e_g orbitals involved in the degeneracy point directly at the ligands, so distortion can result in a large energetic stabilization. Strictly speaking, the effect also occurs when there is a degeneracy due to the electrons in the t_2g orbitals (i.e. configurations as d^1 or d^2, both of which are triply degenerate). However, the effect is less noticeable in the last cases, because the t_2g orbitals do not point directly at the ligands. The Cr^{III} has a d^3 electronic configuration and Jahn-Teller effect is not present. The Mn^{III} has a d^4 electronic configuration in a low-spin configuration in this compound, so the expected Jahn-Teller effect is small [89]. As the ligands of Cr^{III} and Mn^{III} are the same in both compounds, this difference may be attributed to some effect related with the cation substitution.

In addition to distortions in the octahedral environment, the distances between magnetic atoms in the same plane or from different planes are very relevant, because they can influence on the magnetic ordering. They can be seen at table 2.5 for the nuclear structure of Gn-MnMn refined at 25K. If we compare them with the distances found for the GN compound at 43K shown in table 1.3, we find that the intralayer Mn^{III}-Mn^{II} distance in GN-MnMn (5.25Å) is similar to the equivalent Cr-Mn (5.27Å) distance in GN compound. The interlayer distances between magnetic atoms are also similar tin both compounds.

Table 2.5: Shortest distances between magnetic atoms in the same layer (intra) and from differents layers (inter).

Atoms	d (Å)
Mn^{III}-Mn^{II}(Intra)	5.2528(5)
Mn^{III}-Mn^{III} (Inter)	8.098(1)
Mn^{II}-Mn^{II}(Inter)	8.359(1)
Mn^{III}-Mn^{II}(Inter)	7.358(1)

2.4.2 Magnetic phase

This subsection is devoted to the analysis of the magnetic structure of GN-MnMn. Due to the small size of crystals of GN-MnMn obtained ($\sim 1mm^3$), we have performed our experiments in VIVALDI, where samples up to $\sim 1mm^3$ can be measured. However, VIVALDI is not the best neutron diffractometer to solve magnetic structures, specially if the propagation vector is equal to zero (see chapter A.4.2). This limitation is inherent to VIVALDI. Due to its geometry and λ range, VIVALDI does not allow to observe reflections at very low angle because they are very close of the beam. In addition to this geometrical limitation, the reflections that we can detect at low angle, present the problem of the chromatic overlap. As the magnetic contribution to the reflections intensity decreases with high θ, solving magnetic structures in VIVALDI is not immediate. In spite of this difficulty, we have solved the magnetic structure with a procedure described in the next paragraphs.

In order to solve the magnetic structure is advisable to refine accurately the nuclear structure. To refine the nuclear structure at 2K, we have sorted our data two groups: high θ reflections (θ>30^o) and low θ reflections (θ<20^o), and use the hight θ reflections for the nuclear refinement . Such distinction is due to the fact that the magnetic form factor decreases for high $\mathbf{q}$, therefore, the magnetic contribution to the diffracted intensity becomes negligible at high values of θ. The choice of the θ limits has been done according to our own experience in neutron diffraction and after comparing the intensity of reflections at 25K and 2K. We have considered that the magnetic contribution to the diffracted intensity is negligible for reflections above θ>30^o. With these considerations and starting from the nuclear structure at 25K, we have used the reflections at θ>30^o to refine the atomic positions and thermal parameters of all atoms in SHELX (see tables C.1 and C.2 in appendix C). The agreement factor for the nuclear refinement at 2K is R=0.1076 for reflections whose intensity is bigger than 4σ.

Once that the nuclear structure at 2K has been refined using the high θ reflections, we can determine the magnetic structure. The refinement of the magnetic data was guided by the irreducible representation (IR) theory (for more information, see section A.5). According to this, the first step is the identification of the propagation vector $\mathbf{k}$. For this compound, we have determined that $\mathbf{k} = \mathbf{0}$ because the patterns at 2K have been indexed with the same cell parameters as the paramagnetic phase. The second step is the determination of the little group of vector $\mathbf{k} = \mathbf{0}$ and its IRs with the help of BASIREPs code. This method is based in the procedure of ZAK provided within the program KAREP [90] and has been adapted by Juan Rodriguez-Carvajal and included in the FULLPROF suite. For the GN-MnMn, four different one-dimensional IRs were obtained, called Γ_1, Γ_2, Γ_3 and Γ_4 in the notation of Kovalev. Each of them is included three times in the reducible magnetic representation Γ. The basis vectors for these irreducible representations are listed in table 2.6

As SHELX can not refined magnetic structures, we have used the FULLPROF programm to determine which IR describes the magnetic symmetry of Gn-MnMn and to refine the magnetic moments of the atoms. For this purpose,

Table 2.6: Irreducible Representations for GN-MnMn and their basis vectors. m_1, m_2, m_3 and m_3 represent the magnetic atoms of each magnetic specie.

Atom	Position	Γ_1	Γ_2	Γ_3	Γ_4
$\mathbf{m}_1$	(x,y,z)	(u, v, w)	(u, v, w)	(u, v, w)	(u, v, w)
$\mathbf{m}_2$	(-x+1/2,-y,z+1/2)	($\overline{u}$, $\overline{v}$, w)	($\overline{u}$, $\overline{v}$, w)	(u, v, $\overline{w}$)	(u, v, $\overline{w}$)
$\mathbf{m}_3$	(-x,y+1/2,-z+1/2)	($\overline{u}$, v, $\overline{w}$)	(u, $\overline{v}$, w)	($\overline{u}$, v, $\overline{w}$)	(u, $\overline{v}$, w)
$\mathbf{m}_4$	(x+1/2,-y+1/2,-z)	(u, $\overline{v}$, $\overline{w}$)	($\overline{u}$, v, w)	($\overline{u}$, v, w)	(u, $\overline{v}$, $\overline{w}$)

we have used the reflections measured at θ<30º, and it has been possible to determine and refine the magnetic structure. The two magnetic sites, Mn^{III} and Mn^{II}, order in the same IR Γ_4, that is the same IR that we found for the Phase I of GN. The magnetic moments for Mn^{II} and Mn^{III} along each axis and the total magnetic moment obtained are shown in table 2.7. The magnetic agreement factor for the reflections at θ<20º is R_{Mag}=7.24.

The magnetic structure consist in two sublattices, one of Mn^{II} and one of Mn^{III} as it is shown in the figure 2.8. According to the Goodeneough-Kanamori rules [76] explained in section 1.3.2, the two sublattices order antiferromagnetically one respect to the other. It is due to the fact that the unpaired electrons of Mn^{II} lie in t_{2g} and e_g orbitals, so the Mn^{II}-Mn^{III} interaction is antiferromagnetic. The IR Γ_4 allows a ferromagnetic component parallel to the *a* axis, which is the easy axis. As *v* and *w* are of the same order and due to the symmetry imposed by Γ_4, the magnetic structure can be seen as spins along the *a* axis describing a spiral and turning around 90º as can be seen in figure 2.9. As in the GN compound, the magnetic moments of Cr and Mn atoms are not collinear, which may be caused by the DM interaction, because there is not a symmetry element that can discard it, or by the anisotropy of the ions. The net magnetic moments along the *a* axis of different layers are directed in the same sense.

Table 2.7: Magnetic moments for Mn^{II} and Mn^{III} atoms placed in (x, y, z)

Atom	u	v	w	$\mathbf{m}\mu_B$
Mn^{II}	-4.5(2)	-1.1(5)	-0.8(9)	4.7(3)
Mn^{III}	2.2(2)	1.0(3)	0.7(8)	2.5(3)

In order to discuss the validity of the magnetic moments found, we revise the magnetochemistry of both magnetic ions, Mn^{III} (d^4) and Mn^{II} (d^5) in an octahedral environment. In an octahedral symmetry the d-orbitals split in the energy levels as shown in figure 1.8. Mn^{II} in a low ligand field octahedral

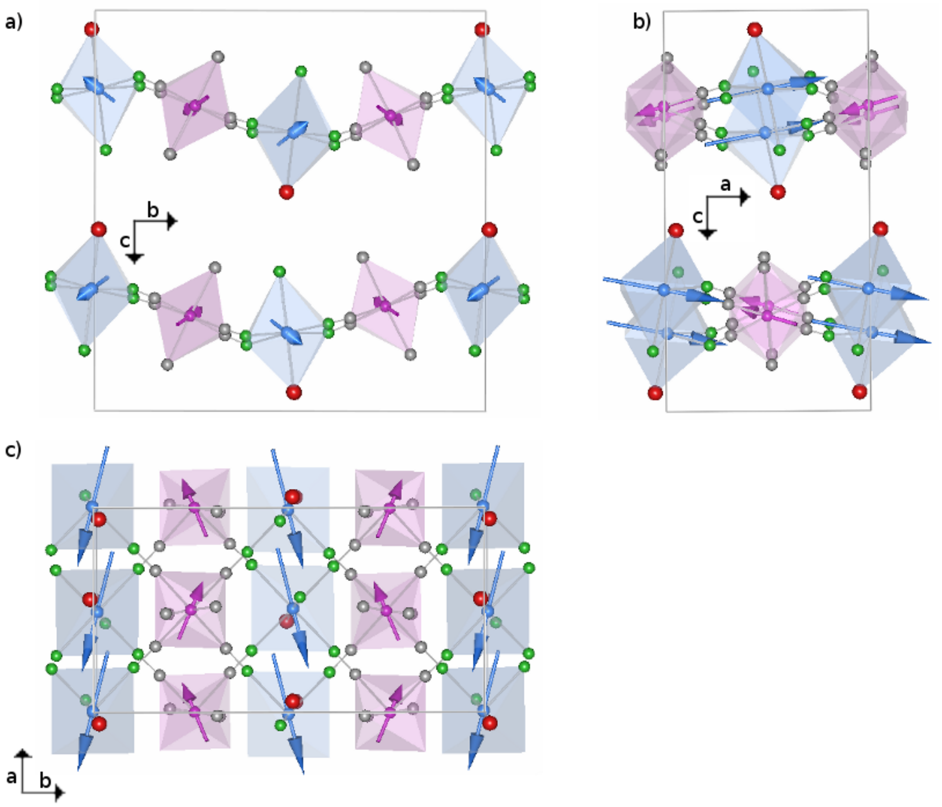

Figure 2.8: Magnetic structure of GN-MnMn. Views along the a, b and c axes. Mn^{II} atoms are in blue and Mn^{III} atoms are in pink

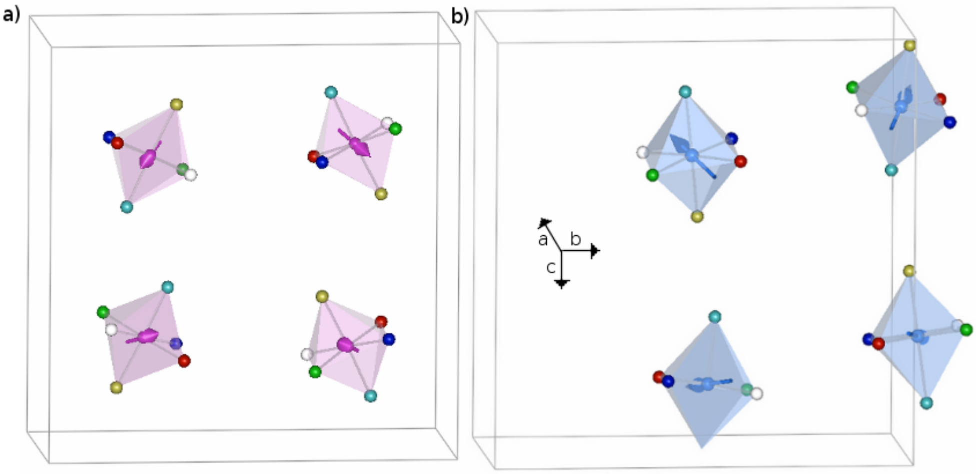

Figure 2.9: Orientation of each sublattice magnetic moments. a) Octahedral environment of Mn^{III}: C1 (deep blue), C2 (red), C3 (light blue), C4 (yellow), C5 (green) and C6 (white). b) Octahedral environment of Mn^{II}: N1 (deep blue), N2 (red), N7 (light blue), O1 (yellow), N5 (green) and N6 (white).

environment presents a ground term $^6A_1$ ($t_{2g}^3e_g^2$) which is a high spin state with S=5/2. If the ligand field is strong enough, the splitting of the d-orbitals causes a transition to a ground term $^2T_2$ (t_{2g}^5) where the Mn^{II} has spin S=1/2, and the state is denoted as low spin. The ground term for the Mn^{III} in a low ligand field octahedral environment is ^5E ($t_{2g}^3e_g^1$), where the cation has a spin equal to S=4/2, which is a high spin state. For a strong enough ligand field, the ground term becomes $^3T_1$ (t_{2g}^4) where the spin is S=2/2). In general, in the case of Prussian Blue Analogues whose general formula is $M_xA[B(CN)6]_z \cdot nH_2O$, the A ions (Mn^{II}) are low-spin species due to the large ligand field splitting induced by the cyanide ligands; and the B ions (Mn^{III}) generally remain as high-spin species because the N-coordinated cyanide are weak field ligands. In this compound, Mn^{II} is surrounded by nitrogen and oxygen atoms and the ligand field is low enough to have a ground state $^6A_1$ and a spin S=5/2. Mn^{III} is surrounded by carbon atoms and the ligand field is high enough for the Mn^{III}, to present a low spin configuration with S=2/2.

The magnetic moments we have obtained, are close to the spin-only value for high-spin Mn^{II} and low-spin Mn^{III}, $5\mu_B$ and $2\mu_B$, respectively and according to $S = g{\cdot}S{\cdot}\mu_B$, with a Lande factor equal to g=2. For the Mn^{III} some contribution of the angular moment in expected, as it is not totally quenched, which could explain the higher value. No orbital contribution to the magnetic moment is expected for Mn^{II} ion, as the ground state presents L=0. Similar values have been found in another cyanide compounds with Mn^{II} and Mn^{III} ions [91]

As in the GN compound, the magnetic moments of both atoms lay close to the basal planes of the octahedra. The magnetic moment of the Mn^{II} forms an angle of 14º with the a axis, close to the bisectrix between bonding directions in the plane. As it could be expected, due to the small modification in the environment of this atom, its magnetic moments are very similar in GN and in GN-MnMn. If we focus our attention to Mn^{III} we see that the magnetic moment is directed towards the bisectrix between the bonding directions in the basal plane. In the GN, there is a Cr^{III} instead a Mn^{III} atom in this position, and its magnetic moment is directed almost to C1, through the largest bond. This different behavior could be explained if we look to the distortion of the octahedra for Cr^{III} and Mn^{III}. As it can be seen in table 2.4, the distortion for the Cr^{III} is one order of magnitude higher than for the Mn^{III}, and the distance C1-Cr is 0.08Å higher than the medium Cr-C distance. The magnetic moment of Cr^{III} tends to be along this bonding direction. For the Mn^{III}, the environment is more regular and there is not an elongated bonding direction, the magnetic moment tends to be in the bisectrix of the bonding direction. This result was unexpected, because a small Jahn-Teller effect could be predicted for Mn^{III} so we hoped a high distorted environment for the Mn^{III}. We can not explain easily the existence of this elongated bond in the GN compound.

Another difference between GN and GN-MnMn compounds is the magnetic order temperature, 38K for the Phase I of GN and 22K for GN-MnMn. Although the interlayer distance is shorter in the GN-MnMn compound, the magnetic moment of Mn^{III} is lower than the magnetic moment of Cr^{III} (2/2 and 3/2) and the octahedral environment of Mn^{III} is less distorted than the environment of Cr^{III}. As in both compounds the exchange pathways are the same, trough the C≡N bonds, these differences play a crucial role in the magnetism and in the ordering temperature.

2.5 New definition for magnetic chirality

As it has been said previously (see Chapter 1.2), there are several local definitions about magnetic chirality. We are interested in finding a definition that cares not only about punctual chirality, but also global chirality. Previously, our work-group has used the definition explained in Dra. Gonzalez's thesis [31], that was based in the Blume [48] and Maleyev's [49] formula to express the intensity scattered by a magnetic sample that includes a new term called chiral term.

In this work we propose a more general definition, we considerer that a system is to be defined magnetically chiral when the cross product $\mathbf{F}_M \times \mathbf{F}^*_M$ is different to zero:

$$\mathbf{C}_M = \mathbf{F}_M \times \mathbf{F}^*_M \neq 0 \tag{2.2}$$

The complex vector $\mathbf{F}_M(\mathbf{q})$ is the magnetic structure factor. The mathematic definition can be seen in equation 2.3 where the summation runs over all the j-atoms in the L-cell, $\mathbf{q}$ is a vector of the reciprocal lattice, and f_{L_j}, $\mathbf{q}_{L_j}$ and $\mathbf{R}_{L_j}$ are the magnetic form factor (which also depends on $\mathbf{q}$), the magnetic moment and the position of the j-atom in the L-cell.

$$\mathbf{F}_M(\mathbf{q}) \sim \sum_{L_j} f_{L_j} \mathbf{m}_{L_j} \exp(i2\pi \mathbf{q} \cdot \mathbf{R}_{L_j}) \tag{2.3}$$

In the most general case where a set of propagation vectors $\mathbf{K}$ are necessary to describe correctly a magnetic structure, the magnetic moment $\mathbf{m}_{L_j}$ of a j-atom placed in the L-cell can be written as a Fourier series on the form shown in equation 2.4, where the Fourier vectors $\mathbf{S}^{\mathbf{K}}_j$ can be complex vectors.

$$\mathbf{m}_{L_j} = \sum_{\{\mathbf{K}\}} \mathbf{S}^{\mathbf{K}}_j \exp(-i2\pi \mathbf{K} \cdot \mathbf{R}_L) \tag{2.4}$$

If $\mathbf{K}$ is at the interior of Brillouin Zone then the vector sum must be extended to the pair $\mathbf{K}$ and $-\mathbf{K}$ taking into account that $\mathbf{S}_j^{\mathbf{K}} = (\mathbf{S}_j^{\mathbf{K}})^*$. Taking into account this considerations, the most general form of the magnetic structure factor is shown in equation 2.5, where the lattice delta function is defined by $\Delta_{\mathbf{K}}(\mathbf{q}) = \sum_G \delta(\mathbf{q} - \mathbf{K} - \mathbf{G})$ and $\mathbf{G}$ is a node of the reciprocal lattice. This general expression for the structure factor allows to apply the definition of magnetic chirality can for any magnetic structure.

$$\begin{aligned}
\mathbf{F}_M(\mathbf{q}) &\sim \sum_{L_j} f_{L_j} \mathbf{m}_{L_j} \exp(i2\pi\mathbf{q} \cdot \mathbf{R}_{L_j}) = \\
&= \sum_j f_j \exp(i2\pi\mathbf{q} \cdot \mathbf{r}_j) \sum_{\{\mathbf{K}\}} \mathbf{S}_j^{\mathbf{K}} \sum_L \exp(-i2\pi(\mathbf{q} - \mathbf{K}) \cdot \mathbf{R}_L) \approx \\
&\approx \sum_j f_j \exp(i2\pi\mathbf{q} \cdot \mathbf{r}_j) \sum_{\{\mathbf{K}\}} \mathbf{S}_j^{\mathbf{K}} \sum_G \delta(\mathbf{q} - \mathbf{K} - \mathbf{G}) = \\
&= \sum_j f_j \exp(i2\pi\mathbf{q} \cdot \mathbf{r}_j) \sum_{\{\mathbf{K}\}} \mathbf{S}_j^{\mathbf{K}} \Delta_{\mathbf{K}}(\mathbf{q}) \qquad (2.5)
\end{aligned}$$

Once we have adopted a definition for chirality, it is advisable to know which structures can present magnetic chirality. Some considerations about this subject are given in this subsection and, at the end, the definition is applied to the magnetic structure of Gn-MnMn compound to check whether is magnetic chiral or not.

2.5.1 Chirality in centrosymmetric space groups

If the space group is centro-symmetric, for obvious symmetry reasons,the vector $\mathbf{F}_M(\mathbf{q})$ is real and, within the proposed definition, magnetic chirality will not be allowed. If we are looking for a magnetic chiral structure, we should focus on non centrosymmetric space groups.

2.5.2 Chirality in no-centrosymetric space-groups

Although chirality can only be present in non-centrosymetric space groups, not all the magnetic structures based in a non centro-symmetric groups will be chiral, each structure should be analized. Several particular cases are listed next.

Collinear magnetic structures

In the case of any collinear magnetic structure (ferro, antiferro, ferri, squared), including those with a modulated amplitude, all the Fourier coefficients describing the magnetic structure are real and parallel. As all the Fourier coefficients are real and parallel, $\mathbf{F}_M(\mathbf{q})$ and $\mathbf{F}^*_M(\mathbf{q})$ are parallel and only differ in a phase, so their cross product is zero and the condition stated for magnetic chirality is not satisfied.

For example, in a helical arrangement of atoms with the magnetic moments aligned along the helix axis, the $\mathbf{F}_M(\mathbf{q})$ vector will be parallel to $\mathbf{F}^*_M(\mathbf{q})$, and their vectorial product will be zero. This case has not to be confused with a helical arrangement of spins, which is not a collinear magnetic structure and is a particular example of a chiral magnetic structure.

Chirality can only be present in structures with non-centrosymmetric space groups and a non-collinear spin alignment.

No-collinear structures

There are different types of non-collinear structures and several cases can be distinguished depending on the nature of the Fourier coefficients and the propagation vector.

Real Fourier coefficients not parallel

A canted magnetic structure could be described by real Fourier coefficients not parallel to each other: $\mathbf{S}_j^{\mathbf{K}} = (u_j, v_j, w_j)$, with $\mathbf{S}_j^{\mathbf{K}} = (\mathbf{S}_j^{\mathbf{K}})^*$

Applying our definition for chirality, the cross product of the magnetic structure factor and its conjugate, can be written as in equation 2.6. It can be seen that the cross product is not vanished and therefore magnetic chirality is present. In this particular case the magnetic chirality arises from the cross product of non-parallel magnetic moments at different sites.

$$\begin{aligned}\mathbf{F}_M \times \mathbf{F}^*_M \sim [\sum_i f_i \exp(i2\pi\mathbf{q}\cdot\mathbf{r}_i) \sum_{\{\mathbf{K}\}} \mathbf{S}_i^{\mathbf{K}} \Delta_{\mathbf{K}}(\mathbf{q})] \times \\ \times [\sum_j f_j \exp(i2\pi\mathbf{q}\cdot\mathbf{r}_j) \sum_{\{\mathbf{K}'\}} \mathbf{S}_i^{\mathbf{K}'} \Delta_{\mathbf{K}'}(\mathbf{q})]^* \\ \sim \sum_{i<j} f_i f_j \sin 2\pi\mathbf{q}\cdot(\mathbf{r}_i - \mathbf{r}_j) \Delta_{\mathbf{K}}(\mathbf{q}) + \Delta_{-\mathbf{K}}(\mathbf{q}) \mathbf{S}_i^{\mathbf{K}} \times \mathbf{S}_j^{\mathbf{K}} \qquad (2.6)\end{aligned}$$

Complex Fourier coefficients and not parallel $\mathbf{S}_j^{\mathbf{K}} = (\mathbf{S}_j^{\mathbf{K}})^*$

The calculation of the cross product of the magnetic structure factor is shown in equation 2.7, which is similar to the expression 2.6 but now including the terms $\mathbf{S}_i^{-\mathbf{K}} \times \mathbf{S}_i^{\mathbf{K}}$ because they do not vanish.

$$\begin{aligned}\mathbf{F}_M \times \mathbf{F}_M^* \sim [\sum_i f_i \exp(i2\pi\mathbf{q}\cdot\mathbf{r}_i) \sum_{\{\mathbf{K}\}} \mathbf{S}_i^{\mathbf{K}} \Delta_{\mathbf{K}}(\mathbf{q})]\times \\ \times [\sum_j f_j \exp(i2\pi\mathbf{q}\cdot\mathbf{r}_j) \sum_{\{\mathbf{K}'\}} \mathbf{S}_i^{\mathbf{K}'} \Delta_{\mathbf{K}'}(\mathbf{q})]^* \\ \sim \sum_{i<j} f_i f_j \sin 2\pi\mathbf{q}\cdot(\mathbf{r}_i - \mathbf{r}_j)|\Delta_{\mathbf{K}}(\mathbf{q})|^2 \mathbf{S}_i^{-\mathbf{K}} \times \mathbf{S}_j^{\mathbf{K}} + \\ + \sum_i f_i^2 |\Delta_{\mathbf{K}}(\mathbf{q})|^2 - |\Delta_{-\mathbf{K}}(\mathbf{q})|^2 \mathbf{S}_i^{-\mathbf{K}} \times \mathbf{S}_j^{\mathbf{K}} \neq 0 \qquad (2.7)\end{aligned}$$

We can distinguish several cases. For example, for a propagation vector $K = 0$ or similar to $(1/2, 0, 0)$ the last term in 2.7 is equal to zero. In the case of one magnetic atom per unit cell the last term is the only one that remains.

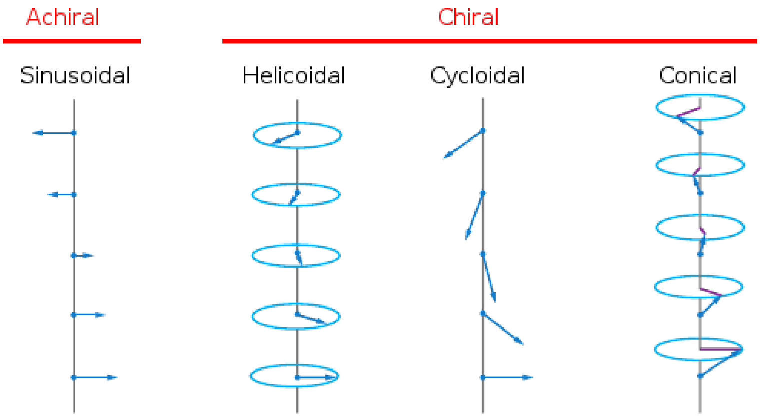

Figure 2.10: Some magnetic strcutures.

2.5.3 Magnetic Chirality in GN-MnMn

In order to determine whether the compound GN-MnMn is magnetically chiral or not, the equation 2.2 has been applied. In the GN-MnMn unit cell are eight magnetic atoms, four Mn^{II} and four Mn^{III} atoms, all of them must be present in the calculation of the magnetic structure factor. In table 2.7 the moments and positions for all the magnetic atoms in a unit cell can be seen.

The magnetic structure factor can be separate into two contibutions, one from the Mn^{II} sublattice and one from the Mn^{III}. Therefore, the cross product between $\mathbf{F}_M$ and $\mathbf{F}_M^*$ can be separated into four terms, one for the Mn^{II}

lattice, one for the Mn^{III} lattice and two cross terms which relates both sublattices, as can be seen in equation . All these terms are functions of the scattering vector $\mathbf{q} = (hkl)$.

$$\begin{aligned}\mathbf{F}_M \times (\mathbf{F}_M)^* &= \{\mathbf{F}_M^{MnII} + \mathbf{F}_M^{MnIII}\} \times \{\mathbf{F}_M^{MnII} + \mathbf{F}_M^{MnIII}\}^* = \\ &= \{\mathbf{F}_M^{MnII} \times (\mathbf{F}_M^{MnII})^*\} + \{\mathbf{F}_M^{MnIII} \times (\mathbf{F}_M^{MnIII})^*\} + \\ &\quad + \{\mathbf{F}_M^{MnII} \times (\mathbf{F}_M^{MnIII})^*\} + \{\mathbf{F}_M^{MnIII} \times (\mathbf{F}_M^{MnII})^*\}\end{aligned} \tag{2.8}$$

The terms corresponding to the two sublattices are different from zero, as they are canted magnetic structures. The cross terms are also different from zero, but anyway, simulations have demonstrated the chiral term is different from zero except for $\mathbf{q} = (hkl) = \mathbf{0}$. We can therefore conclude that $\mathbf{F}_M \times (\mathbf{F}_M)^* \neq 0$ for GN-MnMn and the magnetic structure is chiral.

2.6 Conclusions

The nuclear structure of GN-MnMn have been refined using the neutron diffraction data collected in VIVALDI. Neutron diffraction has enabled us to obtain the hydrogen positions in paramagnetic phase and to determine the anisotropic thermal displacement tensor for all atoms, something that could not be made using conventional X-ray diffraction. The formula of the compound was determined by elemental analysis as $[Mn(CN)_6][Mn(S)pnH(H_2O)]\cdot 2H_2O$ and the number of water molecules depends on the measurement conditions. While the number of water molecules found was at least 1.7 for elemental analysis, neutron diffraction data established one water molecule per unit formula, the volatile one has been lost due to experimental conditions.

In addition, the magnetic structure has been determined and a propagation vector equal to $\mathbf{k} = 0$ has been found. The magnetic phase shows two interpenetrating magnetic sublattices, one of Mn^{II} and another of Mn^{III} which interact antiferromagnetically. The magnetic moments of both atoms try to remain in the local basal planes of their octahedra, following the bisectrix between bonding directions. Due to the lack of a centre of symmetry between interacting sites in this compound, competing Dzyaloshinskii-Moriya interactions may play a role, allowing a certain lack of collinearity in the magnetic moments below T_c.

In spite of an expected weak Jahn-Teller effect for the Mn^{III} it has been found a more regular environment than for the Cr^{III}, which has a high influence in the direction of the magnetic moments and may have influenced to the ordering temperature.

As we are interested in nuclear and magnetic chirality and one of the objectives of our research is to find the coexistence of both chiralities, a new definition has been adopted and discussed for magnetic chirality. This is not a local definition, this is a general definition which considerer the magnetic structure as a whole, and consider that magnetic chiral compounds obey that $\mathbf{C}_M = \mathbf{F}_M \times \mathbf{F}_M^* \neq 0$). With this definition, the magnetic phase of GN-MnMn is magnetically chiral. Therefore, we have found nuclear and magnetic chirality in a molecular magnet.

Chapter 3

Neutron study of the $[Cr(CN)_6][Mn(R/rac) - pnH(DMF)] \cdot 2H_2O$ compounds

3.1 Introduction

As it has been said in the introductory chapter, several chiral compounds of the same family are studied in this part of the thesis. Our objective is to confirm the coexistence of nuclear and magnetic chirality in them and study how modifications in the nuclear structure can affect to the magnetic structure.

This chapter is devoted to the chiral compound similar to GN $[\mathrm{Cr(CN)_6}][\mathrm{Mn(R)\text{-}pnH}(DMF)] \cdot 2H_2O$, and its racemic compound $[\mathrm{Cr(CN)_6}][\mathrm{Mn(rac)\text{-}pnH(DMF)}]\cdot\mathrm{2H_2O}$, where DMF stands for N,N-dimethylformamide and (R/rac)-pn is (R/rac)-1,2-diaminopropane. Due to the similitude between the chiral compound and GN, these compounds are denoted as GN-DMF(R) and GN-DMF(rac).

The nuclear structure of $[\mathrm{Cr(CN)_6}][\mathrm{Mn(R)\text{-}pnH(DMF)}]\cdot 2H_2O$ determined by X-ray measurements at 290K is very similar to GN, the main difference is the substitution of the H_2O molecule linked to the Mn^{II} atom in the GN compound by a DMF molecule. This substitution implies an increasing in the interlayer distance and modifies the corrugation of the layers. The GN-DMF(R) compound is a candidate to present coexistence of nuclear and magnetic chirality due to its resemblance to GN. It also represents a good opportunity to observe how a ligand substitution or the interlayer distance can influence in the magnetism.

The GN-DMF(rac) compound crystallizes in a centrosymmetric space group, so nuclear chirality is absent. If we compare the GN-DMF(R) and GN-DMF(rac) compounds, we can see how the ligand (R)-pn transfers the nuclear chirality to GN-DMF(R) crystal. The knowledge of the magnetic structures of both compounds can allow us to see if the magnetic chirality is also related to the chirality of the ligand.

In order to refine the nuclear structures and to solve the magnetic ones, single-crystal neutron diffraction experiments have been performed at the ILL, in the diffractometers VIVALDI and D15 (see A.3.2 and A.4.2 in appendix A for more information).

The synthesis, the structure previously solved by X-ray measurements and the magnetization measurements of GN-DMF(R) and GN-DMF(rac) are described in 3.2. Then, the neutron diffraction experiments carried on are explained in section 3.3 and results for the nuclear and magnetic structure are presented in 3.4. Our definition of chirality is applied to the samples at section 3.5 and some conclusions can be found at 3.6.

3.2 Synthesis, X-ray structure and magnetic characterization

The GN-DMF(R) and GN-DMF(rac) compounds were synthesized by Prof. Inoue Katsuya and coworkers at the University of Hiroshima (Japan) [7]. Both compounds are synthesized by the same reaction but an enantiomeric or racemic precursor is employed. Green block-like crystals were obtained by slow diffusion of $MnCl_2{\cdot}4H_2O$ (5.1 mmol), (rac)-1,2-diaminopropane-dihydrochloride ((rac)-pn·2HCl, 6.8 mmol), and KOH (6.8 mmol) in a H_2O/N,N-dimethylformamide mixture (1:1) into $K_3[Cr(CN)_6]$ (1.5 mmol) in a H_2O/EtOH (1:1) mixture for several weeks. The synthesis were carried out under argon atmosphere, because manganese ion is air sensitive in the KOH solution.

The unit cell for both compounds is orthorhombic, with cell parameters and space groups a=7.662(2)Å, b=14.581(4)Å, c=19.747(6)Å and $P2_12_12_1$ for GN-DMF(R); and a=14.5459(8)Å, b=7.6509(8)Å, c=19.723(2) Å and Pnma for GN-DMF(rac). In the unit cell of the GN-DMF(rac) compound there has been a changed of the *a* and *b* axis respect to the definition of the unit cell in GN-DMF(R). As in other compounds studied in this thesis, each $[Cr(CN)_6]^{3-}$ ion utilizes four cyanide moieties in order to form bridges to four adjacent Mn^{II} ions within the *ab* plane, building bimetallic sheets piled up along the *c* axis. In addition to Mn^{II} and $[Cr(CN)_6]^{3-}$ ions, an asymmetric unit contains a single molecule of (R/rac)-pnH, a DMF molecule and two water molecules.

The octahedron around the Mn^{II} ion is completed by coordination of the primary amino group of (R/rac)-pnH and the DMF molecules as can be seen in figure 3.1 for GN-DMF(R). The two water molecules occupy gaps between the sheets. The shortest and the second shortest inter-sheet metal separations are observed between the homo-metallic atoms, in contrast with GN, where the shortest inter-sheet metal separations are observed between Mn^{II} and Cr^{III} atoms. This difference may influence on the magnetism.

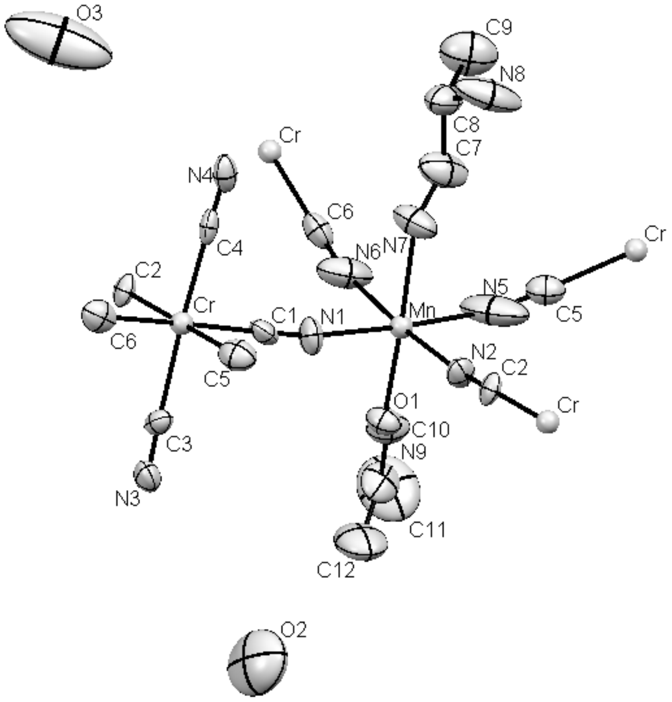

Figure 3.1: ORTEP drawing of $[Cr(CN)_6][Mn(R) - pnH(DMF)] \cdot 2H_2O$, hydrogen atoms are omitted for simplicity. Adapted from [7]

The crystal structures were solved by X-ray measurements on single crystals at room temperature and can be obtained at *www.ccdc.cam.a-c.uk/* with the codes *CCDC 223745* and *CCDC 239941* [7]. All non-hydrogen atoms were refined anisotropically. Hydrogen atoms were placed in calculated positions but not refined, except for the water hydrogen atoms in both compounds which could not been placed. In addition, the hydrogen atoms of the terminal amino group of pn in GN-DMF(rac) were not placed due to some disorder of the nitrogen atom (see the thermal ellipsoid of N9 in figure 3.2). Among others, the impossibility of placing and refining the hydrogen atoms positions by X-ray measurements is one of the reasons that motivated our neutron diffraction studies.

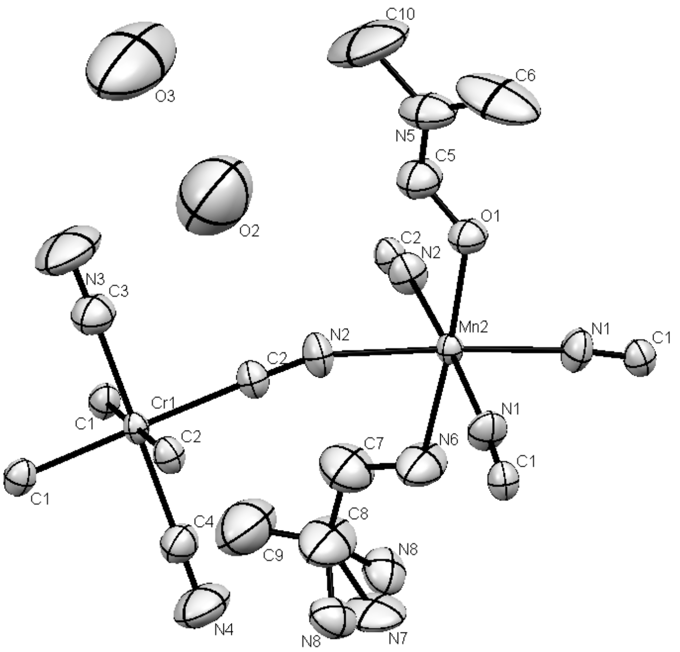

Figure 3.2: ORTEP drawing of $[Cr(CN)_6][Mn(rac)-pnH(DMF)]\cdot 2H_2O$, hydrogen atoms are omitted for simplicity.

The magnetic characterization of the compounds has been performed in polycrystalline samples [7] and in oriented single crystals [92]. The magnetic behavior of polycrystalline samples of the chiral compound shows a $\chi_{mol}T$ value of 4.92 cm^3K/mol (6.28 μ_B) at room temperature, which decreases while cooling down to a minimum value of 3.53 cm^3K/mol (5.31 μ_B) at 82 K. Upon further cooling, the $\chi_{mol}T$ value increases to a maximum value of 36.19 cm^3K/mol (17.02 μ_B) at 27 K and decreases below 27 K. The susceptibility obeys a Curie-Weiss law from 300-120K with a Weiss temperature θ=73.5 K, which is an indicator of the antiferromagnetic interaction between nearest neighbor Cr^{III} and Mn^{II} ions through cyanide bridges. The behavior for the racemic sample is very similar.

To confirm the long reach magnetic order around 30K, low field measurements in single crystal have been performed. As can be seen in figure 3.3 for the chiral sample and figure 3.4 for the racemic one, both, the zero field-cooled magnetization (ZFCM) and the field-cooled magnetization (FCM) curves display abrupt increases in the magnetization below 40 K, which reach a maximum at T_N=28.8 K. The magnetic behavior of the two samples below this temperature is different.

In figures 3.5 and 3.6, the magnetization versus magnetic field curves at

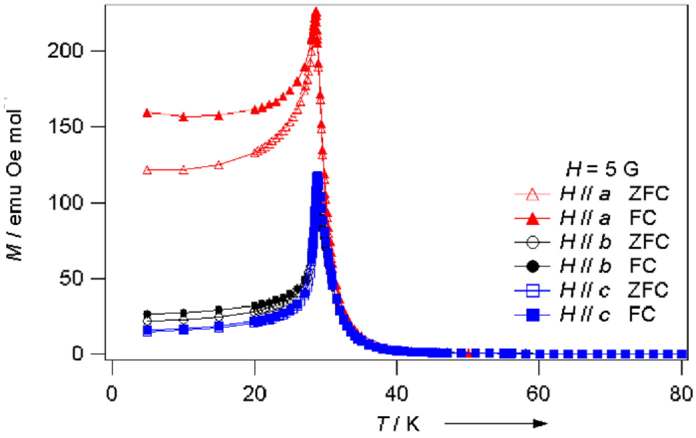

Figure 3.3: Magnetization versus temperature for GN-DMF(R). Taken from [92].

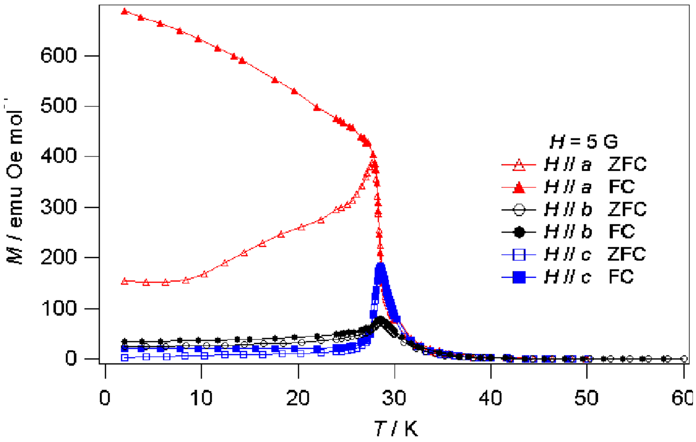

Figure 3.4: Magnetization versus temperature for GN-DMF(rac). Taken from [92].

2K can be seen for the two compounds; the saturation magnetization value per unit formula at 5T is around 2 μ_B, which corresponds to the value of S=2/2 expected for antiferromagnetically coupled Mn^{II} (S=5/2) and Cr^{III} (S=3/2). For the chiral sample, spins are canted and in the *bc* plane and presents a spin-flip transition. While the chiral sample is a a metamagnet with T_N of 28.5 K, the racemic one is a ferrimagnet with T_N of 28 K.

3.3 Neutron scattering experiments

Neutron scattering techniques are used in this thesis as a powerful tool to determine the nuclear and magnetic structure of the studied compounds. As it is said in appendix A, they allow us to refine nuclear structures including the atomic position of light elements, which are more difficult to place with

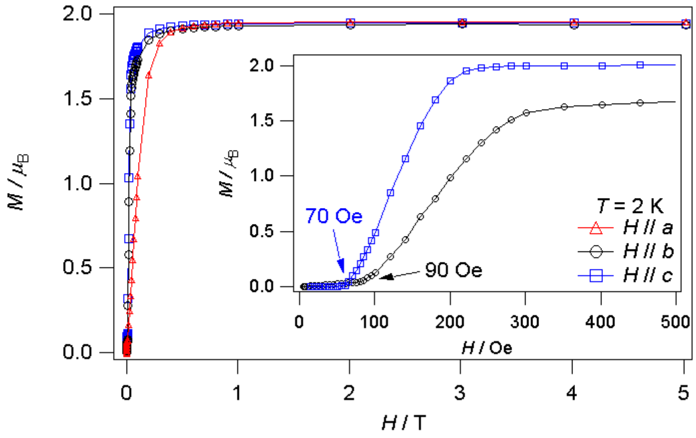

Figure 3.5: Magnetization versus field for GN-DMF(R). The low field region can be seen in the insert

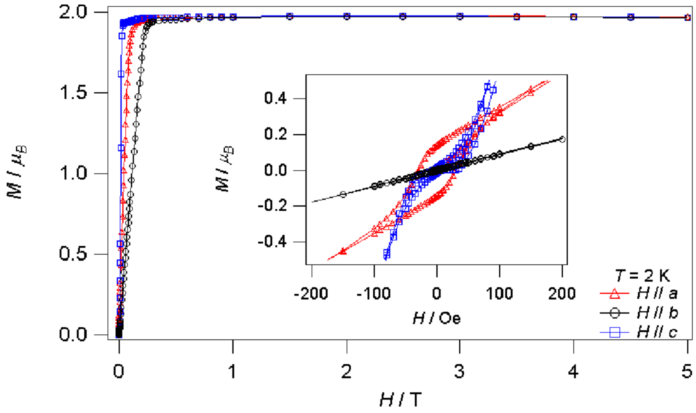

Figure 3.6: Magnetization versus field for GN-DMF(rac). Histeresis cycles are shown in the insert

photons. In addition, as neutrons interact with the magnetic moments of the atoms via the dipolar magnetic interaction and nuclear and magnetic interaction are of the same order of magnitude, neutron diffraction also allow us to determine magnetic structures. As for the compounds described in previous chapters, neutron diffraction have been used to refine the nuclear structure and to determine the magnetic structure of the compounds GN-DMF(R/rac). The diffraction experiments have been done at the instruments D15 and VIVALDI, placed at the ILL (see A.3.2 and A.4.2 in appendix A). VIVALDI offers an almost complete sight of the reciprocal space in a short time, which can be very useful for detecting propagation vectors different from zero, but it is not the best instrument to determine magnetic structures. On the contrary, D15 only allows to collect reflections one by one, which consumes a lot of time in measuring a great number of reflections, but it does not have the problem of chromatic overlap of VIVALDI and can be very useful to determine magnetic structures.

The instrument D15 was operated in four-circle configuration with a wavelength of 1.17Å and reflections were measured through ω scans. The set-up was completed by a displex that allowed us to set temperatures between 2K and 300K for the GN-DMF(R) compound and between 10K and 200K for the GN-DMF(rac) sample. The crystals were glued in aluminium pins with *kwikfill*, a two-part polymer glue suitable for measurements down 200K. The experimental procedure for a typical experiment in D15 in described in section A.3.2. In order to summarize it, some lines are given here. The first step in an experiment is to orientate the crystal and obtain an orientation matrix. The orientation matrix allow us to link the real and reciprocal spaces. For orientating the crystals, we simulated the intensities of some lines at low θ using the X-ray structure with FULLPROF, and localized the most intense reflections in the real space. Their positions in the angles of the instrument were noted and use to build the orientation matrix. After that, some reflections at a temperature above T_N were measured to refine the nuclear structure. In order to determine the magnetic structure, we cooled down the crystal down T_N. As D15 does not allow us to observe all the reciprocal space, we can not determine *a priori* the propagation vector. The typical procedure implies to look for satellite peaks in some selected directions and to check if the magnetic intensity overlaps with the nuclear intensity. For this reason, several q-scans were performer below T_N in smart directions scanning the reciprocal space to discard a propagation vector different from zero. Once the propagation vector was known, the crystals were cooled down, at 2K or 10K for the GN-DMF(R) and GN-DMF(rac) compounds respectively, to collect magnetic reflections which allow us to determine the magnetic structure. For D15 data, all the reflections were integrated and corrected by the Lorentz factor using the programm COLLD15, which is a modification of COLL5 [93]. The absorption correction was performed with the help of the programm DATAP [94].

In order to complete the neutron measurements performed in D15, monocrystals of the same batches as the crystals used in D15 experiments have been measured in VIVALDI. The crystals were wrapped in aluminium and attached with vacuum grease to a 1mm of diameter Vanadium pin. A standard He-flow ILL "Orange" cryostat was used to reach temperatures from 1.5K to 325K. In order to minimize the ratio of background scattering with respect to the scattering from the crystals, the final aperture of the neutron incoming beam was chosen to be 3mm in diameter. As it is said in appendix A, and with the same procedure that we followed with the sample Gn-MnMn, all the Laue patterns were indexed using the programm LAUEGEN [85]. The reflections were integrated following a two-dimensional version of the $\sigma(I)/I$ algorithm [86] implemented in the ARGONNE_BOXES program and corrected by absorption with the help of the programm LADIABS. The wavelength normalization was obtained using a curve derived by comparing equivalent reflections and multiple observations, via the programm LAUENORM [87].

Nuclear structure refinement and magnetic structure determination were done with SHELX [88] and Fullprof [9] programs. The experimental procedures to collect and analyze data are described in this section.

3.3.1 GN-DMF(R)

In this subsection, details of the neutron diffraction experiments performed for GN-DMF(R) in D15 and VIVALDI are given.

D15. Experimental procedure for GN-DMF(R)

For the measurements in D15 experiment, a 4x2x1mm^3 crystal was employed. The long dimension was identified with the a axis, which is the shortest cell parameter, and placed vertical in the pin, therefore along the ϕ axes of the Eulerian cradle. The slits used to optimize the ratio background/signal were 8mmx8mm at the font and 8mmx6mm at the detector.

After aligning the crystal, it was cooled down to 35K, where 779 lines were acquired to refine the nuclear structure. To determine the magnetic propagation vector, the crystal was cooled down to 2K and a total of 27 qscans were performed. No evidence of a propagation different from zero was found. In order to check if the propagation vector was zero and to find out the magnetic structure, 39 lines at low angle were measured at 35K and 2K. Several of these lines have a magnetic contribution to their intensity at 2K, which is another sign of a propagation vector equal to zero. The reflections with the most significant magnetic intensity contribution were measured as a function of the temperature near the transition region, which can be used to determine the critical exponent β of the transition. All relevant experiment details (temperature, number of reflections, wavelength,etc...) are summarized in (table 3.1). In Figure as 3.7 a typical ω-scan can be observed.

VIVALDI. Experimental procedure for GN-DMF(R)

The dimensions of the crystal used in this experiment were 1.65x3.0x0.8 mm^3. The crystal was aligned, its diffraction quality was checked and presence of twining was discarded before cooling down or acquiring any data. To refine the nuclear structure at room temperature 8 Laue patterns at 290K were recorded

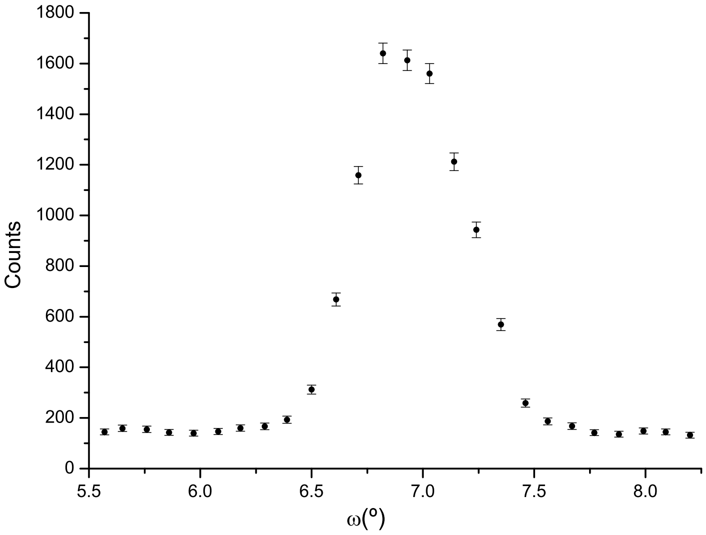

Figure 3.7: ω-scan measured for the line(-1 2 1) measured at 35K.

Table 3.1: Experimental details for GN-DMF(R) in D15.

GN-DMF D15			
Compound	$[Cr(CN)_6][Mn(R)-pnH(DMF)]\cdot 2H_2O$		
Space Group	$P2_12_12_1$		
Z	4		
Temperature	35K	2K	290K (X-ray)
a, b, c (Å)	7.677(11)	7.710(16)	7.662(2)
	14.55(2)	14.72(3)	14.581(4)
	19.72(2)	19.91(3)	19.747(6)
Measured reflections	720	39	
Unique Reflections	600	39	
$(sin\theta/\lambda)_{max}$ (Å^{-1})	0.4215	0.1074	
Resolution (Å)	1.19	4.66	
θ_{max}	29.55	7.22	
R_{Int}	0.016	–	
R_{σ}	0.0267	–	
hkl range	-6<h<2	-1<h<0	
	-11<k<12	-3<k<2	
	-14<l<16	-3<l<4	

and 10 Laue patterns were collected at 35K to refine the nuclear structure at a temperature near T_C. In order to determine the magnetic structure, the crystal was cooled down the transition temperature and 10 Laue patterns were recorded at 2K. For each data set at each temperature, there is a ϕ interval of 20^o between patterns. The times of exposure were selected to be high enough to record clearly the weaker diffraction spots at each temperature. The exposure time of the patterns taken at 290K was set as one hour, while the exposition time at 33K and 2K was set as 45 minutes. This increasing is due to the thermal motion, which makes the intensity of the reflections decrease.

All relevant experiment details (temperature, exposure times, number of reflections, wavelength range,etc...) are summarized in table 3.2. As can be seen in the table, the number of reflections extracted from the Laue patterns at high temperature is lower than at low temperature, due to the thermal motion which also has an influence in the increasing in d_{min} during the data analysis.

Table 3.2: Experimental details for GN-DMF(R) experiment in VIVALDI

GN-DMF(R) VIVALDI			
Compound	$[Mn^{III}(CN)_6][Mn^{II}(R)-pnH(DMF)]{\cdot}2H_2O$		
Space	$P2_12_12_1$		
a, b, c (Å) (X-ray at RT)	7.662 14.581 19.747		
Z	4		
Temperature	290K	33K	2K
N^o of patterns	8	10	10
Exposure time (min)	60	45	45
λ_{range} (Å)	0.84-2.10	0.82-2.10	0.82-2.10
d_{min} (Å)	0.84	0.70	0.70
Measured reflections	11923	22324	21825
Unique Reflections	1640	1643	2686
$(sin\theta/\lambda)_{max}(^{-1})$	0.59	0.71	0.71
Resolution (Å)	0.84	0.70	0.70
θ_{max}	29.99	36.85	36.85
R_{Laue1}	0.200	0.200	0.200
R_{Laue2}	0.190	0.190	0.189
R_{Laue3}	0.134	0.131	0.133
R_σ	0.155	0.153	0.142
hkl range	0<h<9	0<h<10	0<h<10
	0<l<17	0<l<22	0<l<20
	0<k<23	0<k<27	0<k<27

3.3.2 GN-DMF(rac)

In this subsection, details of the neutron diffraction experiments performed for GN-DMF(rac) in D15 and VIVALDI are given.

D15. Experimental procedure for GN-DMF(rac).

The crystal used in the experiment was a needle-shape crystal of dimensions 2x6x1.5mm^3. The b axis, identified with the shortest dimension of the crystal, was placed vertical in the pin, parallel to the ϕ axes of the Eulerian cradle. The slits used to optimize the ratio background/signal were 8mmx8mm at the font and 8mmx6mm at the detector.

After orienting the crystal, it was cooled down. At 35K, 1126 lines were measured to refine the nuclear structure at this temperature. Cooling down at 10K, a total of 45 qscans were performed to look for a propagation vector different from zero. Once that a propagation vector different from zero was discarded, 174 lines at low angle were measured at 35K and 10K and their intensities were compared so we obtained the magnetic contribution to their intensity. This magnetic contribution has been used to find out the magnetic structure. Finally, 348 lines more were measured at 10K with the aim to refine the nuclear structure at low temperature.

All relevant experiment details (temperature, number of reflections, etc) are summarized in table 3.3.

VIVALDI. Experimental procedure for GN-DMF(rac).

For this experiment, we used a crystal of dimensions $2.0x0.7x0.6mm^3$. The crystal was aligned until it was completely bath by the neutron beam, its diffraction quality was checked and the presence of twining was discarded before cooling down or acquiring any data. To refine the nuclear structure art 290K, we collected ten Laue patterns at 290K at ϕ intervals of 20°. The collection time was set to ninety minutes, which was enough to obtain clear spots in the pattern.

All relevant experiment details (temperature, number of reflections wavelength range,etc...) are summarized in table 3.4.

Table 3.3: Experimental details for GN-DMF(rac) in D15.

GN-DMF(rac) D15			
Compound	$[Cr(CN)_6][Mn(rac)-pnH(DMF)]\cdot 2H_2O$		
Space Group	$Pnma$		
Z	4		
Temperature	35K	2K	290K (X-ray)
a, b, c (Å)	14.83(10)	14.78(9)	14.5459(8)
	7.76(3)	7.77(2)	7.6509(8)
	20.16(7)	20.11(7)	19.723(2)
Measured reflections	1126	522	
Unique Reflections	749	125	
$(sin\theta/\lambda)_{max}$ (Å^{-1})	0.4182	0.2205	
Resolution (Å)	1.20	2.27	
θ_{max}	29.29	14.95	
R_{Int}	0.1596	0.0888	
R_{σ}	0.0847	0.606	
hkl range	-6<h<12	-6<h<6	
	0<k<6	0<k<3	
	-8<l<16	-8<l<8	

3.4 Results

In this section, the results obtained after analyzing the neutron data acquired are presented. The chemical instability of the crystals has been a source of problems to refine the nuclear structures and to find the magnetic ones. Perfect crystals of GN-DMF(R) and GN-DMF(rac) of a emerald green color start to degrade after a few hours exposed to the air, and they turn into a porous greenish yellow crystal. The effect could affect negatively to our data quality. The initial stages of decomposition of samples and loss of crystallinity can affect specially at high-angle reflections. In spite of this problem, we managed to succeed.

We have performed neutron diffraction experiments in D15 and VIVALDI and each technique of measure has its own advantages and disadvantages, which can are summarized in table 3.5. VIVALDI allow us to record an important part of the reciprocal space in a short time, but due to the chromatic overlap it can not be used to refine the cell parameters and can present some problems to determine magnetic structures. On the contrary, D15 measure a single reflection in each ω-scan so it can take a long time to acquire enough reflections to refine a nuclear structure, but allow us to refine the cell parame-

Table 3.4: Experimental details for GN-DMF(rac) experiment in VIVALDI.

GN-DMF(rac) VIVALDI	
Compound	[Cr(CN)$_6$]$[Mn(rac)-pnH(DMF)]\cdot 2H_2$O
Space Group	$Pnma$
a, b, c (Å) (X-ray at RT)	14.5459(8) 7.6509(8) 19.723(2)
Z	4
Temperature	290K
N^o of patterns	10
λ_{range} (Å)	0.84-2.10
d_{min} (Å)	0.90
Measured reflections	13224
Unique Reflections	1416
$(sin\theta/\lambda)_{max}$ (Å^{-1})	0.5821
Resolution Å	0.86
θ_{max}	24.43
R_{Laue1}	0.288
R_{Laue2}	0.243
R_{Laue3}	0.149
R_σ	0.1148
hkl range	0<h<16
	0<l<8
	0<k<22

ters and solve magnetic structures. Comparing the tables that summarizes the relevant details for each experiment, we can see how the resolution of VIVALDI for nuclear structures is higher than the resolution of D15 for our compounds.

Table 3.5: schematic summarize of the characteristic of the instrument used in the nuetron experiments for GN-DMF(R) and GN-DMF(rac).

D15	VIVALDI
monochromatic technique	chromatic technique
no limitations at low angle	low angle limitations
high time of acquisition	wide sight of reciprocal space in a short time

When we performed the experiments our intention was to refine the cell parameters and solve the magnetism using D15 data, which does not have the geometrical limitations or chromatic overlap of VIVALDI at low **q**. The data of VIVALDI were supposed to be used to improve the refinement of the atomic positions and thermal parameters due to the high number of reflections that it can record. Solving the nuclear structures of these compounds and determining the nuclear structures has been a challenge.

3.4.1 GN-DMF(R)

In this subsection, the results of refining the nuclear structure and solving the magnetic structure of the compound GN-DMF(R) with the acquired neutron diffraction data are exposed.

Nuclear phase.

To refine the nuclear structure in the paramagnetic phase, we performed diffraction experiments at 35K at D15 and at 290K and 33K at VIVALDI.

The 720 reflections acquired in D15 at 35K have been used to refine the nuclear structure using as starting point the X-ray solved structure [7]. In the previously reported structure, the hydrogen positions could not be determined and they were placed in calculated positions. To refine the structure, it has been necessary to set several conditions, the hydrogens of the groups CH_2, CH_3 and NH_3 have been refined as a rigid group and the distance between oxygen atoms and hydrogens in the water molecules is constrained. Due to the shortage of the reflections, it has not been possible to refine the thermal parameters anisotropically. As a result of the refinement, all the atomic coordinates have determined and all the thermal parameters refined isotropically by full-matrix least-squares technique based on F^2 using the programm SHELXL97 [88]. Experimental data details are summarized in table 3.1, and the fractional coordinates and isotropic thermal parameters are listed in Appendix D (table E.1). The agreement factor obtained with SHELX is R=0.1267 for reflections whose intensity is bigger than 4σ, and 0.1357 for all data.

With the objective to improve the refinement of the nuclear structure and to define the thermal parameters as anisotropic, the refined nuclear structure obtained with D15 data has been set as a starting point to refine the nuclear structure with VIVALDI data. It has been necessary to keep the constrain in the distance between the oxygen and hydrogen atoms of the water molecules and to restrain the shape of some thermal ellipsoids. Unfortunately, we have found that the thermal ellipsoids are unusually high and they have an unnatural cigar shape as can be seen in figure 3.8. In an effort to reduce the size of the thermal ellipsoids for the hydrogen atoms we tried to split the atomic positions, but the refinement was not improved. According to several recommendations to solve troublesome crystal structures [95], we checked the space group, the unit cell and the atom types and discarded any error. The R value for the adjustment is R=0.0984 for reflections whose intensity is bigger than 4σ and 0.1075 for all data. the fractional coordinates and isotropic thermal parameters are listed in Appendix D (table E.1).

The fuzzy structure and the unnatural size and shape of the thermal ellipsoids could be explained by two phenomena. An early stage of a degradation process and the loss os crystallinity may be the responsible of this anomalous ellipsoids. A visual inspection confirms that the crystals start to degrade after some time exposed to the air, they change their color from an emerald green to a greenish yellow and become porous. In addition, a lack of crystallinity has been observed in other Prussian Blue Analogues [75], specially if there are synthesized using a organic solvent as in the GN-DMF(R) compound. The other explanation is related to the disorder and the possibility of a interchange between the positions of the pnH and the DMF ligands. Due to the likeness between the (R)-pnH and DMF ligands, some disorder may be present and, in some small percentage, they positions may be interchanged. This last hypothesis is supported, for example, by the fact that eliminating the hydrogens H7A-H7B of the structure, one unexpected Q-peak appears in the refinement, which may be related to the interchange and the position of H10 (see figure 3.8). Improvements have not been observe after trying to solve a disorder situation with different occupancies for (R)-pnH and DMF ligands.

Solving the structure at 290K with VIVALDI data presents the same problems and challenges as for 33K, with and R=0.0939 for reflections whose intensity is bigger than 4σ and 0.1175 for all data. The positions and thermal parameters for the refinements of the nuclear structure can be seen in Appendix D (table E.1).

In spite of these problems, we accept the main features of the nuclear structure of the compound, which can be seen in figure 3.9. It consist of bimetallic planes containing Cr^{III} and Mn^{II} atoms in a octahedral environments and linked by cyanide groups, where the Mn^{II} is also linked to a DMF molecule and a (R/rac)-pnH group. There are two water molecule per f.u. of crystallization. The two dimensional networks are arranged almost perpendicularly to the *c* axis. Due to the precarious nuclear structure determination, we are not focusing in hydrogen bonds.

If we compare the nuclear structure of GN and GN-DMF(R) we can observe that, the substitution of the H_2O ligand of Mn^{II} for a DMF changes the piling of the layers, as can be seen in figure 3.10. In this figure, it can be seen as the upper layer in the unit cell of GN-DMF(R) is displaced b/2 along the *b* axis. This displacement may be due a stereo effect related to the higher volume

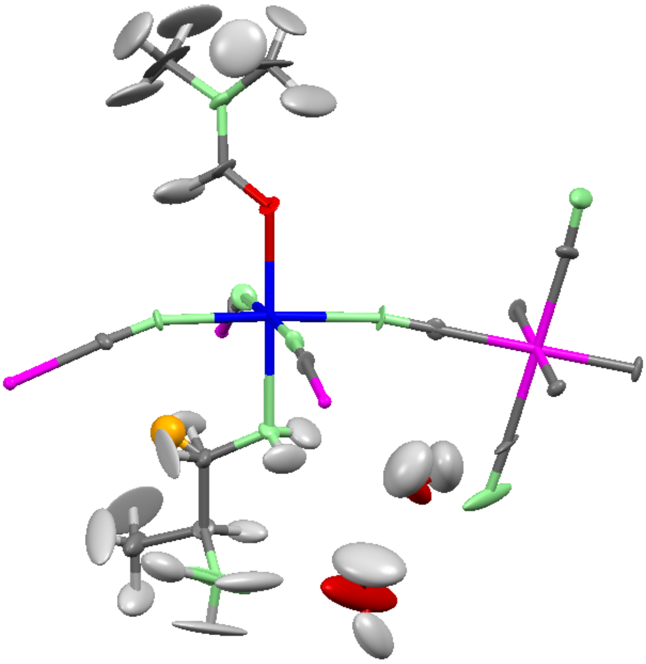

Figure 3.8: Structural unit of $[Cr(CN)_6][Mn(R)-pnH(DMF)]\cdot 2H_2O$ refined at 33K. The orange atom stands for the phantom peak obtained.

of DMF ligand. As a consequence, the interlayer distances are increased (see table 3.6) and the valleys of different layers are not in-phase. In addition, the shortest interlayer distances are different, while in GN the shortest distance between atoms is heterometallic (Mn-Cr 7.285(2)Å), in GN-DMF(R) the shortest distance is homometallic (Mn1-Mn2 8.776(2)Å). All this modifications in the nuclear structure may have some influence in the magnetic behavior of the compound. The intralayer distance Mn-Cr is the same within an experimental error for GN and GN-DMF(R) (5.319(11)Å at 35K for GN-DMF(R)).

Table 3.6: Interlayer distances between equal atoms and the shortest and largest heterometallic distances in GN-DMF(R) at 35K and GN at 43K.

Atoms	d (Å) GN-DMF(R)	d (Å) GN
Mn1-Mn2	8.776(2)	8.279(3)
Mn3-Mn4	12.466(3)	8.279(3)
Cr1-Cr2	10.551(3)	8.041(3)
Cr3-Cr4	10.551(3)	8.592(2)
Mn1-Cr2	9.246(2)	7.285(2)
Mn4-Cr1	11.683(3)	9.043(2)

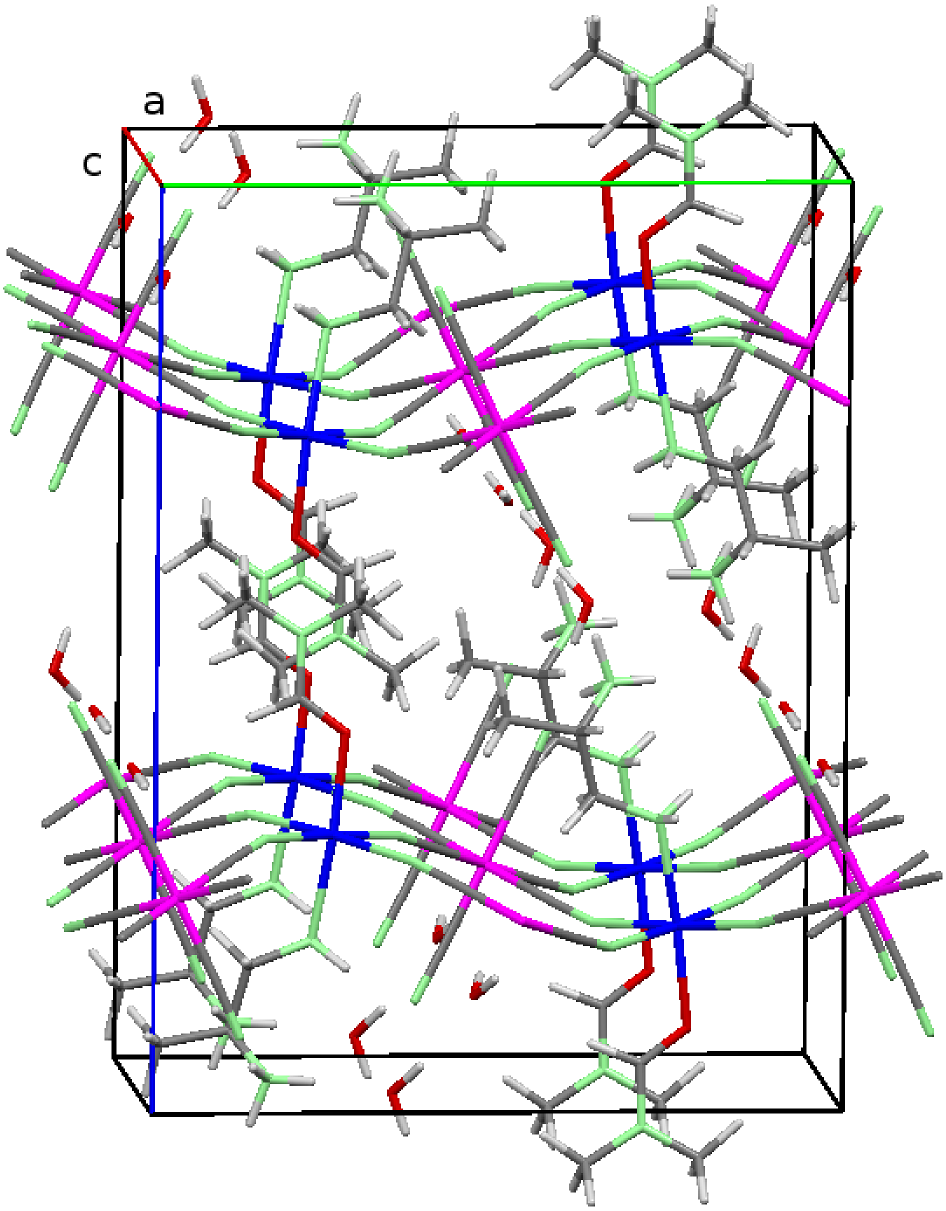

Figure 3.9: Nuclear structure of GN-DMF(R) refine with VIVALDI data at 33K.

The Cr^{III} and Mn^{II} are in an octahedral environment. The distances and angles of these octahedra can be seen in table 3.7 and are similar to what has been found in another compounds. The distortion of Cr^{III} and Mn^{II} octahedra in GN and GN-DMF(R) can be seen in table 3.8.

If we compare the octahedral environment of Cr^{III} and Mn^{II} in GN and

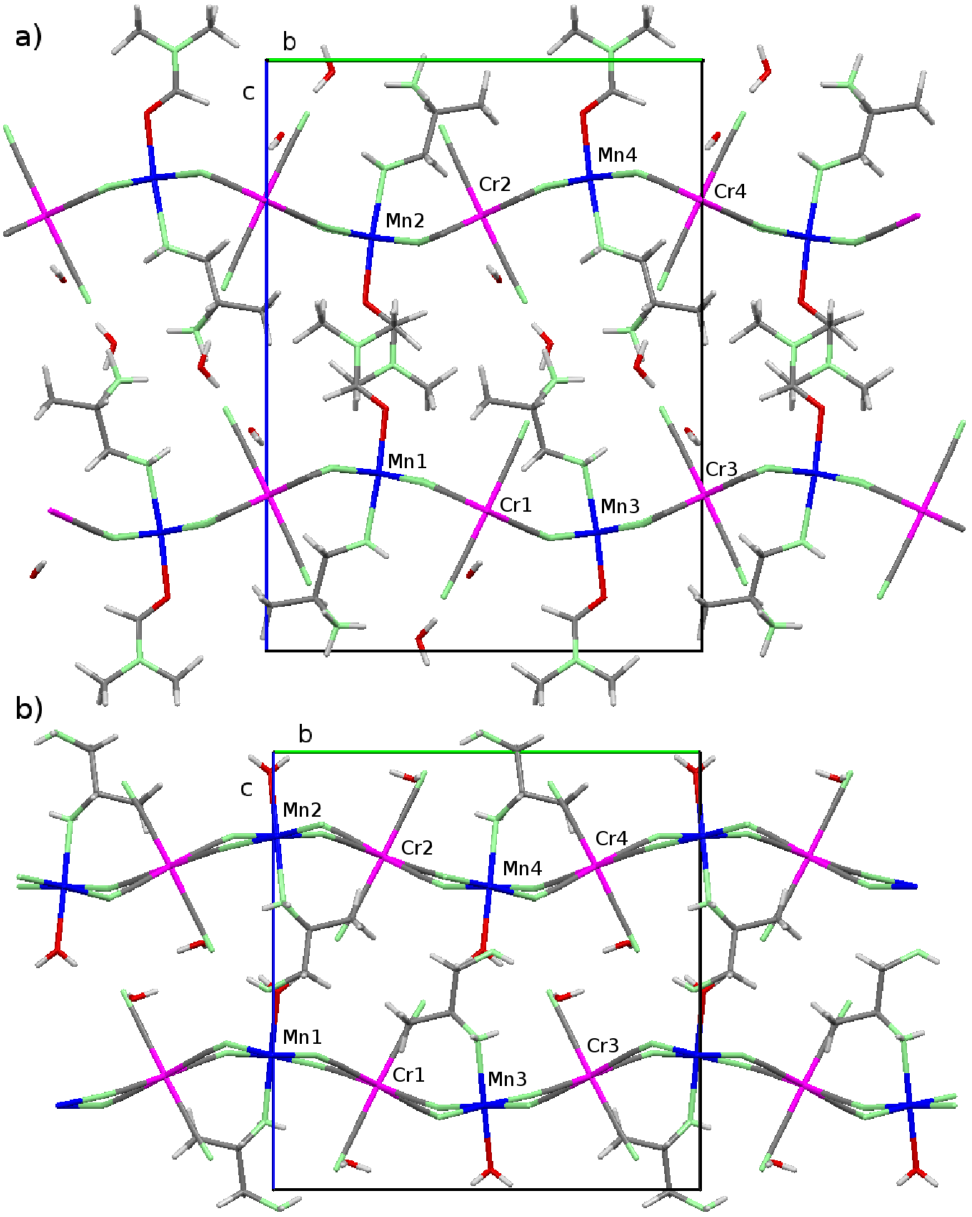

Figure 3.10: a)Interlayer separation in GN-DMF(R). b)Interlayer separation in GN

GN-DMF(R), we found that the distortion has the same order of magnitude for Mn^{II} in both compounds, but for Cr^{III} the distortion is one order of magnitude higher in the GN compound. The C-Cr^{III}-C angles for no opposite C atoms, are in the range 95.3°-86.5° for the GN and 91.0-89.2° for the GN-DMF(R). The C-Cr^{III}-C angles for opposite C atoms are in the range 173.2°-178.1° for the GN and 179.3°-179.9 for the GN-DMF(R). The higher distortion in the Cr^{III} in the GN compound, can be relevant in order to compare the magnetic behavior of both compounds. Another important feature that we want to remark is the angles in the Mn^{II} octahedra. Although the distortion of the Mn^{II} octahedra is similar in GN and GN-DMF(R) compounds, there is a remarkable difference in the N7-Mn^{II}-O1 angle, whose value is 177.8° in GN and 172.7° in GN-DMF(R). The increase of the deviation of the theoretical 180° value for the GN-DMF(R) compound is due to the higher volume of the DMF molecule, the DMF ligand is tilted and the value of the angle is different from 180° in order to avoid the spatial proximity of another DMF molecule.

Table 3.7: Bond lengths and angles for Cr^{III} and Mn^{II} at 25K.

A-Mn-B	d_{A-X}(Å)	d_{B-X}(Å)	$\widehat{AXB}$
C1-Cr-C6	2.07(1)	2.08(1)	179.9(7)
C2-Cr-C5	2.06(1)	2.05(1)	179.3(7)
C3-Cr-C4	2.06(1)	2.08(1)	179.3(7)
N1-Mn-N5	2.22(1)	2.21(1)	176.4(5)
N2-Mn-N6	2.16(1)	2.26(1)	176.3(6)
N7-Mn-O1	2.34(1)	2.19(1)	172.7(5)

A-Cr-B	$\widehat{ACrB}$	A-Mn-B	$\widehat{AMnB}$
C4-Cr-C5	90.0(5)	O1-Mn-N2	94.6(4)
C4-Cr-C6	89.0(5)	O1-Mn-N5	90.1(4)
C4-Cr-C2	90.0(5)	O1-Mn-N6	89.1(4)
C4-Cr-C1	91.0(5)	O1-Mn-N1	92.7(4)
C3-Cr-C6	90.8(6)	N7-Mn-N2	92.6(4)
C3-Cr-C5	90.7(6)	N7-Mn-N5	90.8(4)
C3-Cr-C1	89.2(6)	N7-Mn-N6	83.7(4)
C3-Cr-C2	89.3(6)	N7-Mn-N1	86.1(4)
C6-Cr-C5	89.3(5)	N1-Mn-N2	89.7(4)
C5-Cr-C1	90.6(5)	N2-Mn-N5	92.3(4)
C1-Cr-C2	90.1(5)	N5-Mn-N6	87.8(4)
C2-Cr-C6	90.0(5)	N6-Mn-N1	90.1(4)

Magnetic phase

The next paragraphs are devoted to the analysis of the magnetic structure of GN-DMF(R). We have two data set to determine the magnetic structure. As it has been said before, during the analysis of GN-MnMn, VIVALDI is not the best neutron diffractometer to solve magnetic structures, specially if the propagation vector is equal to zero due to the overlap of reflections at low angle

Table 3.8: Distortion calculated of the octahedral environment for GN and GN-DMF(R) magnetic atoms at 43K for GN and 33K for GN-DMF(R).

Cation	Δ_d
GN Cr	$4.6{\cdot}10^{-4}$
GN Mn	$8.4{\cdot}10^{-4}$
GN-DMF(R) Cr	$2.8{\cdot}10^{-5}$
GN-DMF(R) Mn	$6.7{\cdot}10^{-4}$

(see A.4.2). In spite of this inconvenience, we were forced to measured in it due to the small size of the available crystals at the time the first neutron diffraction experiments were performed. In addition, it allow us to refine the nuclear structure at 2K. To analyze VIVALDI data, we had the same consideration as for GN-MnMn.

The proceeding followed to determine the magnetic structure in described in the next paragraphs. To obtain the nuclear structure at 2K we used in SHELX the high angle reflections (θ>30°) to refine the atomic positions and thermal parameters found at 33K (see tables E.1 and E.2 in appendix D). The agreement factor for the nuclear refinement at 2K is R=0.1052 for reflections whose intensity is bigger than 4σ. Once that the nuclear structure at 2K has been refined, we can determine the magnetic structure. The refinement of the magnetic data was guided by the irreducible representation (IR) theory (for more information, see section A.5). The first step it to determine the propagation vector. For this compound we have concluded that $\mathbf{k} = \mathbf{0}$ at 2K, because the patterns collected in VIVALDI at 2K have been indexed with the cell parameters of the paramagnetic phase. In figure 3.11 a pattern collected at 25K for $\phi = -45^o$ is shown together with the same pattern at 2K indexed with the nuclear cell parameters. In addition, twenty-seven q-scans at 2K were done in D15. The directions of the q-scans were selected to look for propagation vectors as (1/2,0,0), (0, 1/2, 0)... No extra peaks that evidence the existence of a propagation vector different from zero have been found (for example, see figure 3.12). This absence of satellite peaks, together with the fact that we observe magnetic intensity superimpose to nuclear intensity in our reflections at 2K, corroborated that $\mathbf{k} = \mathbf{0}$.

Once that the propagation vector has been identified, we have determined the little group of vector $\mathbf{k} = \mathbf{0}$ and its IRs with the help of BASIREPs code. There exists two magnetic sites corresponding to the Cr and the Mn sublattices. The little group of vector $\mathbf{k} = \mathbf{0}$ and its IRs are the same that for the GN and GN-MnMn compounds. Four different one-dimensional IRs were obtained for each magnetic specie, called Γ_1, Γ_2, Γ_3 and Γ_4 in the notation of Kovalev.

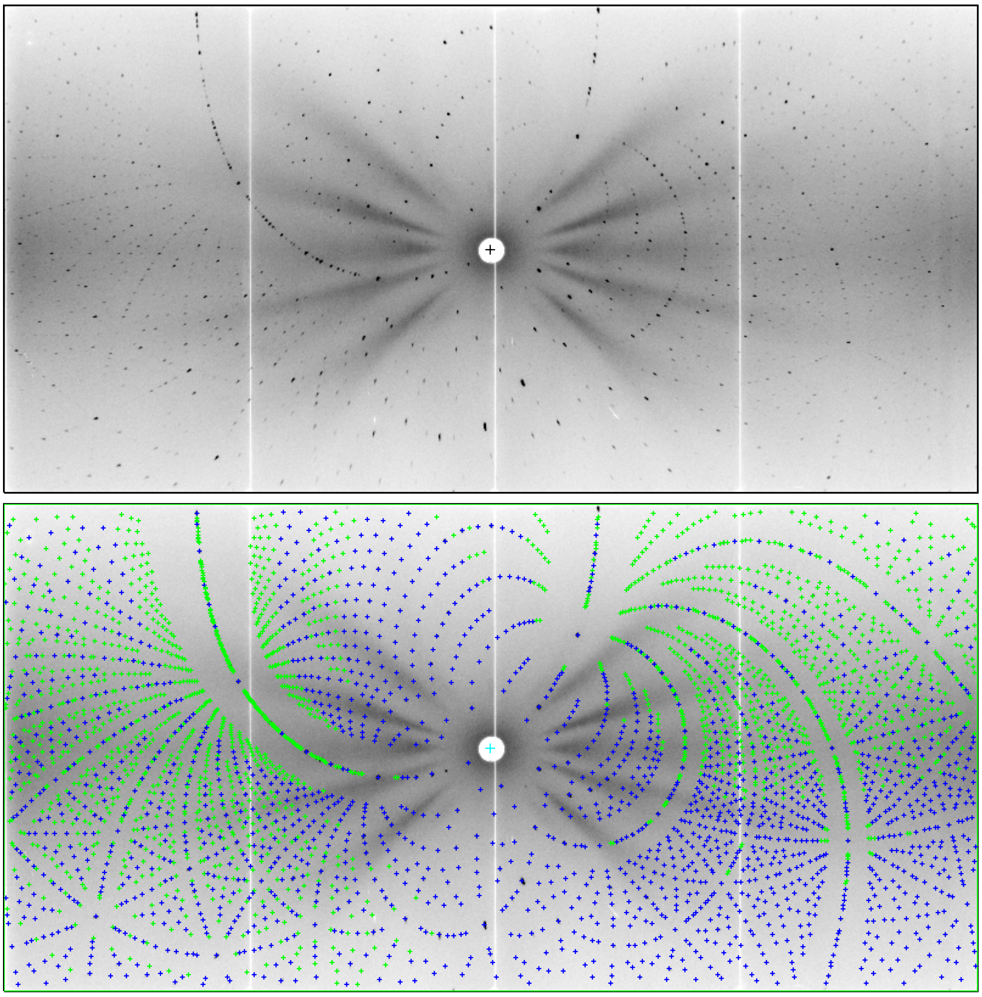

Figure 3.11: Laue patterns for Gn-MnMn at T=25K and 2K at $\phi = 45^o$ for GN-DMF(R). On the bottom, the pattern at 2K has been indexed with the same lattice parameters as in the paramagnetic phase.

Each of them is included three times in the reducible magnetic representation Γ. The basis vectors for these irreducible representations are listed in table 3.9.

In order to decide which representation correspond to magnetic structure of the GN-DMF(R), we compare the calculated values for each IR and the experimental values of the magnetic contribution to the intensity of the measured lines. In order to simplify the process, we can discard some IRs by symmetry arguments. The theoretical magnetic intensity depends on the perpendicular component to the scattering vector of the magnetic structure factor, which can be calculated for each sublattice as can be seen in equation 3.1.

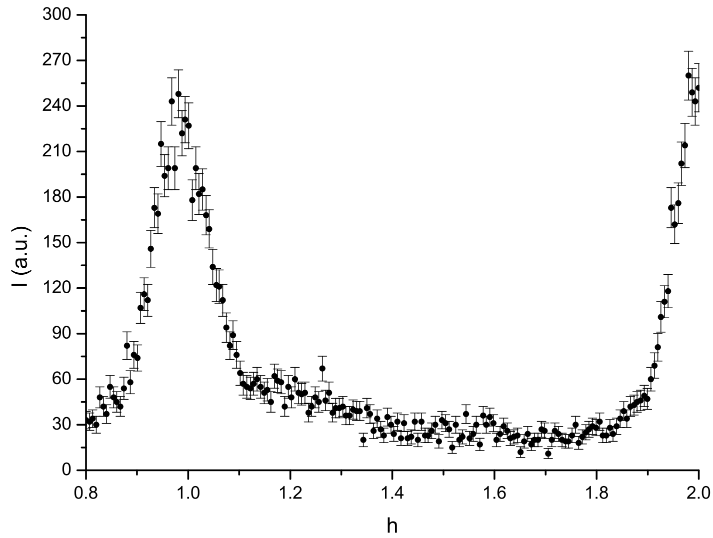

Figure 3.12: q-scan performed at 2K in the direction *h00* for the compound GN-DMF(R)

Table 3.9: Irreducible Representations for GN-DMF(R) and their basis vectors. m_1, m_2, m_3 and m_3 represent the magnetic atoms of each magnetic specie.

Atom	Position	Γ_1	Γ_2	Γ_3	Γ_4
$\mathbf{m}_1$	(x,y,z)	(u, v, w)	(u, v, w)	(u, v, w)	(u, v, w)
$\mathbf{m}_2$	(-x+1/2,-y,z+1/2)	($\overline{u}$, $\overline{v}$, w)	($\overline{u}$, $\overline{v}$, w)	(u, v, $\overline{w}$)	(u, v, $\overline{w}$)
$\mathbf{m}_3$	(-x,y+1/2,-z+1/2)	($\overline{u}$, v, $\overline{w}$)	(u, $\overline{v}$, w)	($\overline{u}$, v, $\overline{w}$)	(u, $\overline{v}$, w)
$\mathbf{m}_4$	(x+1/2,-y+1/2,-z)	(u, $\overline{v}$, $\overline{w}$)	($\overline{u}$, v, w)	($\overline{u}$, v, w)	(u, $\overline{v}$, $\overline{w}$)

$$\begin{aligned}
\mathbf{F}_M(\mathbf{q}) &= \sum_i \mathbf{m}_i \exp\left(i2\pi\mathbf{q}\cdot\mathbf{r}_i\right) = \\
&+ \mathbf{m}_1 \exp\left[i2\pi\mathbf{q}\cdot(x,y,z)\right] \\
&+ \mathbf{m}_2 \exp\left[i2\pi\mathbf{q}\cdot(-x+1/2,-y,z+1/2)\right] \\
&+ \mathbf{m}_3 \exp\left[i2\pi\mathbf{q}\cdot(-x,y+1/2,-z+1/2)\right] \\
&+ \mathbf{m}_4 \exp\left[i2\pi\mathbf{q}\cdot(x+1/2,-y+1/2,-z)\right] \qquad (3.1)
\end{aligned}$$

The line $\mathbf{q} = (-1, 0, 0)$ has no nuclear contribution to the diffracted intensity due to the reflection conditions of the group $P2_12_12_1$((h,0,0) with h=2n). Hence, the experimental intensity of 1748±32 counts at 2K is due to a magnetic contribution. The magnetic structure factor of one magnetic sublattice for this line can be seen in equation 3.2.

$$\mathbf{F}_M(-1,0,0) = 2i\sin(2\pi x)(\mathbf{m}_1 + \mathbf{m}_2 - \mathbf{m}_3 - \mathbf{m}_4) \qquad (3.2)$$

The value of $\mathbf{F}_M$ of each sublattice for the line $\mathbf{q} = (-1,0,0)$ is (0,0,4w) for Γ_1, (0,0,0) for Γ_2, (4u,0,0) for Γ_3 and (0,4v,0) for Γ_4. As this line has an experimental magnetic intensity that depends on the perpendicular component to the scattering vector of $\mathbf{F}_M$, the IRs Γ_2 and Γ_3 can be discarded. The FULLPROF programm has been used to fit the experimental magnetic intensities of Γ_1 and Γ_4, determine which IR describes the magnetic structure of GN-DMF(R) and to refine the magnetic moments of the atoms.

To refine the magnetic structure, the data collected in D15 can offer a more accurately results due to the characteristic of both instruments, but in order to check the validity of our results, we have refined the magnetic structure with both data sets. For D15, the short number of reflections acquired at 2K does not allow to refine the nuclear structure at this temperature. In order to obtain the magnetic contribution to the intensity, the atomic positions and thermal parameters at 2K and 35K have been considered as equal and the intensities measured at 35K and 2K have been compared. This assumption is supported if we compare the the structural data obtained with VIVALDI at 2K and 33K. Another option could have been to use the nuclear structure refined with VIVALDI at 2K to simulate the intensity of the lines, but the lack of a scale between reflections in both instruments, make us to discard this procedure. The reflections with a significant magnetic contribution and some reflections measured accurately at low angle, independently of their magnetic contribution, have been used in FULLPROF to determine the magnetic structure. In addition, the reflections acquired in VIVALDI at low θ have been examined carefully and the ones measured accurately (low dispersion in the value and low standard deviation), have been selected to perform a parallel refinement.

The magnetic structure corresponds to the irreducible representation Γ_1 and the values obtained for the magnetic moment can be seen in table **??** for a magnetic agreement factor R=4.68 R=10.85 for VIVALDI and D14 respectively. The magnetic moment for the Cr^{III} cation along the a axis could not be determined, there is a contribution that can not be estimated with our data.

If we compare the magnetic structure obtained with VIVALDI and D15 data, we found that although the magnetic structure is the same, there is a small difference in the magnetic moments. The magnetic moments for Mn^{II} and Cr^{III} obtained in VIVALDI are 4.6(2) and 2.1(3)μ_B respectively, while the same moments obtained from D15 data are 5.6(3) and 2.7(1)μ_B. We need to compare these experimental values with the theoretical values given by the magnetochemistry of each cation. As it has been said for the GN-MnMn compound in 2.4.2 Mn^{II} (d^5) in a low ligand field octahedral environment

Table 3.10: Magnetic moments for Mn and Cr along each axis and the total magnetic moment for GN-DMF(R) determined with VIVALDI and D15 data at 2K.

Instrument	Cation	M_x μ_B	M_y μ_B	M_z μ_B	M μ_B
~~VIVALDI~~	Mn^{II}	1.3(6)	3.70(9)	-2.5(3)	4.6(2)
	Cr^{III}	-0.5(9)	2.08(15)	0.2(2)	2.1(3)
Cation	M_x μ_B	M_y μ_B	M_z μ_B	M μ_B	
~~D15~~	Mn^{II}	1.2(5)	5.19(12)	-1.7(9)	5.6(3)
	Cr^{III}	—	2.64(12)	0.2(3)	2.7(1)

present a ground term $^6A_1$ ($t_{2g}^3e_g^2$) which is a high spin state with S=5/2. If the ligand field is strong enough, a transition to a ground term $^2T_2$ (t_{2g}^5) occurs and the Mn^{II} has a spin S=1/2. In this compound, Mn^{II} is surrounded by nitrogen and oxygen atoms and the ligand field is low enough to have a ground state $^6A_1$ and a spin S=5/2. The Cr^{III} (d^3) has a ground state $^4A_2$ (t_{2g}^3) and a spin state S=3/2.

The theoretical spin-only magnetic moments for Mn^{II} and Cr^{III} are $5\mu_B$ and $3\mu_B$, according to $S = g\cdot S\cdot \mu_B$ with a Lande factor equal to g=2. For the Cr^{III} cation, the spin-orbit coupling is small and only a slightly decreased in the value of the magnetic moment can be expected. No orbital contribution to the magnetic moment is expected for Mn^{II} ion, as the ground state present L=0 [89]. The difference between the theoretical and the experimental values may be due to a problem with the scale, specially in D15. The net magnetic moment is higher for the results obtained from D15, which may be due to an underestimation of the nuclear intensity at 2K (therefore, a overestimation of the magnetic contribution) implicity when we assume that the thermal parameters at 2K are equal than the thermal parameters at 35K. The theoretical ratio between magnetic moments is 1.67, and the experimental is 2.2 and 2.0 for VIVALDI and D15 respectively. Although a problem with the scaling process make the difference between experimental and theoretical value higher for D15 results, the ratio is nearer from the theoretical value. The major contribution to the deviation in the magnetic moments comes from the Cr magnetic moment along the a axis, which has not been determined with D15 data due to a low resolution in this direction. As there is not magnetic moment of Cr missed, we supposed that this contribution must be negligible.

AS D15 is better prepared to solve magnetic structures than VIVALDI, we have in better consideration the D15 results for the magnetic moments.

As it is logic, the magnetic structures obtained with the data acquired in VIVALDI and D15 are the same. It consists in two sublattices, one of Mn^{II}

and one of Cr^{III} that order antiferromagnetically one respect to the other, as it is showed in the figure 3.13. This coupling is predicted by the Goodeneough-Kanamori rules [76] explained in the Chapter 1.3.2. It is due to the fact that the unpaired electrons of Mn^{II} lie in t_{2g} and e_g orbitals, so the Mn^{II}-Cr^{III} interaction is antiferromagnetic. The magnetic moments are nearly along the b axis and the magnetic moments of Cr and Mn atoms are not collinear, which may be caused by the DM interaction, because there is not a symmetry element that can discard it, or by the anisotropy of the ions. The net magnetic moments along the b axis of different layers are directed in the opposite sense.

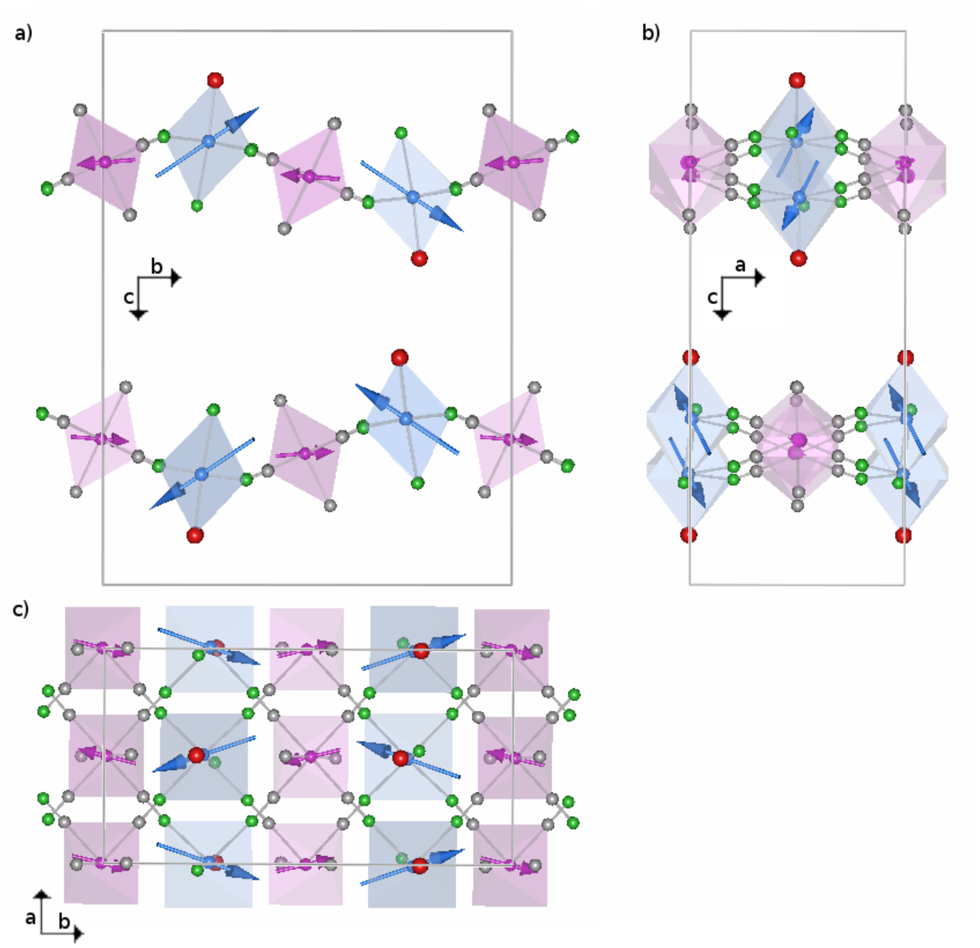

Figure 3.13: Magnetic structure of GN-DMF(R). Views along the a, b and c axes. Mn^{II} atoms are in blue and Cr^{III} atoms are in pink

There exists several differences between the magnetic structure of GN-DMF(R) and GN. If we focus ourselves in just one bimetallic layer, in the GN compound the magnetic moment of Mn and Cr try to be in the basal planes of their octahedra, being the Cr magnetic moment directed to the elongated bond C6-Cr-C1 and the Mn magnetic moment directed to the bisectrix between bonds. On the contrary, in GN-DMF(R) the magnetic moment of Mn cation in directed to the middle point of the face of the octahedra shared by the oxygen atom and two nitrogen atoms, out of the basal plane and directed along the bisectrix between all the bonding directions, not only in the plane. The explanation for the differences in the magnetic moments between both compounds could be in the distortion of the Mn and Cr octahedra. For the Mn in GN-DMF(R), steric hindrance due to the high volume of DMF may distort the angle N7-Mn-O1 until 172^{o}, inclining the DMF ligand towards the plane in order to avoid a DMF ligand from another layer. As a conscience of this distortion, the magnetic moment of Mn is out of the basal plane, directed to middle point of the face of the octahedra shared by the oxygen atom avoiding the ligands directions. The Cr magnetic moment in GN-DMF(R) tries to be in the basal plane of the octahedra and it is directed towards the bisectrix between the bonding directions. The different behavior of the Cr can be explained if we look to the distortion of the octahedra. As it can be seen in table 3.6, the distortion for the Cr is one order of magnitude higher in the GN, and the distance C1-Cr is 0.08Å longer than the medium Cr-C distance. The magnetic moment of Cr tends to be along this bonding direction in GN. For the Cr in GN-DMF(R), the environment is more regular and there is not an elongated bonding direction, the magnetic moment tends to be in the bisectrix of the bonding direction.

Another difference between GN and GN-DMF(R) is the direction of magnetic moments from neighbor layers. In GN the magnetic moments of homometallic atoms are directed towards the same sense of the easy axis, while in GN-DMF(R) they are directed in a opposite sense. This may be explained for the displacement of the layers b/2 along the b axis. As a consequence of this displacement, the shortest interlayer distance is homometallic, whereas the shortest interlayer distance in GN is heteromettalic (see table 3.6). The homometallic interaction between layers could explain the antiferromagnetic character, while the heterometallic interaction may be responsible for a ferromagnetic alignment.

In addition to these differences, GN and GN-DMF(R) compounds present different magnetic order temperature, 38K for the Phase I of GN and 28.8K for GN-DMF(R). As in both compounds the intralayer exchange pathways are the same, through the C≡N bonds, the explanation may be in the interlayer distance, which is shorter in the GN compound, and the octahedral environment of Cr, which is more distorted in GN compound.

In addition to the data acquired at low temperature and high temperature, several reflections with a significant magnetic intensity contribution have been measured at different temperatures: *(012)*, *(0-12)*, *(014)*, *(0-14)*, *(021)*, *(0-21)*, *(023)*, *(0-23)*, *(-100)*, *(-102)*, *(-10-2)*, *(-113)*, *(-1-13)*, *(-113)*. A graphic with the most significant of them can be seen in figure 3.14. As it well know, as the critical temperature is approached from below, the sublattice magnetization drops to zero following a power law. From the data represented in figure 3.14 it is possible to estimate the critical exponent β of the transition according to the equation 3.3, where I_M is the intensity in the magnetic phase and I_N is the nuclear intensity.

$$ln(I_M - I_N) = 2\beta \ln(1 - \frac{T}{T_N}) \tag{3.3}$$

As the magnetic diffracted intensity in neutron diffraction is proportional to the component of the magnetic structure factor perpendicular to **q**, the lines that can be used for a more accurate estimation of β are perpendicular to the magnetization. The magnetic moments in GN-DMF(R) almost lie on the plane yz so the line (-1,0,0) has been used to find a value for β=0.315(5). Due to the roughness of this method to estimate β, we may not adventure if it correspond to three dimensional Ising, XY or Heisenberg model (see [96] for a wide compilation of results for critical exponents).

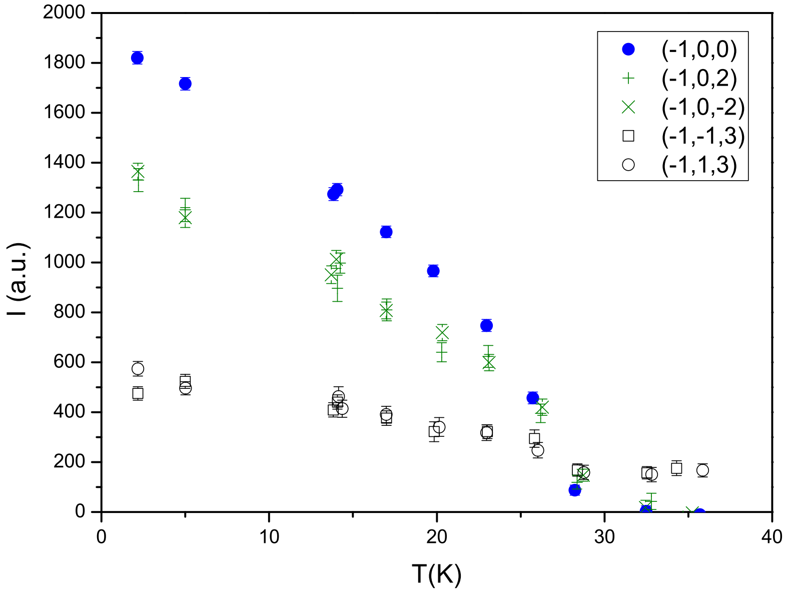

Figure 3.14: Intensity of several lines for GN-DMF(R).

3.4.2 GN-DMF(rac)

As it has been said before, neutron diffraction experiments have been performed in the GN-DMF(rac) compound with the aim of refining the nuclear structure and obtain the magnetic structure. In the next pages, the nuclear and magnetic structures of GN-DMF(rac) found are described.

Nuclear phase

The nuclear structure of the GN-DMF(rac) compound in the paramagnetic phase has been refined at 290K and 35K using VIVALDI and D15 data respectively.

A nuclear structure solved by X-ray at 290K has been previously reported [7]. In this reported structure, the positions of the hydrogen atoms could not be determined. With the data acquired in VIVALDI at 290K and using the reported structure as a starting point, we have refined the nuclear structure with the help of SHELX. Thanks to our refinement all the atoms have been placed and their thermal parameters have been set as anisotropic. To obtain the this result, it has been necessary to set some restrictions for the water molecules. The agreement factor for the analysis is R=0.1231 for reflections whose intensity is bigger than 4σ and 0.1937 for all.

The 749 reflections acquired in D15 at 35K have allowed us to refine the nuclear structure at a temperature near T_c. The nuclear structure solved by VIVALDI at 290K has been used as a starting point. In this refinement, the thermal parameters of Mn and Cr atoms are set as isotropic, because they are too small. The constraints in the water molecules are maintained and some restrains are applied to the thermal parameters of some hydrogens. The R-factor obtained in this adjust is R=0.1514 for reflections whose intensity is bigger than 4σ and 0.1681 for all data.

The fractional coordinates and thermal parameters for the refined nuclear structures at 290K and 35K are listed in Appendix E.

The thermal ellipsoids determined for GN-DMF(rac) at 290K and 35K are unusually high and they have a cigar shape, as can be seen in figure 3.15, where an asymmetric unit is showed. In an effort to reduce the size of the thermal ellipsoids for the hydrogen we tried to split the atomic positions, but the refinements were not improved. As for the GN-DMF(R) compound, there are two possible explanations for the anomalous size and shape of the thermal ellipsoids of this compound. One of them may be the loss os crystallinity due to the early stages of a degradation process. This hypothesis is supported by a visual inspection of the crystals after some time exposed to the air, they change their color from an emerald green to a greenish yellow and become porous. Lack of crystallinity has been observed in other Prussian Blue Analogues [75] specially if there are synthesized using a organic solvent as in GN-DMF(R) and GN-DMF(rac) case. The other explanation is related to the disorder and the possibility of a interchange between the positions of the pnH and the DMF ligands.

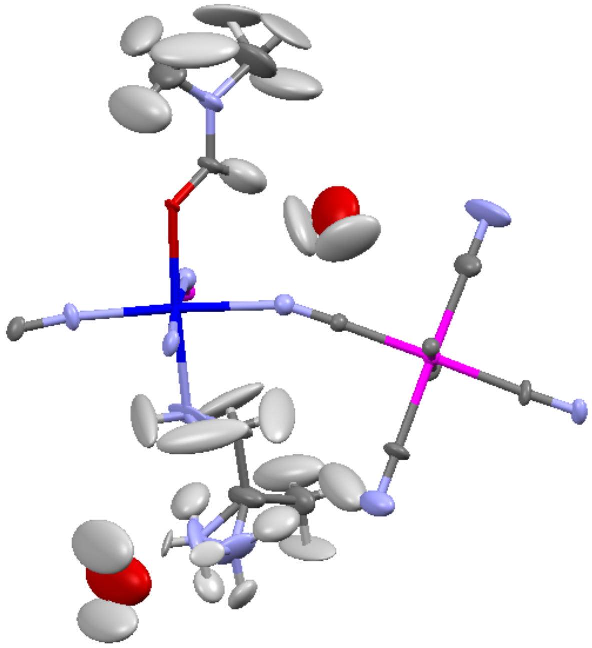

Figure 3.15: Asymmetric unit for the GN-DMF(rac).

In spite of the relative high values of R-factor for the adjustments and for the purpose of this thesis, the main features of the nuclear structure of this compound are accepted. It consist of bimetallic planes containing Cr^{III} and Mn^{II} atoms in octahedral environments and linked by cyanide. The Mn^{II} ions are also linked to a DMF molecule and pnH group which may be (R)-pnH or (S)-pnH. The two dimensional networks are arranged almost perpendicular to the c axis and there are two water molecules of crystallization per unit formula. The structure can be seen in figure 3.16.

If we compare the nuclear structure of GN-DMF(rac) and GN-DMF, we can observe that the main difference resides in the chiral carbon. The corrugation of the layers and the shortest distance between magnetic atoms remains almost equal. The distances between magnetic atoms in the same plane or from different planes, which may be relevant for the magnetism, are shown at table 3.11. The distances obtained using the VIVALDI data at 290K are larger than the distances obtained at 35K with D15 data.

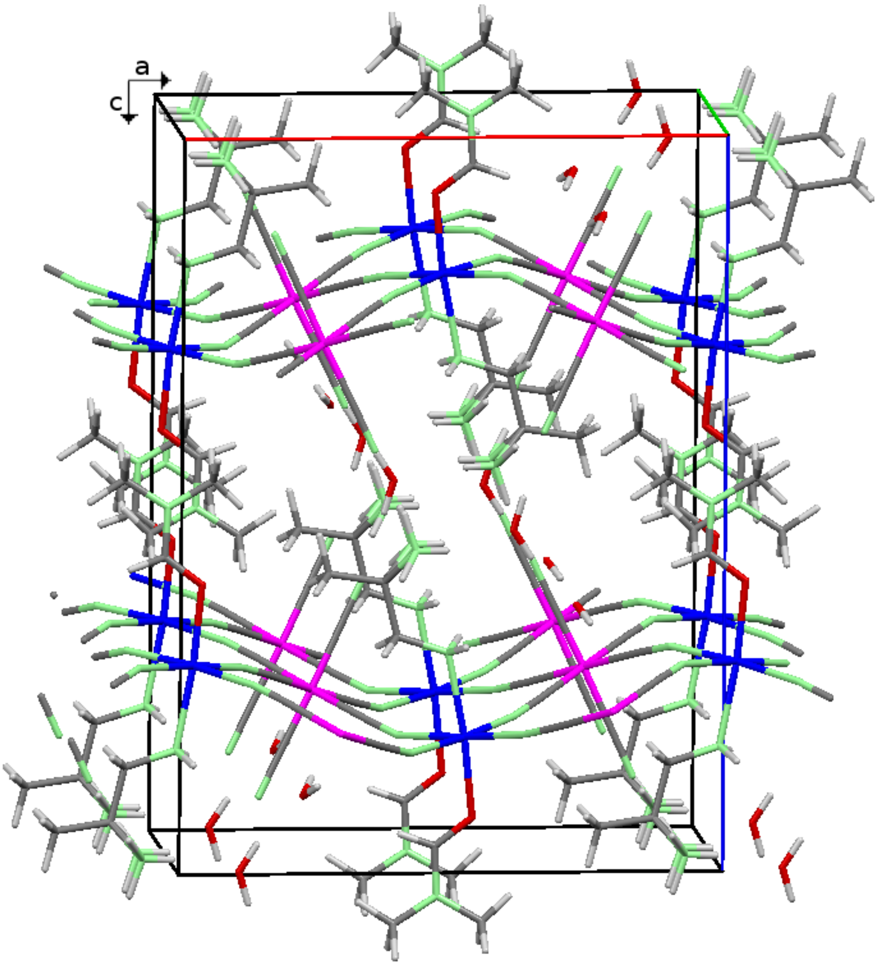

Figure 3.16: Nuclear structure for the GN-DMF(rac) compound..

Table 3.11: Shortest distances between magnetic atoms in the same layer (intra) and from different layers (inter) for the nuclear structure of GN-DMF(rac) determined with D15 data at 35K, VIVALDI data 290K and X-ray at 290K.

Atoms	d(Å) 35K	d(Å) 290K	d(Å) 290K(X-ray)
Mn-Cr(Intra)	5.46(4)	5.359(9)	5.358(2)
Mn-Cr(Inter)	9.44(3)	9.31(2)	9.278(1)
Cr-Cr(Inter)	10.78(3)	10.58(1)	10.578(1)
Mn-Mn(Inter)	8.94(3)	8.83(2)	8.796(1)

The Cr^{III} and Mn^{II} are in an octahedral environment. In order to compare the magnetic structure of this compound with the magnetic structure of GN-DMF(R), the distortion of their octahedra may be relevant, so it can be seen in table 3.13. If we compare the distorstion of the octahedra in GN-DMF(R) (see table 3.8) and GN-DMF(rac), we found that the distortions are of the same order of magnitude. The distance and angles inside the octahedra can be seen in table 3.13 and within the experimental error they are equal to the distance and angles found in the octahedra of GN-DMF(R), except for the angle N4-Mn-O whose value is 174.6(8)^{o} in the GN-DMF(rac) and the equivalent angle in GN-DMF(R) is 172.7(5). The deviation of this angle from the theoretical 180^{o} value is due to a stereo effect due to the volume of the DMF molecule.

Table 3.12: Distortion calculated of the octahedral environment for GN-DMF(rac) magnetic atoms at 35K.

Cation	Δ_d
GN-DMF(rac) Cr^{III}	$8.6{\cdot}10^{-5}$
GN-DMF(rac) Mn^{II}	$7.4{\cdot}10^{-4}$

Table 3.13: Bond lengths and angles for Cr^{III} and Mn^{II} in GN-DMF(rac) at 35K.

A-Mn-B	d_{A-X}(Å)	d_{B-X}(Å)	$\widehat{AXB}$
C1-Cr^{III}-C2	2.09(2)	2.07(2)	179(1)
C3-Cr^{III}-C4	2.07(3)	2.12(2)	178(1)
N1-Mn^{II}-N2	2.20(2)	2.27(2)	175.6(9)
N4-Mn^{II}-O1	2.36(2)	2.22(2)	174.6(8)

A-Cr-B	$\widehat{ACrB}$	A-Mn-B	$\widehat{AMnB}$
C3-Cr^{III}-C1	89.7(9)	O1-Mn^{II}-N1	94.2(6)
C3-Cr^{III}-C2	91.3(9)	O1-Mn^{II}-N2	89.6(6)
C4-Cr^{III}-C1	89.1(9)	N4-Mn^{II}-N1	89.6(6)
C4-Cr^{III}-C2	89.9(9)	N4-Mn^{II}-N2	86.5(6)
C1-Cr^{III}-C1	89.1(8)	N1-Mn^{II}-N1	91.3(6)
C2-Cr^{III}-C2	89.3(8)	N2-Mn^{II}-N2	91.3(6)
C1-Cr^{III}-C2	90.8(8)	N1-Mn^{II}-N2	86.8(6)

Magnetic phase

In order to determine the magnetic phase of the GN-DMF(rac) compound we have the D15 data acquired at 10K. It would be advisable to refine the nuclear structure at this temperature before starting the magnetic analysis, but the shortage of reflections at this temperature make us discard this option. Instead, as a first order of approximation, the atomic position and thermal parameters at 10K have been assumed to be equal than a 35K.

As usual, the first step is to determine the magnetic structure is to find the propagation vector. With this objective, several lines at low q were measured at 10K and 35K and their intensities at both temperatures compared. The increase in the intensity at low temperature was observed, which indicates that the magnetic cell and the unit cell are the same, and hence the propagation vector is equal to zero. In order to confirm this hypothesis, we scanned the reciprocal space along strategic directions in a search for magnetic satellite peaks with (h,k,l) no integers. A total of forty-five q-scans at 10K have been performed and no evidence of a propagation vector different from zero has been found. We accept that the propagation vector for the GN-DMF(rac) is ($\mathbf{k} = \mathbf{0}$. An example of a q-scan at different temperatures is shown in figure 3.17. In this case, we measured along the direction (h,0,0) and found a magnetic peak at (1,0,0).

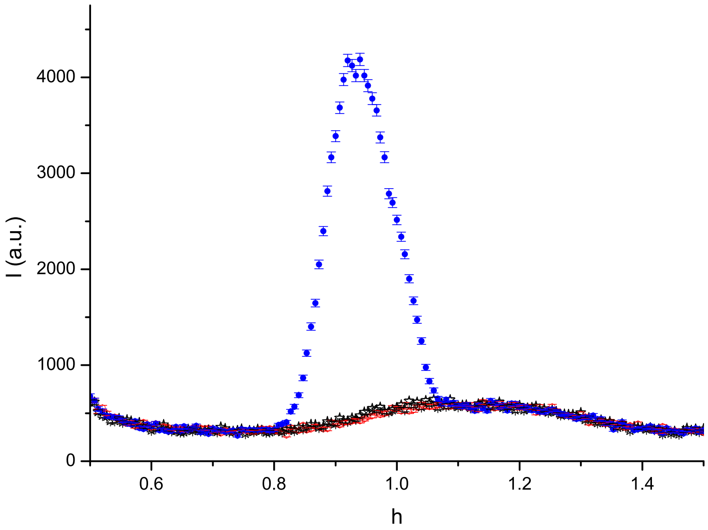

Figure 3.17: Qscan performed in the direction *h00* at 50K (⋆), 35K (○) and 10K (●)

As in the study of the previous compounds, the IR theory has been used to determine the magnetic structure. The IRs have been determined by BASIREPS code and the magnetic moments have been calculated by using FULLPROF. The space group of GN-DMF(rac) is Pnma and there are two magnetic sublattices in which the magnetic atoms are in special positions *(x, 0.25, z)*. Eight different one-dimensional IRs were obtained for this space group, and the reducible magnetic representation can be written as $\Gamma = \Gamma_1 + 2\Gamma_2 + 2\Gamma_3 + \Gamma_4 + \Gamma_5 + 2\Gamma_6 + 2\Gamma_7 + \Gamma_8$. The basis vectors for these irreducible representations are listed in table 3.4.2.

Table 3.14: Irreducible Representations for GN-DMF(rac) and their basis vectors. m_1, m_2, m_3 and m_4 represent the magnetic atoms of each magnetic specie.

Atom	Position	Γ_1	Γ_2	Γ_3	Γ_4
$\mathbf{m}_1$	(x,0.25,z)	(0,v,0)	(u,0,w)	(u,0,w)	(0,v,0)
$\mathbf{m}_2$	(-x+1/2,-0.25,z+1/2)	(0,-v,0)	(-u,0,w)	(-u,0,w)	(0,-v,0)
$\mathbf{m}_3$	(-x,0.75,-z)	(0,v,0)	(-u,0,-w)	(u,0,w)	(0,-v,0)
$\mathbf{m}_4$	(x+1/2,0.25,-z+1/2)	(0,-v,0)	(u,0,-w)	(-u,0,w)	(0,v,0)
Atom	Position	Γ_5	Γ_6	Γ_7	Γ_8
$\mathbf{m}_1$	(x,0.25,z)	(0,v,0)	(u,0,w)	(u,0,w)	(0,v,0)
$\mathbf{m}_2$	(-x+1/2,-0.25,z+1/2)	(0,v,0)	(u,0,-w)	(u,0,-w)	(0,v,0)
$\mathbf{m}_3$	(-x,0.75,-z)	(0,v,0)	(-u,0,-w)	(u,0,w)	(0,-v,0)
$\mathbf{m}_4$	(x+1/2,0.25,-z+1/2)	(0,v,0)	(-u,0,w)	(u,0,-w)	(0,-v,0)

In order to decide which representation correspond to magnetic structure of the GN-DMF(rac), several attempts of fitting have been performed using FULLPROF. In the fittings, the theoretical magnetic intensity and the experimental magnetic intensity are compares. The theoretical magnetic intensity depends on the perpendicular component to the scattering vector of the magnetic structure factor, which can be calculated for each sublattice as can be seen in equation 3.4.

$$\begin{aligned}
\mathbf{F}_M(\mathbf{q}) &= \sum_i \mathbf{m}_i \exp\left(i2\pi\mathbf{q}\cdot\mathbf{r}_i\right) = \\
&+ \mathbf{m}_1 \exp\left[i2\pi\mathbf{q}\cdot(x, 0.25, z)\right] \\
&+ \mathbf{m}_2 \exp\left[i2\pi\mathbf{q}\cdot(-x+1/2, -0.25, z+1/2)\right] \\
&+ \mathbf{m}_3 \exp\left[i2\pi\mathbf{q}\cdot(-x, 0.75, -z)\right] \\
&+ \mathbf{m}_4 \exp\left[i2\pi\mathbf{q}\cdot(x+1/2, 0.25, -z+1/2)\right] \qquad (3.4)
\end{aligned}$$

The line $\mathbf{q} = (0, 1, 0)$ has no nuclear contribution to the diffracted intensity due to the reflection conditions of the group ((0,k,0) with k=2n). Hence, the experimental intensity of 2176±37 counts measured at 10K for this lines corresponds to the magnetic contribution. The magnetic structure factor of one magnetic sublattice for the line (0,1,0) can be seen in equation 3.5.

$$\mathbf{F}_M(0, 1, 0) \propto [\mathbf{m}_1 - \mathbf{m}_2 - \mathbf{m}_3 + \mathbf{m}_4] \qquad (3.5)$$

The expression $\mathbf{F}_M(0, 1, 0)$ becomes zero for all the IRs except for Γ_2 and Γ_6, for which its value is (4u,0,0) and (0,0,4w). For this reason, the only IRs that can correspond to our magnetic structure are Γ_2 and Γ_6. Two fittings of the magnetic structure imposing the symmetry of Γ_2 or Γ_6 clarify that Γ_2 describes the magnetic symmetry for both magnetic species as can be seen in table 3.15. The magnetic moments found with an agreement factor of R=11.2 are shown in table 3.16.

Table 3.15: Experimental and calculated magnetic contribution to the intensity of several lines for the compound GN-DMF(rac).

(h, k, l)	$I_{35K} - I_{2K}$	I_{Γ_2}	I_{Γ_6}
(-1, 0, 0)	0±25	4	0
(1, 0, -2)	292±28	282	278
(0, 1, 0)	2120±43	2444	1353
(-2, 0, 1)	366±55	277	1122
(-1, 1, 1)	54±49	78	499
(0, 1, 2)	1796±48	1756	700
(-1, 0, 3)	74±42	73	6
(1, 1, 2)	69±50	69	10
(-2, 0, -3)	704±59	645	403
(-1, 1, -3)	472±52	498	557
(-1, 0, 4)	766±55	750	302
(-3, 0, -2)	59±55	14	228
(0, 0, -5)	187±50	193	0
(-1, 2, -2)	270±73	244	404
(-3, 0, -4)	368±62	258	407
(-2, 2, -1)	1383±71	1236	877
(-1, 0, 6)	573±69	603	232
(-4, 1, -2)	300±56	334	682
(-3, 1, 5)	458±72	407	111
(0, 0, -7)	578±66	634	0

Table 3.16: Magnetic moments for Mn and Cr along each axis and the total magnetic moment for GN-DMF(rac).

Cation	M_x μ_B	M_y μ_B	M_z μ_B	M μ_B
Mn	-3.69(4)	0	-1.5(4)	4.0(4)
Cr	1.97(5)	0	-0.3(1)	1.99(15)

The magnetic moments for Mn^{II} and Cr^{III} obtained are 4.0(4) and 1.99(15)μ_B respectively. As for the chiral compound GN-DMF(R), the theoretical values given by the magnetochemistry of each cation are $5\mu_B$ and $3\mu_B$, according to

$S = g \cdot S \cdot \mu_B$ and with a Lande factor equal to g=2. The difference between the experimental values and the theoretical ones could be attributed to the fact that the data were acquired at 10K, so the saturation regimen may not be reached.

The magnetic structure can be described as two sublattices, one of Mn and one of Cr, that order antiferromagnetically one respect to the other. The reason for the antiferromagnetic ordering has been already explained in the Chapter 1 and it is predicted by the Goodeneough-Kanamori rules [76]. The IR Γ_2 does not allow a magnetic component along the b axis and hence the magnetic moments lie in the plane ac, which the major contribution along the a axis. The net magnetic moments along the a axis of different layers are directed in an opposite sense. The magnetic structure can be seen in figure 3.18. The magnetic moments are not collinear, which could be due to the anisotropy of the ions of the DM interaction. A inspection of the symmetry elements of the group Pnmma reveals and inversion center in the middle point of the lines that join $\mathbf{m}_1 - \mathbf{m}_3$ and $\mathbf{m}_2 - \mathbf{m}_4$. According to the symmetry rules published by Moriya [55], this symmetry element discards the existence of a DM interaction between these atoms, but not between the other magnetic atoms.

$P2_12_12_1$ is a subgroup of Pnma and the symmetry operations of the space group Pnma of the GN-DMF(rac) compound are all the symmetry operations of the space group $P2_12_12_1$ for the GN-DMF(R) compound plus the inversion. Attending to the symmetry of the magnetic structures, the magnetic structure of GN-DMF(R) is described by the IR Γ_1 of the space group $P2_12_12_1$ (see table 3.9) while the magnetic structure of GN-DMF(rac) is described by the IR Γ_2 of the space group Pnma (see table). Both IRs becomes the same one if we suppose a magnetic moment with no component along the b axis for Γ_1. For this reason, the magnetic structure of GN-DMF(rac) is equivalent to the magnetic structure of GN-DMF(R) except for the component along the b axis. As for the GN-DMF(R), the magnetic moment of the Cr atom in GN-DMF(rac) is almost in the basal plane along the bisectrix between basal plane bonds, and the magnetic moment of the Mn atom is directed towards the center of a face of the octahedra. This behavior may be explained by the same arguments given for GN-DMF(R). Comparing the direction of magnetic moments from different layers in GN-DMF(rac), an antiferromagnetic alignment can be seen as for the GN-DMF(R) compound. Due to the similitude between GN-DMF(R) and GN-DMF(rac) and their exchange pathways, we considerer that the explanation for this alinement may be the same for both compound, already described in 3.4.1.

Several reflections with a significant magnetic intensity contribution have

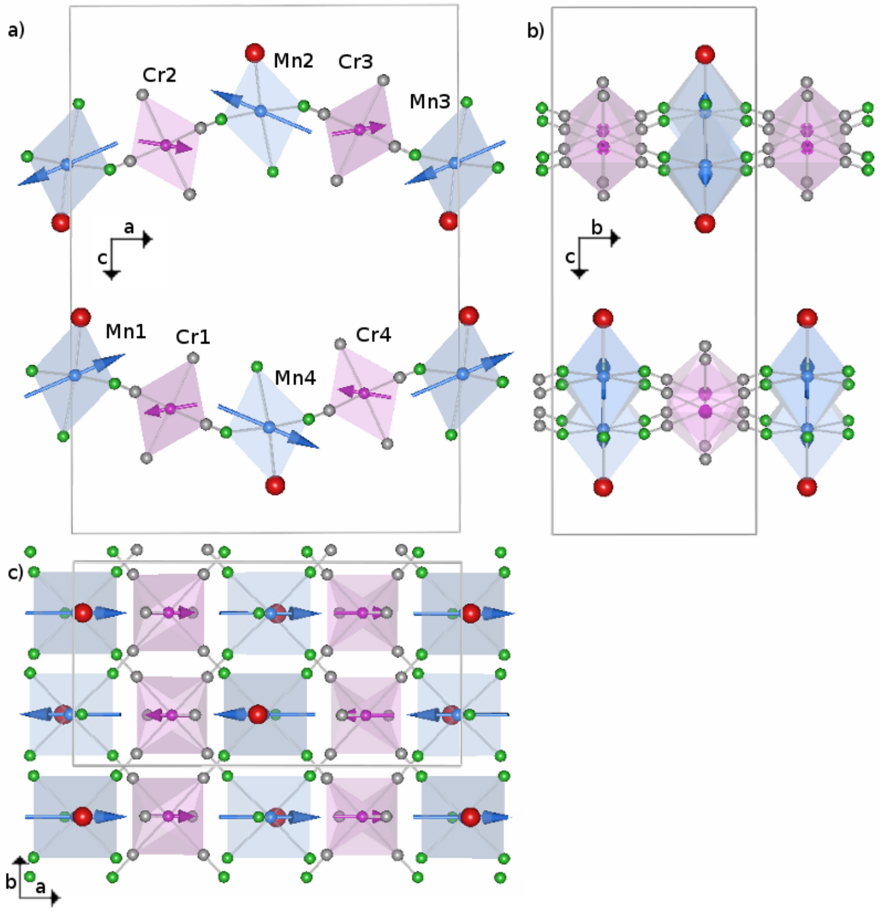

Figure 3.18: Magnetic structure GN-DMF(rac)

been measured at different temperatures: *(221)*, *(22-1)*, *(-102)*, *(223)*, *(-10-4)*, as can be seen in figure 3.19. As the magnetic moments in the GN-DMF(rac) compound are in the plane xz, the best lines to estimate the critical exponent β are the lines (0,k,0), but unfortunately none of these lines has been measured. A fitting with the data of the line *(223)*, gives a value of $\beta = 0.32(3)$. Within the experimental error, this value could correspond to a three dimensional Ising, XY or Heisenberg model (see [96] for a wide compilation of results for critical exponents).

3.5 Chiral term calculation

The chiral compound GN-DMF(R) compound crystallizes in the space group $P2_12_12_1$, which is chiral, so the compound presents nuclear chirality. The possibility of being magnetically chiral depends on the cross product $\mathbf{F}_M \times$

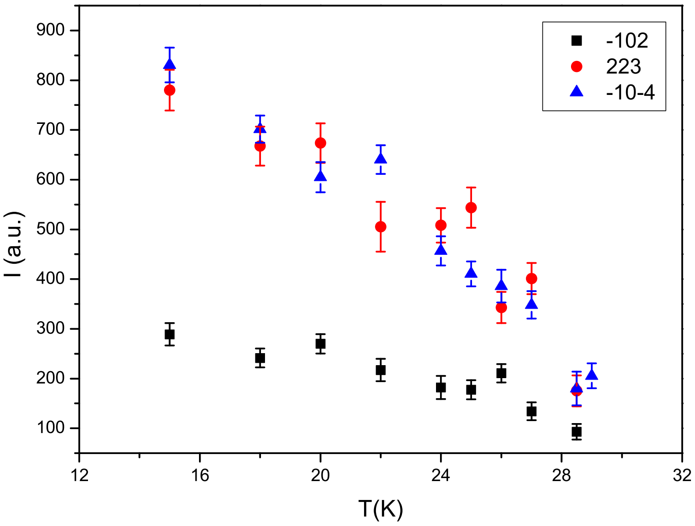

Figure 3.19: Intensity of several lines as T was decreased.

$(\mathbf{F}_M)^*$ as it has been explained in section 2.5. In the unit cell there are eight magnetic atoms, four Mn^{II} and four Cr^{III}, which must be present in the calculation of the magnetic structure factor. As for the GN-MnMn compound, the chiral product can be decomposed in a term due to the Mn_{II} cations, a term related to the Cr_{III} sublattice and two mixed terms as can be seen in equation **??**. The terms corresponding to the two sublattices are different from zero, as they are canted magnetic structures, and the cross terms are also different from zero. We can conclude that nuclear and magnetic chirality coexist in the GN-DMF(R).

$$\begin{aligned}\mathbf{F}_M \times \mathbf{F}_M^* &= \{\mathbf{F}_M^{Cr} + \mathbf{F}_M^{Mn}\} \times \{(\mathbf{F}_M^{Cr})^* + (\mathbf{F}_M^{Mn})^*\} = \\ &= \{\mathbf{F}_M^{Mn} \times (\mathbf{F}_M^{Mn})^*\} + \{\mathbf{F}_M^{Cr} \times (\mathbf{F}_M^{Cr})^*\} \\ &+ \{\mathbf{F}_M^{Cr} \times (\mathbf{F}_M^{Mn})^*\} + \{\mathbf{F}_M^{Mn} \times (\mathbf{F}_M^{Cr})^*\} \qquad (3.6)\end{aligned}$$

The racemic compound GN-DMF(rac) crystallizes in an centrosymmetric space group, so it is not nuclear chiral. In section 2.5.1, it has been said that magnetic chirality can no exist in centrosymmetric space groups, so the GN-DMF(rac) must be nuclear and magnetic achiral. Although the inversion is a symmetry operation of the space group Pnma, and the magnetic sites $\mathbf{m}_1$-$\mathbf{m}_3$ and $\mathbf{m}_2$-$\mathbf{m}_4$ are related by an inversion center, there are two sublattices that are not related by symmetry operations and whose magnetic moments are not collinear. The no collinearity of this sublattices may create rise doubts about the magnetic achiral structure of this compound. The no chirality of the magnetic structure can be corroborate by an inspection of the magnetic structure factor for each sublattice, which can be written as in equation by taking into account that $\mathbf{r}_1 = -\mathbf{r}_3$, $\mathbf{m}_1 = -\mathbf{m}_3$, $\mathbf{r}_2 = -\mathbf{r}_4$, $\mathbf{m}_2 = -\mathbf{m}_4$. The structure factor and its conjugate are equal except by a phase, so the chiral term is zero and the magnetic structure is achiral, as it has been postulated.

$$\mathbf{F}_M(\mathbf{q}) = 2i(\mathbf{m}_1 \sin(2\pi\mathbf{q}\cdot\mathbf{r}_1) + \mathbf{m}_2 \sin(2\pi\mathbf{q}\cdot\mathbf{r}_2)) \tag{3.7}$$

3.6 Conclusions

In this chapter, the nuclear structures of the compounds GN-DMF(R) and GN-DMF(rac) have been refined using neutron diffraction. In addition, we have determined the atomic positions of the hydrogen atoms, which were not determined previously [7].In the refinement performed with neutron data, all the thermal parameters of the atoms have been set as anisotropic, except for Mn and Cr in GN-DMF(rac) at 35K. Is spite of acceptable agreement factors for the refinements, we have found an anomalous size and shape of the thermal ellipsoids. This anomaly may be attributed to a lack of crystallinity or some structural disorder. If we compare the nuclear structure of GN-DMF(R) and GN-DMF(rac) with the nuclear structure of GN compound, we can see how the substitution of a H_2O ligand in GN by a DMF molecule modifies the corrugation of the layers and the shortest interlayer distances.

In addition to the refinement of the nuclear structure, the neutron data acquired have allowed us to solve the magnetic structures for both compounds. A propagation vector equal to zero $\mathbf{k} = 0$ has been determined for GN-DMF(R) at 2K and GN-DMF(rac) at 10K, so the nuclear and the magnetic cells are the same.

For the chiral compound, the magnetic phase can be described with the IR Γ_1 of the space group $P2_12_12_1$. Below the critical temperature, the compound presents two interpenetrating magnetic sublattices, one of Mn^{II} and another one of Cr^{III} which interact antiferromagnetically. The magnetic moments of the Cr atoms try to remain in the basal plane, while the magnetic moments of Mn are out of the plane. The magnetic moments try to follow the direction of the bisectrix between bonds. The lack of a center of symmetry between the magnetic atoms allows the existence of a DM interaction, which may be the responsible of the non-collinearity of magnetic moments. The interaction between layers in GN-DMF(R) compound is antiferromagnetic in contrast with GN and GN-MnMn where it is ferromagnetic. This could be justified by the difference in the interaction pathways between layers. Considering our the definition for a magnetically chiral compound $\mathbf{C}_M = \mathbf{F}_M \times (\mathbf{F}_M)^* \neq 0$), the magnetic phase of GN-DMF(R) is magnetically chiral, therefore, nuclear and magnetic chirality coexist in this compound.

The symmetry of magnetic phase of the racemic compound GN-DMF(rac) can be described with the IR $\Gamma 2$ of the space group Pnma. As for the chiral compound, the magnetic structure of GN-DMF(rac) can be described as two interpenetrating and antiferromagnetic layers, one of Mn^{II} and another one of Cr^{III}. The inversion center between pairs of magnetic atoms in the GN-DMF(rac) is the main difference between the GN-DMF(R) and the GN-DMF(rac). As a consequence of the inversion center, the component of the magnetic moments along the b axis is set equal to zero and magnetic chirality no longer occurs.

General conclusions for Part I

- **Global definition for magnetic chirality.** In a context where the concept of magnetic chirality is sometimes confused with nuclear chirality or defined as a local concept, we have proposed a global definition for magnetic chirality in section 2.5. According to our criterium, a magnetic structure is chiral if the cross product $\mathbf{F}_M \times (\mathbf{F}_M)^*$ is different from zero. Magnetic chirality is only possible in non collinear structures where the magnetic sites are not related by an inversion center.

- **Effect of substituting Cr^{III} atom in GN for Mn^{III} atom in GN-MnMn.** The substitution of the Cr^{III} atom in GN for Mn^{III} atom in GN-MnMn has a negligible effect in nuclear structure, except by the environment of the substituted atom, and has no effect in the symmetry of the magnetic structure. Both magnetic structures can be described with the same IR, Γ_4 of the group $P2_12_12_1$, and can be seen as a conical quadrangular structure along the a axis. The only difference resides in the orientation of the magnetic moment of the M^{III} atom in the basal plane, whereas Cr^{III} is directed toward an elongated bond, Mn^{III} is directed toward the bisectrix between bonds. The substitution of Cr^{III} atom in GN for Mn^{III} atom in GN-MnMn has lead to a of the critical temperature of the sample.

- **Effect of substituting a H_20 ligand in GN for a DMF ligand in GN-DMF(R).** The substitution of the H_2O for a DMF as modified the stacking of the layers and increased the interlayer separation. This structural changes modifies the symmetry of the magnetic structure that corresponds to Γ_1 of the $P2_12_12_1$ group. While the magnetic structure for GN compound can be seen as a conical quadrangular structure along the a axis. the IR Γ_1 does not allow a ferromagnetic component along any axis and correspond to an antiferromagnetic structure. As a consequence of the changes in the interlayer separation and piling up, the interaction pathways between layers are different and magnetic order between layers changes from ferromagnetic in GN compound to antiferromagnetic in

GN-DMF(R) compound. In addition to this differences between GN and GN-DMF(R), the octahedral environment of Cr and Mn are modified and it has influence in the orientation of their magnetic atoms.

- **Influence of a chiral ligand in the magnetic chirality.** While in the GN-DMF(R) compound all the chiral ligands are the same enantiomer, in the GN-DMF(rac) there is equal number of the two enantiomers as ligands for unit cell. As a consequence, the space group is centrosymmetric and the nuclear structure is not longer chiral. The inversion point that relates pairs of magnetic sites modifies the symmetry of the magnetic structure, which can be describe by the IR Γ_2 of the group *Pnma*. The existence of the inversion points neglects the possibility of having a chiral magnetic structure.

- **Magnetic Chirality in bimetallic ciano-compounds.** All the compound studied in this thesis with a chiral nuclear structure have been determined to present also magnetic chirality. As a consequence, this synthesis strategy seems to be adequate to obtain chiral magnets.

Part II

SMM compounds

Chapter 4

Introduction to SMMs. Concepts and objetives

4.1 Introduction

The second part of this thesis is devoted to the study of the magnetic properties of Single Molecule Magnets (SMMs) and the influence that the environment can have on them. Our objective is double, we want to verify how small structural differences can affect the energy barrier of a SMM and observe the possible effects of arranging SMMs in 2D or 3D structures. This arranging can lead to the loss of the SMM properties or conduct to a new phenomenology as the coexistence of magnetic order and blocking. For this purpose, in a complementary thesis, Elena Forcén is synthesizing and characterizing structurally new Co(II) cubane compounds, where cubanes are isolated or forming extended crystallographic arrays. The study of the physics of these complex systems has provided a necessary feedback helping new compounds with new arrays. Consequently with the complementary of the synthetic and crystallographic work, we will provide here only the necessary crystallographic information to support the analysis of the magnetic data.

In this introductory chapter to the second section of the thesis, a brief explication of the SMM properties is given in 4.2 with the aim to facilitate the understanding of our result. Also, we summarize some studies where SMM are networked or in the vicinity of SMM that can generate a bias field that modify their energy levels in 4.3. As our clusters are Co(II)-cubanes, a glimpse of the exceptional magnetic properties of the ion Co(II) is given in 4.4 before a revision of the literature of similar clusters in 4.5. To end this chapter, the objectives and the techniques used are described.

4.2 Single Molecule Magnets (SMMs)

If we try to give a compact definition for SMM, we could say, in a general way, that they are a class of metalorganic compounds that, below a blocking temperature, show superparamagnetic behavior and exhibit magnetic hysteresis of purely molecular origin. Using a rigorous definition for a magnet, the name itself is not correct, because to have a magnet it is necessary to have an infinite number of coupled centers. It should be, therefore, clear that the denomination of magnet in the SMM name is just evocative of the common property of hysteresis that these compounds have with real magnets and should not be extended to other properties. These molecular materials are characterized by an isolated high spin ground state and a high magnetic Ising-anisotropy, which generates a non negligible energy barrier (Δ) that held up the reversal of the magnetization by thermal activation for temperatures below the blocking temperature (T_B). Below this temperature, the system is said to be blocked and the magnetization decays exponentially with the time. However, the richness of their physical behavior in not limited to this phenomenon. Their size and number of atoms can vary from just one to the limits of nanoparticles, so their properties can be studied in the frame of quantum or classical physics. Therefore they represent an excellent scenario to connect the classical and quantum world and to test the validity of fundamental quantum mechanics theories. In addition, the SMMs can be seen as functional building blocks that can be used for constructing high dimensional frameworks, constituting a new branch for the bottom-up methods.

In the vast pool of existent options, we will focus on single molecule magnets formed by a small number of atoms, which are also excellent candidates to study the nature of the exchange interaction, the anisotropy, the dipolar order and other basic concepts of physics. The limited amount of magnetic atoms allows, in the most cases, to write a complete hamiltonian and solve it analytically, obtaining the value of magnetic interaction parameters or anisotropic parameters among others.

The first single molecule magnet discovered was synthesized in 1980 [34]: $Mn_{12}ac$, $[Mn_{12}O_{12}(CH_3COO)_{16}(H_2O_4)] \cdot 4H_2O \cdot CH_3COOH$, and it is still one of the most studied SMM and a typical paradigm. One of the milestones in the study of this compound was in 1993 [97] when the relaxation time of the magnetization was observed to follow an exponential law with the temperature below the blocking temperature. The relaxation of the magnetization to its thermal equilibrium can be written as in equation 4.1 for an ensemble of identical particles, where τ is the "spin-lattice" relaxation time. τ depends exponentially on the ratio between the energy barrier and the temperature, with a pre-factor τ_0 that is the characteristic time for the system. This dependence

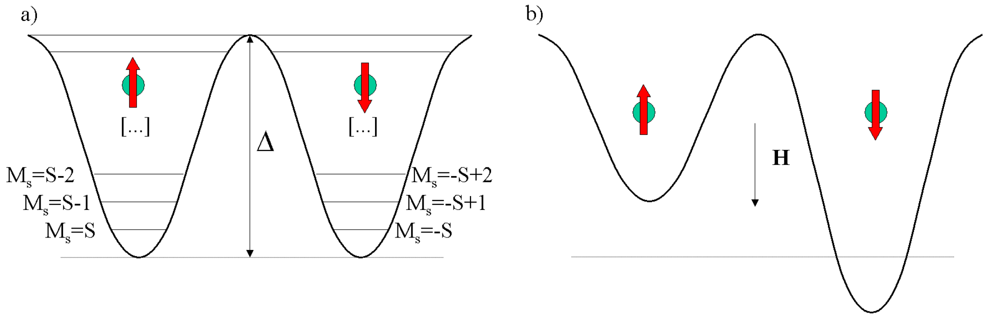

Figure 4.1: a). Schematic drawing of the Δ created by a high anisotropy. b) Modifications in the energy levels due to an external magnetic field.

is shown in equation 4.2 and is known as a Arrhenius law.

$$M(t) = M_0 \cdot (1 - \exp(-t/\tau) \qquad (4.1)$$

$$\tau = \tau_0 \exp(\Delta/kT) \qquad (4.2)$$

An alternative to calculate the energy barrier and the relaxation time is based on an average magnetic relaxation time τ_{av}, that can be estimated with the relation given by equation 4.3. This equation is often used to analyze magnetic dynamics of spin glasses and other complex magnetic system [98]. This relation is specially useful when two superposed frequency-dependent signals coexist or the blocking phenomenon can be hardly observed and it is not easy to determine the peak position in the out-of-phase signal.

$$\tau_{av} = \lim_{(\omega \to 0)} [\chi"/\omega\chi'] \qquad (4.3)$$

The origin of the energy barrier in a cluster lies in a high spin ground state in addition to an Ising magnetic anisotropy. Its magnitude is given by the difference between energies of the lowest lying level and the top lying level as can be seen in figure 4.1a. It can be calculated as $\Delta = |D|S^2$ if the spin of the cluster is an integer, or $\Delta = |D|(S^2 - 1/4)$ if the spin is a half integer, where D reflects the axial anisotropy, selecting a preferred orientation of the magnetization along z (easy-axis anisotropy). If the D parameter is negative, major projections of the spin $|m_S >= \pm S$ lie lowest. A positive D term corresponds to easy-plane anisotropy with preferred orientation of the spins in the xy plane.

In absence of an external field and at very low temperature, if D is negative, the state levels $|m_s >= +S$ and $|m_s >= -S$ are degenerate, lie lowest and are the unique levels populated. Magnetization is zero. If a magnetic field parallel to the anisotropy axis is applied, a sense of magnetization is favored as can be seen in figure 4.1b. If the external field is high enough, only one level ($|m_s >= +S$ or $|m_s >= -S$) is populated and the magnetization reaches its saturation value. When the field is removed the system must go back to thermal equilibrium, so it "relaxes". Classically, this process is possible by the coupling of the spin system to the environment, i.e. spin-phonon interaction. In this situation, spins absorb energy from phonons to reach the higher level energy and then loss energy by exciting vibrational modes of the lattice, until equilibrium exists.

As the energy barrier depends directly on the anisotropy and the net magnetic moment of the system, a smart rational design for SMMs will look for clusters with high magnetic anisotropy and a high spin ground state to increase the energy barrier and hence the blocking temperature of a SMM. With this objective, efforts to achieve a smart design have been performed in several directions: clusters containing larger numbers of metal centers to increase the spin, the use of metals with a large anisotropy to increase D, or by using a directed synthesis approach toward specific cluster geometries. For example, in homometallic compounds, a good strategy is to use brigding angles close to 90^{o}. Other consideration that have to be taken into account, is the fact that the exchange coupling should be as large as possible, so the resultant spin ground state that characterize the cluster is isolated from the excited states. A synthesis strategy based on increasing the D value or the spin cluster and to hope for the best for the other parameter has been followed for a long time. However, recent studies show that S and D are correlated [99, 100]. For the same compound, increasing S will generally result in enhancing the energy barrier, but not as S^2 as it could be expected. The magnitude of the barrier is mainly determined by D, therefore, increasing the anisotropy of the cluster and the single-ion anisotropy of each magnetic site given by the local tensor D_i, results a more promising strategy than increasing the number of metal ions and their spins. In this scenario, atoms with spin-orbit coupling are promising candidates to increase the energy barrier in cluster. For an ion with a ground state S, orbital contributions may be mixed into the ground state through spin-orbit coupling $H = \lambda{\cdot}L{\cdot}S$, so the $|m_S >$ components of a given S state are split in zero field, leading to a preferred orientation of the magnetization with respect to the anisotropic axis of the molecule. The magnitude of this splitting and therefore of the anisotropy is proportional to λ^2, the spin-orbit coupling constant. Transition metal ions which a large spin-orbit coupling show larger anisotropies and Co(II) complexes results very interesting due to the spin-orbit coupling which can generate an important zero-field-splitting (ZFS). This phenomenon causes a single-ion anisotropy and as the main contribution to the cluster magnetic anisotropy is the sum of the single-ion anisotropies of the metal ion constituents, it enhances the energy barrier. Often, ZFS contributes to magnetic anisotropy of the cluster more than dipolar or exchange interactions. The size of D parameter depends upon the metal ions present and its coordination environment.

A tendency to increase the nuclearity (and hence the maximum spin value) has lead to clusters up to 84 atoms [101], whose size is approximating the magnetic nanoparticles. However, a large number of metal centers do not guarantee a large total molecular spin. One approach is to have a cluster topology that provides ferromagnetic interactions such as a metal-oxo cubane structure that can promote ferromagnetic interactions via superexchange. The metal-oxo cubane structure is described in next section. The control of the magnetic properties of polynuclear complexes is in an early stage of development. The highest energy barrier described until the present is 86.4K with a blocking temperature of 4.5K for a $[Mn_6]$ cluster [102]

4.2.1 Relaxation pathways

The magnetic moment reversal implies overcoming an energy barrier, which classically is a very slow process at temperatures much cooler than the blocking temperature. But SMMs are in the limit between classical and quantum physics, and beyond the thermally activated relaxation, they can also relax through quantum tunneling mechanisms [35]. The SMMs are the best superparamagnets to study these complex relaxation processes, because distribution of sizes and anisotropy axis that can difficult the study with nanoparticles are absent.

At very low temperature only the degenerate $|m_s >= \pm S$ levels are populated. If only exits an axial anisotropy, the two states $|m_s >= +S$ and $|m_s >= -S$ are degenerate and orthogonal to each other, and there is no possibility of tunneling. However, with a suitable perturbation, the eigenstates of the full Hamiltonian are are linear combination of states with different sign of m_s and the wavefunction is therefore partially delocalized on both wells. In these conditions, tunneling may be observed. As a consequence of the mix of states, the degenerate levels with different sign of m_s are split in an energy quantity Δ_T, the so-called tunnel splitting; one of the two levels is of lower energy than the degenerate levels, while the other is of higher energy. There exist different perturbations that allow the existence of quantum tunneling: dipolar forces between molecules, hyperfine fields or an anisotropy in the perpendicular plane, E, called transverse anisotropy or rhombic anisotropy. A convenient form for the perturbational hamiltonian that takes into account the anisotropy in the perpendicular plane can be seen in equation 4.4

$$H = E(S_x^2 + S_y^2) \tag{4.4}$$

Equation 4.4 directly couples states differing in m_S by 2 in a first order of approximation. Therefore, states $|m_s >= +S$ and $|m_s >= -S$ are mixed in a higher order in perturbational theory and their Δ_T will be low. As the possibility of tunneling is related to the relative energies of the tunnel splitting and of the barrier, the smaller the ratio between the two the smaller the possibility of observing tunneling, it is very important the contribution to the higher levels in the tunneling.

If the spin of the cluster is a half integer, the transverse term of the anisotropy does not admix the ground states and the tunnel splitting is zero. These states remain degenerate as predicted by the Kramers theorem, according to which the minimum possible degeneracy of the states of odd-integer spin systems is two. Therefore, in principle, no tunneling is possible for a system with half-integer spin in rigorously zero field.

Tunneling can occur also between different pairs of degenerate excited states, and it is called phonon-assisted or thermally activated tunneling mechanism. Phonons are absorbed in order to populate excited states involved in the tunneling process. As the tunneling frequency is expected to increase on decreasing the value of m_s this mechanism is very important when these levels are populated. Molecules may not need to go over the maximum of the barrier even at relatively high temperatures, but may find a shortcut and tunnel.

The former quantum phenomenons occur in absence of a external magnetic field. If a magnetic field is applied parallel to the anisotropy axis, it modifies the energy levels as can be seen in figure 4.1b, so it removes the degeneracy between pairs of levels with the same m_s. However, the modification in the level structure, implies that for some values of the magnetic fields, levels at different sides of the energy barrier will meet, so the conditions for resonant tunneling are restored. If the field is applied parallel to the hard axis, it generates an oscillating phenomenon that modulates the tunnel splitting making it even zero for certain values [103]. This phenomena generates the typical stepped hysteresis cycle for SMM as can be seen in figure 4.2. The steps are observed at the fields at which pairs of levels become degenerate. They correspond to relative minima in the relaxation times, because at these fields two mechanisms are operative: thermally activated and quantum tunneling.

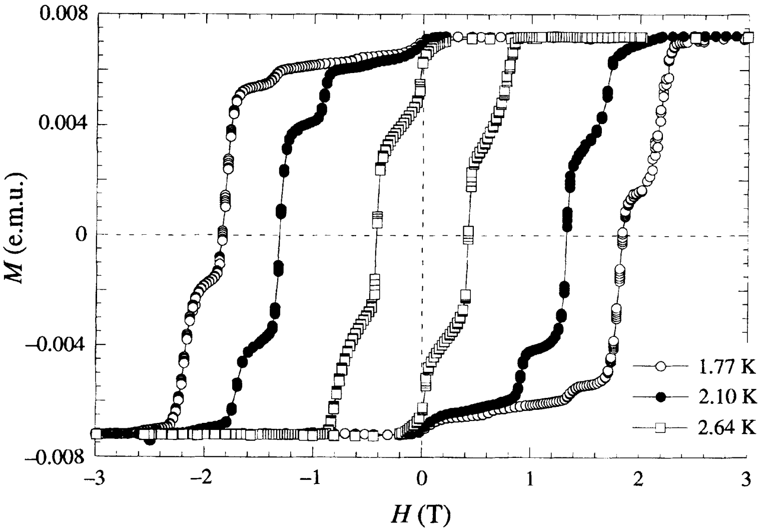

Figure 4.2: Magnetic hysteresis loop for a single crystal of Mn12ac with the field parallel to the tetragonal axis at 2.1 K. [104]

4.2.2 Applications

SMMs are materials that have important potential applications in several fields. Below the blocking temperature, a SMM behaves like a magnet, in the sense that if magnetized by an applied field it retains the magnetization a time, rising to magnetic hysteresis. The ground state doublet is separate by the energy barrier, therefore stabilizing two effective spin states at low temperatures. After these discovers, it was suggested that the SMMs may be used as information storage units, being each molecule a bit with two binary states switched by an external magnetic field . This goal is still out of reach, but some progresses are being done. In order to have the possibility to used the SMM as information storage units, it is necessary to increase the relaxation time to significant values at accessible temperatures which implies to increase the energy barrier until very high limits. This future technological application helped to rise the interest in this field. In a more broad horizon, SMM are not limited to data storage at incredible high limits. Other potential technological application of SMM, is the possibility to integrate them as building blocks in quantum computers [36] [105]. The physical laws governing these small devices are in the frame of quantum physics and classical Boolean logic may not be valid at this scale or there may exist other logics more appropriate at this case. This will imply a deep revolution, not only in the materials, but also in their functionalities and applications, as the final objective is to store information in a molecule, process information in a molecule and communicate the result to a (supra-)molecular device. In a classical device, a bit can be only 0 or 1, but in a qubit, it can be coded as any linear superposition of the two states associated with the logical 1 and 0. Linear superpositions are very important during the dynamics, allowing quantum algorithms that performs computational tasks at inaccessible rates for classical computers. For the case of SMM, the physical magnitude to be manipulated is the spin state of the molecule, giving rise to the development of the spintronics [5] [37].

In addition, the finite number of atoms in SMMs made them excellent model systems to study the exchange interactions at the molecular scale, anisotropy effects. Due to the possibility to achieve an uniform size and distribution of SMM in a crystal, there are also excellent probes to study long range order (as produced purely by dipolar forces [13]), spin-glass-like-dynamics or competition between single-particle blocking and collective blocking. Its unique properties in the frame of quantum physics made them unvaluable sceneries where new quantum theories can be tested.

4.3 Networked SMMs

If one of the final objectives of the work with SMM is to use them as devices for data storage, it is necessary to organize the molecules so they can be addressed. Some attempts have been done to organize them in Langmuir-Blodgett films [106] or on polymeric thin films [107], to network them by polymers [108], or to transfer SMMs onto various substrate materials [109], as the first attempts performed on gold surfaces [110]. An alternative approximation may be the self-assembly of SMM, especially in regular 2D arrays of SMM [111]. Some of the compounds presented in this thesis are self-organized in bidimensional or tridimensional covalent networks, which makes the organization of SMMs trivial.

Several studies in nanoparticles have been performed to study long range order, spin-glass-like-dynamics or competition between single-particle blocking and collective blocking [112], but due to the usual distribution of particle size and interparticle distance as well as the random localization of the particles, make this task very difficult. Therefore, SMM arranged on a regular lattice represent a more convenient scenery. Different collective behaviors can be observed when there is an aggregate of SMMs or networked SMMs, and they can provide an understanding of collective phenomena occurring in an interacting SMM system or among nanosized magnets.

The first evidence for the influence of the environment in the behaviour of SMMs was given by W. Wernsdorfer et al. on dimers of Mn_4 [113] where antiferromagnetic interactions through H bonds appear, the interactions between SMMs modify their energy levels leading to an exchange bias of the quantum resonances and may allow the control of their quantum properties. Therefore, organizing SMMs into supramolecular architectures became a very interesting field. In addition, linking SMMs in networks can give rise to new magnetic materials whose properties lie in the boundary between classic and quantum effects.

We would like to remark, that linking clusters in networks may present a wide variety of different behaviors, where relaxation process and magnetic order phenomenons can appear together. We are focusing ourselves in clusters that have shown a SMM behavior as isolated entities and have been bridged through different ligands to form nets. But also clusters different from SMM can be part of networks and show magnetic order and relaxation process of different nature [114].

Several regimens in temperature and field frequency are expected in a network of SMM [115]. If we attend to the field frequency regimen, the superparamagnetic behavior of SMM is revealed in presence of AC magnetic fields, therefore, this characteristic can be neglected in DC fields, where long magnetic order may appear. As the frequency of an AC field is increased, the nature of the SMM manifests more significantly until no conventional order can appear and SMM behaves as individual clusters. However, in the intermediate situation, there is a magnetic aggregation of SMM whose may shown a glassy response. Attending to the temperature regime, the blocking phenomenon tends to freeze the cluster spins in random directions, in contrast to interclusters interactions which favor magnetic order. If long magnetic order is presented by a compound, its origin can be purely from dipolar interaction, as it was seen for first time in a crystal of Mn_6 cluster [13], from magnetic superexchange interaction origin or a mix of both phenomenons [116].

Due to the different considerations that have to be taken for temperature and field regimens, there are a wide variety of different behaviors at the moment and no prediction exists to anticipate the magnetic response of a compound.

In our compounds studied in Chapters 6 and 7, SMMs are linked covalently through bridges with one Co(II) ion, so we expected that superexchange pathways exist and the dipolar interaction is negligible. Focusing our attention in SMMs linked covalently, the most part of them are based on Mn (see for example refs. [117–120]) and among them, a family of related compounds based on a Mn_4 SMM [121] that has been studied while it forms a 1D chain of SMM showing canted antiferromagnetic coupling[122], 2D networks exhibiting canted antiferromagnetic coupling [123] and a 3D structure with ferrimagnetic order at 4.1K [11, 12] and where no sign of SMM behavior is found, represents a very complete study. In the 2D structures, differences in the orientation of the [Mn_4] unit, lead to different properties, from SMM behavior to a ordered magnetic phase at 4.2K without sign of magnetic relaxation, going through a state where canted ferromagnetic order below 2.1K coexist with a slow relaxation of the magnetization process.

In contrast to Mn compounds, the number of Co(II) SMM networked is significantly lower, for example ref. [124], where a relaxation phenomenon for a pentanuclear Co(II) cluster is found around 5K with a characteristic time two orders of magnitude higher than the expected, and although no peak in χ" appears below it, the existence of a divergence in the ZFC-FC magnetization around 3K is used to postulate a magnetic order. If we restrict our attention to networks of Co(II)-cubanes, only a few examples have been synthesized. Modifying the synthesis of the Co(II) citrate cubane reported in 2003 [125], a 3D network of cubane units linked by octahedral Co(II) centers crystallizes [126], where the SMM character of the cubane is present around 5K and ferromagnetic interactions between clusters appears at lower temperature. For this compound, a long magnetic order is suspected although not observed in the temperature range explored. In another 3D framework build up from Co(II) and dicyanamide bridges, the SMM behavior typical of Co(II)-cubanes has been lost and neither SMM blocking neither magnetic order are observed in the 3D structure [127] down to 2K. During all this chapter, we are overlooking a supramolecular structure of Co(II) cubanes arranged in a 3D network [128], but whose structure contents some features that makes us be cautious about it.

Our working group is doing some progress in arranging Co-cubanes in different dimensionality networks with different cations, morphologies and Co(II) content. A 1D chain of cobalt(II) citrate cubanes with peripherical octahedral Co(II) centers which can be transformed into a 2D network by dehydration has been synthesized [129], but its magnetism can not be studied due to the impossibility to asses the purity of the phase. A series of 2D networks of cobalt(II) citrate cubanes with peripherical octahedral Co(II) centers were obtained and magnetically characterized, the results are partially published [14, 15] and the fully magnetic characterization can be found in chapter 6. A 3D structure studied in chapter 7 keeps on with the work increasing the dimensionality of the network.

The study of these compounds, might provide clues on how to modulate the SMM properties.

4.4 The Co(II) ion and it magnetochemistry

As it has been said in 4.2, a tendency to increase D dominates the efforts to achieve a smart design for SMM. Co(II) represents an excellent candidate for SMM due to its high spin-orbit coupling and anisotropy, but the difficulty to treat analytically problems where Co(II) ions appear, has made Co(II) not very used for SMMs. Several Co(II)-cluster of different nuclearity and geometry show SMM behavior, as Co(II)-cubanes (see next section), Co_4 molecular squares [130], Co_5 square pyramids and higher nuclearity clusters. There exist also SMMs where different oxidation states are mixed and different atoms combined, even rare earths (for a more extended discussion, see the review of ref. [10]). There are even mononuclear compounds of Co(II)-organic radicals systems that exhibit slow magnetic relaxation [131]. In this section a brief revision about Co(II) magnetic behavior and its possibilities is exposed.

The Co(II) ion is a d^7 which can present a wide variety of magnetic behaviors and interesting magnetic phenomenon. Among all the opportunities and advantages that can be found in Co(II) complexes: variable coordination number (4-6), different lengths in coordination bonds, stability in air, different colors... we are interested in Co(II) due to the high spin that it presents in weak ligand fields (S=3/2), its spin-orbit coupling and its magneto-crystalline anisotropy. The Co(II) complexes can show large values of D that increases the energy barrier for the relaxation. In these compounds is very common a situation where the anisotropy is of the same order of magnitude or even larger than the exchange coupling [53].

Solving the Hamiltonian of a magnetic system leads to know its energy levels and to analyze theoretically its magnetic and spectroscopic properties. The origin of the magnetic exchange interaction between neighboring spins can be direct exchange between orbitals of interacting paramagnetic ions or superexchange through a diamagnetic bridge and the overall type of exchange interaction (ferro- or antiferromagnetic) depends on the orbital overlap integrals, the interatomic distances and the bond angles. The exchange is modeled using effective exchange parameters J. Magnetic susceptibility, heat capacity, EPR, and INS [132] are some experimental methods used to determine J, where the first two methods are adequate as long as one is dealing with relatively simple clusters. For more complex systems, having more than one or two J parameters, INS is the best technique, since it allows a direct, spectroscopic access to the energy levels and therefore the exchange interactions.

In Co(II) clusters, solving the hamiltonian of the system can become an not easy task due to the spin-orbit coupling terms. Recently, a very complete review about exchange coupling in molecular magnets with unquenched orbital angular momenta performs a complete analysis of the different problems and approaches to this problem [133]. For a long time, the exchange interactions in these clusters have been modeled using the Heisenberg-Dirac-Van Vleck (HDVV) Hamiltonian, which is magnetically isotropic and expressed in terms of spin operators and therefore it is only applicable to clusters whose magnetic centers have isolated ground spin states. But the magnetic coupling in clusters with unquenched magnetic orbital momentum cannot be described in terms of spin operators only (with some exceptions), and orbital operators must be included in the Hamiltonian. The effect of the unquenched orbital angular momentum causes a strong magnetic anisotropy and anisotropic interactions between ions that can be of the same magnitude as the isotropic ones. If a general orbitally-dependent hamiltonian is build, it usually contains a pure orbital part, a mixed spin-orbital part and a third part which is of the same form as HDVV Hamiltonian. The description of the interactions in these clusters requires a great number of parameters, making necessary magnetic and spectroscopic characterizations to adjust them. Due to the difficulty of elaborating accurate models for systems with unquenched orbital momentum and the existence of friendly-use computing programs to solve it (as MAGPACK [134]), the HDVV model is frequently used for cases where it is incorrect. As a result, the parameters obtained from fitting the experimental data to the theoretical model are artificial. For this reason, several models and approximations have been used in the study of theses clusters.

The first approximation for compounds with Co(II) appears in 1971 by Lines [135] and it is only valid for highly symmetric environments. For a free Co(II) ion, the lowest levels are ^4F (L=3 and S=3/2) and ^4P ((L=1 and S=3/2) and the energy difference between them is 15000K, so we can take into consideration only the ^4F level. In the presence of an octahedral crystalline field, which is a very common feature, the ^4F is splitted in $^4A_{2g}$, $^4T_{2g}$ and $^4T_{1g}$ being this last one, the unique level populated for our purposes. If the octahedral field is perfect, the spin-orbit coupling splits the $^4T_{1g}$ state in six Krammer's doublets. The population of this levels depends of the temperature, so the magnetic moment can be temperature dependent and not follow a Curie-behavior. Lines defined a pseudo-spin-1/2 hamiltonian to describe interactions between Co(II) in a prefect octahedral environment and the exchange interactions were simulated as HDVV hamiltonian for the lowest lying Krammers doublet. The result was a fictitious g factor that depends on the temperature and includes the effect of the spin-orbit and the excited levels.

However, in real complexes, the Co(II) environment is usually distorted and the local geometry at each Co(II) plays a very important role in the magnetic properties. Distortions in octahedral field remove the degeneracy of the $^4T_{1g}$, i.e., a tetragonal distortion gives as a result a ground level $^4A_{2g}$ and a excited level ^4E_g, and the spin-orbit coupling split this new levels. In the former example, the result is a Kramer's doublet which is the only populated at low temperature (~30K) with $S = \pm 1/2$ and an excited doublet with $S = \pm 3/2$. The separation between this two doublet can be considered as ZFS of the quartet state, so the orbital momentum has been incorporated in D. The theory has been improved and applied for systems were the Co(II) ions are not in a perfect octahedral environment and a small distortion is included, for example, in a dimer [136]

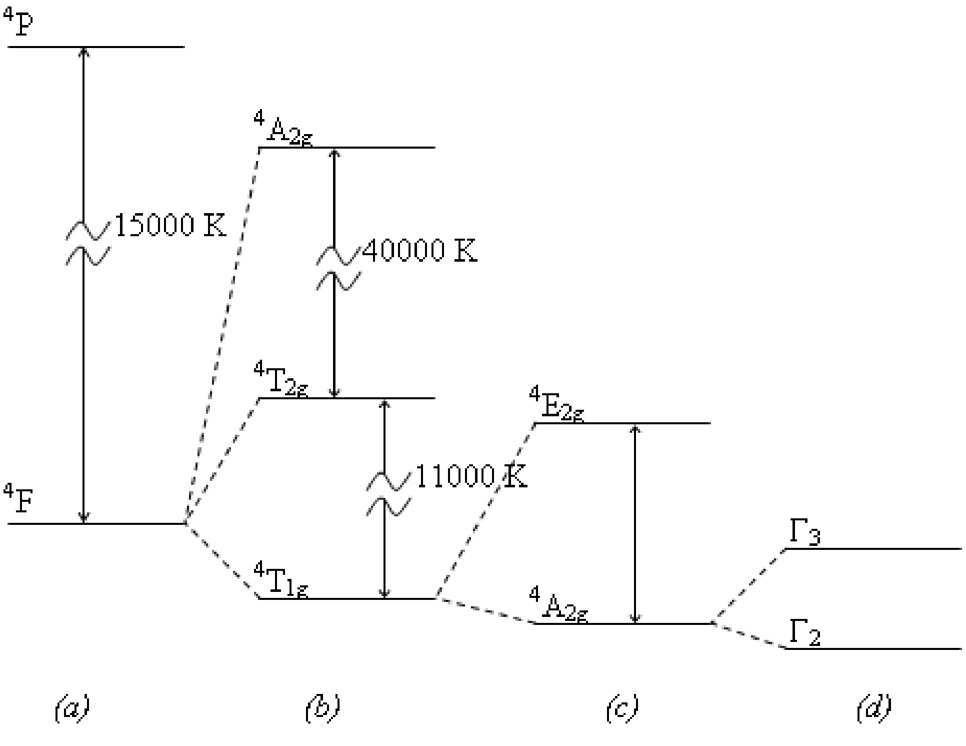

Figure 4.3: Splitting of the energy levels for a Co(II) ion due to:(a) electron-electron interaction; (b) octahedral field; (c) axial distortion; (d) spin-orbit coupling

A orbitally-dependent hamiltonian can be derived in principe for all electronic configurations and crystal field terms following a microscopic approach and starting from the Anderson's description of the kinetic exchange as is illustrated in the review of 2011 [133], but for the Co(II) the problem has been only approached in octahedral environments with slight distortions. The hamiltonian resulting can be treated with the use of the irreducible tensor operator technique as it has been done for a Co(II) dimer [137–139]. For this case, a effective pseudo-spin-1/2 Hamiltonian for not strongly distorted systems was solved and analytical expressions for the components J, the g-tensor and the temperature independent magnetism derived. The main problem of this approach is the increasing matrix sizes in polynuclear complexes, specially if we realize that each parameter has different values for it components *(x, y, z)*because of the anisotropy of the system.

Another approach was proposed by Lloret et al in 2008 [140] based on a perturbational theory and the Lines theory. This approach is valid in the limit where the strength of the magnetic interaction is lower than the spin-orbit coupling. An empirical expression is deduced for the magnetic susceptibility of magnetically isolated mononuclear high-spin cobalt(II) complexes with an axial distortion for an octahedral environment. As in Lines' model, the exchange interaction only operates between the ground Krammer's doublet, but now the g factor depends on the temperature and on the exchange interaction parameter J. This causes a drastic reduction in the matrix sizes, but involves a great number of parameters.

In this scientific context there is not an uniform criterium to study Co(II) cluster and authors use Hamiltonians that can include or not spin-orbit coupling, distortions, exchange interactions or Zeeman interactions. The Lines' model is a good approach, but it is only applicable to highly symmetrical octahedral Co(II) and modifications only include slight distortions of this configuration. Overparametrization can become a problem if a very complex hamiltonian is used to describe the magnetic system and magnetic measurements are the only experimental data. The Co(II) ions that form part of the cubanes studied are mainly in a C_3 distorted environment, so none of the previous methods can be applied. Our working group has decided to elaborate a model specially adequate to the symmetry of Co(II) ions in our cluster. Dr. Javier Luzón is performing *ab initio* calculations that clarify the nature and intensity of the magnetic interactions and zero-field-splitting in the compounds studied in this thesis. The research is still in progress and no results are shown in this thesis.

4.5 Cubanes

As it has been said, there is an enormous quantity of different SMMs: from SMMs that only have a pair of magnetic atoms to SMMs that are like nanoparticles, SMMs based on d-row elements or rare-earth ions, mixed-valence, highly anisotropic or regular, ... They have different properties depending of the magnetic ions present and their environment and geometry. It would be almost impossible to review and summarize all of this compounds and it is out of the scope of this chapter, so we are limiting ourselves to a brief revision of Co(II)-cubanes because the building blocks used in our compounds are Co(II)-cubanes.

Cubanes are regular cube type structures (abbreviated as M_4X_4), more or less distorted, where alternate vertex are occupied by metal atoms or the X units. The X sites can be occupied by several atoms, as S in the Fe_4S_4 cubane well know in biology [141]. Our interest lies in the M_4O_4 units which show interesting magnetic exchange properties and some of them are reported to behave as SMMs.

An ideal cube has twelve equal bond lengths and twenty-four bond angles of 90^o, but this perfect structure can not synthesized in practice, because three bonds at 90^o are hardly ever found for an oxygen atom. A more realistic approach considers a M_4O_4 unit as two interpenetrating M_4 and O_4 tetrahedra, the whole possessing T_d symmetry. In a very interesting review of 2007 [142], a total of 70 cubane structures are compared. In these cubanes the average M-O-M angles are greater than 90^o (mean value of 97.2^o), and the O-M-O angles are less than 90^o. The M-M distances provide a method to analyze the distortion of the M_4 tetrahedron and to characterize it: a distortion by extension along a S_4 axis, will increase four M-M distances and two others will remain the same; two sets of three equal M-M distances are a sign of a distortion along a C_3 axis; and a distortion which maintains three C_2 axes will give three pairs of M-M distances. The D_2 symmetry may be further distorted to a C_2 system. These distortions are represented in figure 4.4. The larger the standard deviation of the M-M distances, the greater is the distortion.

If we restrict ourselves to study cubanes that behave as SMM, we are still covering a very broad field. The different magnetic properties of the metal ions influence in the magnetic behavior of the samples and made almost impossible to generalize or to find general statements. There are cubanes with Ni(II), Co(II), Co(III), Mn(II), Mn(III)... and mixed valence complexes. We are intentionally excluding more complicated structures with face-sharing cubanes or defected cubanes. In addition, the use of derivatives or different ligands can modify significantly the effective energy barrier for magnetization reversal by changing the ground spin state or anisotropy of the cluster. A well documented example is a family of hexanuclear Mn^{III} SMM where a structural distortion of the molecule induces a switch from antiferromagnetic to ferromagnetic interaction between atoms in the cluster [143]. As a result, the ground spin state is modified and hence the energy barrier.

In M_4O_4 compounds, the interaction between the metal ions can be through two pathways. The first and the main pathway, is the anion-cation-anion through the two oxygen that bridge each pair of metals atoms in the cubane. The other is due to the common face of the cubane that two Co(II) ions share, as the distance between them is 3.1Å and the covalent radius of Co(II) is 1.5Å, it may be a direct overlap of orbitals. It is commonly accept for

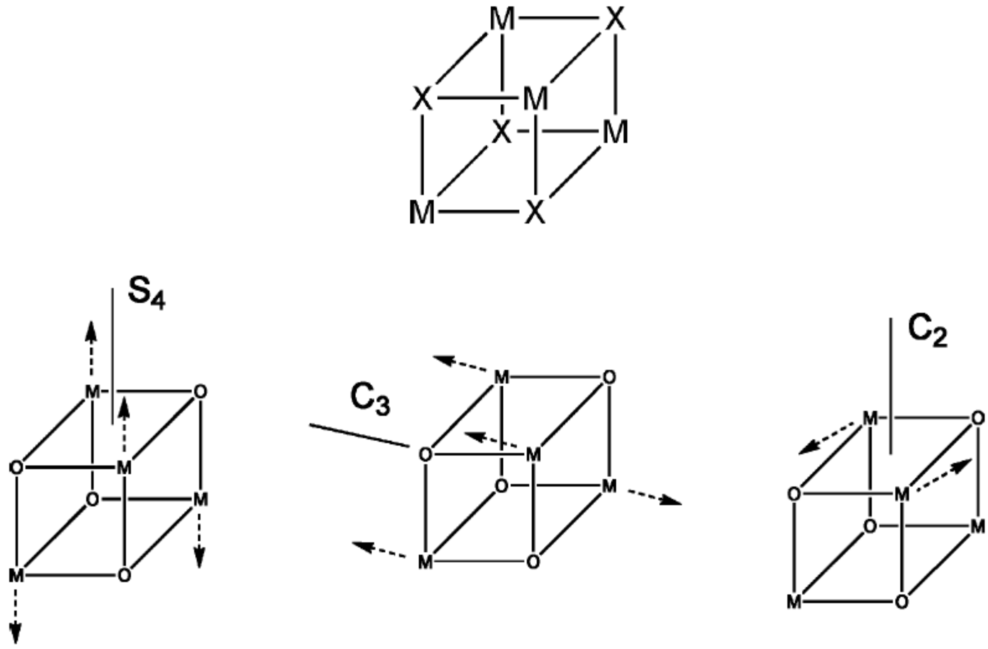

Figure 4.4: Schematic structure of a regular cubane and its possible distortions. For the D_2 distortion only one C_2 axis is shown. Adapted from ref. [142]

Ni(II) cubanes that there is a critical angle Ni-O-Ni near 98º-99º, below which the interaction between metals is ferromagnetic and and above this angle, it will have antiferromagnetic behavior [144, 145]. The M-O-O-M dihedral angle has been also related to the sign of the exchange interaction, dihedral angles lower than 170° being associated with ferromagnetic interactions for Ni atoms. The distance between two metal centers also has influence in the strength of the interaction. Of course, any distortion can change these angles by several degrees and modify the exchange pathways. Another consideration to take into account is that the more distorted the system is, the more difficult is to establish *a priori* a relationship between the interaction and the M-O-M angles, because it may be necessary to use two or even three J parameters of interaction. In addition, other pathways additional to the cubane core or magnetic atoms in the neighborhood may interfere in the interaction between the cubane metal centers.

The effect of the structural geometry in exchange pathways is more difficult to predict in Co(II)-cubanes due to the unquenched orbital momentum, the expected first order spin-orbit coupling and the wide variety of magnetic behavior that it can present. For this reason, nowadays there is not possible to establish a magnetoestructural correlation to predict the magnetic behavior.

4.5.1 Co(II)cubanes

In contrast with the wide literature about Manganese or Nickel cubanes, not many Co(II)-cubanes have been reported. Among them, some have not been classified as SMMs due to the absence of a signal in AC measurements that reveals this behavior [127, 142, 146, 147], others shown a dependence of the AC signal with the frequency but the blocking temperature has not been reached [128, 148]. The blocking phenomenon and the relaxation processes in cluster are very complexes and the environment of the Co(II) ions has a lot of influence in the relaxation process. For example, a loss of solvent can cause distortions in the cluster geometry and structural changes that affect both the barrier height and the tunneling probability [125]. Also variations in the ligands coordinated to cobalt can dramatically influence the magnetic behavior [149], we can reduce our field of interest to the citrate Co(II)-cubanes reported to date. The citrate cubane has a general formula $[M(II)_4(cit)_4]^{8-}$.

To the present, two zero-dimensional discrete cobalt citrate cubane ($[Co(II)_4 citrate_4]^{8-}$) with $C(NH_2)_3^+$ as counterion [150, 151] or two $[Co(II)(H_2O)^5]^{2+}$ groups bonded to external oxygen atoms of the citrate ligands and $N(CH_3)_4^+$ and Na^+ as counterions (3:1 ratio) [125] have proved to be SMMs. Our working group has also prepared an interconvertible 1D to 2D compound based on $[Co(II)_4 citrate_4]^{8-}$ cubanes [129], but due to the complexity of the polymers and a unique reversible crosslinking reaction between them in the solid phase at room temperature the magnetic characterization has not been done by the moment. In table 4.1 citrate Co(II)-cubanes isolated that have a relaxation process and for which the energy barrier had been calculated are shown. In all of these compounds, the blocking phenomenon can be observed around 5K in the AC signal.

Table 4.1: Energy barriers for Co(II)-cubanes, characteristic time and interaction between adjacent metals. $[(NMe_4)_3NaCo_4(cit)_4[Co(H_2O)_5]_2]\cdot 7H_2O$ and $[(NMe_4)_4Co_4(cit)_4[Co(H_2O)_5]_2]\cdot 6H_2O$ are dehydrated samples, no results have been found for hydrated compounds.

Formula	I	ΔE (K)	τ_0 (s)
$[(NMe_4)_3NaCo_4(cit)_4[Co(H_2O)_5]_2]\cdot 7H_2O$ [125]	F	26	$8.2\cdot 10^{-19}$
$[(NMe_4)_4Co_4(cit)_4[Co(H_2O)_5]_2]\cdot 6H_2O$ [125]	F	32	$2.1\cdot 10^{-19}$
$[C(NH_2)_3]_8[Co_4(cit)_4]\cdot 8H_2O$ [150–152]	AF	20.5	$1\cdot 10^{-7}$

Although a ground state with a ground level with a spin-cluster different from zero is necessary for the existence of an energy barrier, a cluster with a spin total S_T equal to zero [150] has been reported to behave as a SMM [151]. This is as a consequence of the influence of upper energy levels near the ground state [152].

The coexistence of several relaxation mechanism and modifications on the tunneling probability due to interactions with the environment also difficult a clear interpretation of the magnetic data and physical phenomenons.

4.6 Objectives

In this part of the thesis, several compounds based on Co(II) citrate cubanes are magnetically characterized. In chapter 5, a interconvertible crystalline compound with clusters of Co_8 with a Co_4 core is presented. The two phases that could be isolated and magnetically studied present a different symmetry that may cause changes in the SMM behaviour of the phases. The dimensionality is increased from isolated cubanes to two dimensional networks in chapter 6. In this chapter, the compounds have cubanes linked to form two dimensional networks with different topology and cations, that causes slight variations on the cubane. In chapter 7, a 3D structure similar to diamond where Co-cubanes are used as building blocks is investigated.

The objective of this part of the thesis is double. One objective if to verify how small structural differences can affect the energy barrier of a SMM. For this purpose, we can compare the two phases of the 0D compound, the loss or gain of water modifies the symmetry of the clusters. Also the differences in the angles and distances between the cubanes of the two dimensional networks and the existence of different topologies are expected to be relevant in the relaxation process of the cubanes. The other objective is to observe the evolution of the magnetic behavior of the cubanes from isolated clusters to the situation when they are arranged in nets of different dimension, where magnetic order can appear. The coexistence of magnetic order and blocking is a exciting possibility.

4.7 Techniques

The characterization of the samples presented in the second part of this thesis has involved magnetic and heat capacity measurement. These experiments have been carried out in two commercial set-ups: MPMS and PPMS from Quantum Design [153], which are part of the Research Support Services of the University of Zaragoza [154]; and a magnetometer SQUID in a dilution refrigerator from the group of F. Luis. The MPMS equipment has provided us information between 300K and 1.8K about the magnetization and AC behavior at frequencies from 0.1Hz to 1000Hz and has been the first sonde used to characterize the samples. The PPMS has been used to wide the frequency range in AC measurements from 0.01 Hz to 10KHz and calibrate the data obtained with the dilution. It has also been used for heat capacity measurements between 1.4K and 120K to characterize possible magnetic transitions. The dilution allow us to increase the temperature range for the AC characterization down to 90mK and frequencies up to 13333Hz.

To perform magnetic measurements in the MPMS and the PPMS, around 10 or 20 milligrams of polycrystalline sample were mixed with some vacuum grease to prevent torquing. The mixture was deposited in a gelatine capsule stuck in a straw. Diamagnetic corrections were made using Pascal's constants and the diamagnetic contribution of the sample gelatine capsule can be considered as negligible if it is compared with the magnetic signal of the samples. The diamagnetic contribution of the straw is considered negligible as it is as large as the space region seen by the SQUID sensor and its contribution can be due only to inhomogeneities.

A special case is the compound $Co_4(citr)_4[Co(H_2O)_4]_4$, which is called Co_8 for simplicity and it is studied in chapter 5. It has three different phases, two of them interconvertible at room temperature by losing or absorbing water molecules through the surface of the crystals. It exits the possibility to go through a phase transition in a few minutes in the frame of the lab by absorbing water from the environment or losing it by heating a few degrees, creating vacuum, drying with a flow of nitrogen ... it was necessary to isolated each phase and sealed it. The gelatine capsules does not prevent the sample from losing water due to the purging operations in the equipments, so PIREX capsules were used instead. Phase 1 is stable at laboratory conditions, so around 20 milligrams of polycrystalline sample were deposited in a PIREX test tube of 3mm of diameter. The tube was sealed by applying heat at the 3cm from the sample extreme with a gas welding torch for less than one second, forming a PIREX capsule that sealed the sample. For isolating phase 2, some milligrams stayed in a dryer camera for two days and were introduced in a PIREX test tube. The capsule with the sample was sealed by heat as quickly as possible in order to avoid contamination. The PIREX capsules were introduced in a straw as usually in a commercial SQUID magnetometer. The contribution of the homemade PIREX capsules was measured separately. From 300 to 200 shows a diamagnetic contribution and paramagnetism appear below 80K. As can be seen in graphic 4.5, the signal of the Pirex capsule can be neglected due to the higher values for the samples.

Several tries to measure monocrystals of Co_8 were also done. The volume of samples was lees than 1 mm^3. Each time, one monocrystal of Phase 1 (stable at normal conditions) was covered to prevent water exchange and glued

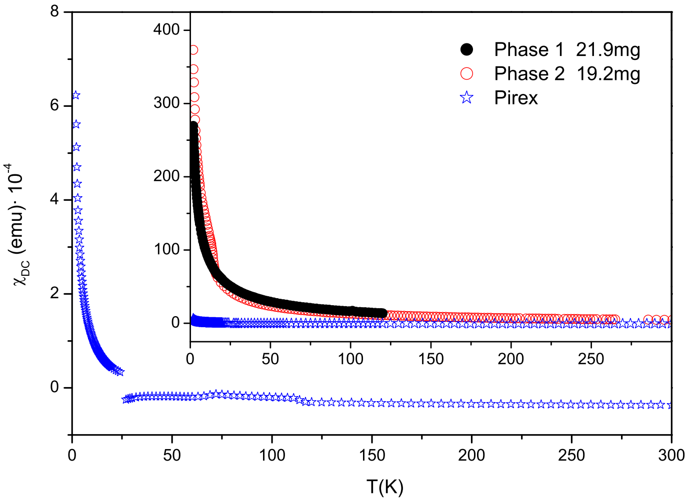

Figure 4.5: χ versus T plot measured at 500Oe for phase 1 (21.9mg), phase 2 (19.2mg) and a PIREX capsule

on a plastic strip. Araldite, Superglue or transparent nail polish were used as coverture and glue. The crystal was manually oriented with the long dimension parallel to the strip and the strip was rotated to measured magnetization along the different axis. The magnetic contribution of a drop of Araldite, Superglue or transparent nail polish was measured separately as can be seen in figure 4.6. Superglue is the only material that only has a diamagnetic contribution and the magnetic signal of a monocrystal is at least five times stronger than the drop used in the test experiment. In addition, the drop used finally to cover the crystal was less than a third part of the drop used in the test, so the superglue contribution can be neglected. For this reason, it was used as coverture.

The possibility to observe a structural transition *in situ* motivates another experimental set up. Around 20mg of polycrystalline sample were introduced in a gelatine capsule stuck in a straw, the sample chamber purged as usual and the powder was cool down to 10K suddenly. After that, the capsule was holed, the sample was heated at 300K and the sample space was purged again before cooling down. To be sure of the loss of water, the same process was done but increasing the temperature before purging at 350K for 90 minutes and at 260K for 3 hours.

To measured in the dilution, some milligrams of powder with vacuum grease were put in a plastic tube. The dilution equipment present the disadvantage of not being calibrate, so it was necessary to do it externally using the PPMS. Comparing the AC signals obtained from both instruments, and applying a multiplicative and additive factor to the signal from the dilution, it is possible

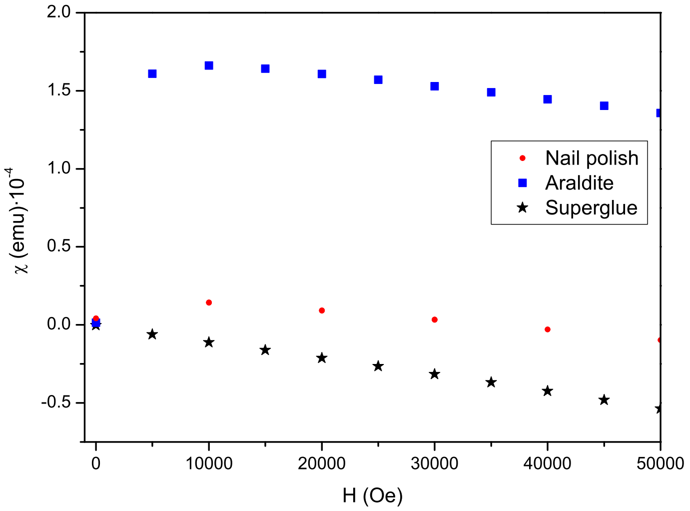

Figure 4.6: χ versus H plot measured at 1.8K for different covertures

to relate the dilution data to the desired units.

The heat capacity of the sample $(K_4\{Co_4(citr)_4[\mu-Co(H_2O)_4]_2\}\cdot 8H_2O)_n$, denoted as $Co_4/3D$, was measured in the PPMS. For this purpose, a small amount of powder was several times pressed in a hydraulic press until a pill of dimensions 3x3mm^2 and 0.74mg was obtained. It was glued to a sample holder with some grease and the contribution of the sample holder and the grease was subtracted.

Chapter 5

Interconvertible Co(II)-cubanes

5.1 Introduction

This chapter is devoted to the magnetic characterization of isolated Co_8 clusters based on Co(II)-citrate-cubane very similar to the ones that are arranged in layers presented in chapter 6 or the three dimensional structure studied in chapter 7. The objective is to understand the magnetic behavior of the isolated cluster and how distortions and symmetry can influence its magnetism. For this purpose, polycrystalline samples of several phases of a compound were magnetically characterized. The cubane presents different symmetry in each phase. The synthesis and structure of the phases is described in section 5.2 and the magnetic properties presented in section 5.3. A discussion about the results and some conclusions can be found at the end of the chapter.

5.2 Synthesis and structure

Starting from a water solution of citric acid and cobalt carbonate, pink single crystals of clusters $Co_4(citr)_4[Co(H_2O)_4]_4$ (which is called Co_8 for simplicity) are obtained after a chemical process. Three interconvertible phases can be isolated due to two reversible solid-state reactions. Each phase is reached after a dehydration or hydration process, where crystallization water molecules are lost or absorbed through the surface of small monocrystals. In each phase cubane cores with four adjacent Co(II) ions are found, but they present different topologies.

Phase 1. Modulated structure.

This phase has space group *C2/c*, a=23.1494(9)Å, b=9.6555(2)Å, c=23.5036(8)Å, β=111.017º(4) and V=4904.0(3)Å^3. Phase 1 is the stable one at room temperature and normal conditions of humidity. It can be describe as a sub-periodic crystalline material with a modulated structure produced by a hopping of peripheral Co(II) ions between neighboring molecules as the ones existing in Phase 2. The refined modulated vector is (0 0.372 0) and the modulation affects to the direction of the hoping, but the clusters present in the structure are all of the same species an can be found in figure 5.1a. There are four clusters per unit cell. A two-fold axis parallel to *b* cell axis goes through the cubane, orthogonal to two faces, but the outer Co(II) centers broke a possible C$_2$ symmetry for the cluster. Inside the cubane, there are two pairs of M-M distances and other two different distances. We can not considered the cubane as an isolated cluster, because there are three Co(II) that are called peripheral, but whose distances to the Co(II)-cubanes are of the same magnitude that the intra-cubane distances and they are linked by two oxo-bridges, as can been in tables 5.1 and 5.2. The interaction with the outer Co(II) ions is expected to be of the same magnitude as the intra cubane interaction. *Ab initio* calculations show that the easy axis of anisotropy for the Co(II) centers of the cubanes are directed towards the center of the cubane. Looking in this direction, the metal atoms present a C3 environment, as can be seen in figure 5.2a, where the oxygen atoms of the cubane are represented in red and the oxygens from the citrate in green. The peripheral Co(II) atoms are in slightly distorted octahedral environments.

Table 5.1: Characteristic distances and angles for the cubane in Phase 1

Distance	
Co1-Co2	3.1736(1)
Co1-Co2'	3.1307(1)
Co2-Co2'	3.2325(1)
Co1-Co1'	3.2383(2)

Angle	
Co2-O-Co2'	100.02º(1)
Co1-O-Co1'	100.77º(1)
Co1-O-Co2	98.74º(1) / 96.66º(1)
Co1-O-Co2'	97.82º(1) / 96.33º(1)

Table 5.2: Characteristic distances and angles for the outer Co(II) atoms to the cubane in Phase 1

Distance	
Co1-Co3	3.2958(2)
Co2-Co4	3.2880(1)

Angle	
Co1-O-Co3	101.68º(1) / 102.34º(1)
Co2-O-Co4	100.48º(1) / 103.24º(1)

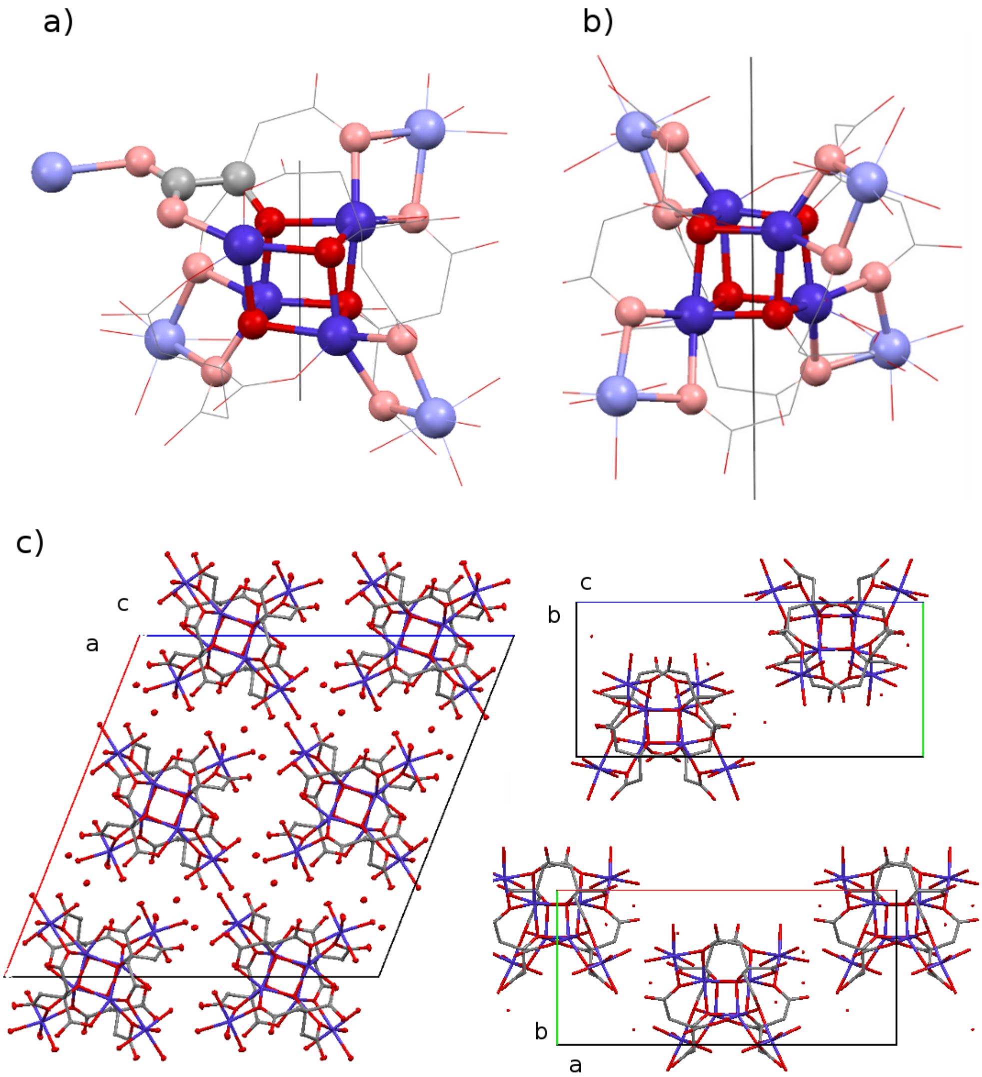

Figure 5.1: *a)* Cluster for Phase 1, the outer Co(II) and O atoms are lighter. *b)* Cluster for Phase 2, the outer Co(II) and O atoms are lighter. *c)* Unit cell for phase 2, hydrogens are omitted for the shake of clarity.

Phase 2.

If a loss of water is produced as consequence of heating, drying with a nitrogen flux or creating vaccum, the modulation disappears and a new phase can be isolated. The structure has the same space group that the hydrated phase but the cell parameters change as a result of the lost water: a=22.8070(17)Å, b=9.6745(4)Å, c=23.3079(14)Å, β=111.643°(8), Z=4, V=4780.23Å^3. This phase has four high symmetric Co_8 clusters as the ones shown in figure 5.1b per unit cell, which can be seen as a cubane and four more Co(II), forming an octanuclear cluster with a cubane core. The cubane is distorted and a two-fold axis, parallel to *b* cell axis, is orthogonal to two faces. The distances and angles between Co(II) centers in the cubane are detailed in table 5.3. There are two pairs of M-M distances and other two different distances. As for phase 1, we can not considered the cubane as an isolated cluster, because distances from peripheral Co(II) ions to the Co(II)-cubanes are of the same magnitude that the intra-cubane distances and they are linked by two oxo-bridges, as can be seen in table 5.3. The interaction with the outer Co(II) ions is expected to be of the same magnitude as the intra cubane interaction. *Ab initio* calculations show that the easy axis of anisotropy for the Co(II) centers of the cubanes are directed towards the center of the cubane, and they present a C3 environment, as for phase 1. The peripheral Co(II) atoms are in slightly distorted octahedral environments.

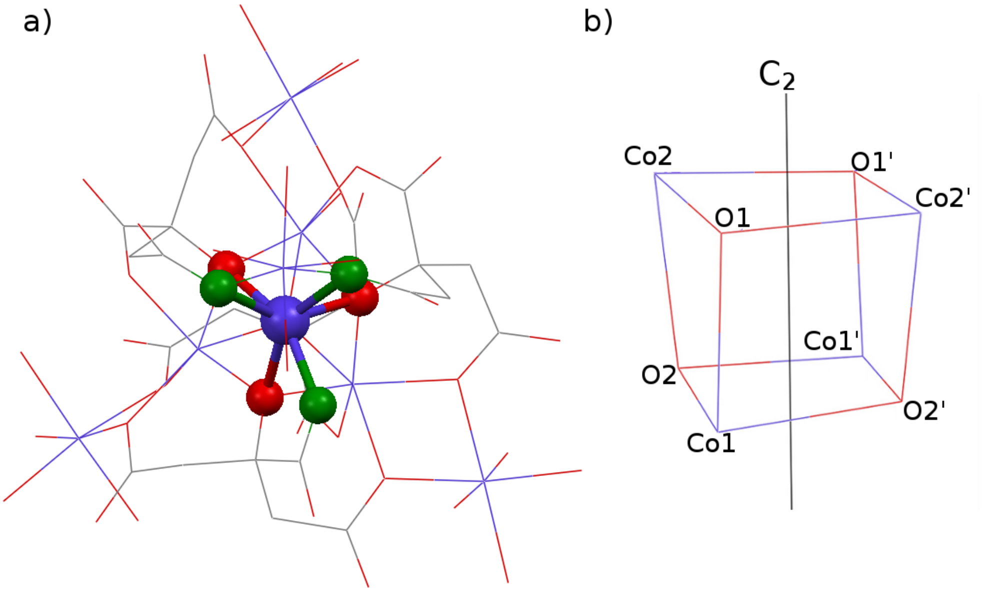

Figure 5.2: *a)* C_3 environment for the Co(II) centers in the cubane. Oxygen atoms of the cubane are represented in red and the oxygens from the citrate in green. *b)* C_2 symmetry for the cubane

For Phase 1, the cluster is distorted as a consequence of the hoping of one Co(II) peripherical and the symmetry decreases. Although the cubane core keeps the C_2 symmetry, the angles and distances are different from Phase 2.

Table 5.3: Characteristic distances and angles for the cubane in Phase 2

Distance	
Co1-Co2	3.1910(7)
Co1-Co2’	3.1337(7)
Co2-Co2’	3.2340(8)
Co1-Co1’	3.2210(6)

Angle	
Co2-O-Co2’	100.4°(1)
Co1-O-Co1’	99.5°(1)
Co1-O-Co2	99.2°(1) / 97.3°(1)
Co1-O-Co2’	97.3°(1) / 95.6°(1)

Table 5.4: Characteristic distances and angles for the outer Co(II) atoms to the cubane in Phase 2

	Distance
Co1-Co3	3.2833(6)
Co2-Co4	3.2829(8)

	Angle
Co1-O-Co3	100.0°(1) / 102.3°(1)
Co2-O-Co4	100.4°(1) / 102.1°(1)

Phase 3.

A third phase can be reached if we keep on dehydrating the compound but, unfortunately, the structure can not be isolated and measured. A polymerization process takes place and its nature is under study.

5.3 Magnetic properties

The two phases were magnetically characterized as described in section 4.7. These samples were manipulated with special care due to a potential phase transition in the frame of the lab. To asses the purity of the phases, polycrystalline samples were isolated and sealed in PIREX capsules.

For both samples, the magnetization at a field of 500Oe has been measured from room temperature to 1.8K, as can be seen in figure 5.3. The $\chi_M{\cdot}T$ (χ_M is the magnetic susceptibility per mol) at 300K is $22.75emu{\cdot}mol^{-1}{\cdot}K$ for both compounds. This value is consistent with eight independent Co(II) ions with an effective magnetic moment of $4.77\mu_B$, given by to S=3/2 and $g{\geq}2.4$ as it was expected [53]. The value of g different from 2 is due to the existence of a unquenched orbital moment. The $\chi_M{\cdot}T$ value remains constant for both samples until 200K. Below 200K, the signal for Phase 1 increases slightly to $22.9emu{\cdot}mol^{-1}{\cdot}K$ and then star to decreases at 120K reaching $6.6emu{\cdot}mol^{-1}{\cdot}K$ at 1.8K; for Phase 2, the decrease begins at higher temperature (around 200K) but it is smoother until reaching $8.8emu{\cdot}mol^{-1}{\cdot}K$ at 1.8K. The only difference between both signals is quantitative.

The slight increase for phase 1 near 150K is predicted for a Co(II) ion [53]. The decreases of $\chi_M{\cdot}T$ at low temperature may be due to an antiferromagnetic interaction between the Co(II) ions and/or the depopulation of the higher energy Kramers doublet.

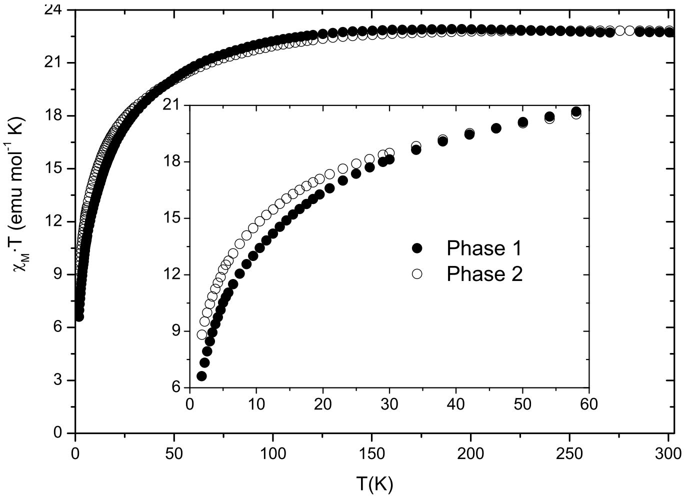

Figure 5.3: $\chi_M{\cdot}T$ versus T plot for phases 1 (full circles) and 2 (open circles). The inset shows in detail the low temperature region.

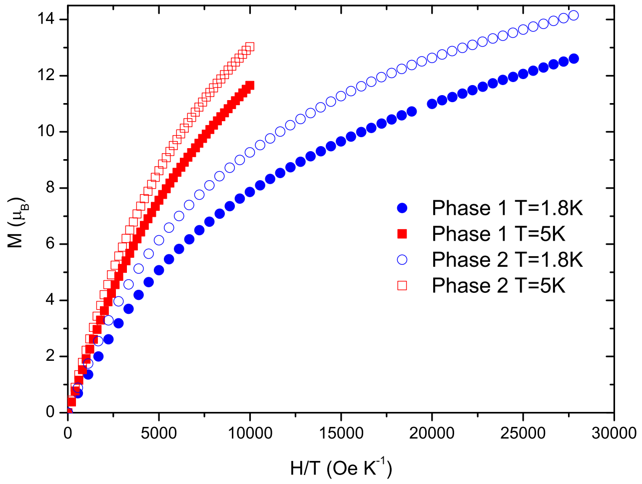

Figure 5.4: Magnetization in Bohr magnetons per unit formula versus the ratio H/T for phases 1 (full figures) and 2 (open figures) at two temperatures

No maximum of the magnetic susceptibility is observed in the χ_M versus T graphics and a Curie-Weiss adjust to a eight independent Co(II) ions give as parameters: g=2.758(2), θ=4.7(3)K (ferromagnetic interaction) and g=2.850(1), θ=-0.3(2)K for phase 1 and phase 2 respectively. Due to the depopulation for

Co(II) ions that allow us to considerer them with an effective spin of S=1/2 below 30K, and the deviation from the Curie law expected for Co(II) ions [53], the meaning for the θ is questionable at low temperatures.

The dependency of the magnetization with the field has also been measured at 1.8K and 5K. As can be seen in graphic 5.4 the curves for both phases do not match, the signal for phase 1 is smaller as it happens at low temperature in figure 5.3. There is factor of 1.12 between the signal of the two phases. The magnetic curves at 1.8K and 5K do not scale if they are normalized by the temperature, indicating the existence of an antiferromagnetic interaction which may exist inter-clusters. At 1.8K and 5T, the magnetization has not reach saturation and it has a value of 11.65 and 13.03 μ_B for phase 1 and phase 2 respectively. In this temperature region, we can use an effective spin S$_T$ and g value for the molecule although is an oversimplified picture, and the S$_T$ classification is applicable only in the case of isotropic exchange. A S_T equal to $8 \cdot \frac{1}{2} = 4$ will give us a g∼2.7 for 1.8K and 5T, which is a much lower than the value around 4.6 expected for Co(II) ions in powder at this range of temperature [155]. If we approach the problem of estimating S$_T$ in the inverse sense, a typical g value of 4.6, gives a S$_T$ $\geq$2.8. In any case, a ground state different from zero for the cluster is found, so a SMM behavior is possible.

To confirm the possibility of a SMM behavior in this compound, the AC susceptibility has been measured at different frequencies in the low temperature range. As can be seen in figure 5.5, the slow relaxation of the magnetic moments becomes apparent below 7.5 for both phases, giving to a blocking process, which is observable only for frequencies up to 10Hz for phase 2. One of the most intriguing features of the graphics that can be appreciated in the first look, is the crescent in-phase and out-phase signals below the characteristic blocking peak. The structural analysis of the phases discards the existence of isolated Co(II) ions to which the signal may be attributed of any other magnetic aggregate that can contribute paramagnetically to the signal. The increment in the signal can be only due to the existence of another relaxation process or a magnetic order below the blocking temperature. The possibility of another relaxation process may be due to the modifications that neighbor clusters may induced in the energy levels of a cluster, which can affect the tunneling relaxation process making necessary a thermal assistance to observe the process. Dipolar interactions between clusters can also be responsible of a magnetic order as in other compounds [13], which may also justify the increment in the AC signals below the blocking phenomenon. However, these are only hypothesis, and measurements at lower temperatures would be necessary to clarify this behavior that have also been observed in other clusters.

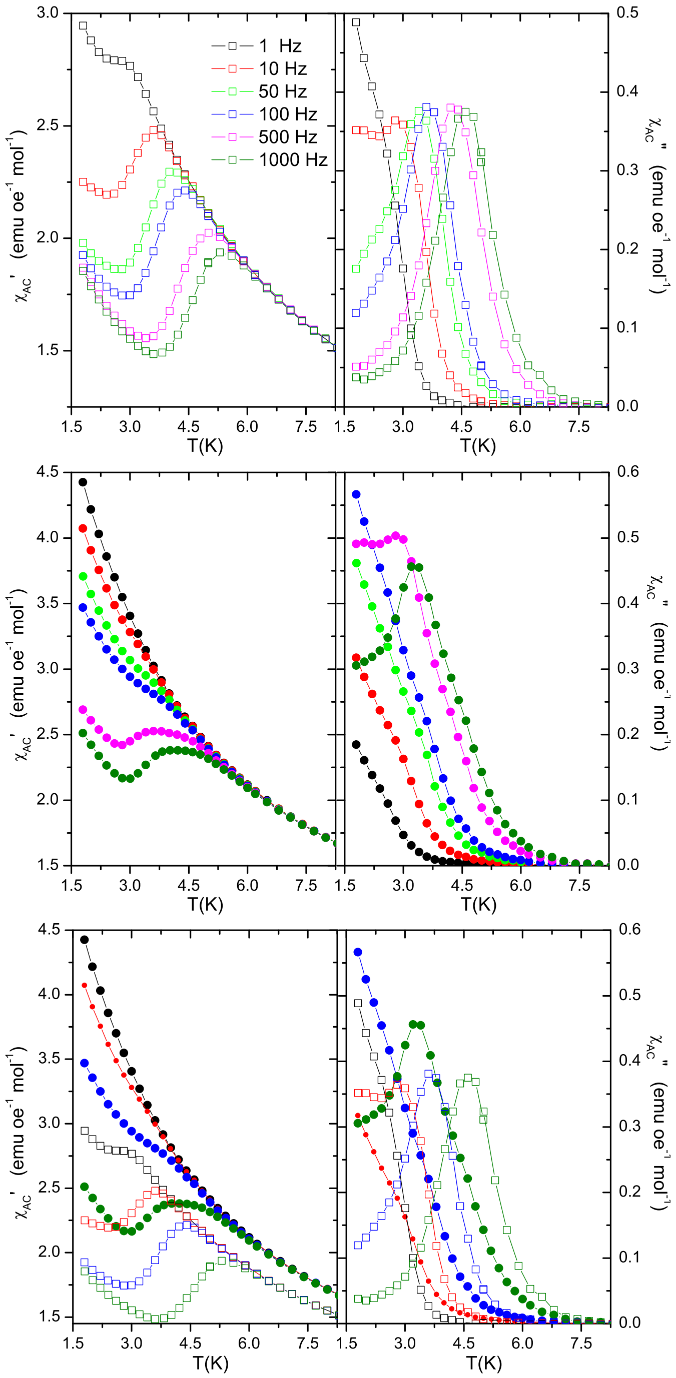

Figure 5.5: χ_{AC} measurements at different frequencies for Phase 1 (Up) and Phase 2 (Middle). At the bottom, both phases are compared for some frequencies, Phase 1 (open squares) and Phase 2 (full circles)

The AC signals for both phases are compared in the bottom of figure 5.5. It can be seen that the sample of Phase 2 was slightly contaminated and have a small contribution of Phase 1, that explains the small shoulder in the out of phase susceptibility for Phase 2 at the same temperature that the blocking phenomenon for Phase 1. The magnetic blocking occurs at higher temperatures and is visible at lower frequencies for Phase 1 than for Phase 2, which is easily understood if we considerate that the hoping of one of the peripheral Co(II) ions modifies the symmetry of the cluster, increasing the anisotropy and hence the energy barrier. This fact also has to be significant in the difference between the energy barriers and relaxation times of both phases.

As the blocking phenomenon results relevant for phase 2 only at high frequencies and there exists another contribution that keeps on increasing when lowering the temperature, not enough peak position in χ" can be determine accurately. It is not possible to adjust to an Arrhenious plot and obtain the energy barrier and characteristic time with precision by using method. We have determined the relaxation parameters with the equation 4.3. The plotting of τ_{av} versus *1/T* can be seen in figure 5.6, where the different behavior of both phases becomes more relevant. Attending to the out of phase signal, Phase 2 is only blocked for frequencies 500Hz and 1000Hz, while Phase 1 is blocked from 1 Hz. As the sample of Phase 2 is contaminated, the plotting of τ_{av} shows the blocking of Phase 1 for low frequencies and the blocking of the phase 2 is only visible for 500 and 1000 Hz. In the graphics, the blocking of the amount if Phase 1 in the sample of Phase 2, is marked as *a* and *b* stands for the point where the Phase 2 is blocked.

The relaxation parameters for Phase 1 have been determined for the lowest frequency whose $[\chi"/\chi']$ quotient is not noise (1 Hz), while for Phase 2, it has been necessary to employ data at 500 Hz. Table 5.5 contains the results. As it was expected, the higher anisotropy for the cluster of Phase 1 influences the energy barrier, making it four times the energy barrier for Phase 2.

Table 5.5: ΔE and τ_0 for Phase 1 and Phase 2.

	ΔE (K)	τ_0 (s)
Phase 1	39.8(11)	$0.26(8)\cdot10^{-7}$
Phase 2	9.2(3)	$34(2)\cdot10^{-7}$

No evidence of hysteresis of irreversibility has been found in these compounds. The velocity of the relaxation process due to quantum tunneling process makes no possible to observe hysteresis in most clusters, specially in Co(II) clusters.

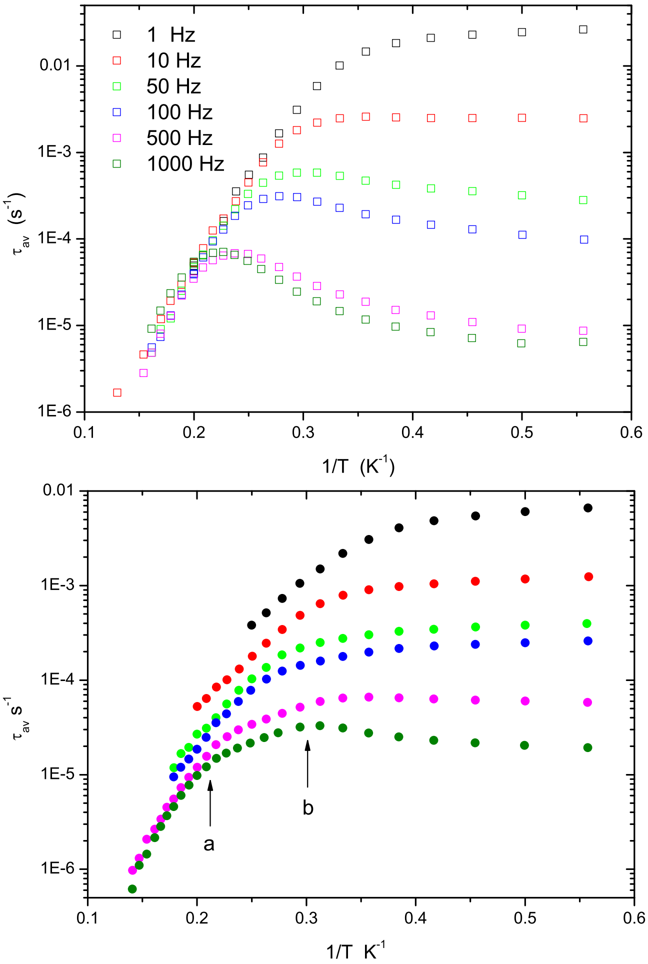

Figure 5.6: τ_{av} versus *1/T* plotting for several frecuencies. Phase 1 (open squares) and Phase 2 (full circles)

In an effort to characterize the magnetic behavior of pure phases, we measure the magnetism of single crystals of Phase 1, which is stable at normal conditions. In a crystal, the water interchange process is expected to be slower than in powder, due to the lower superficie/volume ratio. We covered a crystal Superglue and measure its magnetization. Unfortunately, when we sample was recovered, the crystal was chapped, so we can not assure the phase. In addition, the AC signal was too weak to be measured. This measurements have not been taken into account.

We wanted to check if the vacuum created in the purging process of the MPMS is enough to remove water molecules and cause a phase transition from Phase 1 to Phase 2 *in situ*. Comparing the magnetic behavior of the sample after several purges and heating process, it can be seen as the blocking process occurs at different frequencies and temperatures. The impossibility to assure the phase measured each time makes these data discarded.

Several efforts were made to isolate the phases and even to observe a structural transition in situ in the magnetometer by heating a sample, vacuuming and quenching it, but no conclusive results were obtained. The best results obtained are presented in this thesis and correspond to samples sealed in PIREX capsules, which has not been enough to prevent a small contamination of phase 2. In spite of this handicap, the magnetic behavior for both phases has been determined.

5.4 Discussion and Conclusions

In this chapter, two phases of a single-crystal interconvertible compound formed by octanuclear Co(II) clusters have been magnetically characterized. A SMM behavior has been found in both phases.

Unfortunately, the compound is very sensitive to the environment, as it gains or losses water molecules in few minutes in normal conditions. Several tries of growing monocrystals which may slow down the water interchange process due to the lower superficie/volume ratio have produced tiny crystals whose AC signal is too weak to be measured in the SQUID. The lack of an AC signal makes no possible to identify the phase. Several efforts were made to isolate the phases and even to observe a structural transition in situ in the magnetometer by heating a sample, purging the sample chamber and quenching the sample, but no conclusive results were obtained. The best results obtained are presented in this thesis and correspond to samples sealed in PIREX capsules, which has not been enough to prevent a small contamination of phase 2. In spite of this handicap, the magnetic behavior for both phases has been determined.

The magnetization for both phases is equivalent at high temperature, showing a small difference below 100K, revealing a decreases in the magnetization more relevant for phase 1. No magnetic order is found. We have not been able to fit or perform theoretical simulation for the magnetization curves at low temperature, but a cluster ground state S_T=0 can be discarded, which is one condition for a SMM. The SMM behavior expected for the samples manifest itself in the blocking phenomenons observed in the AC measurement, which occurs around 5K, in good agreement with the blocking found in another cubanes with similar distances and Co-O-Co angles.

As it could have been predicted, the hoping peripheral Co(II) ion breaks the symmetry of the cluster, increasing the energy barrier and the blocking temperature. For phase 1, the energy barrier is four times than for phase 2. This result remarks the importance of the D parameter in the energy barrier, being in good agreement with the synthetic approach which tends to increase the anisotropy instead the spin cluster to obtain higher energy barriers.

The compound studied present a third phase if Phase 2 loses more water, but the structure has not been determined and we couldn't isolated the phase to characterize it magnetically.

Chapter 6

Two dimensional arrays of Co(II)-cubanes

6.1 Introduction

In this chapter, two dimensional networks of linked Co(II)-citrate-cubane cluster through Co(II) ions bridges are characterized magnetically. The linked citrate cubanes are similar to isolated citrate cubanes that have been proved to behave as SMM [125, 150, 151]. Therefore, we are interested in checking if the SMM behavior is conserved when the cubanes are arrange in layers, and moreover, if there is a possibility to observe the transition for an individual blocking behavior to a spin-glass phase or a magnetically ordered phase where the clusters interact.

For this purpose, our working group has synthesized five different two dimensional compounds where Co(II) citrate cubane units are bridged by single Co(II) centers. Three of them are anionic structurally square 2D polymers and have been obtained with different cations, K, Rb and Cs; we called them as $cationCo_4/Square$: KCo_4/S, $RbCo_4$/S and $CsCo_4$/S; another one is a square lattice with extra Co(II)ions named $CsCo_4$+1 and the last one present a rhombic lattice, $CsCo_4$/R. The differences in the cluster geometry and net topology may also give us information about the influence that the environment can have on the magnetic behavior of the cubanes.

The synthesis and structure of the compounds are described in section 6.2 and the magnetic properties explained in section 6.3. A discussion about the results and some conclusions can be found at 6.4.

6.2 Synthesis and structure

All the compounds presented in this chapter are synthesized following a very similar procedure, and small modifications cause different topologies into the nets or distortions on the cubane. As it has been said before, we will provide here only the necessary crystallographic information to support the analysis of the magnetic data.

6.2.1 Two dimensional square polymers

Our working group has already reported two square grid compounds for Rb and Cs as counterions [14]. The linkage of $[\mathrm{Co_8citrate_4}]^{8-}$ through $\mathrm{Co(H_2O)_2ETG}$ (ETG= ethylene glicol= ethane-1,2-diol) bridges gives two dimensional square networks with cubanes in the nodes of formula $[Co_4(citr)_4Co(H_2O)_2ETG_2]_n^{4-}$. The nets are piled up perpendicularly to the c axis and the compounds crystallize in the tetragonal system, acentric space group P(-4)2_1c. Counterions K^+, Rb^+ and Cs^+, water molecules and ETG molecules connect the layers trough electrostatic interactions.

The complete formulae are $(C_{28}H_{36}Co_6O_{36}K_4)_n{\cdot}9.5{\cdot}nX(H_2O){\cdot}Yn(C_2H_6O_2)$, $(C_{28}H_{36}Co_6O_{36}Rb_4)_n \cdot 9.5 \cdot n(H_2O) \cdot 2n(C_2H_6O_2)$ and $(C_{28}H_{36}Co_6O_{36}Cs_4)_n \cdot 4.5 \cdot n(H_2O) \cdot 2.5n(C_2H_6O_2)$, but they are abbreviated as $\mathrm{KCo_4}$/S, $\mathrm{RbCo_4}$/S and $\mathrm{CsCo_4}$/S. The cell parameters for the compounds can be found at table 6.1

Table 6.1: Cell parameters for $\mathrm{KCo_4}$/S, $\mathrm{RbCo_4}$/S and $\mathrm{CsCo_4}$/S

Compound	a	b	c
$\mathrm{KCo_4}$/S	12.6136(3)Å	12.6136(3)Å	19.1005(13)Å
$\mathrm{RbCo_4}$/S	12.5307(2)Å	12.5307(2)Å	19.6730(5)Å
$\mathrm{CsCo_4}$/S	12.5873(2)Å	12.5873(2)Å	19.6730(5)Å

The building block of the polymers is a cobalt citrate cubane formed by four Co(II) centers and four hydroxy oxygen atoms from an equal number of quadruply deprotonated citrates. Neighboring cubanes are bridged by a six-coordinated Co(II) centers coordinated by two carboxylate oxygen atoms. The charge of each polymer unit, which is formed by one cubane and two Co(II) bridges is balanced by the alkali metal cations. The four bridging Co(II), called nexus, are linked through two arms formed by *Co-O-C-C-C-O-Co* and *Co-O-C-O-Co* to the cubane, as can be seen in figure 6.1, so they can interact with the cluster but the interaction strength is expected to be weaker than the intra-cubane interaction. Therefore, in a simplified approximation, we can considered only the cubane as a cluster.

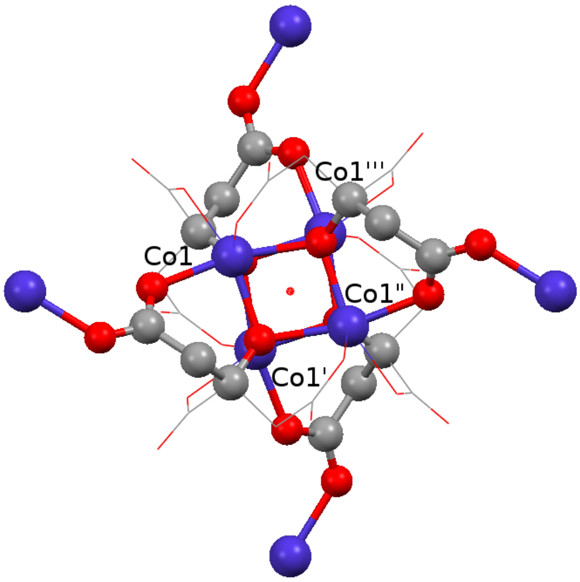

Figure 6.1: Symmetry for the cubane. A C_2 and a S_4 axis parallel to the *c* cell axis goes through the cubane. The cubane, the Co(II) nexus and the bridges between them are remarked.

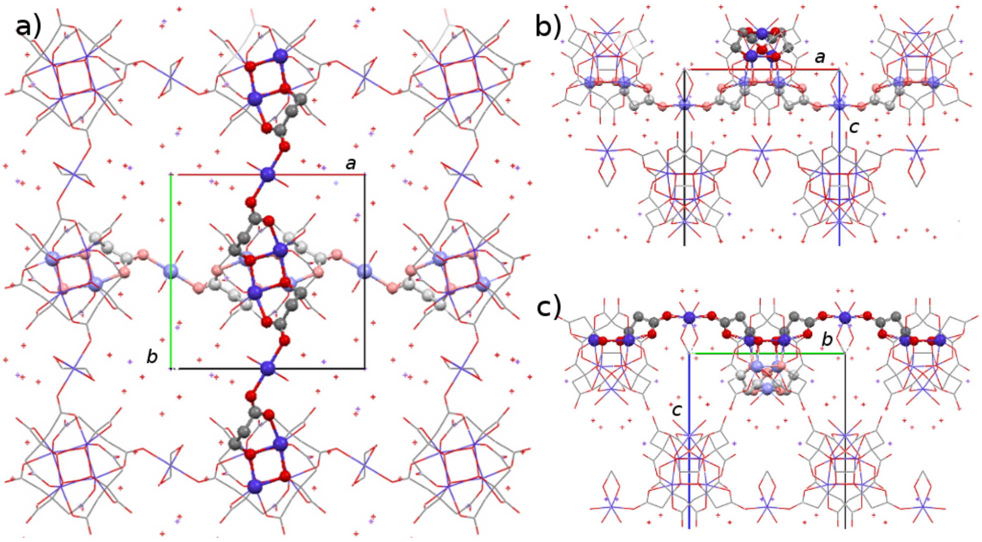

Figure 6.2: Network structure for the KCo_4/S compound. *a)* View along the *c* axis for a single layer, the upper links along the *b* axis are remarked and along the *a* axis are remarked and lighter; only one layer is shown. *b)* view along the *a* axis. *a)* view along the *b* axis

The cubanes are linked along the *a* and *b* crystallographic axis as can be seen in figure 6.2a, where the links are established for the uppers faces of the cubanes in one direction and the bottom faces for the perpendicular direction. The layers are stacked in a way that the projection of the cubanes of a upper layer fits on the holes of a bottom layer, so along the *c* axis, the large spaces between nodes in one layer are blocked by cubanes from the neighboring layers and channels do no exist. Layers are piled up in such a way that the cubanes seem to be teeth of a zipper, and the distance between them is gave by *c/2*.

For the three compounds with K^+, Rb^+ and Cs^+ as counterions, the cubane is distorted and a four-fold rotoinversion axis with the inversion center at the center of the cube and parallel to *c* cell axis goes orthogonally to two faces. As a result, the cubane presents a S_4 symmetry that increases four M-M distances while the other two remain shorter and equal. The main distances and angles can be seen in table 6.2. The distances and angles inside the cubane are different for the three compounds, showing the influence of the counterion used in the synthesis. The environment of cubane Co(II) ions is a distorted C_3 while nexus Co(II) are in an distorted octahedral field.

Table 6.2: Characteristic distances and angles for cubanes in KCo_4/S, $RbCo_4/S$ and $CsCo_4/S$.

	Distance		Angle	
KCo_4/S	Co1-Co1’	3.139(2)	Co1-O-Co1’	96.1°(2)/97.5°(2)
	Co1-Co1"	3.240(2)	Co1-O-Co1"	100.8°(3)
$RbCo_4/S$	Co1-Co1’	3.148(1)	Co1-O-Co1’	96.3°(2)/97.2°(2)
	Co1-Co1"	3.196(1)	Co1-O-Co1"	99.1°(2)
$CsCo_4/S$	Co1-Co1’	3.155(1)	Co1-O-Co1’	96.0°(2)/97.6°(2)
	Co1-Co1"	3.190(1)	Co1-O-Co1"	98.7°(2)

6.2.2 Two dimensional rhombic polymer

A small modification in the synthesis described in 6.2.1, replacing the ETG by water, carries a very important modification in the structure of compound with Cs as counterion. The water molecules occupy positions in the nexus Co(II) coordination sphere, modifying the linkage between the citrate cubanes. The result is a two dimensional rhombic network with cubanes in its nodes of formula $[Co_4(citr)_4Co(H_2O)_{42}]_n^{4-}$. The nets are piled up perpendicular to the *b* axis and the compounds crystallize in the monoclinic space group *C2/c* with counterions Cs^+ and water molecules connecting the layers trough electrostatic interactions.

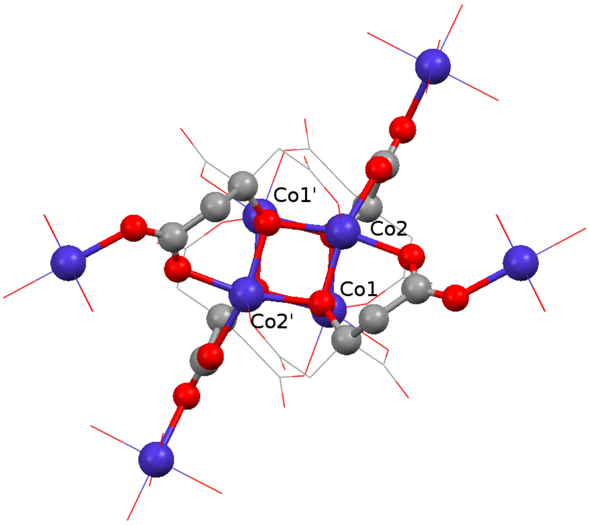

Figure 6.3: Symmetry for the cubane. A C_2 parallel to the *b* cell axis goes through the cubane. The cubane, the Co(II) nexus and the bridges between them are remarked.

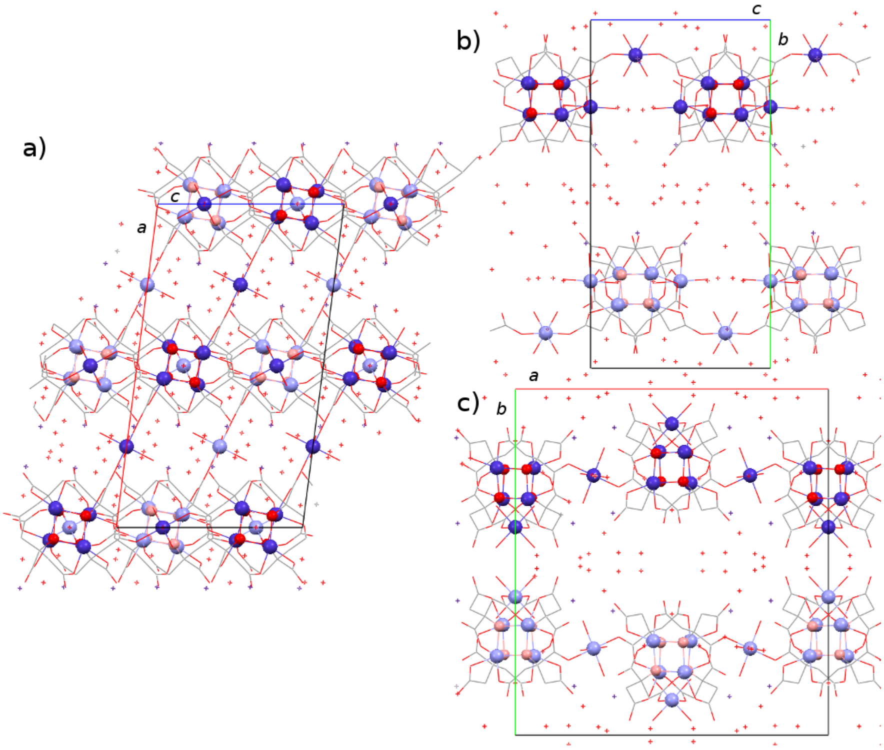

Figure 6.4: Network structure for the $CsCo_4/R$ compound. *a)* View along the *b* axis for two layers, the upper layer is remarked and the bottom layer is lighter. *b)* view along the *a* axis. *a)* view along the *c* axis.

The complete formula is $Cs_4\{[Co(C_6H_4O_7)]_4\mu(Co(H_2O)_4)_2] \cdot 16H_2O$, and it has been abbreviated as CsCo$_4$/R. The cell parameters for this compound are a=22.1255(10)Å, b= 24.3019(13)Å, c=12.6289(5)Å, β=97.308°(4). As can be seen in figure 6.4, the layers are piled up along the *b* axis in such a way that there is no longer a crenellated effect as in square net compounds; tunnels exist in the space between cubanes, that may open the possibility to use this compound as a Metal Organic Framework (MOF).

In the square grid compounds, each cubane Co(II) ion present the same ligands, but in the CsCo$_4$/R compound, there exist two different cubane Co(II) places depending on if they are linked to the bridges that connect cubanes or not. In the figure 6.3 can be seen clearly as only $Co2$ and $Co2'$ atoms are part of the bridges between cubanes. This connectivity array makes the symmetry of cubanes in CsCo$_4$/Rlower than the symmetry of cubanes in the square lattice compounds, and only a C$_2$ axis parallel to the *b* axis goes through the cubanes. The main distances and angles for the cubane can be seen in table 6.3. The cubane Co(II) ions are in a C$_3$ environment and two different places could be distinguished; the nexus Co(II) ions are in a octahedral environment.

Table 6.3: Characteristic distances and angles for the cubane in CsCo$_4$/R.

Distance		Angle	
Co1-Co2	3.209(1)	Co2-O-Co2'	99.4°(2)
Co1-Co2'	3.119(1)	Co1-O-Co1'	100.5°(2)
Co2-Co2'	3.217(1)	Co1-O-Co2	98.7(2) / 99.0(2)
Co1-Co1'	3.2361(9)	Co1-O-Co2'	95.8(2) / 96.0°(2)

6.2.3 Two dimensional square polymer with extra Co(II) ions

The high reactivity of the citrate cubane favors the crystallization of another compound by adding a Co(II) excess in the synthetic process of CsCo$_4$/S. An extra Co(II) ion coordinated to six oxygen atoms, $[Co(H_2O)_6]^{2+}$ cation, occupy the holes between cubanes, as can be seen in figure 6.5, giving crystals of unit formula: $Cs_2[Co(H_2O)_6][Co_6(C_6H_4O_7)_4(H_2O)_8] \cdot 12H_2O_n$ [15]. The space group is the same as for square compounds P(-4)2$_1$c and the cell parameters are very similar a=12.5738(1)Å, b=12.5738(1)Å, c=19.5895(3)Å. The unit building block is one cubane, two Co(II) nexus and two extra Co(II) ions per unit cell. The connectivity between cubanes, symmetry of the cubanes and environment for the Co(II) ions are identical that for the previous square polymers, with the addition of the extra Co(II) ions in a octahedral environment. The angles and distances in the cubane are shown in table 6.4.

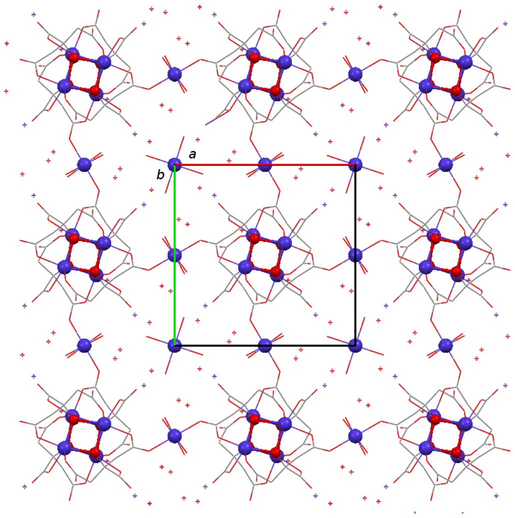

Figure 6.5: Network structure for the CsCo$_4$+1 compound. View along the *c* axis for one layer, the cubanes and the Co(II) ions are remarked.

Table 6.4: Characteristic distances and angles for cubanes in CsCo$_4$+1.

Distance		Angle	
Co1-Co1'	3.1360(8)(2)	Co1-O-Co1'	95.8^{o}(1)/97.3^{o}(1)
Co1-Co1"	3.2258(7))	Co1-O-Co1"	99.7^{o}(1)

6.3 Magnetic Properties

For the square and rhombic grid samples, the magnetization at different magnetic fields between 50000T and 500Oe has been measured from room temperature to 1.8K, as can be seen in figure 6.6 for squared compounds and 6.7 for the rhombic compound. The $\chi_M \cdot T$ at 300K is around $18 emu \cdot mol^{-1} \cdot K$, which agrees with the value expected for six independent Co(II) ions with an effective magnetic moment near to 4.77μ_B, given by S=3/2 y $g \geq 2.4$ as it was expected due to the existence of a unquenched orbital moment [53].

The $\chi_M \cdot T$ value remains constant for all samples until 200K and around 150K there is a small increase. For the square grid compounds, the magnetic behavior becomes field-dependent around 60K, due to the energy levels modification and depopulation. At low fields, the signal increases whereas at high fields a sharper decreasing is observed. This question is frequently obviated, and may lead to errors if the magnetic field at which the measurements have been done is not specified. A peak appears at 5K at fields of 500 and 1000Oe, and below it, the signal keeps on increasing. For higher fields, the signal de-

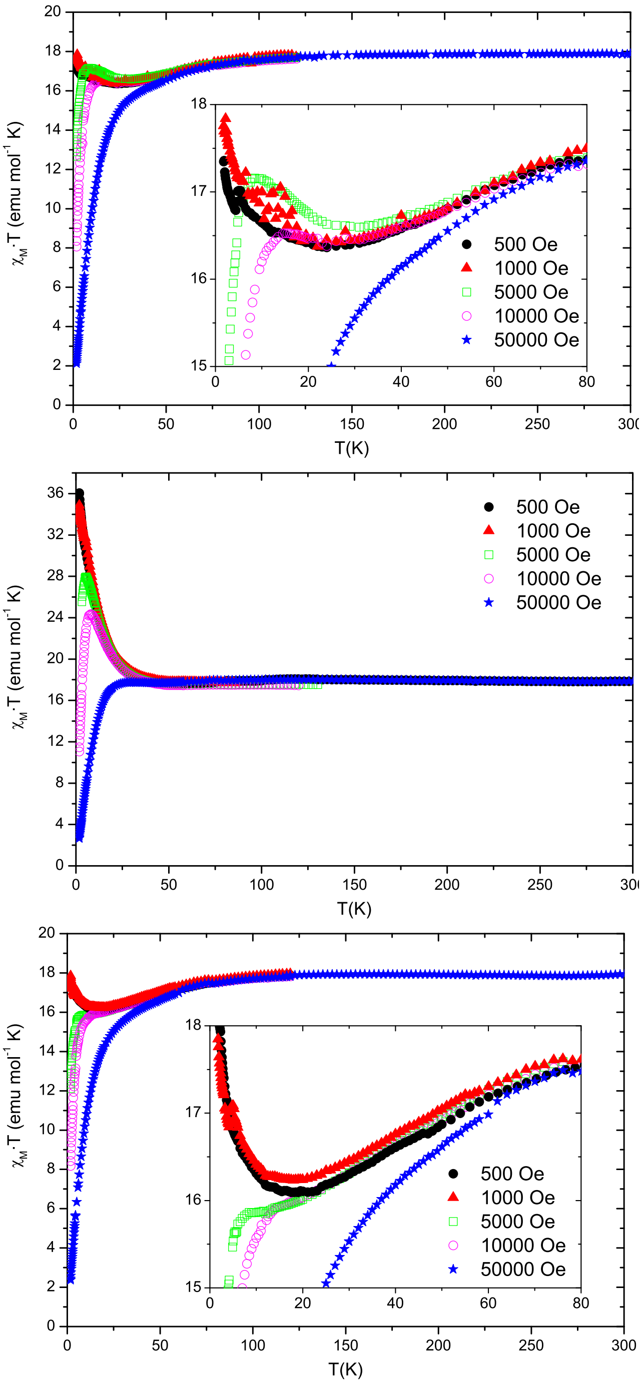

Figure 6.6: $\chi_M \cdot T$ versus T plot for squared grid compounds. The upper figure correspond to the KCo_4/S, in the middle there is shown for the $RbCo_4/S$ and in the bottom for $CsCo_4/S$. The inset shows in detail the low temperature region.

creases sharply and for 50000Oe the peak disappears, as can be seen in figure 6.6. Comparing the compounds where Rb is used as counterion versus the ones with K or Cs, a clear difference can be seen: at low fields the RbCo$_4$/S signal can be twice the signal for the other compounds, indicating the existence of a stronger ferromagnetic interaction between the Co(II) ions.

If we focus our attention in the CsCo$_4$/R compound, whose magnetization versus temperature can be seen in graphic 6.7, the differences with the other compounds become evident at 100K. For 500Oe and 1000Oe fields, the curve presents a peak at 75K which disappear at higher fields and does not exist for other compounds. Although a similar behavior has not been observed for Co(II) SMM, this can be associated to the more different environment for the Co(II) ions in this compound [53]. Another peak can be seen at 5K for a 1000Oe field, analogous to the ones observed for the square grid compounds .

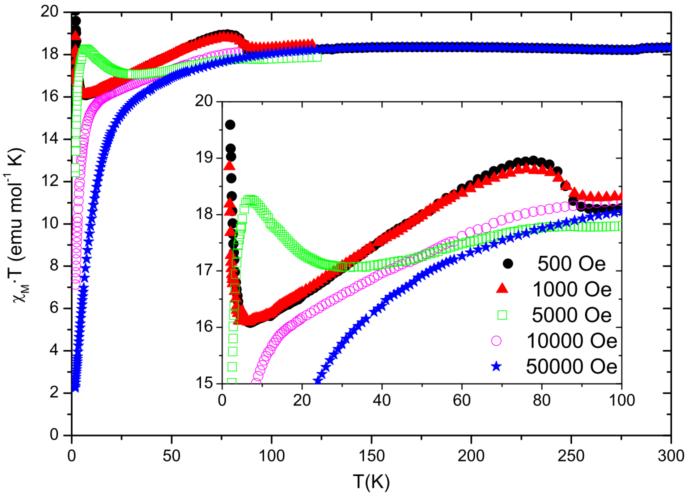

Figure 6.7: $\chi_M \cdot T$ versus T plot for the rhombic grid compound CsCo$_4$/R. The inset shows in detail the low temperature region.

The magnetization at 500Oe for all the two dimensional compounds is compared in figure 6.8. The behavior of CsCo$_4$+1 is analogous to the behavior of the other compounds. It shows a peak at 500Oe and a value at high temperature correspondent to seven independent Co(II) with S=3/2 and g=2.4. For all the compounds, the adjust to a Curie-Weiss law gives a g=2.5 and θ values near to zero for KCo$_4$/S, CsCo$_4$/S, CsCo$_4$/R, but $\theta = 3.5 \pm 0.3$ and $\theta = 11.5 \pm 0.5$ for RbCo$_4$/S and CsCo$_4$+1. Due to deviation from the Curie law expected for Co(II) ions [53], the meaning for the θ is questionable at low temperatures.

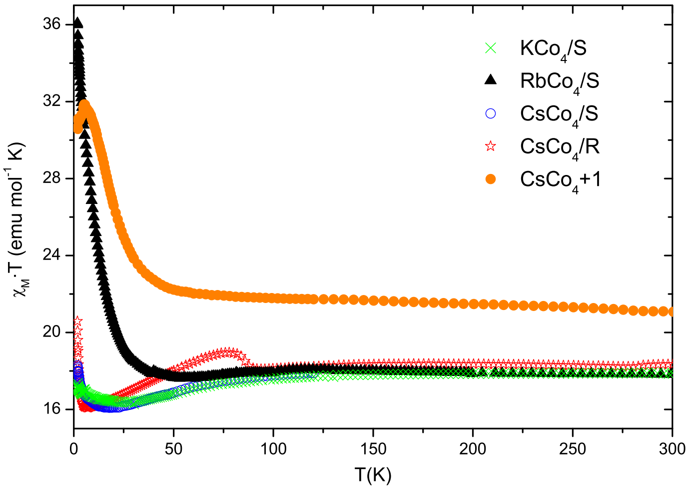

Figure 6.8: $\chi_M \cdot T$ versus T plot for the the bidimensional networked compounds measured at 500Oe

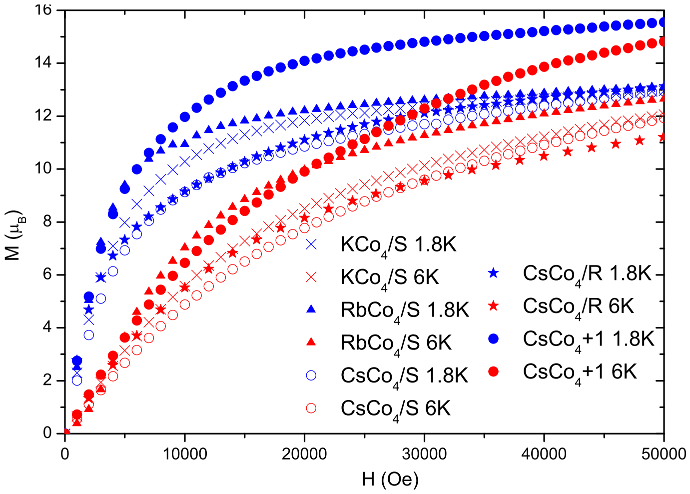

Figure 6.9: Magnetization in Bohr magnetons per unit formula versus the ratio H/T for the bidimensional compounds KCo_4/S, $RbCo_4$/S, $CsCo_4$/S, $CsCo_4$/Rand $CsCo_4$+1

Magnetization versus field for all the compound have been measured at 6K and at 1.8K and results are shown in graphic 6.9. The signal of $RbCo_4$/S reaches higher values of magnetization at low fields than the other samples with the same number of Co(II) per unit cell, which may be indicative of a stronger ferromagnetic interaction between cubane Co(II) ions in this compound. Although saturation has not been reached at the highest field at 1.8K for any of the compounds, it is not very far away and we can make several considerations. For the square and rhombic grid compounds, a value of $13\mu_B$ per unit formula is reached, and the $CsCo_4$+1compound present a maximum value of

$15.5\mu_B$. Scaling the curves with the ratio field/temperature, they don't match for different temperatures, probably due to the presence of interactions between cubanes or nexus and cubanes, being the curve at 6K above the curve at 1.8K, which suggest that the interactions are antiferromagnetic. The separation between curves start around 3000OeK^{-1} for KCo$_4$/S, 3600OeK^{-1} for RbCo$_4$/S, 4000OeK^{-1} for CsCo$_4$/S and CsCo$_4$/R, and 6000OeK^{-1} for CsCo$_4$+1.

In an oversimplified way we can take a S$_T$ for the cubane and keep the nexus with an isolated spin value of 1/2 and an experimental g value of g=4.6 [155]. Using this approximation, each nexus contributes with 2.3 μ_B to the magnetization of saturation. That would give us an S$_T$ around 2 for all the compounds, which would be consistent with ferromagnetic coupling between the Co(II) ions in the cubane and make a SMM behavior possible. Several tries to fit the experimental curves with oversimplified models have not produce satisfactory results, so waiting for a complete knowledge of the energy levels for these compounds is mandatory before analyzing the magnetic properties.

Until now, the static magnetic behavior of the compounds has been explained, but what really is going to determine if our compounds behaves as SMM is the AC behavior. For this reason, the AC signal was measured at different frequencies down to 1.8K for all the compounds, obtaining the results shown in graphic 6.10 for KCo$_4$/S, CsCo$_4$/R and CsCo$_4$+1. As can be observed, the signal becomes frequency-dependent below 7K and two signal appears superimposed: a continuously crescent signal and a blocking phenomenon around 5K, which is clearer observed for the CsCo$_4$/R compound.

In order to clarify the origin of the crescent signal motivated very low-temperature measurements in a dilution refrigerator have been done for RbCo$_4$/S (see graphic 6.11), which present the most different behavior, and CsCo$_4$/S (see graphic 6.12).

A frequency-dependent shoulder is observed in the in-phase and out-phase signals around 4K. As this anomaly is present in other compounds which present isolated Co-cubanes, it can be associated with the superparamagnetic blocking of the total cubane spin S$_T$. Another anomaly around 400mK is present for which $\chi" \neq 0$, indicating the existence of non-equilibrium effects. The magnetic behavior of the compounds is slightly different at low temperature.

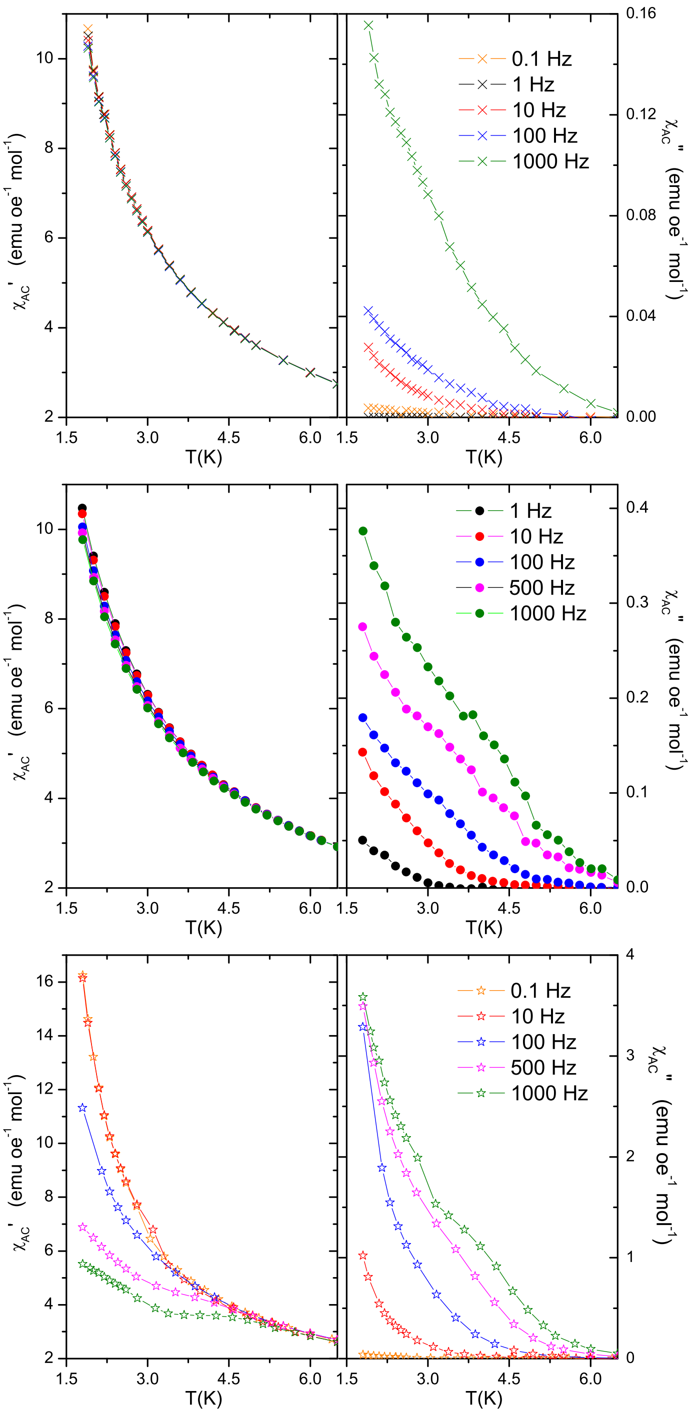

Figure 6.10: χ_{AC} measurements at different frequencies for KCo$_4$/S, CsCo$_4$+1 and CsCo$_4$/R.

For the $RbCo_4/S$ compound and frequencies below 33Hz, $\chi" \approx 0$, so we can considered there is an equilibrium situation and the maximum in χ' near 0.2K can be attributed to a phase transition to a ordered magnetic phase. For higher frequencies, the dominant phenomenon is a blocking process as it can be deduced for the existence of a frequency-dependent peak.

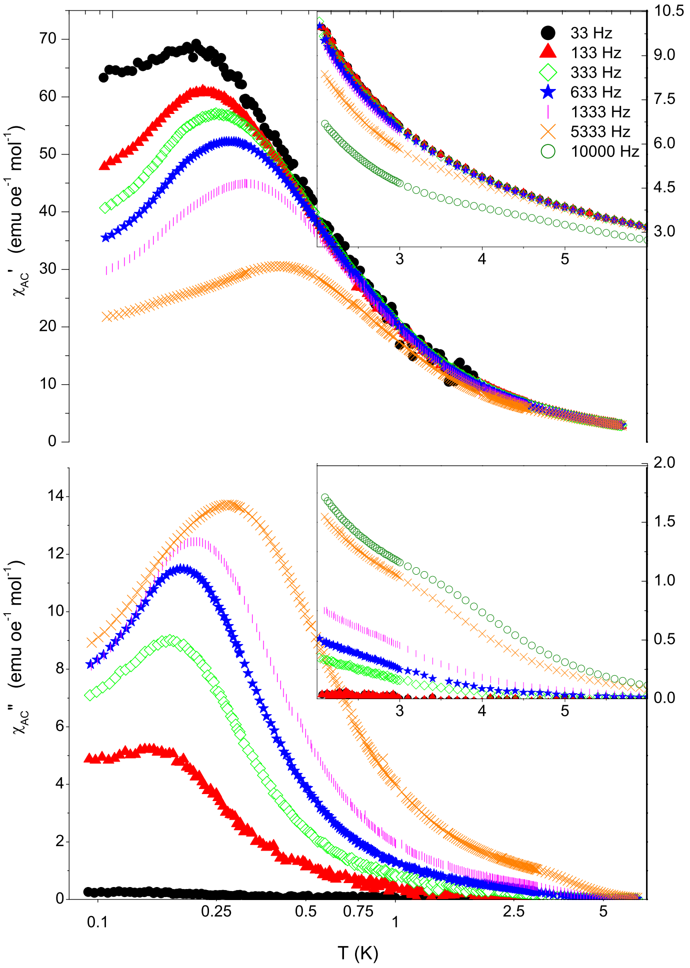

Figure 6.11: χ_{AC} measurements at different frequencies for $RbCo_4/S$

For the CsCo$_4$/S compound a superimposition of a frequency-independent peak and a frequency-dependent peak is observed. The peaks are attributed to a blocking process and a phase transition to an ordered magnetic phase that occur at near the same temperature.

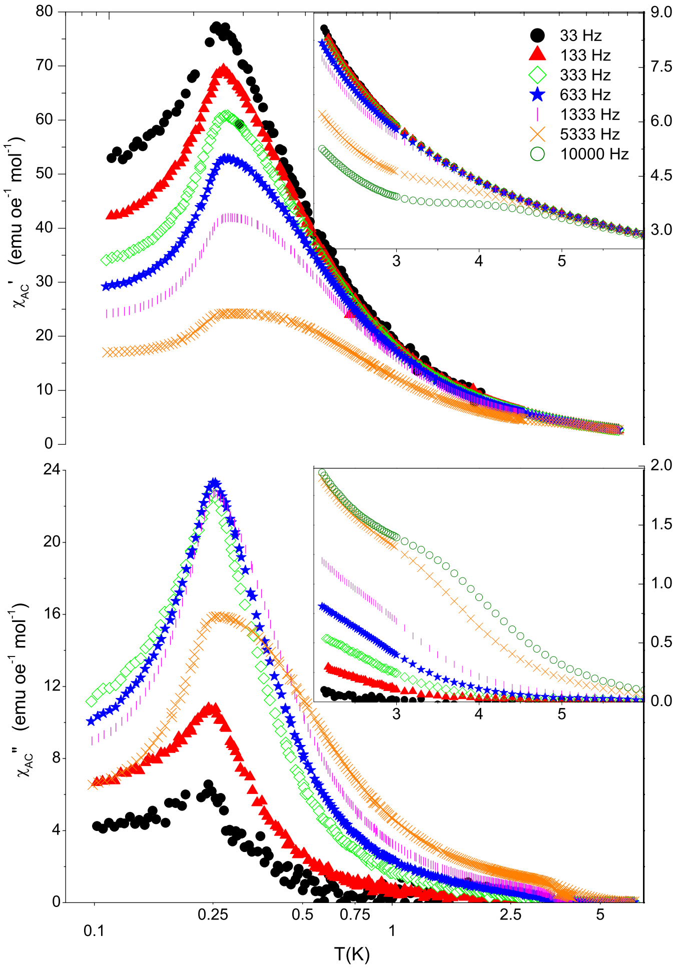

Figure 6.12: χ_{AC} measurements at different frequencies for CsCo$_4$/S

From the graphics, a critical temperature (T$_c$) of 0.20K and 0.25K for RbCo$_4$/S and CsCo$_4$/S compounds is determined. The superimposition of signals makes difficult to determine the blocking temperature for each frequency very difficult. For this reason, in order to obtain the energy barriers and the characteristic time of the compounds, the τ_{av} is represented versus the reciprocal temperature in figure 6.13. Above 3K, τ_{av} indicates thermally activated behavior with activation energies ΔE = 13(2)K for the RbCo$_4$/S and ΔE = 14(1)K for the CsCo$_4$/S. This is attributed to the relaxation of the Co$_4$ cluster, which causes the anomaly around 4K and whose activation energy is similar to the barriers determined for isolated Co-cubanes clusters (see table 4.1). Below 3K, τ_{av} becomes independent of the temperature due to the domination of quantum tunneling processes in the relaxation. However, below 0.5K, τ_{av} increases again and become temperature-dependent, indicating the existence of a thermally activated process with lower activation energy $\Delta E = 0.46(1)$K for the $RbCo_4/S$ and $\Delta E = 0.55(1)$K for the $CsCo_4/S$. To explain this behavior, several hypothesis are plausible. One explanation is the existence of another blocking process due to the freezing of the individual spins of the Co(II) nexus, which can be blocked due to their high anisotropy. Another explanation could reside in the magnetic interaction between the Co(II) nexus and the cubanes. This interaction will modify the energy levels of the cubanes, removing the energy degeneracy and neglecting the quantum tunneling in the cubane as an isolated entity. In this later situation, the quantum tunneling could be assisted by thermal activation and occur in three steps. First, the nexus Co(II) are reversed by a thermal fluctuation of energy equal to the magnetic coupling between the nexus and the cubane. Second, the cubane is allowed to relax via tunneling to an excited state of the same energy. Finally the group relax by flipping the Co(II) nexus spin. This mechanism is more efficient than a direct tunneling between the ground states of the coupled system which would imply the simultaneous tunneling of the cubane and the nexus. The effect of a magnetic bias in the quantum tunneling has been observed before in exchange-coupling dimers [113] and near the long-range magnetic order of polyoxometalate-based SMMs [156].

In graphic 6.13 the maximum and minimum experimental times are also shown. If our measuring technique has a characteristic time lower than the relaxation time (high frequency measurements), we could not seen the relaxation process as the system would be blocked. On the contrary, if our measuring time is higher than the relaxation time (low frequency measurements), we allow the system to relax and reach the equilibrium. For this reason, at low frequencies for the $RbCo_4/S$ the system is almost in equilibrium and the magnetic AC susceptibility can be compared the static susceptibility, which give us a clue of the nature of the interaction, ferromagnetic in this case. This fact has to be taken into account when an experiment is design, to prevent misunderstanding of the relaxation behavior.

In a similar way, we determined the energy barrier and characteristic relaxation times for the other two dimensional networked compounds as can be seen in table 6.5. The values obtained are similar to the ones for other cubanes.

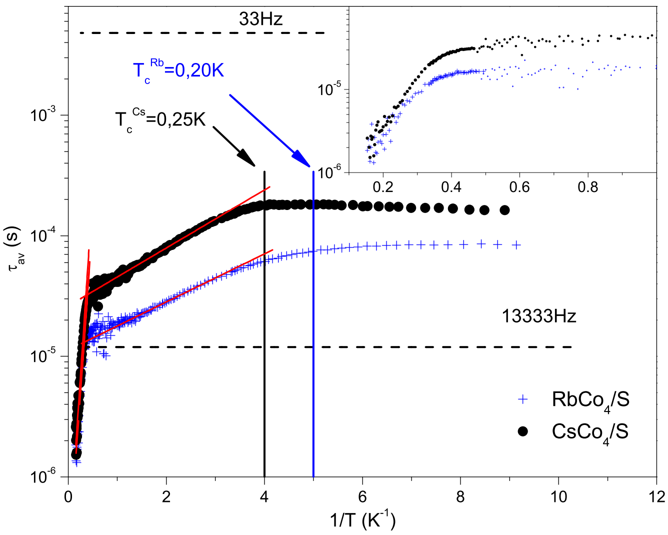

Figure 6.13: Average magnetic relaxation time (τ_{av}) versus the reciprocal temperature for the RbCo$_4$/S and CsCo$_4$/S compounds. Critical temperatures (T$_c$) are 0.2K and 0.25K. Dashed lines indicate the maximum and minimum experimental times measured and correspond to frequencies of 33 and 13333Hz respectively. The red lines correspond to the best Arrhenius fit from which activation energies are determined. The inset shows the high temperature region.

6.4 Discussion and Conclusions

In this chapter, bidimensional networks of linked Co(II)-citrate-cubane cluster through Co(II) ions bridges have been magnetically characterized. The objectives fixed at the beginning of this study were to find out if the SMM behavior of the cubanes is conserved when the cubanes are arrange in layers, and to explore the possibility of a transition from an individual blocking behavior to and hypothetic magnetically ordered phase where the clusters interact.

Magnetization measurements lead us to think that the ground state of the cubane is different to zero with a global spin $S_T = 2$ for all the compounds, so a SMM behavior is possible. In all cases, a blocking phenomenon appears around 4K, which matches with the blocking temperature of other similar cubanes [125, 150–152]. The energy barrier for the reversal of the magnetization for each compound can be seen in table 6.5, where it is easy to see that the barriers for cubanes are of the same order of magnitude and the relaxation times are around 10^{-7}s, which is expected for SMM.

The small differences in ΔE for the square net compounds have been attributed to the slight differences in the angles and distances into the cubane. The high number of angles and variables into each cubane, makes not pos-

Table 6.5: Energy barriers and τ_0 for KCo$_4$/S, RbCo$_4$/S, CsCo$_4$/S, CsCo$_4$/R and CsCo$_4$+1.

	High T		Low T	
	ΔE (K)	τ_0 (s)	ΔE (K)	τ_0 (s)
KCo$_4$/S	8(1)	$2.0(4)\cdot 10^{-7}$	-	-
RbCo$_4$/S	13(2)	$1.9(8)\cdot 10^{-7}$	0.459(5)	$1.13(1)\cdot 10^{-5}$
CsCo$_4$/S	14(1)	$2.1(3)\cdot 10^{-7}$	0.554(7)	$2.62(4)\cdot 10^{-5}$
CsCo$_4$/R	30(2)	$0.4(3)\cdot 10^{-7}$	-	-
CsCo$_4$+1	23(1)	$0.3(1)\cdot 10^{-7}$	-	-

sible to give an advice about the most suitable M-O-M angle to favor and increase the ferromagnetic exchange. In table 6.6 all the angles and distances intracubane are shown as a reminder. The addition of a extra Co(II) ion in the space between cubanes has an effect on the energy barrier, doubling it. This fact can be explained if we remind that the cubanes are not isolated, they are part of a net and other magnetic centers can interact with them. Adding another magnetic center modifies the molecular magnetic field around each cubane and influence in the relaxation process.

The differences in the net topology between CsCo$_4$/S and CsCo$_4$/R cause a distortion in the cubane that may explain the increase in the energy barrier from 14K to 30K, which is in good agreement with the increase expected when the symmetry is broken and the axial symmetry is increased.

Table 6.6: Characteristic distances and angles for cubanes of KCo$_4$/S, RbCo$_4$/S, CsCo$_4$/S, CsCo$_4$/R and CsCo$_4$+1.

	Distance		Angle	
KCo$_4$/S	Co1-Co1'	3.139(2)	Co1-O-Co1'	96.1°(2)/97.5°(2)
	Co1-Co1"	3.240(2)	Co1-O-Co1"	100.8°(3)
RbCo$_4$/S	Co1-Co1'	3.148(1)	Co1-O-Co1'	96.3°(2)/97.2°(2)
	Co1-Co1"	3.196(1)	Co1-O-Co1"	99.1°(2)
CsCo$_4$/S	Co1-Co1'	3.155(1)	Co1-O-Co1'	96.0°(2)/97.6°(2)
	Co1-Co1"	3.190(1)	Co1-O-Co1"	98.7°(2)
CsCo$_4$+1	Co1-Co1'	3.1360(8)	Co1-O-Co1'	95.8°(1)/97.3°(1)
	Co1-Co1"	3.2258(7)	Co1-O-Co1"	99.7°(1)
CsCo$_4$/R	Co1-Co2	3.209(1)	Co2-O-Co2'	99.4°(2)
	Co1-Co'	3.119(1)	Co1-O-Co1'	100.5°(2)
	Co1-Co1'	3.2361(9)	Co1-O-Co2'	95.8(2)/96.0°(2)

Although the temperature region below 1.8K has been explored only for $RbCo_4/S$ and $CsCo_4/S$, an equivalent behavior is expected for all of the two dimensional arrays of Co(II) cubanes due to the similarities between them. At very low temperatures, another relaxation process occurs around 0.5K with a lower activation energy, and magnetic order appears at 0.2K for $RbCo_4/S$ and 0.25 for $CsCo_4/S$. The relaxation process can be identified as a freezing of the individual Co(II) centers. This Co(II) ions have enough anisotropy to block themselves. Another plausible explanation is that the exchange coupling between the Co(II) nexus and the neighboring cubanes produces a magnetic bias in the energy levels of the cubane that blocks the quantum tunneling between the ground states. In this case, it is necessary to activate it thermically. The difference in the low temperature blocking in $RbCo_4/S$ and $CsCo_4/S$ can be a consequence of the intersticial disorder, which is higher in the $RbCo_4/S$ and will favor the relaxation. It is not so easy to find a solid explanation for the difference of 0.05K between the T_c of both compounds, because the $CsCo_4/S$ has a higher T_c but the interlayer space is 0.2 Å longer. A small difference in the alignment of the easy axis of the Co(II) nexus and the cubane Co(II) ions may be the cause.

The coexistence of two relaxation processes with different energy barriers and time scales can open the door to study a wide variety of magnetic collective phenomenons ranging from the complete or partial blocking of each of the magnetic entities to a fully magnetic ordered state. Results will depend on the experimental characteristic time. A possible application may be the study of conceptual models such as the random field Ising model (RFIM) [157]. This theoretical model can be described with a two-term hamiltonian that includes an Ising term $-\sum J_{ij}\mathbf{S}_i{\cdot}\mathbf{S}_j$, where the sums extend to the first neighbors, and another term $-\sum \mathbf{h}_i{\cdot}\mathbf{S}_i$ that represents the coupling of the spins $\mathbf{S}_i$ with a magnetic field $\mathbf{h}_i$ that can adopt different random values from site to site: $\overline{\mathbf{h}_i\mathbf{h}_j} = \delta_{ij}\mathbf{h}_0^2$ and $\overline{\mathbf{h}_i} = 0$. The therefore impossible task of creating a random magnetic field distribution can be done by blocking the tunneling of the cubane cores, so they stay frozen randomly below 2K. In this situation, the cubanes generates a random internal magnetic field on the remaining Co(II) centers.

In summary, different cations and topologies have induced modifications in the magnetic behavior of two magnetic entities and the energy barriers and characteristic time of two blocking process. This may allow the possibility to tune the magnetic characteristic of SMM isolated or arranged in layers, even by placing small molecules in the channels between cubanes formed in $CsCo_4/R$ whose potential as MOF in under study.

Chapter 7

Three dimensional network of Co(II)-cubanes

7.1 Introduction

In previous chapters, the magnetism for isolated Co_8 clusters and cubanes arranged in two dimensional layers has been studied. In this chapter a three dimensional structure of diamond type with cubane units in its nodes abbreviated as Co_4/3D is described structurally and magnetically. Once again, the building block is a citrate cubane very similar to already reported SMM [125, 150, 151].

In chapter 6 five different two dimensional compounds where Co(II) citrate cubane units are bridged by single Co(II) centers were studied. Now, we have increase the dimensionality of the net with the objective of studying the influence of the net in the magnetic behavior. The cubanes are expected to keep their SMM properties and possible collective behaviors may appear.

The synthesis and the structure of the compound is described in section 7.2 and their magnetic and calorimetric properties in section 7.3. A discussion about the results and some conclusions can be found at the end of the chapter.

7.2 Synthesis and structure

In a synthesis very similar to the one of KCo_4/S, where the ETG is substituted by another diol, we obtain a high symmetry three dimensional net based on cubanes with bridging Co(II) centers of formula $[\{Co_4(C_6H_4O_7)_4\}\{\mu - Co(H_2O)_2\}_2]^{4+}$. Since the polymeric nets are anionic, there are K^+ acting as counterions located inside the channels present in the compound. It crystallizes in the space group $I4_1/a$, with a unit cell equal to a=20.7872(3), b=20.7872(3), c=11.3290(2). The complete formula is $(K_4\{Co_4(citr)_4[\mu - Co(H_2O)_4]_2\} \cdot 8H_2O)_n$. For the shake of simplicity, this compound is denoted as Co_4/3D.

The building block of Co_4/3D is a cobalt citrate cubane formed by four Co(II) centers and four hydroxy oxygen atoms from an equal number of quadruply deprotonated citrates. Neighboring cubanes are bridged by a six-coordinated Co(II) centers coordinated by two carboxylate oxygen atoms. The Co(II) nexus are linked to the cubane Co(II) through two arms *Co-O-C-O-Co* and *Co-O-C-C-C-O-Co*, as can be seen in figure 7.1. The Co(II) nexus can interact with the cluster but the interaction strength is expected to be weaker than the intra-cubane interaction. Therefore, in a simplified approximation, we can considered only the cubane as a cluster. The main structural difference between this compound and the two dimensional network compounds rises from the spacial distribution of the Co(II) nexus around the cubane. For Co_4/3D we have a cubane in the centre of a tetrahedron whose vertexes are occupied by four Co(II) units, while the linking Co(II) center in the 2D networks were disposed in the same plane. This connection between the building blocks results in a polymer with diamond-like pattern.

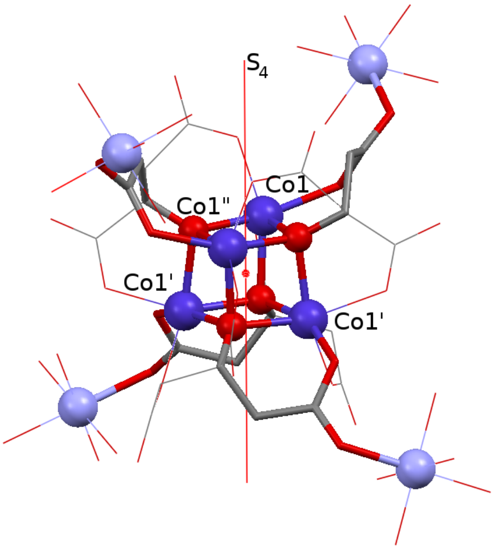

Figure 7.1: Symmetry for the cubane. A S_4 parallel to the *c* cell axis goes through the cubane. The cubane, the Co(II) nexus and the bridges between them are remarked.

The cubane present S_4 symmetry with the axis parallel to the c axis, as cubanes in the square grid compounds, which makes four distances Co-Co equals and a pair different. The distances and angles between Co(II) ions is shown in table 7.1. The cubane Co(II) ions are in a C_3 environment while the nexus Co(II) ions are in a octahedral environment.

In the solid state a crystal of Co_4/3D is formed by tree interpenetrating diamond-like nets, where each network is formed by cubanes linked by Co(II) arms in a octahedral environment, each cubane is bonded to four Co(II) units. The three nets are interpenetrated, achieving a more efficient occupancy of the space, decreasing the distance between cubanes and linking Co(II) centers belonging to different nets: the distance between cubanes and Co(II) nexus of the same net is 10.4Å, while the distance between a cubane and the nearest Co(II) center is 7.8Å. In figure 7.2 the three nets are schematically represented.

Table 7.1: Characteristic distances and angles for cubane in Co_4/3D.

Distance Å		Angle (°)	
Co1-Co1'	3.1225(3)	Co1-O-Co1'	95.88(5)/96.36(5)
Co1-Co1"	3.2147(3)	Co1-O-Co1"	100.34(5)

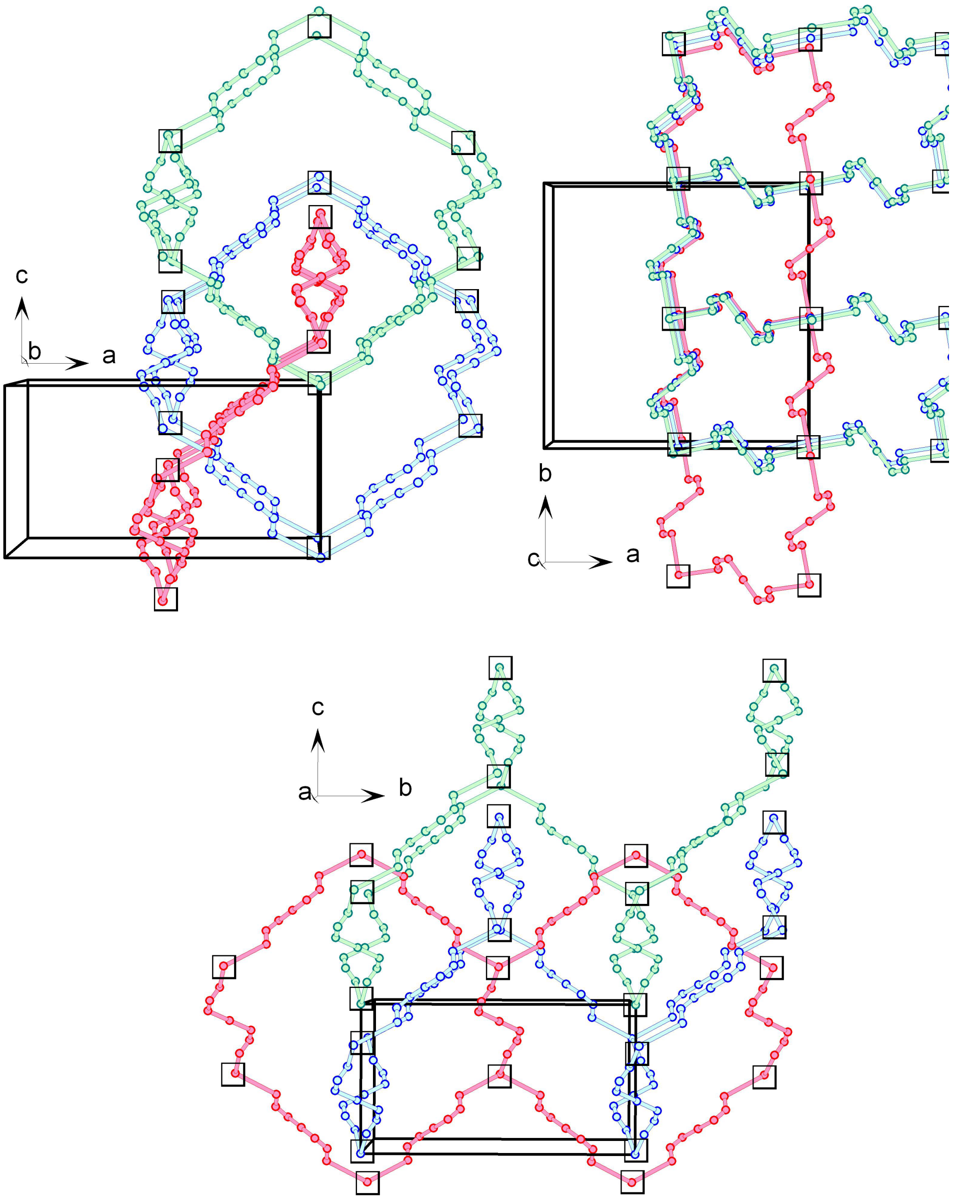

Figure 7.2: View form the *a*, *b*, and *c* axis of a schematic representation for the three interpenetrating nets: blue, red and green. The position occupied by cubanes are marked by a square.

7.3 Magnetic and calorimetric properties

The magnetization versus temperature at 500 Oe has been measured from room temperature to 1.8K, obtaining the curve of $\chi_M{\cdot}T$ represented in figure 7.3. At 300K, the curve has a value of $17 emu{\cdot}mol^{-1}{\cdot}K$, which is consistent with the results expected for a six independent Co(II) ions per unit cell with S=3/2 and g=2.4. From 300K, the signal decreases slowly down to 65K where it reaches a value of $16 emu{\cdot}mol^{-1}{\cdot}K$. Cooling down further, a smooth field-dependent anomaly around 15K can be peeked up before a peak at 2.4K with a value of $114 emu{\cdot}mol^{-1}{\cdot}K$. A fit to a Curie-Weiss function between 200 and 300K gives a g=2.469(2) and θ=-6.9(3)K (corresponding to an antiferromagnetic interaction) for six Co(II) atoms with S=3/2. A ZFC-FC cycle at 50Oe was performed at low temperature, between 20K and 1.8K, finding the irreversibility shown in graphic 7.4.

To confirm the existence of a magnetic order, heat capacity measurements were performed from 0.4K to 151K. As it was expected, a sharp peak appears at low temperature indicating the existence of a magnetic order transition at 2.7K (see inset in graphic 7.4).

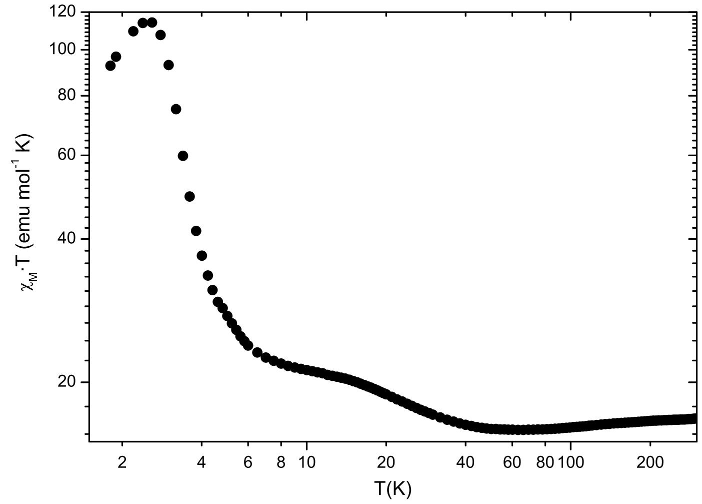

Figure 7.3: $\chi_M{\cdot}T$ versus T plot for the Co_4/3D compound measured at 500 Oe.

The heat capacity has been measured at zero field and at 1T. In figure 7.5, the results at both fields are shown, remarking in red the presence of points where the system where out of equilibrium. The heat capacity is a dynamical technique, where a heat pulse is applied to the sample and the relaxation time is the physical magnitude measured and related to the heat capacity of the sample. In the out of equilibrium points, the adjust to an exponential decay is artificial and a dynamical process of unknown nature takes place in the sample.

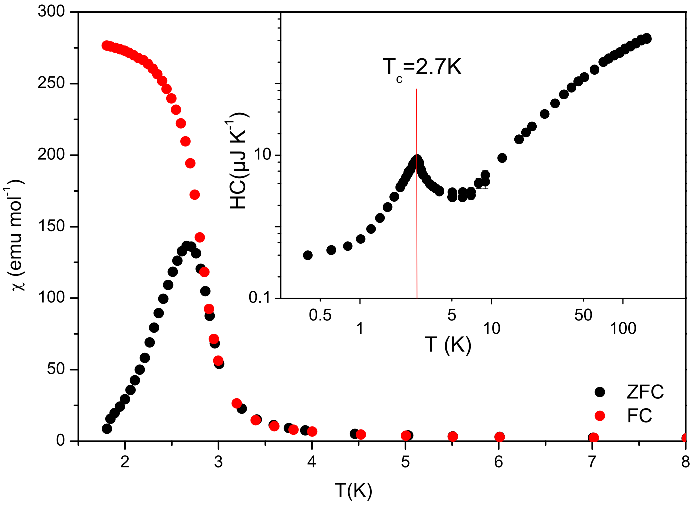

Figure 7.4: χ_M versus T at the ZFC and FC at 50Oe cycles for Co_4/3D. The inset shows the Heat Capacity versus the temperature curve. A phase transition is observed at 2.7K

In order to minimize its effects, we thermalized the sample for several minutes at each temperature and reduced the amplitude of the heat pulse to a 1% of the temperature.

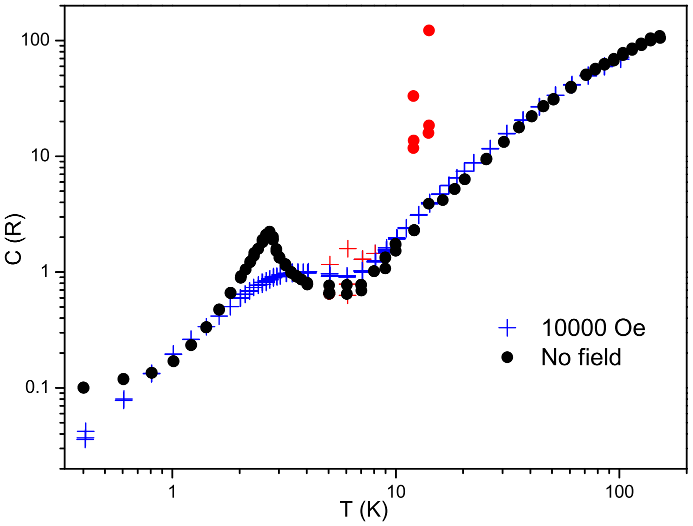

Figure 7.5: Heat Capacity versus temperature at zero field and 10000 Oe. In red the out of equilibrium points are marked.

The first step to analyze the heat capacity data is to isolate the magnetic contribution to the heat capacity. This task can become a difficult challenge for molecular compounds, where even the Debye-model needs to be extended [158].

Due to the complexity of the system, an empirical fit to a cubic polynomial and a Schottky function for the blocking of the cluster (which has an energy barrier of 44K) has been performed. This allow us to subtract all the contributions but the magnetic one (C_m), as in other networked SMM compounds [123]. The total magnetic contribution to the heat capacity can be seen in figure 7.6. To properly obtain the total magnetic entropy, the C_m/T curve was extrapolated at higher and lower temperatures than the experimental ones. We have used a cubic polynomial for the low temperature region and a exponential decay for the high temperature tail. After integrating the area under the curve, a magnetic entropy equal to $\Delta S = 1.24R$ has been found, which is comparable with the sum of two contributions $R \ln 2 = 0.69R$. This has been attributed to the two linking Co(II) per molecule. From this result, we can conclude that sublattice of linking Co(II) is ordered at 2.7K, but the magnetic contribution of the cubane is absent from the heat capacity. This behavior of the cubanes could be explain by a zero ground state, so the cubanes would not be ordered. In this case, SMM behavior would be still possible due to accessible excited levels with non-zero S_T [151, 152]. The magnetization values at 1.8K makes us to discarded this option and attributed to the cubane a ground state with $S_T \neq 0$. The position of the cubanes in the structure and the links between them and the nexus Co(II) ions make them not likely to not participate in the magnetic order. The most plausible explanation is that the cubane is not in equilibrium: the technique employed is dynamical, the experimental time is lower than the relaxation time, and cubanes remain blocked.

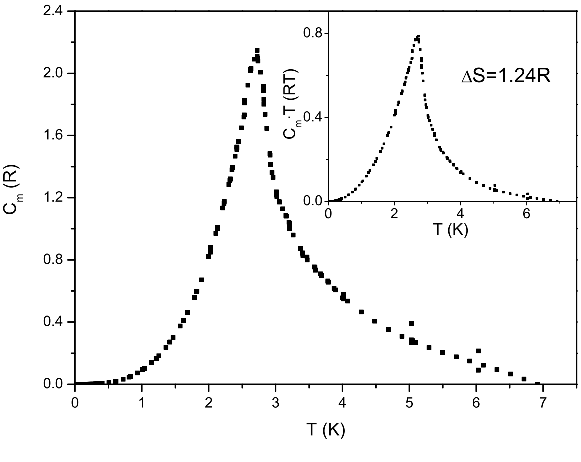

Figure 7.6: C_m versus T. The inset shows the C_mT curve to perform an integral and obtain the ΔS for the transition

The quality of the data in the critical region (considering it as $\frac{|T-T_c|}{T_c} < 0.1$) discourages us of calculating the critical exponent for the transition. However, due to the high anisotropy of the Co(II) atoms, we can expect a 3D Ising systems. To obtain the sign of the interaction between the magnetic species, a study of the spin-wave region is necessary. For a 3D lattice, the spin-wave contribution of a ferromagnet depends on $T^{3/2}$, while the dependency is T^3 for an antiferromagnet, as it happens for the lattice phonons. Data at temperatures below T_c have been well fitted with a T^3 relation, so the magnetic interaction is antiferromagnetic.

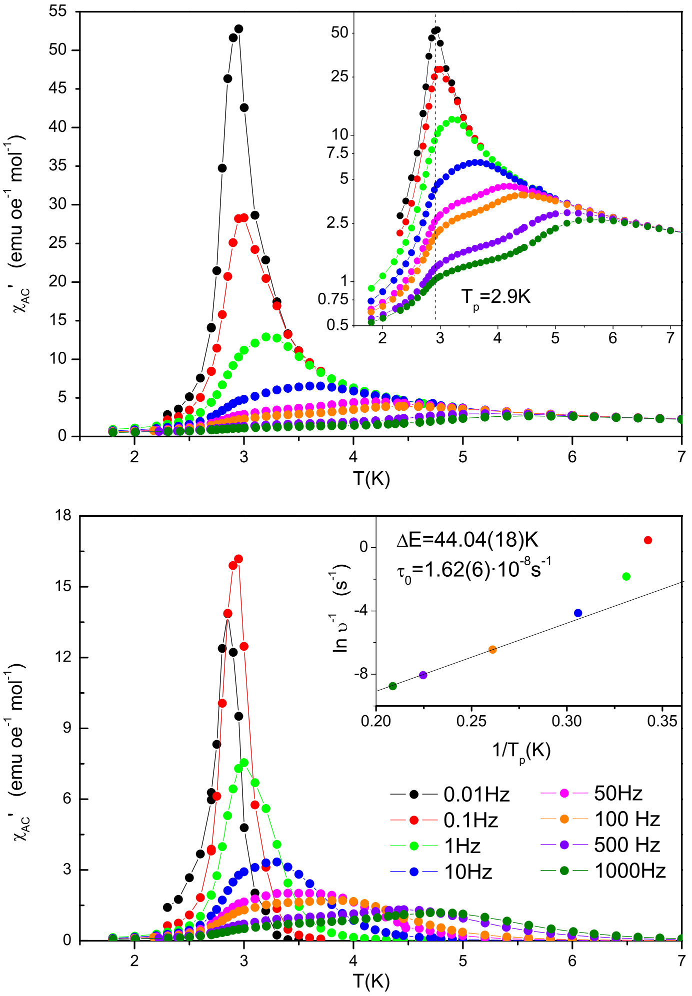

Figure 7.7: χ_{AC} measurements at different frequencies for Co$_4$/3D. In the top, χ' versus T and a logarithmic inset that reflects the existence of two peaks, one frequency-dependent and one at 2.9K. At the bottom, χ" versus T and an inset with an Arrhenious fit.

The magnetic order is also revealed in AC measurements as can be seen in figure 7.7. As a consequence of the phase transition, a frequency independent peak appears around 2.9K. Also the SMM nature of the compound is confirmed. A blocking phenomenon appears around 4K, which agrees with the behavior of other isolated Co(II) cubanes [125, 152]. A non-Arrhenius dependence of the relaxation time and the frequency has been found as can be seen in the inset of the χ" graphic in figure 7.7. At low frequencies, as the blocking temperature is approaching to T_c, the blocking process occurs at higher temperature than the temperature predicted, diverging from the Arrhenius law at frequencies below 100Hz. A fit between 100Hz and 1000Hz gives an energy barrier of $\Delta E = 44.04(18)K$ and a characteristic time of $\tau_0 = 1.62(6) \cdot 10^{-8} s^{-1}$. Using a definition of τ_{av} as in previous chapters, may be a little artificial. This approximation is valid at low frequencies, but for this compound, at lower frequencies the blocking process occurs at temperatures near the critical temperature, which gives fictitious results. For this reason, we have discarded artificial results as an energy barrier of 78(11)K and 65(2)K for 0.01 and 0.1Hz and characteristic times around $10^{-10}s$. For higher frequencies the energy barrier is near 53K and the characteristic time around $3 \cdot 10^{-9} s^{-1}$, which are higher than the calculates by the previous fit. The influence of the magnetic transition in the energy barrier is very relevant in this compound due to the proximity of both phenomenons in temperature. The relaxation time and the energy barrier tend to increase indefinitely at low frequencies due to the magnetic interaction between cubanes and Co(II) ions. The boundary between dynamical and static regimens becomes confuse and the influence of magnetic interactions is relevant at low frequencies.

The presence of hysteresis below 2.7K also confirms the existence of magnetic order. The coercitive fields at 1.8K and 2.1K are 1340Oe and 870Oe and the remanent magnetization 3.20 and 2.10 μ_B respectively, as can be seen in figure 7.8. In graphic 7.9 the first magnetization curve at several temperatures is shown. Below the critical temperature and for fields lower than 100Oe, the signal presents a sigmoidal curve which reaches a magnetization equal to the remanent magnetization (3.20 μ_B at 1.8K)

In the compounds described in chapter 6, a simplified model has been use. A total spin S_T for the cubane has been defined and the linking Co(II) have been treated as an isolated spin value of 1/2 and an experimental g value of g=4.6 [155]. With this model, each liking Co(II) ion contributes with $2.3\mu_B$ to the magnetization of saturation. For the two dimensional compounds, S_T has been estimated around 2, and the contribution of the cubane to the magnetization of saturation near $8.4\mu_B$. Attending to the structure of the cubanes and the magnetic measurements, it seems a reasonable approximation to considerer a similar behavior of the cubane in Co_4/3D. With these

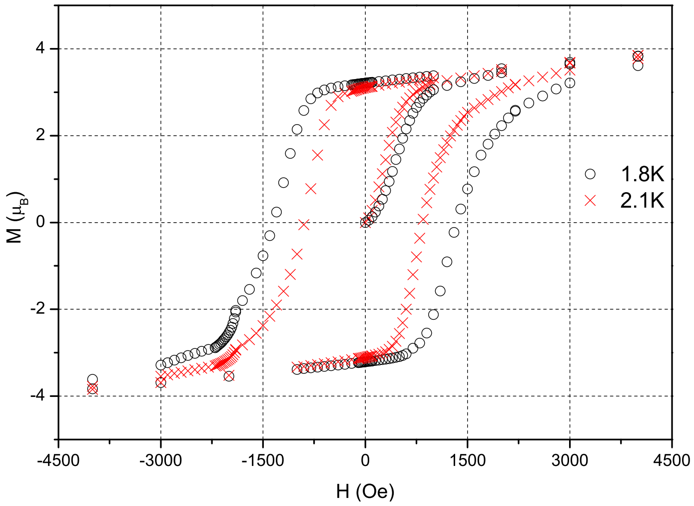

Figure 7.8: Magnetization in Bohr magnetons per unit formula versus T for $Co_4/3D$in hysteresis cycles. The first magnetization curve is also represented as X.

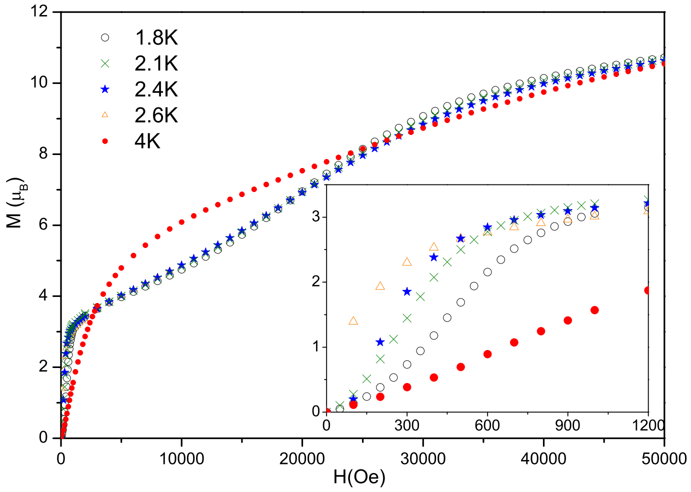

Figure 7.9: Magnetization in Bohr magnetons per unit formula versus T for $Co_4/3D$. The inset show the low field region.

considerations, the magnetization of saturation for $Co_4/3D$ matches with a model where the cubanes and nexus Co(II) ions orders antiferromganetically: $8.4\mu_B - 2{\cdot}2.3\mu_B = 3.8\mu_B$.

Around 21000Oe an inflexion point appears in the magnetization curve, and approaching T_c from below, it becomes less prominent and disappears above T_c. In other samples, the inflexion point has been attributed to a mixing between low lying levels near a ground state with S=0 in the cluster [152], but in this case we attribute it to a reordering of spins with the field. Several tries to fit the experimental curves with oversimplified models have not produce satisfactory results, so waiting for a complete knowledge of the energy levels for these compounds is necessary for a complete analysis of the magnetic properties.

7.4 Discussion and Conclusions

This compounds represented the first Co(II) SMMs arranged in networks where a clear evidence of the SMMs behavior and the magnetic order has been found. A blocking phenomenon around 5K, which agrees with the expected behavior of an isolate Co(II)-cubane [125, 152], and a magnetic order at 2.7K coexist in the sample.

The magnetization at 500Oe presents two anomalies. One around 15K that has been attributed to the energy levels of Co(II) and its depopulation. Another anomaly has been observed at lower temperature, and it corresponds to a magnetic order phase transition. The analysis of the heat capacity data reveals two species with a doublet ground state ordering antiferromagnetically, which have been identified as the linking Co(II) ions with a ground state $S = \pm 1/2$. Due the dynamic character of the measurement technique and the conflict between the experimental characteristic time and the relaxation time of a SMM, the magnetic contribution of cubane to the phase transition has not been observed. This does not mean that the cubane does not participate in the magnetic order, it is difficult to imagine a system where the Co(II) nexus order magnetically and the cubane not. Neutron diffraction measurements are in process in order to determine the magnetic structure of the compound. Another plausible explanation for this behavior would be a ground state $S_T = 0$ for the cubane, which has been discarded by the magnetization measurements.

We have made the assumption that the ground state of the cubane in Co_4/3Dis the same that the state of the cubanes in the two dimensional compounds studied in chapter 6. This simplification leads us to a magnetic model with two sublattices, one of cubanes and one of linking Co(II) ions, that orders antiferromagnetically. Neutron diffraction measurements would be an excellent chance to determine the magnetic structure.

As a consequence of the coexistence of magnetic order and SMM behavior, the relaxation time and the energy barrier become frequency dependent at low frequencies. At this frequencies, the blocking phenomenon occurs at temperatures near T_c, and the effects of the large order interaction becomes relevant, increasing the energy necessary to reversal the magnetization. The boundary between the DC behavior and AC behavior is confused in this regimen of frequencies.

As the crystalline structure presents channels and can absorb different molecules, this compound represents an excellent opportunity to modify T_c by changing the molecules in the channels and observe how it can influence on the SMM behavior.

General conclusions for Part II

- **Influence of the symmetry in SMM properties.** In chapter 5, two different phases of the same compound have been magnetically characterized, both of them contain Co_8 clusters. In Phase 1 clusters are distorted and we can consider that magnetic clusters are formed by seven Co(II), four in the cubane and three outer, and not include the Co(II) ion linked by a citrate bridge. In Phase 2, the cluster is highly symmetrical (C_2) and the interaction between the eight Co(II) and their nearest neighbors is expected to be of the same magnitude. Although the magnetic core has one Co(II) ions less for Phase 1, the break of the symmetry makes the energy barrier for Phase 1 four times the energy barrier for Phase 2. This remarks the importance of focusing our efforts to synthesized high energy barrier SMM into increasing D more than S.

- **Influence of topology and crystalline structure in SMM properties.** The two dimensional net compounds have been obtained with different topologies (square net, rhombic net and square net with an excess of Co(II)). The synthesis with different cations produces small modifications in the angles and distances into the cubanes which have a slight influence in the energy barrier of the cubanes. Also the different topology, symmetry of the cubane and the presence of more magnetic ions near the cubanes modify its value.

- **Magnetic bias of quantum tunneling.** For $RbCo_4/S$ and $CsCo_4/S$, the magnetic interaction between cubanes and nexus Co(II) ions modify the energy levels of the cubanes, which may block the quantum tunneling relaxation and make necessary a thermal assistance.

- **Coexistence of magnetic order and SMM behavior.** In two dimensional and three dimensional compounds, we have been found that SMM blocking and magnetic order can coexist in the same sample at different temperatures.

- **Influence of increasing the dimensionality of the net.** Increasing the dimensionally of the net from two to three has increased the order temperature in a 100 factor.

- **Dynamic and static regimen for SMM.** In the study of the compound Co_4/3D, it has been clearly manifest that SMM are entities whose behavior depends on the experimental time of the technique used to measured. A special care should be taken when analyzing data from dynamical techniques.

Conclusiones generales

El trabajo desarrollado a lo largo de esta tesis ha permitido obtener diversas conclusiones y resultados que podrían contribuir a esclarecer la naturaleza y propiedades de compuestos moleculares magnéticos, en concreto, de imanes quirales e imanes monomoleculares dispuestos en redes. Las conclusiones obtenidas para cada línea de investigación se encuentran detalladas a continuación.

Línea A

- **Nueva defínción global para quiralidad magnética.** Los conceptos de quiralidad nuclear y magnética son habitualmente mezclados y confundidos. Existen varias definiciones de quiralidad magnética, todas ellas locales. En este contexto, en esta tesis se ha propuesto una nueva definición de quiralidad magnética como un concepto global. De acuerdo con el criterio establecido en el capítulo 2, una estructura magnética es quiral si el producto vectorial $\mathbf{F}_M \times (\mathbf{F}_M)^*$ es distinto de cero para un vector cualquiera de la red recíproca. Desarrollando esta definición, se ha encontrado que la quiralidad magnética solo puede encontrarse en estructuras magnéticas no collineares que cristalicen en grupos de espacio no centrosimétricos.

- **Efecto de substituir el átomo $\mathbf{Cr^{III}}$ en el compuesto GN por $\mathbf{Mn^{III}}$ en el compuesto GN-MnMn.** La substitución del átomo Cr^{III} del compuesto GN por un átomo Mn^{III} en el compuesto GN-MnMn tiene un efecto negligible en la estructura nuclear salvo en el entorno del átomo en cuestión. La substitución tampoco afecta a la simetría de las estructuras magnéticas. En ambos casos, la estructura magnética es descrita con la Representación Irreducible (IR) Γ_4 del grupo de espacio $P2_12_12_1$, y puede ser vista como una estructura conica cuadrangular a lo largo del eje a. La mayor diferencia entre los compuestos es su temperatura de orden magnético, la substitución de Cr^{III} por Mn^{III} provoca un descenso de la temperatura de orden de 38K a 28K. La substitución del átomo no tiene efecto sobre la quiralidad, ambos compuestos presentan estructuras nucleares y magnéticas quirales.

- **Efecto de substituir una molécula H_20 en el compuesto GN por DMF en el compuesto GN-DMF(R) como ligando del Mn^{II}.** La substitución de una molécula H_20 por una molécula DMF modifica el apilamiento de las capas y aumenta la separación entre capas. Estos cambios estructurales influyen en el magnetismo y modifican la simetría de la estructura magnética. Mientras que la estructura magnética de GN es descrita por la IR Γ_4 del grupo de espacio $P2_12_12_1$, para el compuesto GN-DMF(R) es Γ_1 la IR que describe la estructura magnética. Esta IR corresponde a una estructura antiferromagnética. Como consecuencia de la modificación introducida en la disposición de las capas, los caminos de interacción magnética entre capas son distintos en ambas muestras, lo que conduce a una cambio de interacción entre ellas, de una interacción ferromagnética en el caso del compuesto GN a una interacción antiferromagnética en el caso del GN-DMF(R). El incremento de la distancia entre capas influye en la temperatura de orden, que pasa de ser 38K en el GN a 33K en el GN-DMF(R). La substitución del ligando y la modificación tanto del apilamiento entre capas como de la interacción entre ellas no ha afectado a la quiralidad de las estructuras, en ambos compuestos quiralidad nuclear y magnética coexisten.

- **Influencia del ligando quiral en la quiralidad magnética.** La quiralidad nuclear en los compuestos estudiados viene dada por la presencia del mismo enantiómero del ligando quiral del átomo Mn^{II} en todo el cristal. En el compuesto GN-DMF(rac) los dos enantiómeros del ligando quiral se encuentran presentes en la misma proporción y dispuestos de forma que el grupo espacial es centrosimétrico. Como consecuencia, la estructura nuclear de este compuesto no es quiral. El centro de inversión que relaciona pares de sitios magnéticos modifica la simetría de la estructura magnética, que puede ser descrita en este caso por la IR Γ_2 del grupo de espacio $Pnma$. La cristalización en un grupo espacial centrosimétrico impide la existencia de una estructura magnética quiral, como se ha demostrado en general al establecer la nueva definición, y en particular para este compuesto.

- **Quiralidad magnética en ciano-compuestos bimetálicos.** Todos los compuestos con una estructura nuclear quiral estudiados en esta tesis presentan también una estructura magnética quiral. La estrategia de síntesis empleada ha demostrado ser una ruta eficiente para la obtención de imanes quirales.

Línea B

El estudio de los SMMs dispuestos en redes de diferente dimensionalidad dentro de la línea B de investigación de esta tesis ha llevado a las conclusiones detalladas a continuación.

- **Influencia de la simetría en la propiedades de los SMMs.** En el capítulo 6, se han caracterizado magnéticamente dos fases diferentes del mismo compuesto. La estructura de ambas fases contiene clústeres de Co_8. En la fase 2 los clústeres presentan simetría S_4, mientras que en la fase I esta simetría se rompe y los clústeres están distorsionados. La ruptura de la simetría en la fase 1 incrementa la barrera energética de inversión de la magnetización en cuatro veces si la comparamos con la barrera de la fase 2. Este hecho puede servir para orientar la síntesis y el diseño de SMM con mayores barreras energéticas hacia rutas que tiendan a incrementar D además de S. Este compuesto es el primero donde se ha observado que una reacción reversible de estado sólido permite seleccionar la estructura de los clústeres, y por tanto su barrera energética, en un mismo monocristal.

- **Influencia de la topología y estructura en las propiedades de un SMM.** Los compuestos bidimensionales estudiados presentan diferentes topologías (red cuadrada, red romboédrica y red cuadrada con un exceso de iones Co(II)). Además, dentro de los compuestos que cristalizan en una red cuadrada, el uso de differentes cationes en la síntesis provoca pequeñas variaciones en los ángulos y las distancias de los cubanos. Se ha comprobado que tanto los cambios en la topología o la presencia de otros iones Co(II), como los pequeños cambios estructurales dentro del cubano, influyen en la barrera energética de los cubanos.

- **Polarización magnética del efecto túnel.** Se ha observado que en los compuestos denotados como $\mathrm{RbCo_4/S}$ y $\mathrm{CsCo_4/S}$, la interacción magnética entre cubanos y iones Co(II) nexos puede modificar los niveles de energía del cubano, lo que influiría en en el proceso de relajación túnel llegando a bloquearlo y haciendo necesaria una activación térmica para superar la barrera energética. En estos compuestos se ha constatado la presencia de dos fenómenos de bloqueo, uno próximo a 5K y otro cercano a una posible transición de orden magnético en torno a 0.25K.

- **Coexistencia de orden magnético y comportamiento SMM.** En los compuestos bidimensionales y tridimensionales con clústeres de Co(II) caracterizados en esta tesis, se ha encontrado que los fenómenos de bloqueo SMM y orden magnético pueden coexistir en una misma muestra a diferentes temperaturas.

- **Influencia de aumentar la dimensionalidad de la red.** Al aumentar la dimensionalidad de la red de cubanos de Co(II) de 2 a 3 dimensiones, se ha observado que la temperature de orden magnético se ha incrementado en un factor 100.

- **Régimen estático y dinámico en un SMM.** Durante el estudio del compuesto Co_4/3D, se ha puesto de manifiesto que los SMM son entidades cuyo comportamiento magnético depende fuertemente del tiempo experimental de la técnica empleada en su caracterización. Este hecho remarca la importancia de una correcta interpretación de los datos obtenidos mediante técnicas dinámicas.

Appendix A

Experimental techniques. Neutron Diffraction

During the development of the work presented in this thesis, several experimental techniques have been used. This chapter is devoted to the neutron diffraction, a powerful tool that has been widely employed to determine the nuclear and magnetic structure of the chiral compounds studied in this first part. The neutron experiments have been performed in the Institute Laue Langvenin (ILL) placed in Grenoble, France. The instruments chosen to performed the single-crystal diffraction studies have been D15, a four-circle single-crystal diffractometer, and VIVALDI, a Laue diffractometer.

In this appendix, the basic properties of the neutron and the fundamentals of neutron diffraction theory are explained, focusing on the methods and configurations employed in the thesis.

A.1 Neutron properties

Neutrons are one of the most important probes for investigating condensed matter due to their unique properties when they interact with matter. Neutrons are subatomic hadron particles discovered in 1932 by James Chadwick [159]. A neutron is composed of one up and two down quarks with charges of $2/3$ and $-1/3$ respectively, so the net charge is zero, but its internal structure leads to an electric charge distribution which gives it a magnetic moment and an electric polarizability. While bound neutrons in stable nuclei are stable, free neutrons are unstable; and they undergo beta decay with a mean lifetime of just under 15 minutes (885.7±0.8 s). In research reactors, free neutrons are produced by nuclear fission to be used in different experiments.

The value of the neutron scattering as one of the most valuable experimental tools for the study of condensed matter lies on the fact that the interaction between neutrons and matter is via the strong interaction with the nuclei and the magnetic dipolar interaction with the unpaired electrons. The strong interaction is a very intense but short-range interaction, which implies that the neutron must be very close to the nucleus to feel the interaction, and the magnetic dipolar interaction arises from the fact that the neutron has a dipolar magnetic moment, even though it has no charge. Neutrons and X-ray diffraction methods have became very useful in physics, chemistry, biology and materials science and both techniques are highly complementary. The most relevant and unique character of slow neutrons can be summarized as follows [160]:

1. Neutrons interact with nuclei and not with the electrons, as photons do. As a consequence, the response of neutrons from light atoms (e.g hydrogen) is much higher than for x-rays; neutrons can distinguish atoms of comparable atomic number; and neutrons can differentiate between isotopes.

2. For the same wavelength as hard x-rays, the neutron energy is much lower and comparable to the energy of elementary excitations in matter. Therefore, neutrons allow not only to determine the static average chemical structure, but also the investigation of the dynamic properties of atomic arrangements which are related to the properties of the materials.

3. The neutron has no net charge, which has important consequences:
   - The neutron produces a very small disturbance of the sample's properties
   - It is not affected by the coulomb interaction neither other charge-dependent interactions, so the neutron has a large penetration depth that allows to study bulk properties of materials. This property also benefits the investigation of materials under extreme conditions (very low or high temperatures, high pressures, magnetic and electric fields...)because neutrons can penetrate through the environment settings
   - There is almost no radiation damage to the objects under study (e.g. living biological objects)

4. The neutron posses a magnetic moment, it has a spin $s = 1/2$. This property makes the neutron to interact with the magnetic moments of the atoms via the magnetic dipolar interaction, so it can be used as a probe for the determination of the static (arrangement of electron spins and density distribution of unpaired electrons) and dynamical magnetic

properties of matter (magnetics excitations and time-dependent spin correlations).

However, not everything in neutrons is an advantage. One of most significant is derived from the fact that they interact with nuclei via the strong interaction, so they see the matter as if it was avoid. For this reason, the sample size must be bigger than with x-rays. The neutron fluxes in reactors are still not comparable with those of the X-ray sources, therefore sometimes we are limited by the flux.

There are several neutron techniques that exploit the properties of neutron as a probe to understand the matter, we are focusing in neutron diffraction and, in particular, in four-circle geometry diffraction and Laue diffraction.

A.2 Neutron diffraction theory [161]

Let us consider a beam of thermal neutrons, all described the same wavevector **g**, spin state $|\sigma\rangle$ and energy E striking in a target. The target is in general a collection of atoms (crystal, amorphous solid, liquid or gas), called *scattering system* and in a state $|\lambda\rangle$ with a energy E_λ. After the scattering process, the neutron leaves the target with $\mathbf{g'}$, $|\sigma'\rangle$ and *E'* whereas the target is in a new state $|\lambda'\rangle$ with a energy E'_λ. According to the energy conservation law, the equation A.1 must be satisfied.

$$E + E_\lambda = E' + E'_\lambda \tag{A.1}$$

The basis quantity to describe a scattering process is the *partial differential cross section* $\partial^2\sigma/\partial\Omega\partial E$, defined as the number os neutrons scattered per second into a small solid angle $\partial\Omega$ with final energy between *E'* and $E' + \partial E'$ divided by $\Phi\partial\Omega\partial E$, where Φ is the flux of incident neutrons. Using as an approximation the Fermi's rule, that supposes that the change of the incident neutron wave by the scattering centre is almost negligible and can be treated as an approximation, the following expression for the partial differential cross section can be obtained:

$$\left(\frac{\partial^2\sigma}{\partial\Omega\partial E'}\right)_{\lambda,\lambda'}^{\sigma,\sigma'} = \frac{k'}{k}\left(\frac{m_0}{2\pi\hbar^2}\right)^2 \left|\left\langle \sigma'\lambda' \middle| \int V(\mathbf{R}) e^{i\mathbf{GR}} d^3R \middle| \sigma\lambda \right\rangle\right|^2 \delta(E' - E + h\omega) \tag{A.2}$$

where $V(\mathbf{R})$ is the interaction potential between the neutron and the target and $\mathbf{G} = \mathbf{g'} - \mathbf{g}$ and $h\omega = E'_\lambda - E_\lambda$ are the scattering vector (momentum transfer) and energy transfer respectively. The delta function introduces the principle of energy conservation. In an experiment, equation A.2 must be summed over all possible final states of the target for a fixed initial state and be averaged over all the possible initial states. The same must be done for the initial and final spin states of the neutron.

Various types of measurements can be made of the neutrons after they have interacted with the scattering system. We will consider only diffraction experiments. In a good approximation, the energy change of the target can be neglected and the scattering is considered an elastic process where there is no energy exchange and the diffracted neutrons have the same energy than the incident neutrons ($h\omega = 0$ and $k = k'$). We won't take into account the polarization of the neutrons, just the number of neutrons scattered in a given direction. In diffraction experiments, the relevant quantity is the *differential cross-section* $\partial\sigma/\partial\Omega$ defined as the number of neutrons scattered per second in a small solid angle $\partial\Omega$ divided by $\Phi\partial\Omega$:

$$\frac{\partial\sigma}{\partial\Omega} = \int \left(\frac{\partial^2\sigma}{\partial\Omega\partial E'}\right) dE' = \left(\frac{m_0}{2\pi\hbar^2}\right)^2 \left| \left\langle \sigma'\lambda' \middle| \int V(\mathbf{R}) e^{i\mathbf{GR}} d^3R \middle| \sigma\lambda \right\rangle \right|^2 = |f(\Omega)|^2 \tag{A.3}$$

As our samples are able to exhibit magnetic ordering, neutrons will interact no only with the nuclei, but also with the atomic magnetic moments, so we will have a nuclear diffraction component and a magnetic diffraction contribution.

A.2.1 Nuclear diffraction

If we ignore the spin of the neutron (the state is specified entirely by its momentum), we can obtain an expression for the nuclear scattering. Neutrons interact with the nuclei of the atoms via the strong nuclear force. This kind of interaction is very strong but its range is much shorter than the neutron wavelength. To describe the interaction, we use the Fermi pseudo-potential:

$$V_j(r_j) = \frac{2\pi\hbar^2}{m} b_j \delta(r_j) \tag{A.4}$$

where b_j is the scattering length for the j-nucleus, and r_j is the distance between the j^{th} nucleus and the neutron. The scattering length gives the strength of the interaction potential between the neutron and the nucleus in the system; it is a complex number that depends on the isotope, the nuclear spin and the neutron energy. The total potential which describes the interaction between the scattering system and the neutron is the sum of the potential for each j-nucleus and the neutron. Developing the expression of the differential cross section (equation A.3) we can obtain:

$$\frac{\partial\sigma}{\partial\Omega} = |f(\Omega)|^2 = \sum_{i,j} b_j^* b_i e^{i\mathbf{G}(\mathbf{r_i}-\mathbf{R_j})} \tag{A.5}$$

As isotopes have different b and it depends on the orientation of the nuclear spin which is usually arbitrary, the scattering length varies from one nucleus to another of the same element. This property causes the existence of coherent and incoherent scattering, where the coherent scattering depends on the correlation between the positions of the same nucleus at different times and the correlation between the positions of different nuclei at different times, giving interference effects. The incoherent scattering depends only on the correlation between the positions of the same nucleus at different times and does not give interference effects. In our experiments, we are interested in the coherent scattering, which will produce intensity peaks called Bragg peaks and whose whose intensity is proportional to:

$$\left(\frac{\partial\sigma}{\partial\Omega}\right)_{coh} = N\frac{(2\pi)^2}{v_0}\sum_{\mathbf{q}} \delta(\mathbf{G}-\mathbf{q})|F_N(\mathbf{q})|^2 \tag{A.6}$$

where $\mathbf{q}$ represents a reciprocal lattice vector, v_0 is the unit cell volume and $F_N(\mathbf{G})$ is the nuclear structure factor:

$$F_N(\mathbf{q}) = \sum_d \bar{b}_d e^{-i\mathbf{G}\cdot\mathbf{r_d}} e^{-W} \tag{A.7}$$

In the previous equation, $\bar{b}_d$ is the average coherent scattering length (we are taking into account only the coherent scattering), the summation runs over the atoms in the unit cell and the exponential e^{-W} is the Debye-Waller factor, which takes into account that the atomic positions are not fixed, the thermal vibrations of the atoms around their equilibrium positions leads to a reduction of the peak intensity. According to equation A.6, the diffraction condition for a Bragg peak is $\mathbf{q} = \mathbf{G} = \mathbf{g'} - \mathbf{g}$, that is, when a reciprocal lattice vector coincides with the scattering vector. This condition is the same as Bragg's law for X-ray scattering and can be expressed in the more usual form of Bragg's law:

$$n\lambda = 2d_{hkl}\sin\theta \tag{A.8}$$

where n is an integer, 2θ is the angle between the incident and the diffracted neutron beam and d_{hkl} is the distance between the (hkl) planes of the crystal.

A.2.2 Magnetic diffraction

This interaction is due to the coupling between the neutron spin σ and the magnetic field $\mathbf{H}$ generated by the unpaired electrons of the target atoms. The interaction potential of this coupling can be written as:

$$V(\mathbf{r}) = g_n \mu_n \sigma \cdot \mathbf{H} \tag{A.9}$$

where g_n is the gyromagnetic ratio of the neutron and μ_n the nuclear Bohr magneton. If we considerer only the magnetic contribution to the neutron diffraction, the expression equivalents to A.6 and A.7 are:

$$\left(\frac{\partial\sigma}{\partial\Omega}\right) = N\frac{(2\pi)^2}{\upsilon_0}\sum_{\mathbf{G}}\sum_{\mathbf{k}}\delta(\mathbf{q}-\mathbf{k}+\mathbf{g})\left|\left\langle\sigma\left|\sigma\cdot\mathbf{F}_{M_\perp}(\mathbf{G})\right|\sigma'\right\rangle\right|^2 \tag{A.10}$$

$$\mathbf{F}_M(\mathbf{q}) = \sum_d \mathbf{f_d}(\mathbf{G})e^{i\mathbf{q}\cdot\mathbf{r_d}}e^{-W} \tag{A.11}$$

where $\mathbf{k}$ is the propagation vector described in section A.5, $\mathbf{F}_{M_\perp}$ is the magnetic structure factor perpendicular to the scattering vector and $\mathbf{f}_i(\mathbf{G})$ is the magnetic form factor. Magnetic scattering peaks will appear in the case $\mathbf{G} = \mathbf{g} - \mathbf{g}' = \mathbf{k} \pm \mathbf{q}$; when $\mathbf{k}$ is zero, the magnetic cell and the nuclear cells coincide, and the magnetic peaks overleaps with the nuclear ones (in the case the nuclear appears, as in some cases some nuclear reflections can be systematically absent, so the magnetic peak would appear there, at the place where the nuclear peak should be). If the propagation vector is different from zero, each nuclear Bragg peak at $\mathbf{q}$ will be flanked by magnetic satellites coupled in pairs. The magnetic form factor, which is the Fourier transform (FT) of the magnetic interacting potential, decreases as $\mathbf{q}$ increases, as can be seen for the case of Cr^{+3} ion in figure A.1, so the magnetic contribution to the intensity will be more relevant at small angles.

A.2.3 Nuclear and magnetic diffraction

In the experimental conditions specified previously, the diffracted intensity is proportional the sum of the square of the nuclear structure factor and the square of the magnetic structure factor:

$$I(\mathbf{G}) \propto |F_N(\mathbf{G})\delta(\mathbf{q}-\mathbf{G})|^2 + |\mathbf{F}_{M_\perp}(\mathbf{G})\delta(\mathbf{q}-\mathbf{k}+\mathbf{G})|^2 \tag{A.12}$$

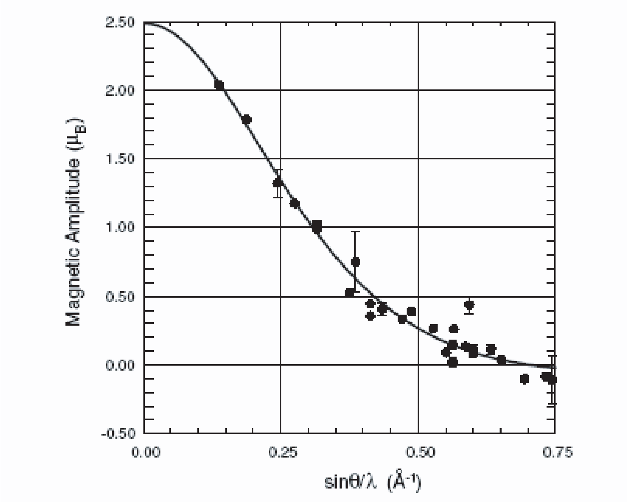

Figure A.1: The magnetic scattering per Cr^{3+} ion corresponding to the magnetic structure factor measured for the (h 0 l) reflections of Cr_2O_3 plotted versus $sin(\theta/\lambda)$ [162]. Unlike the independence of the nuclear structure factor on $sin(\theta/\lambda)$, the magnetic structure factor shows a strong dependence. The full curve is the Cr^{3+} free-ion form factor calculated from the radial wavefunctions given by [163].

The nuclear factor (b) does not depend on $\mathbf{q}$ (or θ), in contrast with the magnetic structure factor. This is due to the fact that the form factor is the FT of the interacting potential. For the nuclear interaction, as nuclei are well localized, the interacting potential is dependent on a delta function, whose FT is a constant function. However, for the magnetic interaction, the interacting potential is a probability distribution because of the spreading of the nuclear magnetic dipolar moment, and its FT will be θ dependent.

A.2.4 Intensity corrections

In neutron diffraction experiments, the intensity is proportional to the square of the modulus of the structure factor (nuclear and magnetic) but some corrections needs to be taken to write an exactly the relationship between them. For the two single-crystal diffraction methods that we have use, the total integrated intensity of one reflection is related to the structure amplitude by:

$$I_{hkl} = \frac{\lambda^3 V/V_c^2}{1/\overline{\omega}} LATE|F(K|^2 \tag{A.13}$$

for a rotating single crystal in a monochromatic beam, and

$$I_{hkl} = \frac{\lambda^3 V/V_c^2}{1/\overline{\omega}} ATE|F(K|^2 \tag{A.14}$$

for a fixed single crystal in a polychromatic beam (Laue technique); where V is the crystal volume, V_c is the unit-cell volume, $\bar{\omega}$ is the angular scanning velocity, L the Lorentz factor which is related to the time-of-reflection opportunity, A the absorbtion factor, T the correction for inelastic phonon or thermal-diffuse scattering and E the correction for extinction and multiple diffraction. In an ideal experiment, corrections due to thermal diffuse scattering, absorbtion and extinction would not be necessary, but few experiments are ideal.

Lorentz factor.

The lorentz factor is a correction introduced to take into account the geometry of the experimental method, because different Bragg peaks are measured with different sample speeds. For a constant velocity of rotation of the crystal, different reciprocal-lattice points pass through the Ewald sphere at different speeds, and therefore have different time of reflection opportunity. For four-circle diffractometers, the correction can be expressed as [164]:

$$L = \frac{1}{\sin(2\theta)} \tag{A.15}$$

Absorbtion factor.

For neutrons at the wavelengths that we use, the absorption coefficient μ is the sum of two terms: true absorption due to nuclear capture processes, and apparent absorption due to scattering, both coherent and incoherent. For single-crystal experiments, we treat the absorption due to coherent scattering separately as extinction and multiple diffraction and we include typically in the absorbtion correction the effects of nuclear capture processes σ_{abs} and incoherent scattering σ_{inc}.

The nuclear capture depends on λ while the incoherent apparent absorption is independent of wavelength for most elements. A notable exception is hydrogen, for which the dependence of σ_{inc} on wavelength is roughly linear [165]:

$$\sigma_{inc} = 19.2(5)\lambda + 20.6(9) \tag{A.16}$$

and is usually the dominant contribution for hydrogenous materials. The values of the σ_{abs} and σ_{inc} cross-sections required to calculate the absorbtion correction write as

$$\sigma = \sigma_{abs}\lambda/1.798 + \sigma_{inc} \tag{A.17}$$

are listed in several tables [166]. Using this values, we can calculate the absorbtion coefficient taking into account all the atoms present:

$$\mu = \frac{S_{Total}}{V} = \frac{\sum_i Z \times N_i[\sigma_{abs}(i)\frac{\lambda}{1.798} + \sigma_{in}(i)]}{V} \tag{A.18}$$

where V is the cell volume, N_i is the number of atoms of the i-th element in the formula, Z is the number of formula units in the unit cell. For diffraction from a crystal bathed entirely in the beam, the absorbtion for the whole crystal is obtained as:

$$I = I_0 \frac{1}{V} \int_V e^{-\mu t}\, dV = A I_0 \tag{A.19}$$

Where I_0 is the incident intensity and the integral is over each infinitesimile volume element with t being the total path length of the incident and diffracted beams within the crystal for that volume element. Analytical integration is feasible for crystals of very regular shape such as spheres and cylinders. For faceted crystals numerical integration is the usual technique [167]. These equations and methods also apply to the Laue technique, but it is necessary to take into account that the beam is polychromatic.

Extinction factor.

If the thickness of the sample is small, it can be assumed that the same incident intensity will arrive to all the atoms and the diffracted intensity will be proportional to the thickness of the sample. However, the incident neutron beam loses intensity as it advances through the sample due to the intensity already scattered. This effect is called extinction, and can be classified in primary or secondary extinction depending on the size and orientation of the domains in the sample. Correction for extinction is made usually following the formulae of Becker and Coppens [168], including the crystal form via the mean absorption-weighted path length which is calculated in a similar manner to the transmission factor.

$$T = \frac{1}{VA} \int_V t e^{-\mu t}\, dV \tag{A.20}$$

Thermal diffuse factor.

The elastic Bragg reflections are observed superimposed on incoherent scattering, which is essentially removed by the background substraction, and inelastic phonon scattering, also called thermal diffuse scattering (TDS), whose peaks are the same positions as the Bragg reflections. For most structural studies, TDS is ignored since omitting it only affects to the thermal displacement parameters in a first order of approximation.

A.2.5 Ewald sphere

The Ewald's sphere is a geometric construction used in electron, neutron, and X-ray crystallography which demonstrates the relationship between the wavevector of the incident ($\mathbf{g}$) and diffracted ($\mathbf{g'}$) beams, the diffraction angle for a given reflection and the reciprocal lattice of the crystal ($\mathbf{q}$) [169]. It can

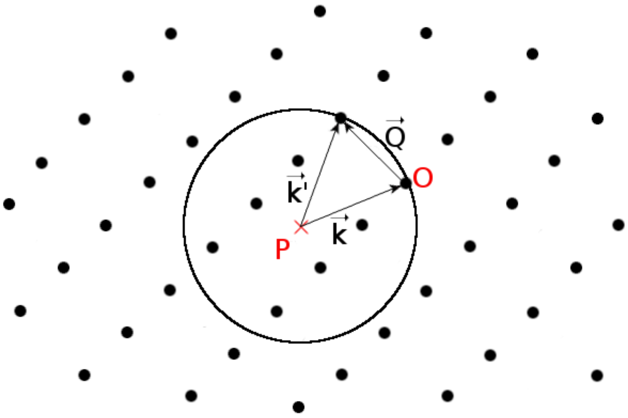

Figure A.2: Ewald's construction in reciprocal space. **g** is the incident wave-vector, **g**′ the diffracted wave-vector in elastic scattering and **q** a reciprocal lattice vector

be used for express geometrically the condition for a Bragg reflection from a crystal.

The construction can be seen in figure A.2, where the reciprocal lattice has been drawn and one node has been picked as the origin of the reciprocal space O. The wavevector ($\mathbf{g}$) of the incident wave, in direction and magnitude is represented with its end at O and starting at P. The Ewald sphere, or sphere of reflection, is a sphere of radius $1/\lambda$ passing through the origin O of the reciprocal lattice and with its center in P. The diffracted beam's wavevector having its origin in P must end on the sphere, to ensure $|\mathbf{g}| = |\mathbf{g}'|$, and also must satisfy $\mathbf{g} - \mathbf{g}' = \mathbf{q}$ in order to produce a Bragg peak. Thus, there will be a diffracted beam if the Ewald sphere goes through the origin and another reciprocal-lattice node.

When the wavelength is large, there are seldom more than two nodes, O and H, of the reciprocal lattice simultaneously on the Ewald sphere. When there are three or more, we speak of multiple diffraction, multiple scattering or n-beam diffraction. This situation becomes increasingly frequent as the wavelength decreases. When the wavelength changes, the radius of the Ewald sphere changes. If the incident beam is a white beam (as the experiments we have performed using the Laue method), with a wavelength range $\lambda_{min} < \lambda < \lambda_{max}$, there will be a nest of Ewald spheres of radA $\frac{1}{\lambda_{min}} > r > \frac{1}{\lambda_{max}}$.

In order to explore the reciprocal space, the Ewald sphere is rotated around the origin O (in practice one rotates the crystal); as the reciprocal lattice nodes pass through the Ewald sphere, the corresponding reflections are successively excited.

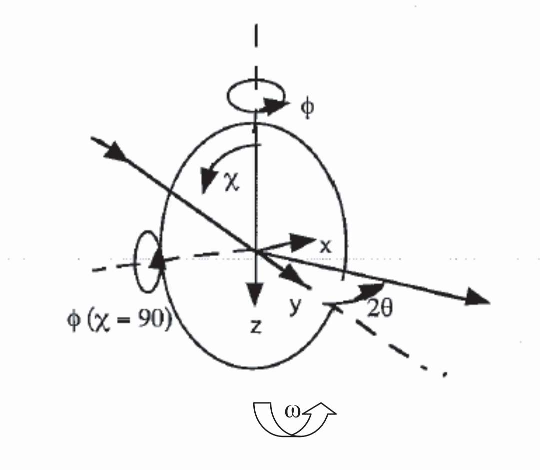

Figure A.3: The Busing and Levy Eulerian angles.

A.3 Four-Circle Geometry on a monochromatic beam

The Laue method is excellent for measuring large number of Bragg reflections, but is not very efficient at measuring a small selection of reflections to follow a phase transition, for example, and does not allow determination of the absolute values of the linear cell parameters. If a large single-crystal is available, we can use monochromatic diffraction for the latter two tasks. We now describe the monochromatic diffraction technique and the instrument that we used following this technique.

A.3.1 Four-Circle geometry

A characteristic of the four-circle diffractometers is the use of Eulerian cradles for orientating the sample crystals, with the detector moving in a horizontal plane. Using a diffractometer in a four-circle geometry, the sample can be moved in the three Eulerian angles ϕ, ω and χ, hence it can describe three circles; the four circle is given by the movement of the detector around the $\gamma = 2\theta$ angle. In the figure A.3, a scheme of the movements appears.

The instrument axis is vertical, and perpendicular to that we find the horizontal equatorial plane, in which the incident beam lies. The incident beam impinges on the sample which is situated at the centre of the goniometer. The detector rotates in the horizontal plane making a rotation of 2θ with the incident-beam direction. The angle 2θ for a particular reflection is determined by Bragg's law. The χ axis is positioned to make an angle ω with the incident beam. The ϕ angle is supported by the χ ring which enables ϕ to be set at an angle χ from the vertical axis (we are using the Busing and Levy notation for the angles χ and ϕ [170]). The sample is attached to the ϕ shaft so that it can be turned about this axis by an angle ϕ.

Rotating the diffractometer and the detector we should get at least two reflections of the sample and then with these reflections we can obtain the product of matrices *UB*, which links the reflections *hkl* with the positions of the diffractometer (the different angles 2θ, ω, ϕ, χ). U is called the orientation matrix, which depends on the way the crystal has been mounted, and it relates a vector expressed in the crystal cartesian system, to the vector in terms of the laboratory system axes when all the instrument angles are set to 0; B is the matrix which relates a vector expressed in terms of the reciprocal lattice vectors to the description in the crystal cartesian axes, so their product relates a vector expresses in terms of the reciprocal lattice vectors to its coordinates in the laboratory system axes.

If we call $\mathbf{v_1}$ the description of a vector in terms of the laboratory system when all instrument angles are set to zero, and we are in the diffraction condition then:

$$\mathbf{v_1} = U \cdot B \cdot \mathbf{h} \tag{A.21}$$

where $\mathbf{h}$ is the column vector in the reciprocal lattice system containing the Miller indices hkl, and consequently

$$|\mathbf{v_1}| = |(v_{11}, v_{12}, v_{13})| = q \tag{A.22}$$

Thus the Bragg condition can be written as $sin\theta{=}\lambda q/2$. Diffraction from the planes with indices hkl can occur when the tip of $\mathbf{h}$ lies on any point of the circle of observation, which is the intersection of the sphere with radius q with the Ewald sphere of radius $1/\lambda$. Hence the instrument angles (ϕ, χ ,ω) can be adjusted so that the diffracted beam occurs anywhere in the cone with semi-angle 2θ about the incident beam.

These diffractometers can be used to find:

- Average atomic positions
- Local atomic distributions
- Magnetic structures and magnetic moment distributions.

Structural data of this kind are required for a large number of systems, ranging from organic molecules to high temperature superconductors. Often, these

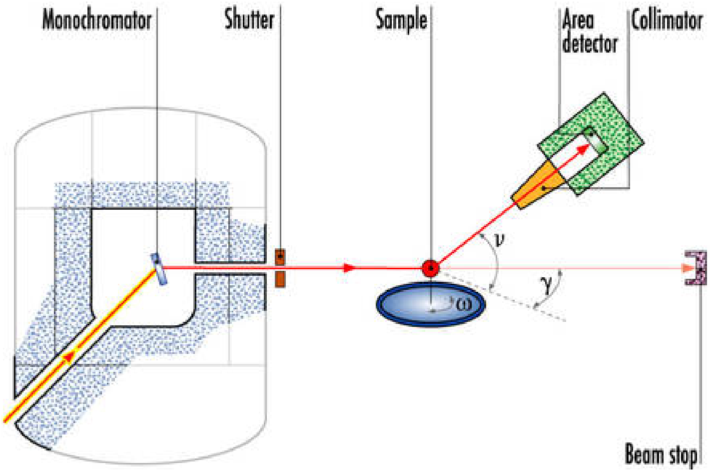

Figure A.4: Schematic drawing of the neutron diffractometer D15

studies are made as a function of temperature, pressure and magnetic fields which may lead to important modifications of the crystal structure.

A.3.2 D15

D15 is a single-crystal thermal neutron diffractometer placed at the ILL that was dismantled at the end of the 2009. The instrument could be operated in either four-circle or normal-beam mode and allowed to choose between a monodimensional or a bidimensional detector. Three wavelengths were available: 0.85Å, 1.17Å, and 1.54Å with corresponding flux at the sample of $1.8{\cdot}10^6$, $7.8{\cdot}10^6$, and $3.0{\cdot}10^6 n/(s \cdot cm^2)$ respectively.

For the normal-beam geometry D15 has its own orange cryostat superconducting magnets that reach 6T and 10T. A low temperature insert can be used in the orange cryostat and the 6T magnet allowing to cool down to 50mK. Pressure cells (up to 3 GPa), uniaxial stress apparatus, and furnaces from ILL can also be installed. In four circle configuration, several displex are available and temperatures of 1.5K can be set.

D15 is specialized in determination of crystallographic and magnetic structures, but its characteristic make D15 suitable for a wide range of physical problems, also in studies of phase transitions, determinations of magnetic field temperature or pressure temperature phase diagrams, which are the compulsory starting points of any investigation of the magnetic properties of solids.

A schematic drawing of the instrument can be seen in figure A.4

All the experiment carried out during this thesis in D15 didn't need large sample environments so they have been performed using the four circle configuration and the monodimensional ^3He detector, which presents a low background and higher efficiency. The direction of the diffracted beam is described by $\gamma = 2\theta$. The reflections have been measured one at a time by $\omega : 2\theta$ step scans.

A.3.3 Typical experiment

In D15 the user has the possibility to choose the wavelength, the geometrical configuration of the instrument and the environmental apparatus he wish to use. Once everything is settle down, the experiment start by choosing a good crystal, mounting it on a pin and insert it in the instrument. The first step is to center the crystal in the beam, so it is fully impregnated, preventing misaligned with respect to translation by moving ϕ back and forth 180°. Once the crystal is centered it is necessary to orientate it and find the orientation matrix UB. For this, we need to know the unit cell of the compound to simulate a list of reflections in function of the 2θ values for the wavelength chosen. Ideally, crystal faces should be indexed in terms of the unit cell directions in order to facilitate the orientation of the crystal in the beam. Introducing the wavelength and the unit cell dimensions on the control computer, setting $\gamma = 2\theta$ and $\omega = \theta$ for the reflections we want to find and running ϕ scans at fixed χ values, we should find some reflections. As it has been said, some knowledge of the crystal faces and experience will help to find the correct value for χ easily. At least three of four reflections are necessary to calculate a primitive UB; then, it's necessary to center 10 or 20 reflections to improve the UB matrix by least-square matching of the observed reflections centroids against the calculated values. The unit cell is also refined simultaneously (the wavelength is supposed to have refined before the experiment).

Once we have measured some reflections, we can adjust the slits at the neutron source and the counter in order to maximize the reception of the reflections without counting direct beam. Before beginning the data collection, it is important to choose the appropriated scan parameters: number of points per scan, counts per monitor for each point, angle covered... Each experiment has a limited amount of time and it should be optimized, collecting the reflections necessary to solve the problem of interest with the best statistic. During the experiment, it is advisable to measure a standard reflection every 50-100 reflections in order to monitor any possible deterioration in crystal orientation, crystal quality, detector stability or any other aspect of the experiment. As a standard reflection, it is better to choose a strong reflection, because it can be collected in a shorter time.

In the experiments we have performed, a number of reflections at a temperature above the transition have been measured in order to determine the nuclear structure. After cooling down, the reciprocal space has been explored performing q-scans in a search for satellite magnetic peaks that will indicate a propagation vector different from zero. Once the propagation vector has been determined, reflections measured at low angle without considering the extinction rules of the paramagnetic space group will help with the magnetic structure determination.

Several reflections with a magnetic contribution have been followed as a function of the temperature to observe the magnetic transition.

The orientation matrix has been built with the help of the programm RACER, that can be used as well to integrate single-crystal reflections using area multidetectors [171], the reflections have been integrated with the program COLLD15 [93] and corrected from absorption with DATAP [94].

A.4 Laue diffraction theory

The Laue method was born in the nineteenth century, as a consequence of important discussions amongst Laue, Ewald, Sommerfield, Wien, Bragg etc. The starting point was the doctoral thesis of Ewald, who proposed a resonator model of crystals where resonators were placed at lattice points. To validate his model, a wavelength similar to the spacing between the resonators should be employed, and Laue suggested that X-rays might suit. Friedrich and Paul Knipping, using a beam of X-rays through a copper sulfate crystal, record the first Laue image on a photographic plate. Laue developed a law that connects the scattering angles and the size and orientation of the unit-cell spacings in the crystal, for which he was awarded the Nobel Prize in Physics in 1914.

The Laue method was the first of many methods developed for the study of crystals by x-ray diffraction. Many of the early determinations of cell dimensions, crystals symmetry and studies of crystal structures were done by Laue method. However, it present several limitations arising for the quasi white beam that is used: it was difficult to know exactly the wavelengths and intensity of the part of the incident radiation that caused the observed Laue spot. For this reason, the Laue method was pushed into the background and was reduced to an aid in determining crystal orientation and crystal perfection as some more powerful methods were developed. Recently, it has been reborn thanks to the use of image plate detectors and advanced computing algorithms. It present a great advantage for crystals of small size, because, due to the fact that all orders of reflection from a plane *(hkl)* cooperate to produce a single

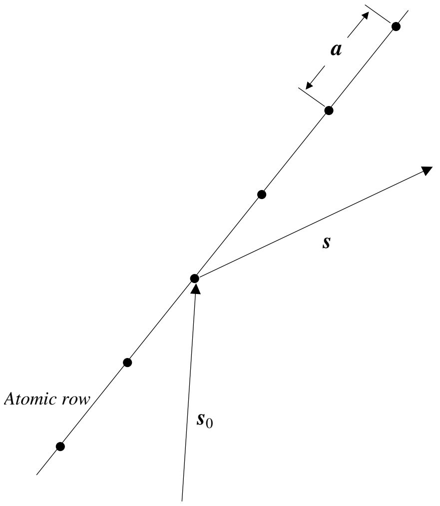

Figure A.5: The Laue model of diffraction by a row of atoms

spot, it reduced the exposure time considerably.

A.4.1 The conventional Laue method [172]

For explaining the existence of the spots in the patterns, Laue realized that he needed to formulate the diffraction equation three times, one for each periodicity of the space lattice. The Laue equations in vectorial form can be seen in equation A.23, where $\mathbf{a}_1$, $\mathbf{a}_2$, and $\mathbf{a}_3$ are the monoatomic crystal translations, and h_1 ,h_2 and h_3 are the Laue numbers that give the orders of the interference and $\mathbf{s}_0$ and $\mathbf{s}$ are the directions of the incident beam and the diffracted beam respectively. Each of these equations represents the diffraction produced by a single row of atoms with an interatomic interval such as $\mathbf{a_1}$ as it is shown in figure A.5

$$\mathbf{a}_1(\mathbf{s}-\mathbf{s}_0)=h_1\lambda \qquad \mathbf{a}_2(\mathbf{s}-\mathbf{s}_0)=h_2\lambda \qquad \mathbf{a}_3(\mathbf{s}-\mathbf{s}_0)=h_3\lambda \tag{A.23}$$

Each spot is explained as a partial reflection of the incident beam in sets of parallel planes on which atoms are arranged in the crystal.

Basically, in a Laue experiment, a pencil of radiation limited by a collimator reaches the crystal and the diffracted radiation is register on a photographic film, or nowadays on image plates. Usually, the crystal remains in a fixed orientation.

General geometry

One of the characteristic of the Laue photographs (which introduces serious limitations) is that many of the Laue spots are the superposed records of several orders of reflections. This can be easily seen if we have a look to the Bragg's equation A.24, where d_{hkl} is the distance between planes (hkl) whose integers h, k and l contain no common factor, and n is the order of the reflections from this plane. It can be expressed saying that θ is invariant for equal values of λ/n, so the wavelength range can cover several orders of reflections for any stack of planes *(hkl)*. This fact implies a limitation, but doesn't make Laue technique useless because wavelengths near the short-wavelength limit cannot be accompanied by submultiple wavelengths, which makes Laue spots produced by short wavelength contain only first-order contributions.

$$n\lambda = 2d_{hkl}sin\theta \tag{A.24}$$

A small value of lambda implies a small value of θ, so the single-component Laue spots are near the center of the Laue photograph.

On Laue photographs, the spots appear localized along ellipses running through the center of the photograph. The spots occurring at the same ellipse are reflections of planes that lie in the same zone, that is, that contain a common rational crystallographic direction. Every rational crystal plane contains many rational axes, so every Laue spot is located at the intersection of several conic sections.

When a crystal is oriented so the beam is along a symmetry element of the Friedel class of the crystal, the Laue pattern displays the projection of the symmetry along this direction.

Interpretation of the reflections

Each spot on a Laue photograph correspond to a crystal plane described by indices *(hkl)*. In order to identify which plane correspond to each spot, the plane is represented in the gnomonic projection. The gnomonic projection is widely used in crystallography and gives the projection of a point contained in a reference sphere, on a plane normal to the line of sight, when the eye is placed at the center of the sphere. This projection has the advantage that there is a close relation between it and the reciprocal lattice.

The transformation from the Laue location of a Laue spot to the gnomonic projection of the plane that produces can be seen derived in figure A.6. If the distance from the crystal to the detection plane (placed normal to the beam) is

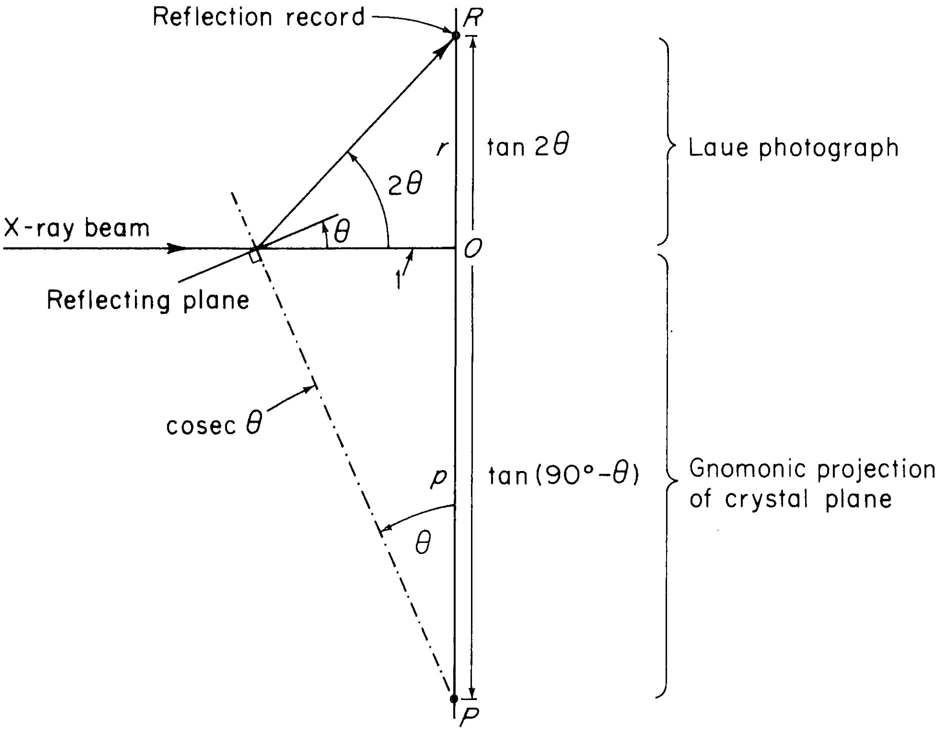

Figure A.6: Relation of the position of a Laue spot to the corresponding gnomonic projection point,where θ represents the direction of the reflection plane respect to the incident beam direction, r is the distance between the transmitted direct beam and the diffracted beam, and p is the point where the normal from the reflecting plane reaches the vertical line.

taken as the unity, the distance r between the direct beam and the diffracted beam can be written as in equation A.25

$$r = tan(2\theta) \Longrightarrow \theta = tan^{-1}r \tag{A.25}$$

The normal to the reflecting plane reaches the detection plane at a distance p from the transmitted direct beam given by equation A.26. With this expression we can connect the locations of each spot in a Laue pattern with the gnomonic projection of the plane whose reflections produces it.

$$p = tan(90 - \theta) = cot(\theta) = (cot\frac{1}{2}(tan^{-1}(r))) \tag{A.26}$$

In a more general form, if the distance between the detection plane and the crystal is M instead of unity then the relation between r and p is given by equation A.27.

$$p = (cot\frac{1}{2}(tan^{-1}(r/M))) \tag{A.27}$$

Once the spots on the Laue pattern are linked with the gnomonic projection, they can be related to the reciprocal lattice, using the representation properties.

In the reciprocal lattice, the points corresponding to the various orders of reflections of a stack of planes constitute a row of points placed in a line perpendicular to the stack of planes and equally equally spaced ($1/d_{hkl}$). In the gnomonic projection, a point representing a plane lies on the normal to the plane, and its position depends on θ (see figure A.6). Therefore a stack of planes hkl, $2h$ $2k$ $2l$, $3h$ $3k$ $3l$......nh nk nl are represented by the same point in the gnomonic projection. In other words, the gnomonic projection does not have record of the order of a reflection and may correspond to several orders at once, exactly as it happens with a spot in a Laue pattern.

If the orientation of the crystal with respect to the beam is arbitrary, the interpretation of the gnomonic projection is not straightforward. However, is a rational axis is parallel to the beam , and hence, perpendicular to the image to the projection plane, the relation is very simple. For example, if the crystal axis [0 0 1] is oriented parallel to the beam, and then the reciprocal-lattice planes $(00l)^*$ are normal to the beam, in the projection plane a net whose points are the reflections corresponding to the planes $(hkl)^*$ appears in the projection plane. The points on the nodes of the net in the same line are equally separated and their separation depends on a/c in one direction, and b/c in the other direction.

The observed gnomonic projection can of course be readily transformed via modern computers to put any observed symmetry axis along the beam.

Polychromatic radiation

The wavelength range should be such that the range is large compared to the beam divergence and the crystal mosaic. Synchrotrons for instance, have a $\triangle\lambda/\lambda$ of approximately 1% while in thermal-neutron Laue diffraction $\triangle\lambda/\lambda \approx 100\%$. The beam should have continuous λ over a wide range, because a fixed crystal requires a continuous variation of either λ or 1/d for diffraction. Using the Ewald sphere construction, we can see all the reflections that lie in a circumference of radius $k_i = 2\pi/\lambda$, having a wide range of λ allow us access to a major number of reflections. There are an upper and lower limit to the reflections we can observed, delimited by the spheres whose radius are $1/\lambda_{min}$ and $1/\lambda_{max}$. The spheres touch each other at the origin of the reciprocal lattice,

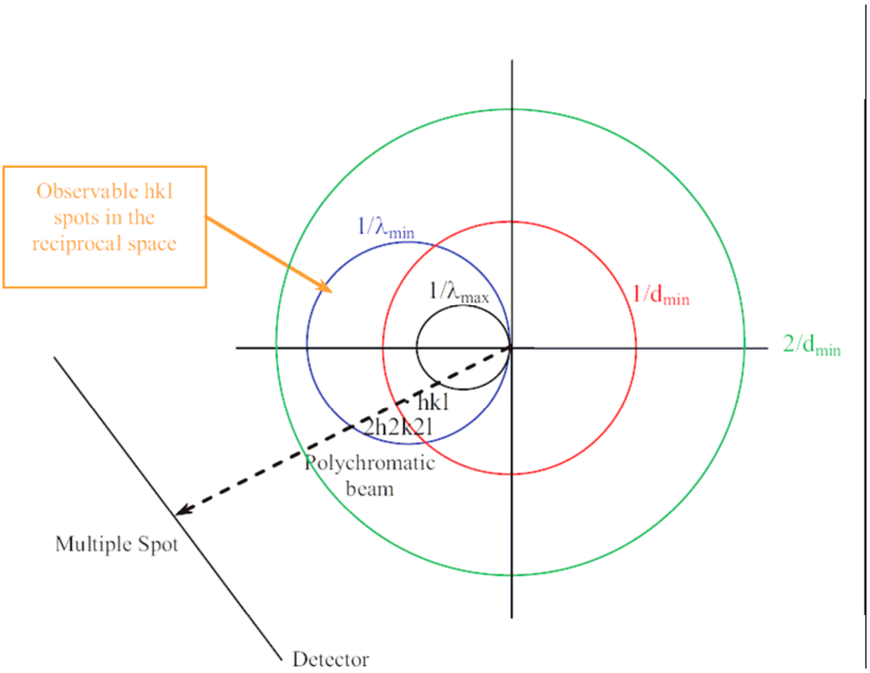

Figure A.7: Ewald sphere construction for the Laue technique. This construction shows that the reciprocal-lattice points whose reflections can be recorded are those lying between the Ewald spheres of radious $1/\lambda_{max}$ and $1/\lambda_{min}$, and these spheres touch each other at the origin of the reciprocal lattice. The circle of radius $1/d_{min}$ corresponds to the limit of observability for a particular sample.

as shown in figure A.7. As it has been said before, several order of reflection form a plane produce the same Laue spot; when the crystal is illuminated with a polychromatic beam many orders of each Bragg reflection can simultaneously appear in the Laue pattern, overlapping occurs exactly at the same angle, i.e. Bragg's law is simultaneously satisfied by the reflections (d,λ), (d/2,λ/2), (d/3,λ/3), etc. all multiple reflections are second-order reflections.

Determination of the reciprocal lattice

In order to determine the reciprocal lattice, several hints can be very helpful. Certain regions of a Laue photograph and its correspondent gnomonic projections have spots with likely only firs-order component. This can happen by two ways.

As you can see in the Ewald construction in figure A.8 the reciprocal-lattice points having simple indices (•) are on rays radiating from the origin, which have short intervals between points. The reflections due to these reciprocal-

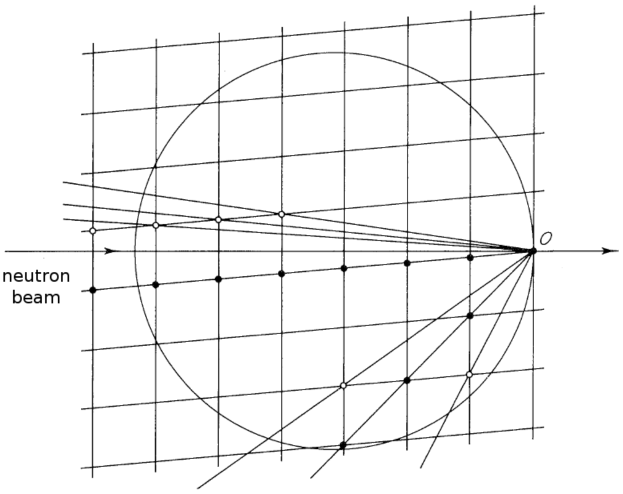

Figure A.8: Geometry used in explaining the blank areas in a Laue photograph that occur in the immediate vicinity of very intense spots with simple indices. (•) are reciprocal lattice points having simple indices; (○) are reciprocal lattice points having complicated indices

lattice points within the limiting sphere contribute to the same Laue spot, so usually it is very intense. Due to its simple indices such a spot is at the intersection of several zone ellipses also having simple indices, and the ellipses are usually prominent too. The neighboring spot positions on the ellipses are locations of missing or very weak spots. This is due to the fact that these neighboring points are on rays (○) with such a large interval between points that none, or only one point per ray, falls within the sphere of minimum wavelength. These points can therefore give rise to spots representing first-order reflections only. Spots of first-order component can be recorded also by purely geometrical reasons. As can be seen in figure A.9 there is a region on the outer edge on the gnomonic projection between the radA r_1 and r_2 where the spots can only come from lattice points in the outer edge of the first level. These points are first-order reflections. It is easy derive the values for the different radA. As it has said before, if a crystallographic axis is parallel to the beam, in the projection plane there is a net whose dimensions are related to the reciprocal lattice cell dimensions. Focusing in the reflections of the first level, it possible to identify the net and index all the reflections.

Symmetry determination

Space group symmetry is normally approached through a study of absent reflections. Using the Laue method, the determination os diffraction symmetry

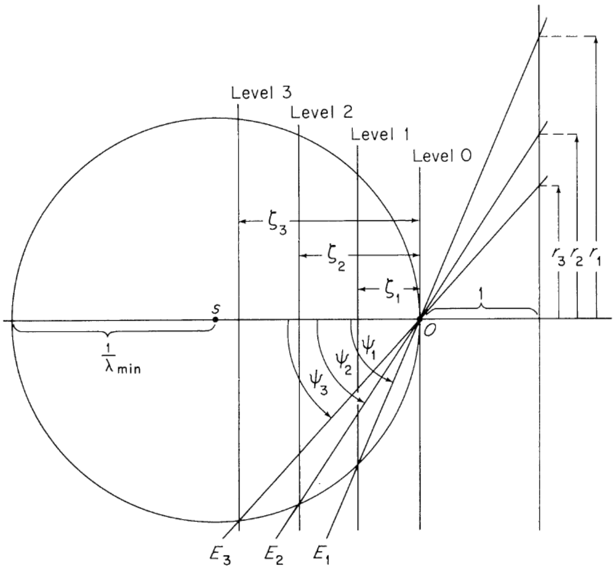

Figure A.9: Regions of Laue spots with limited orders of reflection

is limited to the determination of the Friedel symmetry and the lattice type.

The dimensions of the unit cell can not be obtain accurately from Laue method. This is due to the dependence of a linear dimension to d in Bragg equation (see equation A.28); which is a function of the λ causing the reflection which is in general unknown. However, the ratio between dimensions of the cell is accurately determinable.

$$\begin{aligned} \lambda = 2dsin(\theta) = \frac{2sin(\theta)}{|\mathbf{t}^*_{hkl}|} \Rightarrow |\mathbf{t}^*_{hkl}| = \frac{2sin(\theta)}{\lambda} \\ \mathbf{t}^*_{hkl} = h\mathbf{a}^* + k\mathbf{b}^* + l\mathbf{c}^* \end{aligned} \tag{A.28}$$

As $\mathbf{t}^*_{hkl}$ is not well determined, $\mathbf{a}^*$, $\mathbf{b}^*$ and $\mathbf{c}^*$ (or $\mathbf{a}$, $\mathbf{b}$, $\mathbf{c}$) cannot be either. We can however determine unit-cell angles and the ratios between the unit-cell lengths.

One of the important features of the Laue method, is that patterns show the symmetry along the direction of the incident beam. This advantage allows to recognize elements of symmetry by inspecting the pattern. To determine the Friedel point group patterns along different directions must be taken.

In Laue method, not all the 32 crystallographic point groups can be determined. This is because reflections hkl and $\bar{h}\bar{k}\bar{l}$ are identical in magnitude although they differ in phase. As only he magnitude of a reflection can be

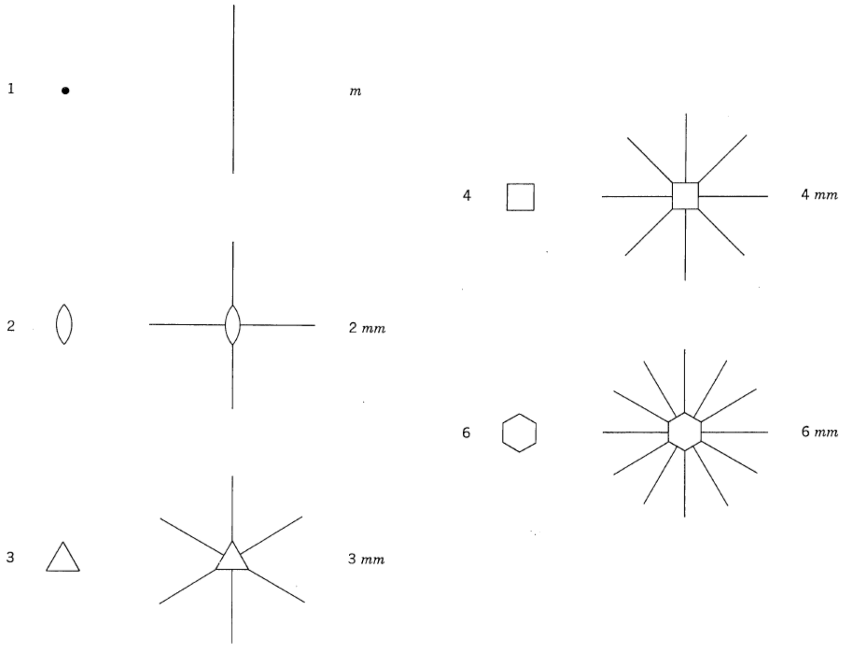

Figure A.10: The 10 crystallographic point groups in a plane

measured, and both reflections contribute to the same spot, the diffraction effect is as had a center of symmetry. We can just distinguish the crystal symmetries of the 11 centrosymmetrical crystallographic point groups, called also Friedel's class. The Friedel law requires the intensity function to have a center of symmetry at the origin of the reciprocal lattice, and only a Laue photograph can not show the centrosymmetry of the whole diffraction space. A Laue photograph give information about the Friedel symmetry of the direction of the beam; the only finite symmetries that can be displayed in two dimensions can be seen in figure A.10, so several projections are needed to obtain the three-dimensional Friedel symmetry. Taking several photographs along appropriate directions allows to determine the symmetry of the crystal. If a cylindrical film with is axis perpendicular to the incident beam is used instead of a flat plane, the amount of directly observable information is reduced, owing to the lower symmetry of the cylinder as compared with the flat plane. however, it presents the advantage that all the information about the crystal is collected at once and on one film. Information is obtained not only for the symmetry along the direction parallel to the beam, but also for that along any other direction of the crystal inside the Ewald sphere that correspond to λ_{min}. To retrieve such information is necessary a proper analysis of the projection. Of course the larger volume of reciprocal space is only of use if the sample scatters to high angle.

About the observable Laue spots and their multiplicity distribution

As it has been said before, the reciprocal space that can be explored is lying between the Ewald spheres of radA $1/\lambda_{max}$ and $1/\lambda_{min}$. The spheres touch each other at the origin of the reciprocal lattice, as shown in figure A.7.

Using a polychromatic beam implies that many orders of each Bragg reflection can simultaneously appear in the Laue pattern, overlapping occurs exactly at the same angle, i.e. Bragg's law is simultaneously satisfied by the reflections (d,λ), (d/2,λ/2), (d/3,λ/3), etc. 50% of all multiple reflections are second-order reflections. If we consider an unrestricted angular acceptance of the detector, 72.8% of all Bragg reflections occur on single rays for the case of an infinite range of incident wavelengths. By choosing appropriate λ_{min} and λ_{max} values, the percentage can be increased to greater than 83% [173]. By reducing the difference between λ_{min} and λ_{max}, the number of single reflections will increase, but in total we will lose reflections as the portion of reciprocal space we can access is lower (a decrease in the wavelength range results proportional to the decrease in the total number of observable spots). The proportion of single reflections also depends on the unit-cell dimensions, on the crystal orientation and also on the sample resolution limit d^*_{max}, with the proportion of single or double rays being generally lower at low resolution than at high resolution.

To treat the energy overlap deconvolution techniques have been developed [174], using the wavelength-normalization curve and Laue spots measured at different wavelengths [175], [176], however this deconvolution has not been applied to our data and we have just consider the single reflections. Another important factor is the spatial overlap between reflections, which occurs when the angular separation of adjacent diffracted beams is very small [177]. The maximum density of spots occurs at $\theta_c = sin^{-1}(\lambda_{min} d^*_{max}/2)$, having the majority of spots in this θ region short λ.

Both effects, that of energy overlap and that of spatial overlap do make the Laue method complex, and for large unit cell sizes the number of spatial overlaps can considerably exceed the number of energy overlaps.

To reduce the spatial overlap, the angular acceptance of the detector can play a very important roll. It is important to have a big angular detector acceptance as the majority of the lost reflections due to the angular acceptance limitations are single reflections.

In principle, by increasing the distance between the crystal and the detector, the proportion of spacial overlaps should be substantially reduced, but of course the installations would be much bigger, the VIVALDI detector for instance would be much more expensive, and this may not even be technically feasible.

Also by decreasing λ_{min} we can reduce the number of spatial overlaps, but then, the total number of observable reciprocal lattice points will be reduced.

We need to take all these factors into account when measuring on a Laue diffractometer.

A.4.2 VIVALDI

The Laue technique has passed through ups and downs throughout history, but nowadays its applicability at synchrotron sources to static and also to time-resolved structure determination is well established. The employment of this technique with neutrons in chemical crystallography and molecular materials is however still new. Further development of Laue instrumentation to use detectors that can cover almost 2π sr of solid angle, has enabled the study of structures on a shorter time scale, larger unit cells (organic compounds usually have large cell parameters), charge-density analysis, hydrogen bonding studies etc. The use of small crystals is feasible, with a typical volume of $1mm^3$. As it is a fast technique and it can cover a big solid angle it is suited to survey reciprocal space to help to study for example of incommensurate structures. We will not consider here the technique of time-of-flight Laue diffraction, as used on spallation neutron sources, although it does share some of the difficulties of the technique, such as normalisation to a common wavelength. Time-of-flight Laue diffraction does however allow resolution of the different orders of reflections.

At the ILL, four neutron diffractometers have been created specially for the Laue technique. First, it was LADI [178], which has been improved several times and is used on a cold neutron beam for protein crystallography, extending the size and complexity of systems that can be studied ~ 150 on cell edge while lowering the sample volumes required $\sim 0.1 - 0.2mm^3$. Then VIVALDI [179], which is placed at the end of the thermal-neutron guide H22, which has been used for the Laue diffraction experiments performed in this theses. In the last, ORIENT-EXPRESS [180] and CYCLOPS [181] have been implemented. LADI AND VIVALDI use cylindrical detectors, while ORIENT-EXPRESS uses a plane film as a detector and CYCLOPS uses eight films that forms and octagon. The construction of more Laue diffraction instruments, as KOALA on the OPAL reactor at ANSTO in Australia, is an evidence of the nowadays peak of this technique.

VIVALDI stands for Very Intense Vertical-Axis Laue DIffractometer, and is a Laue diffractometer placed at the ILL that has been in operation since late 2001 [179], although many improvements have been performed until reach the actual high efficiency. It is based on a cylindrical image-plate detector (see figure A.11 placed at the end of the thermal-neutron guide H22, that will accept a variety of standard and adapted sample environments for fast single-crystal experiments in physics, chemistry and materials science. The detector consist of neutron-sensitive image plates upon which the diffraction pattern from a stationary crystal is recorded. After each exposure, the stored pattern is read out in phonographic mode by fast rotation detector coupled with translation of a simulating laser and photomultiplier detector along the length of the cylinder. Image plates offer high spatial resolution. good homogeneity, a large and linear dynamical range and no deadtime. VIVALDI's image plates are base on the same storage phosphor ($BaFBr$ doped with $Eu^{2+}ions$) commonly used for X-ray image plates, with Gd_2O_3 added; the Gd nuclei act as neutron scintillators by creating a cascade of X-rays and conversion electrons. A detector like this, is cheap compared to electronic detector and can be constructed to subtend very large angles at the sample. By using the single-crystal Laue technique with a large solid-angle detector and a thermal neutron beam, the two-dimensional projection of a large volume of reciprocal space of small-unit-cell materials can be seen in a single exposure. Complete structural data can thus be obtained in a time shorter by one to two orders of magnitude than for a monochromatic experiment, with only a modest loss in precision. The dramatically shortened data-acquisition time allows structural and magnetic phase transitions, which often result in complex incommensurable structure, to be observed and followed in detail as a function of temperature or pressure.

On VIVALDI, the crystal lies in the axis of the detector and its irradiated by the white beam from a thermal neutron guide. It presents the advantage that its detector cylinder axis is vertical, so it can accept cryostat for 1.5K to 600K which can be combined with standard dilution inserts (down to 50mK)and high-pressure cells up to 49mm in diameter. The sample/cryostat support is a robust high-precision rotation unit, which sits above the detector on a translation platform to allow the positioning of the crystal on the detector axis and to compensate for contration/dilatation of the sample stick as the temperature is varied.

Since its implementation, VIVALDI has proved to be a very multifunctional diffractometer [182] which relevant contribution in a lot of different fields as in localization of hydrogens atoms or precise characterization of water molecules in molecular structures, rapid crystallography though phase transitions, magnetism, high pressure experiments....

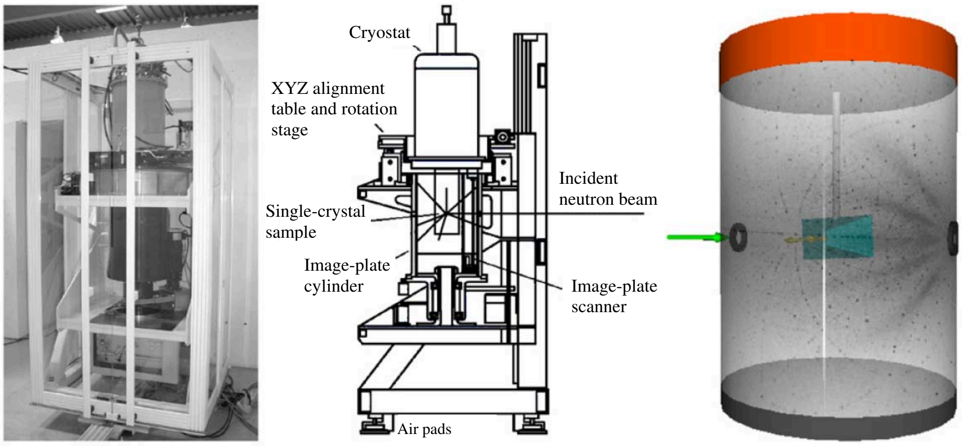

Figure A.11: The neutron Laue diffractometer, VIVALDI. The sample, located in the middle of the image-plate detector, is bathed in the un-monochromatic incident thermal-neutron beam. At the left, there is a general view; a schematic of the diffractometer showing the main components can be seen in the middle; and in the left, a schematic of the detector with typical Laue pattern superimposed can be seen. The crystal size is exaggerated.

A.4.3 Typical experiment

In VIVALDI, we can mount our samples in different ways. If our crystal has a strong cohesion, it can be glued directly on a Vanadium pin, but if we need to avoid stress due to the change of temperature that can break the crystal, it is advisable to wrap it with some aluminium foil. In case of crystals sensitive to air or that need some special atmosphere, VIVALDI also admit sealed glass tubes. Knowing the geometry of the crystal once it is mounted, will be necessary to perform the absorption correction.

Once our crystal is ready, it must be aligned. We must ensure that the sample stick is centered with respect to rotation of the cryostat, that the initial and final apertures that defines the beam path are aligned with the axis of rotation of the cryostat, and that sample height makes it to be in the center of the beam. To perform the centering, several low exposure images at different position of x, y and z of the crystal need to be taken; in the center position of the crystal, the intensity of Laue spots will be maximum. It is very important that the beam irradiates all the sample. A pin-hole of 2, 3, or 4 mm in diameter limits the final aperture to minimize the background scattering form air and from the aluminium cryostat.

The Laue experiment is itself very simple, entailing collection of four to ten successive diffraction patterns, distinguished by a rotation of typically $20^{\rm o}$ o

30° of the crystal about the detector axis. taking several patterns, allow us to collect reasonably complete diffraction data. In a usual phase transition study, complete experiments are performed at one or two temperatures, and a series of single patterns at one setting of the crystal is recorded at small temperature intervals through the transition. It can be very useful to subtract patterns at equal orientation and different temperature in order to unveil weak properties of the transition.

However, this apparently facility in the set up, is does not imply an easy and quickly experiment. In VIVALDI, the difficulty arises when one treats the data. Several programs have been developed to analyze the VIVALDI data and there is a extensive explanation about how to proceed in Dra. Clara González thesis [31]. Here, only a brief glimpse about the process is offered.

Laue patterns processing

After recording the Laue patterns and writing them in an appropriate format with the help of the program REORDER, the first step is basically to index the pattern. This task is done with the help of the programm LAUEGEN [183][184][85]. LAUEGEN is an X-Windows-based programm with an intuitive interface distributed as part of the *Daresbury Laboratory Laue Software Suite.* It displays Laue simulations and Laue patterns; finds and refines crystal orientations; and determines the spots size and the soft limits in λ and d.

To index a pattern, it is important to have a good starting point: the unit cell previously determined and a good approximation to the cell parameters at that temperature. As it has been said before, spots at the intersection between zones have probably lower indices, and some spots with high intensity can satisfy this property; for this reason, these spot are selected and use to index the pattern. With the selected spots and the cell parameters, LAUEGEN propose several solutions, among them we choose the best one (or retry the process if neither of them satisfy us) whose simulated Laue pattern will be likely to the experimental pattern. Once the solution is found, by comparing the position of the predicted spots and the measured spots we can refine PhiX, PhiY and PhiZ,the angles of the orientation matrix that relates the reciprocal lattice to the Cartesian laboratory framework of reference; c_f, the beam ratio; x_c and y_c, the crystal alignment; and the relative values of the cell parameters. The refinement is considered successful when the $RMS \sim 0.1$ for the most spots possible and taking into account a reasonable number of spots far from the central beam, i.e. with high hkl indices. Once the cell has been refines, we can do the refinement of the soft limits: limits of the wavelength range minimum space between planes. The program can calculated them, but seeing the predicted pattern with the limits automatically predicted, they can be improve if some spots are not predicted or some predicted spots are missed. Finally, by inspection, we can assign a medium value for the spot size.

Spots Integration

The program ARGONNE_BOXES has been used to integrate the spots indexed in the previous step using a two-dimensional version of the $\sigma(i)/I$ algorithm [86]. In this programm, the user must specify which regions have to be considered and some parameters to discriminate peaks from background and to model the peak geometry using a elliptical geometry. The programm LAUEGEN allows us to visualize the peaks integrated by ARGONNE_BOXES and check if the most part of them have been integrated properly: no overlapping between peaks, models according to the peak geometries, background substrated... An example of a pattern integrated can be seen in figure A.12.

Absorbtion Correction

The absorbtion correction can be performed using different programs. We are used the programm LADIABS, which corrects intensities for the absorption in the crystal and in the cylindrical Al cryostat shields. Each reflection is corrected for absorption of incident and diffracted beams in the crystal and through the Al shield. The correction is estimated by Gaussian integration over a 3D grid of points within the crystal. The absorbtion coefficient has been calculated as in A.18. LADIABS also generates an output that allows to visualize the crystal inside the detector, which can be very useful to check that the description of the crystal is adequate by comparing its projection on the detector with the form of the spots.

Wavelength normalization

The process of wavelength normalization must be done in different runs for different temperatures, and is performed with the help of the program LAUENORM [87], of the Daresbury Laboratory Suite. LAUENORM will determine an empirical normalization curve by comparison of repeated observations and symmetry equivalents at different wavelengths and then, it will rescale each reflection for the variation of the incident intensity with wavelengths. The user must employ his skills to optimize the lambda range and to obtain the best normalization curve with the most possible reflections accepted. To appreciate the goodness of the fitting and the quality of the data after all the treatment, we used the Laue merging R factors. They give the agreement factor for the weighted mean intensities; R_1 uses the mean intensity from all measurements for the reflection, R_2 the mean intensity from all the measurements of the same sign and R_3 the mean intensity from small measurements of the same sign and with λ within 0.1 Å. They should be as small as possible (at least 0.2)

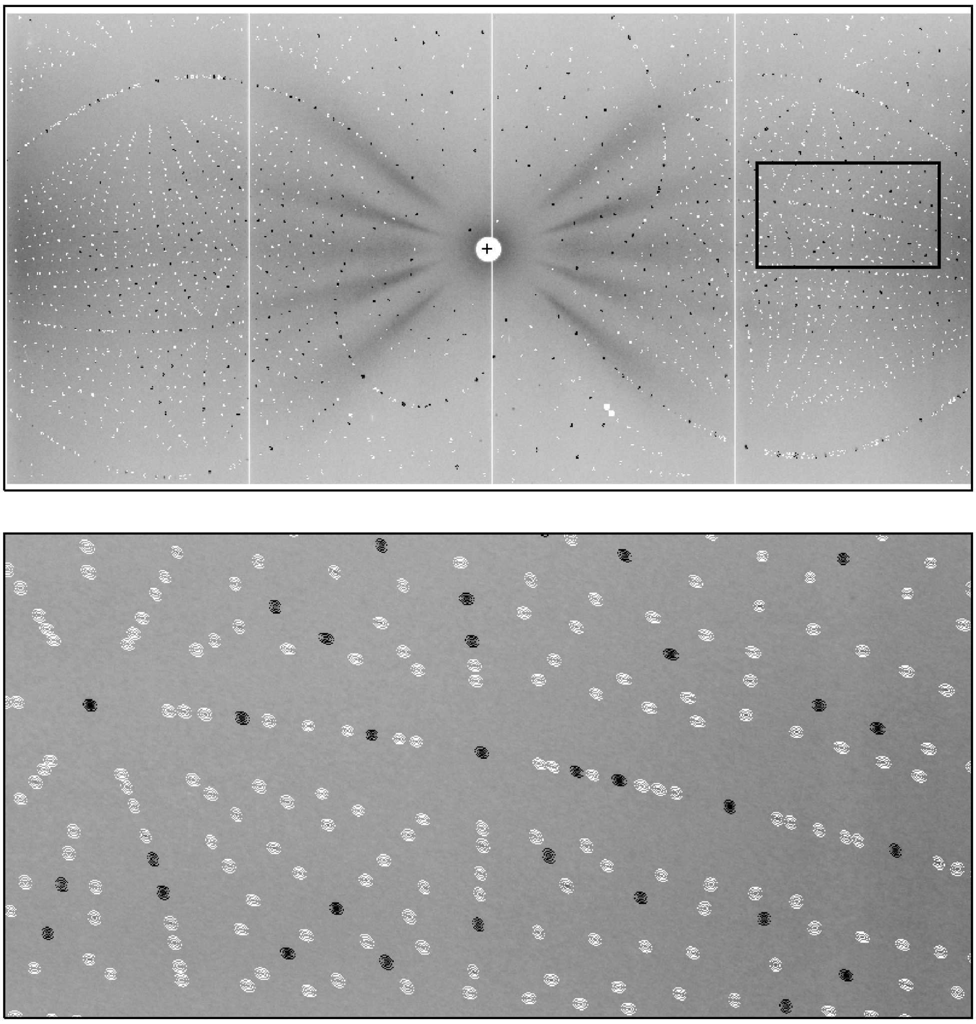

Figure A.12: Integrated Laue patterns for Gn-MnMn at T=25K and $\phi = -45^o$. On the bottom, a detail is shown.

$$R_{Laue} = \frac{\sum |I - I_{MEAN}|}{\sum I} \tag{A.29}$$

A.5 Magnetic Structure Determination. Irreducible Representation Theory

Determination of magnetic structures is a challenge that can be solved only by neutron diffraction techniques. Some information about magnetic structure of magnetic materials can be obtained from other techniques, but only neutron diffraction is a direct method of determining the magnetic structure of a crystal. By magnetic structures, we refer to the mutual alignment of the magnetic moments of the atoms in a crystal and their overall alignment relative to crystallographic axes.

The magnetic structure of a crystal develops from a particular crystal structure and the Landau's [185][186] theory establishes that the development of the free energy at the second order must be invariant under the action of the symmetry operators of the crystal's space group in its paramagnetic state. Therefore, the set of magnetic structures which can develop in a certain crystal and their symmetry depend significantly upon the crystal structure and symmetry, which can be described by space groups. A preliminary analysis of crystal symmetry allows to obtain the the magnetic structures available, the true one can be selected by best fit of the calculated observed pattern to the observed pattern. To determine the magnetic structures, we have used the irreducible representation (IR) theory analysis; therefore, for the understanding of the next chapters, important notions on its basis will be given in this section, starting from the concept of the propagation vector.

Magnetic moments in a crystal interact due to the unpaired electrons of the atoms. The exchange energy depends on the mutual orientation of the moments, and for the whole crystal it can be written as:

$$H = -\sum_{jj'} J_{jj'} \mathbf{m}_j \mathbf{m}_{j'} \tag{A.30}$$

where $J_{jj'}$ is the exchange integral between the atoms j and j', $\mathbf{m}_j$ and $\mathbf{m}_{j'}$ are the magnetic moments of the atoms j and j' and the summation is extended over all the pairs of atoms. The interaction depends on the distance and falls off quickly when the distance increases. At low temperature, the interaction between magnetic moments can lead to a magnetic order.

For the sake of simplicity, we will considerer only one magnetic atom in the lattice interacting via Heisenberg interaction with the first neighbor magnetic atoms. The magnetic moments can be written as a FT of some coefficients called Fourier coefficients ($S_j^{\mathbf{k}}$), which can be real or complex vectors and are the FT of the magnetic moments.

$$\mathbf{m}_l = \int \mathbf{S}_j^{\mathbf{k}} e^{-\imath \mathbf{k}\cdot\mathbf{r}_j} d^3\mathbf{k} \tag{A.31}$$

where $\mathbf{k}$ is the propagation vector which will be described in the next section, $\mathbf{r}_j$ is the position vector of the atom j. The Fourier coefficients, which can be written as linear combinations of some basis vectors $\mathbf{\Psi}_\nu^{\mathbf{k}}$ as can be seen in equation A.32.

$$\mathbf{S}_l^{\mathbf{k}} = \sum_\nu C_\nu^j \mathbf{\Psi}_\nu^{\mathbf{k},j} \tag{A.32}$$

C_ν^j represent the coefficients of the linear development of the Fourier coefficients.

If we generalize equation A.30 for several atoms per lattice, the resulting Hamiltonian is:

$$H = -\sum_{l,l'}\sum_{j,j'}\sum_{\alpha,\beta} J_{ll'jj'\alpha\beta} m_{jl\alpha} m_{j'l'\beta} = -\sum_{j,j'}\sum_{\alpha,\beta} J_{jj'\alpha\beta}(\mathbf{k}) S_{j\alpha}^{\mathbf{k}} (S_{j'\beta}^{\mathbf{k}})^* \tag{A.33}$$

where l and l' refer to the crystal cells, j and j' refer to the magnetic atoms, α and β represent the axes x, y or z. $J_{jj'\alpha\beta}(\mathbf{k})$ is $\sum_l J_{jj'll'\alpha\beta} e^{-\imath\mathbf{k}\cdot(\mathbf{r}_l - \mathbf{r}_{l'})}$, and $\mathbf{r}_l$ and $\mathbf{r}_{l'}$ are the origin vectors of the cells l and l' respectively.

Expressing the Fourier coefficients as a function of their basis vectors, the hamiltonian becomes diagonal as can be seen in equation A.34. Thus, to describe a magnetic structure, we will need to know first $\mathbf{k}$ (if it can be defined), and after that the Fourier coefficients, which depend on the basis vectors $\mathbf{\Psi}_\nu^{\mathbf{k}}$. These vectors can be found with the help of the irreducible representation theory analysis.

$$H = -\sum_{\mathbf{k}}\sum_{\nu,\nu'} C_{\nu\nu'}^{\mathbf{k}} \mathbf{\Psi}_\nu^{\mathbf{k}} (\mathbf{\Psi}_\nu^{\mathbf{k}})^* \tag{A.34}$$

A.5.1 Propagation vector

As it has been said before, at low temperature, the interaction between magnetic moments can lead to a magnetic order. In this magnetic order, the periodicity can be the same as for the unit cell, an integral multiple of it or the periodicity can be not an integral [187]. The relationship between the unit cell and the magnetic cell is given by the propagation vector $\mathbf{k}$, for example, with a propagation vector equal to zero $\mathbf{k} = \mathbf{0}$, the magnetic cell and the nuclear cell are the same; and with a propagation vector equal to $\mathbf{k} = (0, 0, 1/2)$ the magnetic cell doubles the nuclear cell in the **c** direction. The propagation vector also gives us the relations between the orientations of the magnetic moments of the equivalent magnetic atoms in different nuclear cells as it is expressed in equation A.35

$$\mathbf{m}_{lj} = -\sum_{\mathbf{k}} \mathbf{S}_j^{\mathbf{k}} e^{-i\mathbf{k}\cdot\mathbf{r}_l} \tag{A.35}$$

where $\mathbf{m}_{lj}$ is the magnetic moment of the atom j situated in the cell l. As the magnetic moment of an atom is a real vector, and $e^{-i\mathbf{k}\cdot\mathbf{r}_l}$ is a complex quantity except for certain values of **k**, to any vector **k** is associated a vector $-\mathbf{k}$ with $\mathbf{S}_j^{\mathbf{k}} = (\mathbf{S}_j^{\mathbf{k}})^*$ such as:

$$\mathbf{m}_{lj} = \mathbf{S}_j^{\mathbf{k}} e^{-i\mathbf{k}\cdot\mathbf{r}_l} + \mathbf{S}_j^{-\mathbf{k}} e^{i\mathbf{k}\cdot\mathbf{r}_l} = 2\left|\mathbf{m}_j^{\mathbf{k}}\right| \mathbf{u} cos(\mathbf{k}\cdot\mathbf{r}_l + \phi) \tag{A.36}$$

where **u** is a unitary vector.

Attending to the propagation vector, we classify the magnetic structures in:

Incommensurate There is not a simple relation between the magnetic and nuclear cell. For incommensurate magnetic structures, we can not define a propagation vector with accuracy and it is no possible to define a magnetic cell, although the magnetic structure can be determined. There is a special case, when there is only a magnetic ion per unit cell; in such case, the propagation vector can not be defined but the magnetic structure can be solved. From the neutron diffraction point of view, a commensurate structure with a long period will behave as an incommensurate one. Two types of incommensurate structures are:

- Sine wave modulated structures. The magnetic moments order according to $\mathbf{m}_{lj} = \mathbf{u}_j cos(\mathbf{k}\cdot\mathbf{r}_l + \varphi_j)$. A sine wave modulated structure implies that all the moments have different lengths. Such structures are often observed at higher temperature, near T_N, where the differences in the length of the ordered moments is due to thermal disorder. At lower temperatures, the moments tend to have the same length by a squaring of the modulation and a occurrence of new harmonics of **k**
- Helical structures. The magnetic moments are ordered as an helix according to $\boldsymbol{m}_{lj} = \mathbf{u}_j cos(\mathbf{k}\cdot\mathbf{r}_l + \varphi_j) + \mathbf{v}_j sin(\mathbf{k}\cdot\mathbf{r}_l + \varphi_j)$, where $\mathbf{u}_j$ and $\mathbf{v}_j$ are two vectors orthogonal of the same length. Magnetic structures like these may be found for propagation vector parallel

to a 3, 4, or 6 fold symmetry axis with moments rotating in an easy plane perpendicular to this axis. A helical structure can remain stable down to the lowest temperature.

Commensurate The magnetic unit cell is a multiple of the nuclear unit cell. The propagation vector is $\mathbf{k} = (p, q, r)$ with $p, q, r \in Q$ (rational numbers). If the propagation vector is equal to zero, the nuclear and magnetic cell are identical; which is the case of a ferromagnetic structure if there is only one magnetic atom per unit cell, but it may be antiferromagnetic or triangular when there are several magnetic atoms. A commensurate structure can be a:

- Single $\mathbf{k}$ structure. Only $\mathbf{k}$ and $-\mathbf{k}$ appears in its description.
- Multi $\mathbf{k}$ structure. $\mathbf{k}$ and its harmonics $\boldsymbol{\tau}/\mathbf{2}$... appear in its description. Several propagation vectors are needed to describe the magnetic structure.

To describe the commensurate magnetic structures, the expression A.35 needs to be develop. If we have a single $\mathbf{k}$ structure, the expression becomes:

$$\mathbf{m}_{lj} = \mathbf{S}_j^{\mathbf{k}} \left[cos(\mathbf{k} \cdot \mathbf{r}_l) - isin(\mathbf{k} \cdot \mathbf{r}_l)\right] \tag{A.37}$$

If the Fourier coefficient is real and the imaginary part is zero in equation A.37, the modules of the magnetic moments does not change, it just changes its sign, appearing ferromagnetic, antiferromagnetic or ferrimagnetic structures.

If the Fourier coefficient is real but the imaginary part is different from zero, it is necessary to include $\mathbf{k}$ and $-\mathbf{k}$ in the description in the way:

$$\mathbf{m}_{lj} = \mathbf{S}_j^{\mathbf{k}} e^{-i\mathbf{k}\cdot\mathbf{r}_l} + \mathbf{S}_j^{-\mathbf{k}} e^{i\mathbf{k}\cdot\mathbf{r}_l} = 2\mathbf{S}_j^{\mathbf{k}} \left[cos(\mathbf{k} \cdot \mathbf{r}_l)\right] \tag{A.38}$$

which describes sinusoidal structures.

A complex Fourier coefficient is used to describes helicoidal magnetic structures such as circular magnetic structures or elliptical magnetic structures. As the propagation vector must obey $\mathbf{S}_j^{\mathbf{k}} = (\mathbf{S}_j^{\mathbf{k}})^*$, the expression for the magnetic moments will be:

$$\mathbf{m}_{lj} = \mathbf{S}_j^{\mathbf{k}} e^{-i\mathbf{k}\cdot\mathbf{r}_l} + \mathbf{S}_j^{-\mathbf{k}} e^{i\mathbf{k}\cdot\mathbf{r}_l} = 2Re[\mathbf{S}_j^{\mathbf{k}}]cos(\mathbf{k} \cdot \mathbf{r}_l) - 2Im[\mathbf{S}_j^{\mathbf{k}}]sin(\mathbf{k} \cdot \mathbf{r}_l) \tag{A.39}$$

If the real part $Re[\mathbf{S}_j^{\mathbf{k}}]$ and the imaginary part $Im[\mathbf{S}_j^{\mathbf{k}}]$ of the Fourier coefficients have the same modulus, the structure appears to be a circular helix, but it will be a helical helix if they have a different modulus.

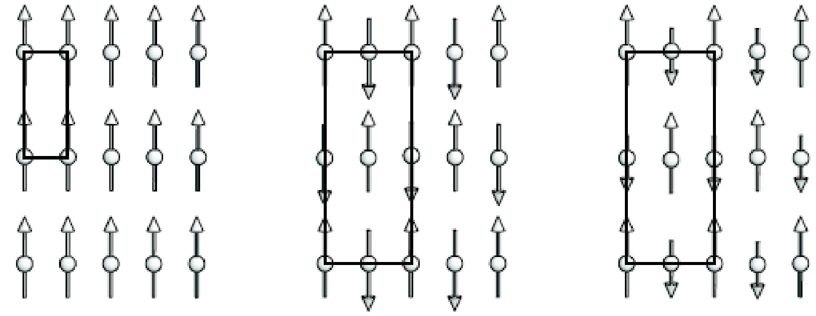
a) ferromagnetic b) antiferromagnetic c) ferrimagnetic

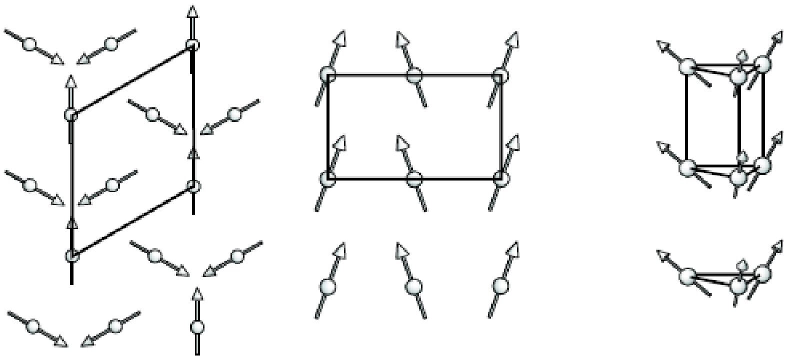
d) triangular e) canted f) umbrella

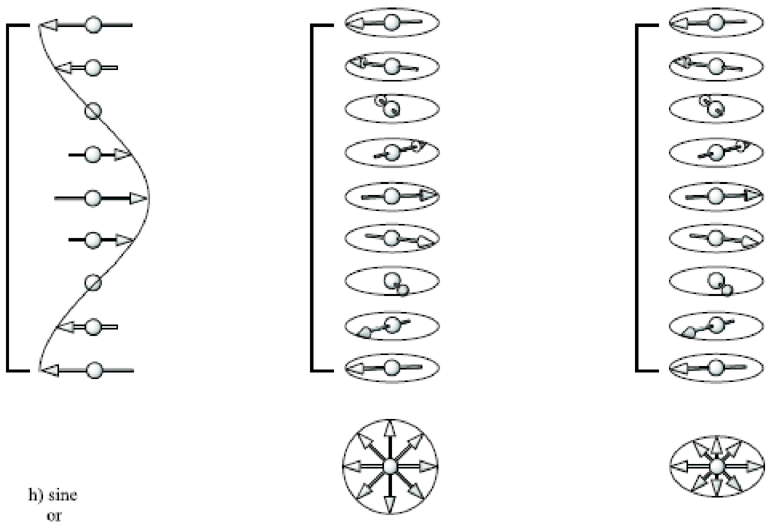
h) sine or cosine i) circular helix j) elliptical helix

Figure A.13: Some different types of magnetic structures

Determining the propagation vector

As it has been said in equation A.10, magnetic scattering peaks appear when $\mathbf{G} = \mathbf{g} - \mathbf{g}' = \mathbf{k} \pm \mathbf{q}$. If$\mathbf{k}$ is zero, the magnetic cell and the nuclear cells coincide, and the magnetic peaks appears where the nuclear reflections are or should be if they are systematically absent. If the propagation vector is different from zero, each nuclear Bragg peak at $\mathbf{q}$ will be flanked by magnetic satellites coupled in pairs at $\mathbf{q} \pm \mathbf{k}$. The Laue diffraction technique allow us to visualize magnetic satellites if existing, just by inspecting and comparing patterns below and above T_C. Therefore, we can determine the propagation vector if the structure is commensurate. For four-circle geometry diffraction technique, it is necessary to explore the reciprocal space by performing several scans and to look for the satellite peaks in direction suspected to present them.

A.5.2 Theory of Irreducible Representations.

To determine the magnetic structure of the compound studied in this thesis, we have used the irreducible representations (IR) analysis. This method is based on expanding the spin density of the crystal in terms of basis functions of the irreducible representations of its space group, so the magnetic structure can be described by the mixing coefficients of the basis functions. The idea arises from Landau's [185][186] symmetry theory of phase transitions. The state of a magnetic crystal is described by the average density of the spin distribution $\mathbf{s}(x, y, z)$. In a phase transition of the second kind, the spin density, which is the magnitude and orientation of the spins in a crystal, varies continuously, but its symmetry changes abruptly, and at the transition point the symmetries of the paramagnetic and magnetic phase are equal. We need to take into account that additional symmetry operations like the time-inversion operation, may be needed to describe a magnetic structure.

In order to classify magnetic structures in a ordered system with a logic structure, several attempts have been done. A natural development is to use the Fedorov's groups, the 230 space groups, and include the atomic magnetic moments. The space group of a crystal is the group os symmetry operations that leave the crystal invariant; to describe magnetic structures is necessary to include an additional operator: **R**, the spin inversion, which change the direction of a spin to the opposite. The groups constructed by combining the 230 Fedorov's space groups and the spin-inversion operator, are called the 1651 Shubnikov groups. In 1968 Bertaut [188] demonstrated that all the Shubnikov groups can be generated from the knowledge of the ensemble of one-dimensional real representations, therefore, they can only describe magnetic structures whose representation is not one dimensional and real. Bertaut established the IR analysis to solve the problem of magnetic structure classification, demonstrating that with the help of this method all possible magnetic couplings in the frame of the 230 crystallographic space groups could be enumerated. He demonstrated that his method was a quite general method, in contrast to the magnetic or Shubnikov groups description, the IR theory analysis can deal with one-dimensional real or complex representations, and even two- or three-dimensional representations. It us based on the transformation of spins in a given lattice site under the symmetry operations of a crystallographic group G or a subgroups G_K of the crystal in which the magnetic structure is imbedded. In order to explain the IR analysis, some basic mathematical concepts such as group, representation, irreducible representation, basis vectors... need to be introduced.

A *group* G is a set of distinct elements G=$\{g_1,\ g_2,...,g_n\}$ endowed with a law of composition such that the product of two elements of the group is also an element of the group, the element identity exists, each element has an inverse, and the associative property is satisfied. The number of elements of the group n(G) defines the *order* of the group G.

A *representation* Γ of the group G is just a mathematical mapping that to each element g_i of G is associated an element $\Gamma(g_i)$, which in our case implies that a representation will match an element with a matrix. The order of the matrices of Γ is called the *dimension* of the representation. These matrices do not have to be diagonal, but by making a proper basis change we can obtain diagonal matrices in blocks. Once the matrices are diagonal in blocks we say that the representation is an IR. The representation Γ will be written as a direct sum of different irreducible representations.

We call G_0 the set of symmetry operators of the space group G, that consider only the rotational part. Therefore, from the 230 space groups, there are just 32 possible G_0 groups, which are the 32 point groups.

To perform a IR analysis, the first thing to do is to relate the symmetry of the propagation vector to that of the lattice. Some of the g_{0n} symmetry operations of the group G_0 will leave $\mathbf{k}$ invariant, i.e. $\mathbf{k}' = g_{0n}\mathbf{k}$ with $\mathbf{k}' = \mathbf{k} + \mathbf{T}$, where $\mathbf{T}$ is a reciprocal lattice vector. Those elements that leave the polar vector $\mathbf{k}$ invariant, form the group of operations $G_\mathbf{k}$, which defines a group compatible with the periodicity of the magnetic structure. From now, we will call Γ the magnetic representation of $G_\mathbf{k}$, and g the elements that form the group $G_\mathbf{k}$.

To determine the magnetic structure we need to obtain the irreducible representations (Γ_ν) of the representation Γ, we need to find the basis vectors which converts the matrices of the different g elements in diagonal matrices in blocks.

The number of IRs Γ_ν coincides with the number of classes of the group, where the class of a group is defined as follows: if A, B and C are elements of the group, when $A^{-1} \cdot B \cdot A = C$ is satisfied, we will say that B and C are part of the same class. By doing this for all the elements of the we will obtain all the group classes.

The dimension of each IR is calculated using the relation $n(G_\mathbf{k}) = \sum_{\nu=1}^{c} l_\nu^2$, where $n(G_\mathbf{k})$ is the order of the group $G_\mathbf{k}$ (i.e. the number of elements of the group), c is the number of classes of the group $G_\mathbf{k}$ (i.e. the number of IR of the group) and l_ν is the order of the IR ν.

Once Γ_ν is found, the magnetic representation Γ, can be written as $\Gamma = = \sum_\nu n_\nu \Gamma_\nu$, where n_ν is the number of times the IR Γ_ν appears in Γ.

We need to take into account that the symmetry operators act not only on the atom positions, but also on the magnetic moments. The effect of the elements in $G_\mathbf{k}$ on the atom positions can be given by an operation which changes the position of an atom at $\mathbf{r_i}$ in the 0 lattice with another atom at position $\mathbf{r_i}$ of the lattice p, i.e. $g(i_0) \rightarrow (j_p)$. The effect of the symmetry operation is to interchange the columns of a matrix which labels the atoms. This operation is the permutation, which is associated with a matrix whose order is the number of magnetic atoms. By applying the different group elements g_i of $G_\mathbf{k}$ to the magnetic ions, we will construct the $\Gamma_{perm}^{g_i}$ matrices, which take into account the effect of the symmetry element g_i on a column vector whose dimension is the number of magnetic atoms. We will call $\chi_{perm}^{g_i}$ the *character* of the matrix $\Gamma_{perm}^{g_i}$, where the character is just the sum of the diagonal elements of the matrix. If we have only two magnetic ions, a permutation matrix Γ_{perm}^{E} will show how the *identity* element E transform the coordinates of the atoms **1**, and **2**. As the identity leaves the coordinates unchanged, Γ_{perm}^{E} will be the identity matrix whose order is the number of atoms.

To take into account the way in which the symmetry operators act on the magnetic moments, we will construct the $\Gamma_{\tilde{V}}^{g_i}$ matrices, which are formed by multiplying the matrix associated with the element g_i with its corresponding determinant, i.e. $\Gamma_{\tilde{V}}^{g_i} = \delta(g_i)R(g_i)$ (where $\delta(g_i)$ is the determinant of the matrix R(g_i) associated with the element g_i of the group $G_\mathbf{k}$). The *traces* of the $\Gamma_{\tilde{V}}^{g_i}$ matrices will be denoted $\chi_{\tilde{V}}^{g_i}$. The determinant $\delta(g_i)$ is included to take into account the fact that the magnetic moment is an axial vector, not a polar one, which is irrelevant in the case of compounds exhibiting nuclear chirality, as all the symmetry elements are proper elements, therefore elements of determinant $+1$.

As we pointed out before, the magnetic representation Γ must describe the result of the symmetry operations g_i on the magnetic moment (which is an axial vector) and on the atom positions. As the effects are independent, the representation for each element can be obtained by the direct product of the $\Gamma^{g_i}_{perm}$ and $\Gamma^{g_i}_{\tilde{V}}$ matrices, i.e. $\Gamma(g_i) = \Gamma^{g_i}_{perm} \times \Gamma^{g_i}_{\tilde{V}}$, and therefore, $\chi(g_i) = \chi^{g_i}_{perm} \times \chi^{g_i}_{\tilde{V}}$, where $\chi(g_i)$ is the character of the matrix of the representation Γ associated with the group element g_i, $\chi^{g_i}_{perm}$ is the character of the matrix $\Gamma^{g_i}_{perm}$, and $\chi^{g_i}_{\tilde{V}}$ the character associated with the matrix $\Gamma^{g_i}_{\tilde{V}}$.

With this knowledge we can now calculate n_ν, i.e. the number of times the IR Γ_ν appears in Γ, with the help of the *Great Orthogonality* theorem, which can be seen in equation A.40

$$n_\nu = \frac{1}{n(G_{\boldsymbol{\tau}})} \sum_{g \epsilon G_{\mathbf{k}}} \chi_\Gamma(g) \chi^*_{\Gamma_\nu}(g) \tag{A.40}$$

where $\chi_\Gamma(g)$ is the character of the matrix associated with the element g of the magnetic representation Γ, and χ_{Γ_ν} is the character of the matrix associated with the element g for the IR ν. The sum acts over all elements g in $G_{\mathbf{k}}$.

We have already seen how to obtain $\chi_\Gamma(g)$ (i.e. by doing $\chi^{g_i}_{perm} \times \chi^{g_i}_{\tilde{V}}$), but to obtain χ_{Γ_ν} we need to construct first the *character table* of the group, which is a table containing the characters of all the irreducible representations for all the classes of the group.

With the information given up to now, we are able to split the magnetic representation into IRs. After that, we need to obtain the basis functions $\Psi^{\mathbf{k}}_\nu$ for each IR ν of the group $G_{\mathbf{k}}$.

As it was shown in equation A.31 the magnetic moments are given by the FT of the Fourier coefficients, which can be written as a linear combination of the basis vectors $\Psi^{\mathbf{k}}_\nu$ (see equation A.32). These basis vectors left the Hamiltonian of the system (equation A.34) diagonal in blocks.

To obtain the basis vectors, we will use the *projection operator*, which is defined as:

$$P^\nu = \sum_{g \epsilon G_{\mathbf{k}}} [\Gamma^{\boldsymbol{\tau}(g)}_\nu]^* \Gamma^{\boldsymbol{\tau}(g)} \tag{A.41}$$

We need to construct this operator for each IR ν, and then P^ν will be applied to a 3N vector, where N is the number of magnetic atoms. By doing this we will obtain the basis vectors $\Psi^{\mathbf{k}}_\nu$ for each IR ν. In fact the number of basis vectors for each IR ν coincides with the number of times the IR Γ_ν appears in the magnetic representation Γ.

Landau stated that in order to keep the magnetic energy invariant under all the symmetry operations of $G_{\mathbf{k}}$, the magnetic structures must be built from basis vectors belonging only to one IR of $G_{\mathbf{k}}$. Bertaut [188] said that this was the case only for second-order phase transitions.

What we do is to make a symmetry analysis to obtain the IRs, and to identify which of them describe the real system, for what we use the neutron data. Obviously, the magnetic structure obtained must be consistent with results of magnetization measurements.

A.5.3 Magnetic Groups

In this thesis, the magnetic structures have been determined by the theory of IR. However, sometimes is not possible to employ this analysis. The potential of the theory is limited by the time-inversion operator that appears in the magnetic symmetry description.

Time-Inversion operator

In order to describe a magnetic structure, sometimes it is necessary to include additional operations like *time-inversion*. Essentially, there are two ways of expressing the time-reversal operator:

- Linear time-inversion operator R.

$$R\mathbf{m_j} = -\mathbf{m_j} = -\sum_{\mathbf{k}} S_j^{\mathbf{k}} e^{-\imath\mathbf{k}\cdot\mathbf{l}} \tag{A.42}$$

- Anti-linear time-inversion operator Θ. This one was introduced by Wigner [189]

$$\Theta\mathbf{m_j} = -\mathbf{m_j} = -\sum_{\mathbf{k}} (S_j^{\mathbf{k}})^* e^{+\imath\mathbf{k}\cdot\mathbf{j}} \tag{A.43}$$

The linear time-inversion operator will change $\mathbf{k}$ into $-\mathbf{k}$, but does not conjugate the Fourier components $S_j^{\mathbf{k}}$.

Bertaut [190] used the anti-linear operator and gave an example in which the introduction of this operator reduced the number of possible magnetic structures.

The need to add this operator was explained by Landau and Lifshits [191]. They showed that it reversed the direction of the electric currents and therefore it reversed the sign of the magnetic moments (axial vectors). Both linear and anti-linear operators keep invariant the magnetic energy, but the linear one has not proved to bring new information [192].

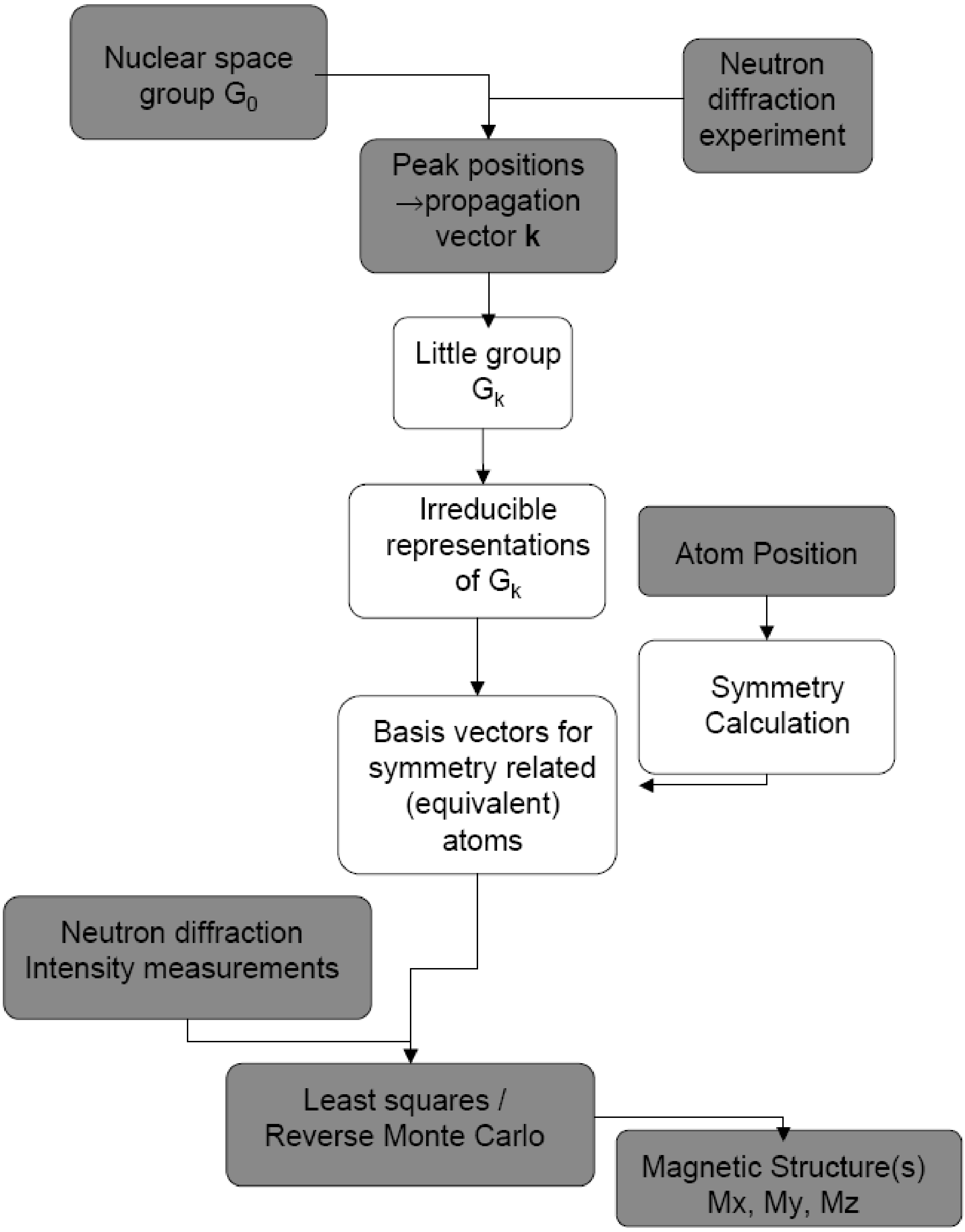

Figure A.14: Flow chart of magnetic structure determination.eps

Attending to the need to include a time-reversal operator in the magnetic symmetry description, three different situation can be distinguished. If we denote by M the magnetic group which is composed of all the elements belonging to the space group $g \epsilon G$ and also of all elements Θg, i.e. the g elements which are time reversed. This leads to three different situations.

1. There is no symmetry operation in the space group that reverses the vector $\mathbf{k}$ (i.e. $-\mathbf{k}$ does not belong to the star $\mathbf{k}$, where the *star of* $\mathbf{k}$ is the set of non-equivalent vectors $\mathbf{k}'$ obtained applying the rotational part of the symmetry elements of the space group to $\mathbf{k}$). Therefore, $M_{\mathbf{k}} = G_{\mathbf{k}}^{\Theta} = G_{\mathbf{k}}$, and the magnetic group is called a *Fedorov group*.
2. $-\mathbf{k}$ is equivalent to $\mathbf{k}$, which means that either $\mathbf{k} = \mathbf{0}$ or $\mathbf{k} = -\mathbf{k} + \mathbf{T}$ where $\mathbf{T}$ is a reciprocal lattice vector. This leads to the so-called *grey groups*, where $M_{\mathbf{k}} = G_{\mathbf{k}}^{\Theta} = G_{\mathbf{k}} + \Theta G_{\mathbf{k}}$
3. If $-\mathbf{k}$ belongs to the star $\mathbf{k}$ but is not equivalent to $\mathbf{k}$, the group is called a *black and white group*, where there exists in G an element g_0 which reverses $\mathbf{k}$ and associated with Θ constitutes the reversing element a_0, and the relations $a_0 = \Theta g_0 = g_0 \Theta$ and $M_{\mathbf{k}} = G_{\mathbf{k}}^{\Theta} = G_{\mathbf{k}} + a_0 G_{\mathbf{k}}$ are satisfied.

The usual group theory cannot be applied when we introduce the anti-linear inversion operator, and we are obliged to employ the *co-representation* theory analysis [189] instead of the IR theory analysis. However, to study the Fedorov and grey groups, the conventional IRs theory analysis is enough to solve the magnetic structure. In all cases the co-representation theory can be applied, as it is similar to a generalization of the IRs method, but it is more complex, therefore it will not be used for Fedorov and grey groups.

As the compounds presented in this thesis present a propagation vector $\mathbf{k} = \mathbf{0}$, they belong to grey groups and the IRs theory is enough to understand their magnetic behavior, the magnetic structure solution has been done using this approach instead of the co-representations theory.

Appendix B

$[Cr(CN)_6][Mn(\boldsymbol{S})-pnH]$

As it has been said in the chapter 1, some doubts about the existence of a magnetic reorientation phase for the GN were risen by dynamical features. In order to search for a possible propagation vector different from zero near the critical temperature, we scanned the reciprocal space at different temperatures in D15 for Phase I.

To perform the experiment, a crystal of 1x5x0.7$mm^3$3 was wrapped in silver film and glued in a aluminium pin with *kwickfilm*. The a axis of the crystal was placed vertical in the pin, parallel to the ϕ axes of the Eulerian cradle. The slits used to optimize the ratio background/signal were 8mmx8mm at the font and 8mmx8mm at the detector. Before cooling down, some lines were measured to check the quality of the crystal ant to obtain an orientation matrix. This orientation matrix was also obtained at 45K and 12K and the cell parameters refined at these temperatures.

A total of eleven q-scans in strategic directions were collected at different temperatures. As can be seen in the figures of this appendix, no extra peeks appeared and a propagation vector different from zero has not been observed. Due to the dependency of the are reorientation matrix and cell parameters with temperature, some peaks are displaced with temperature.

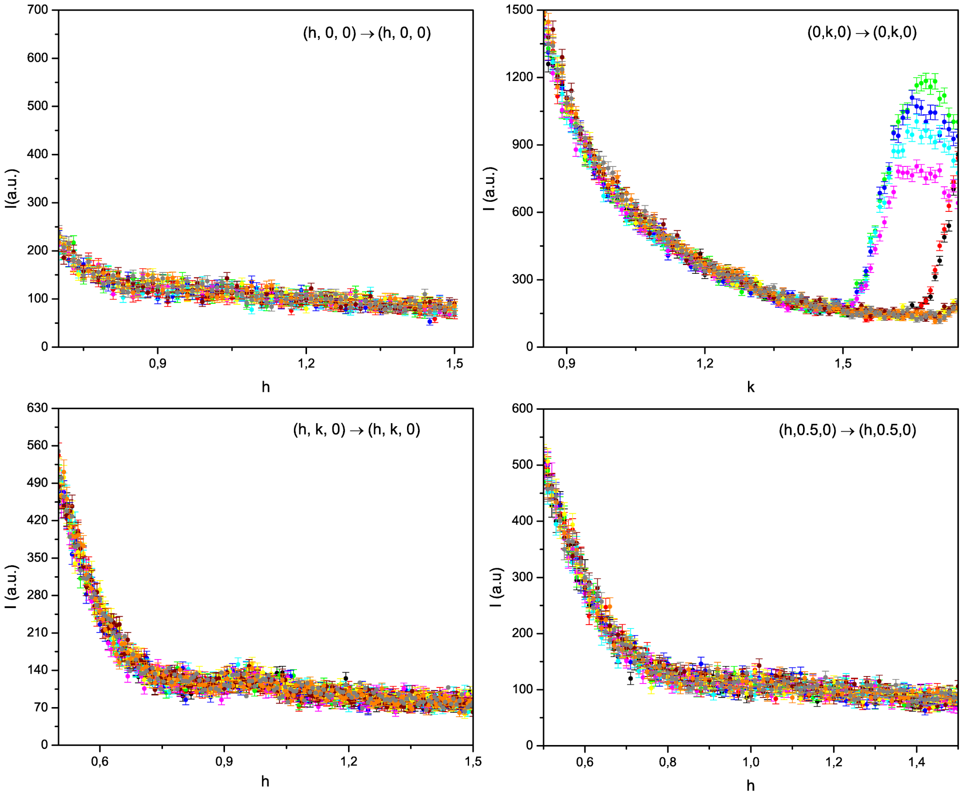

Figure B.1: Q-scan performed for GN compound in D15 at different temperatures: 12K (black), 20K (red), 30 K (green), 32K (dark blue), 34K (pink), 36K (yellow), 37K (purple), 38K (orange), 39K (magenta), 40K (grey).

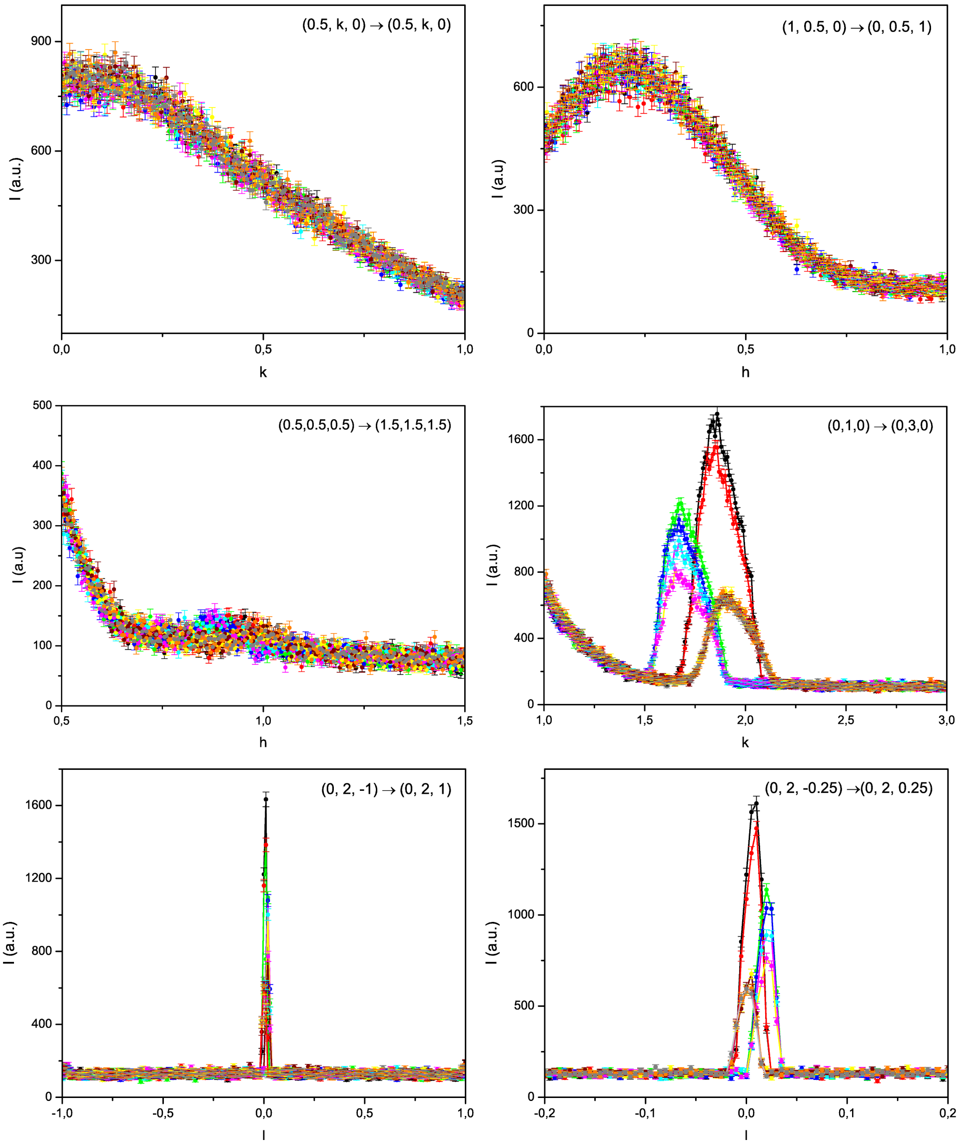

Figure B.2: Q-scan performed for GN compound in D15 at different temperatures: 12K (black), 20K (red), 30 K (green), 32K (dark blue), 34K (pink), 36K (yellow), 37K (purple), 38K (orange), 39K (magenta), 40K (grey).

Appendix C

$[Mn(CN)_6][Mn(S)-pnH(H_2O)]\cdot 2H_2O$

Table C.1: Atomic positions

		X	Y	Z	U_{iso}
Mn1	290K	0.4979(14)	0.2567(5)	0.2615(5)	0.0155(17)
	25K	0.4970(9)	0.2566(4)	0.2623(4)	0.0028(9)
	2K	0.4968(10)	0.2555(4)	0.2627(5)	0.0019(10)
Mn2	290K	-0.0076(11)	0.5070(5)	0.1938(6)	0.0170(15)
	25K	-0.0098(9)	0.5078(4)	0.1955(4)	0.0048(10)
	2K	-0.0084(9)	0.5064(4)	0.1964(5)	0.0027(11)
O1	290K	0.0513(10)	0.4905(6)	0.0469(5)	0.0314(16)
	25K	0.0538(6)	0.4904(3)	0.0473(3)	0.0073(7)
	2K	0.0541(6)	0.4900(3)	0.0477(3)	0.0061(8)
N1	290K	0.1986(6)	0.4016(3)	0.2161(3)	0.0344(10)
	25K	0.1969(4)	0.40215(19)	0.21784(16)	0.0087(5)
	2K	0.1974(4)	0.4021(2)	0.21779(18)	0.0080(5)
N2	290K	0.7787(6)	0.4029(3)	0.1936(3)	0.0328(10)
	25K	0.7784(4)	0.40282(18)	0.19628(16)	0.0085(5)
	2K	0.7771(4)	0.4029(2)	0.19655(18)	0.0071(5)
N3	290K	0.5278(11)	0.3543(4)	0.4496(3)	0.0727(19)
	25K	0.5353(4)	0.34827(19)	0.45554(17)	0.0112(5)
	2K	0.5355(4)	0.3482(2)	0.45510(19)	0.0094(6)
N4	290K	0.4792(8)	0.1528(3)	0.0762(3)	0.0480(13)
	25K	0.4743(4)	0.15103(19)	0.07492(17)	0.0106(5)
	2K	0.4744(4)	0.1512(2)	0.07458(18)	0.0091(6)
N5	290K	0.2166(6)	0.1150(3)	0.3344(3)	0.0315(10)
	25K	0.2152(4)	0.11239(18)	0.33444(16)	0.0069(5)
	2K	0.2151(4)	0.1125(2)	0.33427(17)	0.0073(5)
N6	290K	0.7995(6)	0.1154(3)	0.3131(3)	0.0325(10)
	25K	0.7970(4)	0.11344(18)	0.31257(17)	0.0081(5)
	2K	0.7965(4)	0.1134(2)	0.31287(18)	0.0071(5)
N7	290K	-0.0674(7)	0.5240(3)	0.3449(3)	0.0319(10)
	25K	-0.0634(4)	0.52711(18)	0.34838(15)	0.0078(5)
	2K	-0.0634(4)	0.5270(2)	0.34827(17)	0.0064(5)
N8	290K	0.4435(10)	0.5131(5)	0.0456(4)	0.0511(14)
	25K	0.4380(4)	0.50224(19)	0.05198(17)	0.0094(5)
	2K	0.4391(4)	0.5020(2)	0.05226(19)	0.0078(6)
C1	290K	0.3088(8)	0.3476(4)	0.2308(3)	0.0235(12)
	25K	0.3059(5)	0.3467(3)	0.2324(2)	0.0057(6)
	2K	0.3054(6)	0.3464(3)	0.2327(2)	0.0061(7)
C2	290K	0.6780(8)	0.3477(4)	0.2169(4)	0.0246(13)
	25K	0.6754(5)	0.3470(3)	0.2185(2)	0.0064(6)
	2K	0.6750(6)	0.3469(3)	0.2187(2)	0.0072(7)
C3	290K	0.5170(11)	0.3175(4)	0.3815(3)	0.0360(14)
	25K	0.5169(5)	0.3143(2)	0.3840(2)	0.0069(6)
	2K	0.5169(6)	0.3142(3)	0.3840(2)	0.0063(7)
C4	290K	0.4854(9)	0.1929(3)	0.1427(3)	0.0294(12)
	25K	0.4822(5)	0.1923(2)	0.1417(2)	0.0057(6)
	2K	0.4835(6)	0.1927(3)	0.1418(2)	0.0058(7)
C5	290K	0.3205(7)	0.1688(4)	0.3095(3)	0.0239(12)
	25K	0.3183(5)	0.1673(2)	0.3102(2)	0.0060(6)
	2K	0.3189(5)	0.1676(3)	0.3099(2)	0.0048(6)
C6	290K	0.6907(7)	0.1690(4)	0.2963(3)	0.0210(11)
	25K	0.6863(5)	0.1674(3)	0.2958(2)	0.0065(6)
	2K	0.6870(6)	0.1680(3)	0.2956(2)	0.0067(7)
C7	290K	0.4655(9)	0.4149(4)	-0.0939(3)	0.0306(14)
	25K	0.4601(5)	0.4084(3)	-0.0937(2)	0.0066(7)
	2K	0.4601(5)	0.4080(3)	-0.0935(2)	0.0057(7)
C8	290K	0.4951(13)	0.3122(4)	-0.1175(4)	0.0412(15)

Continued on next page

continued from previous page					
		X	Y	Z	U_{iso}
	25K	0.4959(5)	0.3085(2)	-0.1216(2)	0.0080(6)
	2K	0.4961(6)	0.3088(3)	-0.1210(2)	0.0075(7)
C9	290K	0.5089(13)	0.4258(7)	0.0040(4)	0.040(2)
	25K	0.5072(5)	0.4158(3)	0.0071(2)	0.0073(8)
	2K	0.5082(6)	0.4162(4)	0.0072(2)	0.0055(9)
O2	290K	0.488(3)	0.6727(11)	-0.0731(10)	0.134(8)
	25K	0.5627(7)	0.6582(3)	-0.0452(3)	0.0114(8)
	2K	0.5617(7)	0.6585(3)	-0.0461(3)	0.0092(9)
H1	290K	-0.060(3)	0.4567(11)	0.3658(8)	0.069(5)
	25K	-0.0537(13)	0.4599(5)	0.3718(6)	0.0221(18)
	2K	-0.0527(15)	0.4602(6)	0.3714(7)	0.024(2)
H2	290K	-0.200(2)	0.5422(10)	0.3499(8)	0.055(3)
	25K	-0.1955(12)	0.5422(6)	0.3525(5)	0.0218(17)
	2K	-0.1931(14)	0.5423(8)	0.3527(7)	0.025(2)
H3	290K	0.3248(19)	0.4312(9)	-0.1048(8)	0.045(3)
	25K	0.3202(11)	0.4234(6)	-0.1026(5)	0.0197(16)
	2K	0.3199(12)	0.4237(7)	-0.1023(5)	0.0166(17)
H4	290K	0.631(2)	0.2932(14)	-0.0948(16)	0.087(6)
	25K	0.6308(13)	0.2877(7)	-0.1030(7)	0.030(2)
	2K	0.6304(14)	0.2859(8)	-0.1036(8)	0.0263(15)
H5	290K	0.412(3)	0.2696(12)	-0.0831(15)	0.074(5)
	25K	0.4022(14)	0.2613(6)	-0.0889(7)	0.029(2)
	2K	0.4035(15)	0.2609(7)	-0.0894(8)	0.0263(15)
H6	290K	0.479(3)	0.3001(10)	-0.1866(9)	0.089(6)
	25K	0.4803(14)	0.2998(6)	-0.1934(5)	0.0253(18)
	2K	0.4815(15)	0.2984(6)	-0.1938(6)	0.0241(19)
H7	290K	0.455(3)	0.3695(13)	0.0436(9)	0.080(5)
	25K	0.4484(13)	0.3577(6)	0.0437(5)	0.0217(17)
	2K	0.4478(14)	0.3574(7)	0.0448(6)	0.0219(19)
H8	290K	0.661(3)	0.4284(16)	0.0133(9)	0.083(6)
	25K	0.6516(13)	0.4138(7)	0.0180(6)	0.0260(19)
	2K	0.6524(13)	0.4148(7)	0.0171(6)	0.0205(19)
H9	290K	0.494(3)	0.5214(13)	0.1084(15)	0.096(6)
	25K	0.4811(14)	0.5058(6)	0.1156(6)	0.029(2)
	2K	0.4787(15)	0.5051(7)	0.1171(6)	0.028(2)
H10	290K	0.308(3)	0.5104(13)	0.0518(11)	0.081(5)
	25K	0.3005(13)	0.5042(6)	0.0517(6)	0.0232(18)
	2K	0.3002(13)	0.5025(7)	0.0534(7)	0.0215(19)
H11	290K	0.470(3)	0.572(2)	0.0080(14)	0.089(9)
	25K	0.4834(14)	0.5624(6)	0.0198(7)	0.024(2)
	2K	0.4861(16)	0.5619(8)	0.0193(8)	0.023(2)
H12	290K	0.015(2)	0.5420(10)	0.0132(10)	0.045(4)
	25K	0.0156(13)	0.5468(6)	0.0147(6)	0.0217(17)
	2K	0.0139(14)	0.5454(8)	0.0139(6)	0.019(2)
H13	290K	0.021(2)	0.4375(15)	0.0108(10)	0.053(5)
	25K	0.0167(14)	0.4366(6)	0.0107(6)	0.0217(17)
	2K	0.0175(15)	0.4376(8)	0.0093(7)	0.021(2)
H1W	290K	0.521(5)	0.7268(15)	-0.049(2)	0.150(14)
	25K	0.5096(15)	0.7180(7)	-0.0381(9)	0.038(2)
	2K	0.5088(16)	0.7166(8)	-0.0375(9)	0.033(2)
H2W	290K	0.390(5)	0.689(3)	-0.104(3)	0.18(2)
	25K	0.6868(15)	0.6669(7)	-0.0429(7)	0.031(2)
	2K	0.6864(18)	0.6662(9)	-0.0404(8)	0.034(2)

Table C.2: Anisotropic thermal parameters

		U_{11}	U_{22}	U_{33}	U_{23}	U_{13}	U_{12}
Mn1	290K	0.015(4)	0.011(4)	0.020(3)	-0.003(3)	-0.001(3)	0.002(3)
	25K	–	–	–	–	–	–
	2K	–	–	–	–	–	–
Mn2	290K	0.013(4)	0.013(4)	0.025(4)	0.000(3)	0.002(3)	0.002(4)
	25K	0.008(3)	0.003(3)	0.003(2)	0.0002(16)	-0.0032(19)	0.002(2)
	2K	–	–	–	–	–	–
O1	290K	0.045(4)	0.033(5)	0.016(3)	-0.005(3)	-0.002(3)	-0.003(3)
	25K	0.012(2)	0.006(2)	0.0044(14)	-0.0009(13)	-0.0029(15)	0.0009(14)
	2K	0.00774	0.00475	0.00587	-0.00090	-0.00288	-0.00139
N1	290K	0.023(3)	0.027(2)	0.053(2)	0.009(2)	-0.006(2)	0.0118(18)
	25K	0.0034(13)	0.0089(13)	0.0139(10)	0.0002(9)	-0.0021(9)	0.0038(9)
	2K	0.00585	0.00731	0.01071	0.00163	-0.00133	0.00229
N2	290K	0.029(3)	0.028(3)	0.041(2)	0.0020(19)	0.0004(19)	-0.0119(18)
	25K	0.0096(14)	0.0064(13)	0.0095(9)	0.0007(8)	0.0000(9)	-0.0043(9)
	2K	0.00607	0.00601	0.00907	0.00116	0.00032	-0.00249
N3	290K	0.114(6)	0.063(3)	0.040(2)	-0.025(2)	-0.010(3)	0.012(4)
	25K	0.0133(16)	0.0104(13)	0.0100(10)	-0.0038(9)	-0.0033(9)	0.0007(10)
	2K	0.01019	0.00779	0.01008	-0.00402	-0.00277	0.00003
N4	290K	0.064(4)	0.053(3)	0.0267(18)	-0.016(2)	-0.003(2)	0.007(3)
	25K	0.0139(16)	0.0095(12)	0.0083(10)	-0.0039(9)	0.0006(9)	0.0011(9)
	2K	0.01001	0.00942	0.00785	-0.00368	-0.00118	0.00044
N5	290K	0.023(2)	0.033(3)	0.038(2)	0.0022(19)	0.0028(18)	-0.0108(18)
	25K	0.0036(13)	0.0076(13)	0.0094(10)	0.0010(8)	0.0006(9)	-0.0026(8)
	2K	0.00631	0.00741	0.00828	0.00025	0.00163	-0.00378
N6	290K	0.028(3)	0.025(3)	0.044(2)	0.0088(18)	0.002(2)	0.0070(18)
	25K	0.0058(13)	0.0067(13)	0.0118(10)	0.0023(8)	-0.0010(9)	0.0041(8)
	2K	0.00502	0.00630	0.01013	0.00101	-0.00092	0.00244
N7	290K	0.032(3)	0.039(3)	0.025(2)	0.001(2)	-0.0022(18)	-0.0062(19)
	25K	0.0071(14)	0.0087(13)	0.0077(9)	0.0014(9)	0.0001(9)	-0.0025(8)
	2K	0.00695	0.00798	0.00442	-0.00070	0.00073	0.00015
N8	290K	0.054(4)	0.061(4)	0.039(3)	-0.016(3)	0.010(3)	-0.002(3)
	25K	0.0075(15)	0.0137(14)	0.0071(10)	-0.0030(8)	0.0012(10)	0.0011(9)
	2K	0.00503	0.01236	0.00615	-0.00318	0.00141	-0.00053
C1	290K	0.024(3)	0.022(3)	0.025(2)	0.002(2)	-0.001(2)	0.003(2)
	25K	0.0014(17)	0.0080(17)	0.0077(12)	0.0034(11)	-0.0025(11)	0.0007(11)
	2K	–	–	–	–	–	–
C2	290K	0.022(3)	0.015(3)	0.036(3)	0.001(2)	-0.001(2)	-0.004(2)
	25K	0.0036(19)	0.0048(17)	0.0107(13)	0.0024(11)	0.0006(11)	-0.0019(11)
	2K	–	–	–	–	–	–
C3	290K	0.058(4)	0.027(3)	0.023(3)	-0.006(2)	-0.005(3)	0.010(3)
	25K	0.0058(18)	0.0103(17)	0.0046(12)	-0.0001(11)	0.0010(11)	0.0013(12)
	2K	0.00280	0.00954	0.00661	-0.00142	0.00191	0.00029
C4	290K	0.027(3)	0.030(3)	0.030(3)	0.001(2)	-0.001(2)	0.004(3)
	25K	0.0103(19)	0.0021(15)	0.0048(12)	0.0001(10)	-0.0012(11)	0.0008(11)
	2K	0.00764	0.00460	0.00503	-0.00021	0.00052	0.00222
C5	290K	0.016(3)	0.025(3)	0.030(2)	0.000(2)	0.000(2)	-0.003(2)
	25K	0.0044(18)	0.0047(17)	0.0090(13)	-0.0009(11)	0.0011(11)	-0.0034(11)
	2K	–	–	–	–	–	–
C6	290K	0.018(3)	0.013(3)	0.032(3)	0.001(2)	-0.002(2)	0.003(2)
	25K	0.0042(19)	0.0076(18)	0.0077(13)	0.0006(11)	0.0011(12)	0.0023(11)
	2K	–	–	–	–	–	–
C7	290K	0.029(4)	0.044(3)	0.020(2)	-0.001(2)	0.005(2)	0.002(3)
	25K	0.007(2)	0.0063(17)	0.0061(12)	0.0012(11)	0.0009(11)	0.0012(12)
	2K	0.00679	0.00572	0.00460	0.00209	0.00153	0.00052
C8	290K	0.053(5)	0.032(3)	0.039(3)	0.003(3)	-0.006(4)	0.010(4)

Continued on next page

continued from previous page							
		U_{11}	U_{22}	U_{33}	U_{23}	U_{13}	U_{12}
	25K	0.0055(18)	0.0087(17)	0.0097(13)	0.0021(11)	0.0005(12)	0.0010(13)
	2K	0.00701	0.00798	0.00739	-0.00171	0.00012	0.00068
C9	290K	0.048(6)	0.049(6)	0.024(3)	0.005(3)	0.001(4)	0.005(3)
	25K	0.010(2)	0.009(2)	0.0032(13)	0.0001(11)	0.0009(12)	0.0037(12)
	2K	0.00468	0.00786	0.00405	-0.00099	0.00036	0.00224
O2	290K	0.20(2)	0.074(10)	0.125(12)	-0.047(9)	0.092(15)	-0.047(13)
	25K	0.010(3)	0.009(2)	0.0154(17)	-0.0022(15)	-0.0035(16)	-0.0023(16)
	2K	0.00839	0.00532	0.01380	-0.00096	0.00241	-0.00104
H1	290K	0.137(17)	0.039(8)	0.033(6)	0.000(6)	-0.013(8)	0.002(8)
	25K	0.034(5)	0.007(4)	0.025(3)	0.003(3)	-0.004(3)	-0.004(3)
	2K	0.03351	0.00793	0.03040	0.00257	0.00384	0.00016
H2	290K	0.038(9)	0.080(10)	0.047(7)	-0.013(7)	-0.005(7)	0.000(7)
	25K	0.015(5)	0.027(5)	0.024(3)	-0.004(3)	0.000(3)	0.009(3)
	2K	0.01292	0.03205	0.03056	-0.00807	-0.00285	0.00813
H3	290K	0.037(9)	0.047(8)	0.051(6)	0.008(6)	-0.009(6)	0.003(6)
	25K	0.011(4)	0.025(5)	0.022(3)	-0.002(3)	-0.001(3)	-0.001(3)
	2K	0.01227	0.02279	0.01485	-0.00190	0.00204	0.00762
H4	290K	0.039(10)	0.083(13)	0.140(16)	-0.008(12)	-0.027(10)	0.016(8)
	25K	0.019(5)	0.034(6)	0.036(5)	0.003(4)	-0.013(4)	0.011(4)
	2K	0.02356	0.01565	0.03976	0.00708	-0.00178	0.00278
H5	290K	0.076(12)	0.038(9)	0.107(12)	0.001(9)	0.033(10)	0.009(8)
	25K	0.027(5)	0.016(5)	0.043(5)	0.005(4)	0.012(4)	-0.008(3)
	2K	0.02356	0.01565	0.03976	0.00708	-0.00178	0.00278
H6	290K	0.169(19)	0.056(9)	0.043(7)	-0.013(6)	0.005(10)	0.004(13)
	25K	0.037(6)	0.021(4)	0.018(3)	-0.005(3)	-0.002(3)	-0.004(4)
	2K	0.02996	0.02421	0.01808	-0.00574	-0.00311	0.00586
H7	290K	0.093(14)	0.105(14)	0.041(7)	0.016(8)	0.007(8)	0.008(11)
	25K	0.030(5)	0.019(4)	0.016(3)	0.006(3)	0.007(3)	-0.001(3)
	2K	0.03186	0.01802	0.01570	0.00353	0.00647	-0.00247
H8	290K	0.050(13)	0.153(19)	0.046(7)	-0.003(9)	-0.011(7)	0.016(10)
	25K	0.027(6)	0.031(5)	0.020(3)	0.002(3)	-0.003(3)	0.007(4)
	2K	0.01436	0.02613	0.02088	0.00359	-0.00395	0.00978
H9	290K	0.102(15)	0.105(13)	0.080(12)	-0.049(10)	0.006(11)	-0.015(14)
	25K	0.035(6)	0.038(6)	0.013(3)	0.003(3)	-0.006(3)	0.004(4)
	2K	0.03476	0.03517	0.01283	-0.00242	-0.01217	0.00469
H10	290K	0.063(11)	0.103(14)	0.078(12)	-0.022(9)	0.037(10)	0.006(11)
	25K	0.018(5)	0.019(4)	0.032(4)	-0.006(3)	0.002(4)	0.007(3)
	2K	0.01446	0.01888	0.03102	0.00239	0.00511	0.00249
H11	290K	0.071(16)	0.11(2)	0.082(14)	-0.020(11)	0.045(12)	-0.035(13)
	25K	0.026(6)	0.016(5)	0.031(4)	-0.001(4)	0.006(4)	-0.002(3)
	2K	0.02251	0.02518	0.02214	0.00019	0.00526	-0.00298
H12	290K	0.074(11)	0.017(7)	0.042(6)	0.015(5)	0.005(7)	0.001(7)
	25K	0.030(4)	0.014(3)	0.022(3)	-0.005(2)	-0.003(2)	0.002(2)
	2K	0.02193	0.01850	0.01545	-0.00122	0.00082	0.00433
H13	290K	0.060(11)	0.055(11)	0.045(7)	-0.027(7)	0.001(7)	-0.007(8)
	25K	0.030(4)	0.014(3)	0.022(3)	-0.005(2)	-0.003(2)	0.002(2)
	2K	0.01795	0.01474	0.03121	-0.01267	-0.00267	-0.00864
H1W	290K	0.24(4)	0.049(12)	0.17(2)	-0.033(15)	0.00(3)	-0.052(19)
	25K	0.023(6)	0.027(5)	0.065(7)	-0.004(5)	0.006(5)	0.008(4)
	2K	0.02226	0.02176	0.05559	0.00584	0.00650	0.00288
H2W	290K	0.18(4)	0.13(3)	0.23(4)	-0.01(2)	-0.10(3)	0.09(2)
	25K	0.021(6)	0.029(6)	0.044(5)	-0.002(4)	0.007(4)	-0.006(4)
	2K	0.02876	0.03596	0.03680	-0.00907	-0.00674	-0.00585

Appendix D

$[Cr(CN)_6][Mn(R)-pnH(DMF)]\cdot 2H_2O$

Table D.1: Atomic positions

		X	Y	Z	U_{iso}
Mn1	290K	1.0000(13)	0.2584(4)	0.7006(4)	0.0218(16)
	33K	0.9978(14)	0.2580(6)	0.6997(5)	0.005(2)
	35K	1.003(6)	0.259(3)	0.6998(18)	0.000(10)
	2K	0.9928(17)	0.2581(7)	0.6999(7)	0.009(2)
Cr1	290K	1.4948(18)	0.5046(5)	0.7647(5)	0.0259(18)
	33K	1.4985(19)	0.5056(6)	0.7631(6)	0.008(2)
	35K	1.507(9)	0.505(3)	0.7652(19)	0.005(12)
	2K	1.4988(2)	0.5057(1)	0.76294(9)	0.011(2)
N1	290K	1.2046(6)	0.3617(3)	0.7163(3)	0.0429(14)
	33K	1.2033(6)	0.3639(4)	0.7138(4)	0.0177(15)
	35K	1.204(3)	0.363(2)	0.7137(12)	0.015(7)
	2K	1.2031(2)	0.36396(10)	0.71349(9)	0.021(2)
N2	290K	1.2049(6)	0.1491(3)	0.6915(3)	0.0373(13)
	33K	1.2037(7)	0.1488(4)	0.6898(4)	0.0219(15)
	35K	1.196(3)	0.1476(16)	0.6923(12)	0.001(6)
	2K	1.2038(3)	0.14888(10)	0.68966(9)	0.023(2)
N3	290K	0.7975(6)	0.1493(3)	0.6920(3)	0.0469(15)
	33K	0.7996(7)	0.1482(4)	0.6917(3)	0.0159(14)
	35K	0.798(3)	0.1493(18)	0.6907(14)	0.026(8)
	2K	0.7997(2)	0.14842(10)	0.69156(9)	0.023(2)
N4	290K	0.7978(6)	0.3618(3)	0.7184(3)	0.0410(14)
	33K	0.8000(6)	0.3620(4)	0.7165(4)	0.0157(14)
	35K	0.796(3)	0.3610(17)	0.7159(11)	0.003(7)
	2K	0.8000(2)	0.36221(10)	0.71653(9)	0.019(2)
N5	290K	1.4753(18)	0.4108(5)	0.9110(4)	0.118(4)
	33K	1.494(3)	0.4070(5)	0.9088(4)	0.108(6)
	35K	1.533(4)	0.4087(17)	0.9103(13)	0.055(9)
	2K	1.4943(2)	0.40718(10)	0.90869(9)	0.118(10)
N6	290K	1.4867(15)	0.5944(4)	0.6157(3)	0.088(2)
	33K	1.4999(13)	0.5976(4)	0.6141(3)	0.0387(17)
	35K	1.506(3)	0.5954(12)	0.6142(10)	0.020(6)
	2K	1.5002(2)	0.59770(10)	0.61398(9)	0.045(2)
C1	290K	1.3095(7)	0.4137(4)	0.7334(3)	0.0276(17)
	33K	1.3088(9)	0.4133(5)	0.7314(5)	0.015(2)
	35K	1.301(4)	0.413(2)	0.7292(16)	0.003(9)
	2K	1.3088(2)	0.41353(10)	0.73130(9)	0.022(1)
C2	290K	1.3070(7)	0.0961(4)	0.7053(4)	0.0297(17)
	33K	1.3101(9)	0.0964(5)	0.7055(5)	0.015(2)
	35K	1.302(4)	0.104(2)	0.7062(15)	
	2K	1.3101(2)	0.09661(10)	0.70519(9)	0.021(2)
C3	290K	0.6869(7)	0.0984(5)	0.7070(4)	0.0327(18)
	33K	0.6896(9)	0.0967(6)	0.7065(4)	0.0131(19)
	35K	0.677(4)	0.090(2)	0.7045(16)	0.009(9)
	2K	0.6895(2)	0.09664(10)	0.70644(9)	0.015(2)
C4	290K	0.6907(9)	0.4135(4)	0.7343(4)	0.038(2)
	33K	0.6900(9)	0.4147(5)	0.7330(5)	0.0130(19)
	35K	0.680(4)	0.414(2)	0.7355(15)	
	2K	0.6899(3)	0.41482(10)	0.73283(9)	0.013(2)
C5	290K	1.4951(13)	0.4458(4)	0.8585(3)	0.0525(16)
	33K	1.4977(16)	0.4439(5)	0.8569(4)	0.031(2)
	35K	1.482(4)	0.4431(18)	0.8557(13)	0.014(8)
	2K	1.4980(3)	0.44404(10)	0.85673(9)	0.031(2)
C6	290K	1.5019(13)	0.5634(4)	0.6688(3)	0.0482(15)
	33K	1.5059(13)	0.5660(4)	0.6678(3)	0.0211(16)
	35K	1.508(5)	0.5658(19)	0.6690(14)	0.023(8)

Continued on next page

continued from previous page

		X	Y	Z	U_{iso}
	2K	1.5063(2)	0.56614(10)	0.66770(9)	0.024(2)
O1	290K	0.9953(13)	0.2752(4)	0.5917(3)	0.0440(15)
	33K	0.9962(11)	0.2742(5)	0.5899(3)	0.0131(15)
	35K	1.098(4)	0.2775(18)	0.5916(12)	0.000(8)
	2K	0.9962(2)	0.27424(10)	0.58968(9)	0.018(2)
N7	290K	1.0219(16)	0.2286(4)	0.8162(3)	0.071(2)
	33K	1.0290(9)	0.2293(4)	0.8160(3)	0.0207(14)
	35K	1.017(2)	0.2282(10)	0.8158(8)	0.016(5)
	2K	1.0290(2)	0.22959(10)	0.81585(9)	0.023(2)
H7C	290K	1.137(4)	0.239(2)	0.8269(16)	0.133(13)
	33K	1.146(4)	0.2441(16)	0.8241(12)	0.056(6)
	35K	1.1497	0.2447	0.8329	0.019
	2K	1.14652	0.24428	0.82389	0.062(8)
H7D	290K	0.940(6)	0.2689(18)	0.8413(12)	0.20(3)
	33K	0.956(3)	0.2752(13)	0.8403(11)	0.057(7)
	35K	0.9280	0.2764	0.8413	0.019
	2K	0.95631	0.27531	0.83982	0.083(16)
C7	290K	1.001(2)	0.1328(8)	0.8381(5)	0.066(3)
	33K	0.9852(13)	0.1367(5)	0.8393(4)	0.0243(18)
	35K	0.975(4)	0.1377(3)	0.8398(8)	0.027(5)
	2K	0.9854(3)	0.13685(10)	0.83919(9)	0.032(3)
H7A	290K	1.055(5)	0.1018(19)	0.8152(16)	0.110(12)
	33K	1.057(5)	0.0902(14)	0.8071(11)	0.071(8)
	35K	1.0367	0.0886	0.8047	0.033
	2K	1.05823	0.09040	0.80701	0.073(10)
H7B	290K	0.858(3)	0.115(2)	0.8236(13)	0.118(8)
	33K	0.853(3)	0.1251(19)	0.8274(14)	0.079(9)
	35K	0.8339	0.1288	0.8353	0.033
	2K	0.85386	0.12495	0.82722	0.088(13)
C10	290K	0.9993(15)	0.2105(5)	0.5504(3)	0.0560(17)
	33K	0.9955(17)	0.2070(5)	0.5520(4)	0.034(2)
	35K	0.990(4)	0.2097(19)	0.5542(12)	0.008(7)
	2K	0.9956(3)	0.20711(10)	0.55175(9)	0.041(3)
H10	290K	1.002(5)	0.1433(14)	0.5700(11)	0.136(10)
	33K	0.985(8)	0.1361(16)	0.5724(12)	0.14(2)
	35K	0.964(10)	0.141(5)	0.577(3)	0.06(2)
	2K	0.98466	0.13639	0.57225	0.110(14)
N9	290K	1.0068(10)	0.2187(5)	0.4845(3)	0.0690(16)
	33K	1.0055(8)	0.2098(3)	0.4842(3)	0.0201(12)
	35K	0.997(2)	0.2092(11)	0.4843(7)	0.006(5)
	2K	1.0060(3)	0.21000(10)	0.48405(9)	0.025(2)
C8	290K	1.0363(11)	0.1151(6)	0.9138(5)	0.058(2)
	33K	1.0280(9)	0.1114(5)	0.9113(4)	0.0163(18)
	35K	1.027(3)	0.1091(16)	0.9114(12)	0.000(7)
	2K	1.0279(2)	0.11144(10)	0.91118(9)	0.020(3)
H8	290K	1.161(4)	0.1345(17)	0.9245(13)	0.115(8)
	33K	1.163(2)	0.1330(16)	0.9213(10)	0.044(6)
	35K	1.164(4)	0.129(5)	0.914(4)	0.06(2)
	2K	1.16284	0.13318	0.92127	0.049(7)
N8	290K	0.9031(19)	0.1584(8)	0.9554(5)	0.111(4)
	33K	0.921(2)	0.1623(8)	0.9576(6)	0.103(6)
	35K	0.917(4)	0.1585(19)	0.9617(13)	0.069(11)
	2K	0.9198(3)	0.16206(10)	0.95729(9)	0.109(9)
H8A	290K	0.905(4)	0.2284(16)	0.9610(10)	0.134(10)
	33K	0.890(6)	0.223(2)	0.9587(12)	0.107(10)
	35K	0.9212	0.2326	0.9512	0.103

Continued on next page

continued from previous page

		X	Y	Z	U_{iso}
	2K	0.88914	0.22327	0.95877	0.109(13)
H8B	290K	0.918(5)	0.1369(19)	1.0075(12)	0.145(12)
	33K	0.934(7)	0.139(2)	1.0060(12)	0.134(15)
	35K	0.9666	0.1454	1.0130	0.103
	2K	0.93118	0.13807	1.00596	0.102(15)
H8C	290K	0.784(3)	0.1342(15)	0.9403(13)	0.084(7)
	33K	0.764(4)	0.1324(17)	0.9357(14)	0.060(7)
	35K	0.7814	0.1341	0.9579	0.103
	2K	0.76642	0.13271	0.93560	0.070(10)
C9	290K	1.008(4)	0.0112(9)	0.9230(9)	0.134(6)
	33K	1.001(2)	0.0084(6)	0.9238(5)	0.043(3)
	35K	0.988(3)	0.0088(18)	0.9242(10)	0.037(9)
	2K	1.00070	0.00857	0.92366	0.054(5)
H9A	290K	1.016(6)	-0.0067(14)	0.9750(17)	0.145(10)
	33K	1.028(4)	-0.0073(13)	0.9787(12)	0.071(8)
	35K	1.0138	-0.0075	0.9776	0.056
	2K	1.02878	-0.00712	0.97842	0.079(12)
H9B	290K	1.130(7)	-0.022(3)	0.891(2)	0.21(2)
	33K	1.107(4)	-0.026(2)	0.8944(16)	0.095(12)
	35K	1.0716	-0.0339	0.8917	0.056
	2K	1.10725	-0.02623	0.89420	0.119(18)
H9C	290K	0.905(5)	-0.013(2)	0.919(2)	0.158(16)
	33K	0.908(5)	-0.012(2)	0.9109(18)	0.120(14)
	35K	0.8501	-0.0051	0.9125	0.056
	2K	0.90890	-0.01267	0.91064	0.114(16)
C11	290K	0.999(4)	0.1392(13)	0.4405(9)	0.148(6)
	33K	1.006(4)	0.1283(9)	0.4444(8)	0.095(6)
	35K	0.030(3)	0.1297(17)	0.4422(10)	0.033(10)
	2K	1.0057(2)	0.12832(10)	0.44435(9)	0.113(9)
H11A	290K	1.087(6)	0.138(3)	0.4027(13)	0.185(19)
	33K	1.120(6)	0.131(3)	0.4103(19)	0.116(15)
	35K	1.1342	0.1458	0.4057	0.050
	2K	1.11956	0.13093	0.40952	0.119(12)
H11B	290K	0.867(5)	0.152(3)	0.413(2)	0.206(19)
	33K	0.895(4)	0.117(3)	0.4123(19)	0.100(12)
	35K	0.9106	0.1109	0.4148	0.050
	2K	0.89557	0.11757	0.41254	0.116(12)
H11C	290K	1.016(8)	0.0752(19)	0.472(2)	0.199(19)
	33K	1.020(9)	0.068(3)	0.4754(14)	0.139(17)
	35K	1.0717	0.0719	0.4743	0.050
	2K	1.01893	0.06813	0.47525	0.128(12)
C12	290K	0.989(3)	0.3056(12)	0.4519(7)	0.107(4)
	33K	1.000(4)	0.2925(7)	0.4496(6)	0.082(6)
	35K	1.034(2)	0.2897(15)	0.4483(9)	0.017(8)
	2K	0.9998(2)	0.29265(10)	0.44947(9)	0.088(8)
H12A	290K	1.088(5)	0.317(3)	0.4106(18)	0.174(12)
	33K	1.088(7)	0.296(3)	0.4102(17)	0.147(19)
	35K	1.1435	0.2772	0.4136	0.026
	2K	1.09032	0.29625	0.41058	0.114(16)
H12B	290K	0.930(7)	0.357(3)	0.480(2)	0.174(13)
	33K	1.003(9)	0.350(2)	0.4868(15)	0.17(2)
	35K	1.0690	0.3445	0.4841	0.026
	2K	1.00534	0.34991	0.48651	0.135(16)
H12C	290K	0.881(6)	0.293(3)	0.433(2)	0.164(13)
	33K	0.869(4)	0.292(3)	0.426(2)	0.102(13)
	35K	0.9182	0.3105	0.4191	0.026

Continued on next page

continued from previous page					
		X	Y	Z	U_{iso}
	2K	0.86855	0.29062	0.42661	0.094(13)
O2W	290K	0.999(3)	0.4610(14)	0.8786(14)	0.234(18)
	33K	0.992(2)	0.4649(9)	0.8738(8)	0.072(6)
	35K	1.015(5)	0.468(3)	0.877(2)	0.071(13)
	2K	0.9926(3)	0.46505(10)	0.87382(9)	0.059(6)
H2WA	290K	0.933(6)	0.490(3)	0.8480(15)	0.41(7)
	33K	0.904(4)	0.489(3)	0.851(2)	0.110(16)
	35K	0.942(9)	0.498(6)	0.851(4)	0.09(2)
	2K	0.90426	0.48941	0.85154	0.18(5)
H2WB	290K	1.106(5)	0.483(4)	0.867(3)	0.32(4)
	33K	1.098(5)	0.478(3)	0.859(2)	0.138(19)
	35K	1.127(6)	0.480(7)	0.866(5)	0.10(2)
	2K	1.09958	0.47706	0.85878	0.13(3)
O3W	290K	0.975(7)	0.3440(12)	0.9826(10)	0.29(3)
	33K	1.030(7)	0.3485(15)	0.9800(9)	0.23(3)
	35K	1.032(6)	0.346(3)	0.9769(14)	0.058(14)
	2K	1.0242(3)	0.34811(10)	0.98007(9)	0.23(3)
H3WA	290K	0.984(5)	0.3644(19)	1.0242(9)	0.131(12)
	33K	1.020(4)	0.3684(15)	1.0214(11)	0.074(8)
	35K	1.002(9)	0.365(4)	1.0188(16)	0.026(13)
	2K	1.01996	0.36859	1.02140	0.095(16)
H3WB	290K	0.956(6)	0.400(2)	0.9651(19)	0.37(6)
	33K	0.982(6)	0.386(3)	0.9493(18)	0.132(17)
	35K	1.040(7)	0.381(4)	0.951(3)	0.036(17)
	2K	0.98094	0.38671	0.94934	0.095(2)

Table D.2: Anisotropic thermal parameters

		U_{11}	U_{22}	U_{33}	U_{23}	U_{13}	U_{12}
N1	290K	0.029(3)	0.045(3)	0.053(4)	-0.006(2)	-0.005(2)	-0.019(2)
N2	290K	0.032(2)	0.041(3)	0.037(3)	0.001(2)	0.003(2)	0.017(2)
N3	290K	0.035(2)	0.033(3)	0.072(4)	0.014(3)	0.005(2)	-0.010(2)
N4	290K	0.032(3)	0.022(3)	0.068(4)	-0.007(2)	0.007(2)	0.002(2)
N5	290K	0.230(11)	0.078(4)	0.045(4)	0.019(3)	0.013(6)	-0.013(6)
N6	290K	0.140(6)	0.067(3)	0.056(4)	0.016(3)	0.002(5)	-0.008(5)
C1	290K	0.018(3)	0.022(3)	0.041(4)	-0.001(3)	0.005(2)	0.004(2)
C2	290K	0.027(3)	0.016(2)	0.045(4)	0.019(2)	0.000(2)	0.014(2)
C3	290K	0.016(3)	0.037(3)	0.043(4)	-0.012(3)	-0.005(2)	0.004(2)
C4	290K	0.031(3)	0.026(3)	0.057(5)	-0.010(3)	0.004(2)	0.013(2)
C5	290K	0.079(4)	0.047(3)	0.031(3)	0.004(2)	-0.014(5)	-0.010(4)
C6	290K	0.067(3)	0.042(3)	0.034(3)	0.009(2)	0.022(4)	0.018(4)
O1	290K	0.056(3)	0.040(3)	0.034(3)	0.000(2)	-0.004(5)	0.004(4)
N7	290K	0.126(6)	0.050(3)	0.036(3)	0.002(2)	-0.007(5)	0.001(5)
H7C	290K	0.13(2)	0.15(3)	0.10(2)	0.039(19)	0.02(2)	-0.09(2)
H7D	290K	0.44(7)	0.098(16)	0.052(12)	0.030(10)	0.09(2)	0.14(2)
C7	290K	0.080(7)	0.073(7)	0.045(5)	0.022(4)	-0.021(6)	-0.030(7)
H7A	290K	0.15(3)	0.078(16)	0.09(2)	0.051(13)	0.000(16)	-0.00013)
H7B	290K	0.072(11)	0.16(2)	0.111(16)	0.026(15)	-0.033(11)	-0.050(12)
C10	290K	0.076(4)	0.059(4)	0.031(4)	-0.012(3)	0.013(5)	-0.004(5)
H10	290K	0.25(3)	0.063(11)	0.093(15)	-0.024(10)	0.03(2)	0.052(18)
N9	290K	0.055(3)	0.105(5)	0.045(3)	-0.021(3)	-0.012(3)	0.001(4)
C8	290K	0.055(5)	0.064(4)	0.054(5)	0.013(3)	-0.003(4)	0.008(4)
H8	290K	0.13(2)	0.111(19)	0.097(19)	0.017(15)	0.018(17)	-0.019(15)
N8	290K	0.195(11)	0.081(7)	0.057(6)	0.024(5)	0.053(6)	0.079(7)
H8A	290K	0.28(3)	0.059(12)	0.057(13)	0.029(9)	0.042(15)	0.028(15)
H8B	290K	0.26(3)	0.106(17)	0.067(15)	0.048(12)	0.092(16)	0.054(17)
H8C	290K	0.101(14)	0.069(12)	0.081(17)	0.009(11)	0.003(12)	0.014(10)
C9	290K	0.24(2)	0.064(7)	0.088(10)	-0.022(7)	-0.020(16)	0.040(13)
H9A	290K	0.25(3)	0.062(12)	0.114(18)	0.006(12)	0.00(2)	-0.022)
H9B	290K	0.29(5)	0.14(3)	0.17(4)	0.01(2)	0.03(3)	0.12(3)
H9C	290K	0.18(3)	0.105(19)	0.18(3)	0.052(19)	-0.01(2)	-0.10(2)
C11	290K	0.209(17)	0.152(13)	0.081(11)	-0.067(10)	-0.047(15)	0.034(16)
H11A	290K	0.31(5)	0.19(3)	0.038(15)	-0.071(18)	0.03(2)	0.03(2)
H11B	290K	0.17(3)	0.23(4)	0.20(3)	-0.12(3)	-0.08(2)	-0.01(2)
H11C	290K	0.33(5)	0.069(15)	0.19(2)	-0.055(17)	0.08(3)	-0.00(2)
C12	290K	0.150(11)	0.126(10)	0.044(6)	0.030(6)	0.006(10)	0.005(12)
H12A	290K	0.19(2)	0.22(3)	0.098(19)	0.03(2)	0.02(2)	0.00(2)
H12B	290K	0.24(3)	0.12(2)	0.14(2)	0.013(19)	0.04(2)	0.06(2)
H12C	290K	0.19(2)	0.18(2)	0.11(2)	0.02(2)	-0.02(2)	0.02(2)
O2W	290K	0.19(2)	0.128(16)	0.37(5)	-0.06(2)	-0.16(3)	0.102(17)
H2WA	290K	0.82(16)	0.35(7)	0.053(19)	0.12(3)	-0.09(4)	-0.36(9)
H2WB	290K	0.28(5)	0.17(3)	0.48(9)	0.01(4)	0.28(6)	-0.09(3)
O3W	290K	0.58(7)	0.058(10)	0.24(3)	0.038(16)	-0.21(49	-0.04(2)
H3WA	290K	0.20(2)	0.13(2)	0.046(12)	-0.016(12)	0.021(18)	0.08(2)
H3WB	290K	0.39(7)	0.54(10)	0.18(3)	0.26(5)	-0.19(4)	-0.36(2)

Appendix E

$[Cr(CN)_6][Mn(rac)-pnH(DMF)]{\cdot}2H_2O$

Table E.1: Atomic positions

		X	Y	Z	U_{iso}
Mn1	290K	1.0000(13)	0.2584(4)	0.7006(4)	0.0218(16)
	33K	0.9978(14)	0.2580(6)	0.6997(5)	0.005(2)
	35K	1.003(6)	0.259(3)	0.6998(18)	0.000(10)
	2K	0.9928(17)	0.2581(7)	0.6999(7)	0.009(2)
Cr1	290K	1.4948(18)	0.5046(5)	0.7647(5)	0.0259(18)
	33K	1.4985(19)	0.5056(6)	0.7631(6)	0.008(2)
	35K	1.507(9)	0.505(3)	0.7652(19)	0.005(12)
	2K	1.4988(2)	0.5057(1)	0.76294(9)	0.011(2)
N1	290K	1.2046(6)	0.3617(3)	0.7163(3)	0.0429(14)
	33K	1.2033(6)	0.3639(4)	0.7138(4)	0.0177(15)
	35K	1.204(3)	0.363(2)	0.7137(12)	0.015(7)
	2K	1.2031(2)	0.36396(10)	0.71349(9)	0.021(2)
N2	290K	1.2049(6)	0.1491(3)	0.6915(3)	0.0373(13)
	33K	1.2037(7)	0.1488(4)	0.6898(4)	0.0219(15)
	35K	1.196(3)	0.1476(16)	0.6923(12)	0.001(6)
	2K	1.2038(3)	0.14888(10)	0.68966(9)	0.023(2)
N3	290K	0.7975(6)	0.1493(3)	0.6920(3)	0.0469(15)
	33K	0.7996(7)	0.1482(4)	0.6917(3)	0.0159(14)
	35K	0.798(3)	0.1493(18)	0.6907(14)	0.026(8)
	2K	0.7997(2)	0.14842(10)	0.69156(9)	0.023(2)
N4	290K	0.7978(6)	0.3618(3)	0.7184(3)	0.0410(14)
	33K	0.8000(6)	0.3620(4)	0.7165(4)	0.0157(14)
	35K	0.796(3)	0.3610(17)	0.7159(11)	0.003(7)
	2K	0.8000(2)	0.36221(10)	0.71653(9)	0.019(2)
N5	290K	1.4753(18)	0.4108(5)	0.9110(4)	0.118(4)
	33K	1.494(3)	0.4070(5)	0.9088(4)	0.108(6)
	35K	1.533(4)	0.4087(17)	0.9103(13)	0.055(9)
	2K	1.4943(2)	0.40718(10)	0.90869(9)	0.118(10)
N6	290K	1.4867(15)	0.5944(4)	0.6157(3)	0.088(2)
	33K	1.4999(13)	0.5976(4)	0.6141(3)	0.0387(17)
	35K	1.506(3)	0.5954(12)	0.6142(10)	0.020(6)
	2K	1.5002(2)	0.59770(10)	0.61398(9)	0.045(2)
C1	290K	1.3095(7)	0.4137(4)	0.7334(3)	0.0276(17)
	33K	1.3088(9)	0.4133(5)	0.7314(5)	0.015(2)
	35K	1.301(4)	0.413(2)	0.7292(16)	0.003(9)
	2K	1.3088(2)	0.41353(10)	0.73130(9)	0.022(1)
C2	290K	1.3070(7)	0.0961(4)	0.7053(4)	0.0297(17)
	33K	1.3101(9)	0.0964(5)	0.7055(5)	0.015(2)
	35K	1.302(4)	0.104(2)	0.7062(15)	
	2K	1.3101(2)	0.09661(10)	0.70519(9)	0.021(2)
C3	290K	0.6869(7)	0.0984(5)	0.7070(4)	0.0327(18)
	33K	0.6896(9)	0.0967(6)	0.7065(4)	0.0131(19)
	35K	0.677(4)	0.090(2)	0.7045(16)	0.009(9)
	2K	0.6895(2)	0.09664(10)	0.70644(9)	0.015(2)
C4	290K	0.6907(9)	0.4135(4)	0.7343(4)	0.038(2)
	33K	0.6900(9)	0.4147(5)	0.7330(5)	0.0130(19)
	35K	0.680(4)	0.414(2)	0.7355(15)	
	2K	0.6899(3)	0.41482(10)	0.73283(9)	0.013(2)
C5	290K	1.4951(13)	0.4458(4)	0.8585(3)	0.0525(16)
	33K	1.4977(16)	0.4439(5)	0.8569(4)	0.031(2)
	35K	1.482(4)	0.4431(18)	0.8557(13)	0.014(8)
	2K	1.4980(3)	0.44404(10)	0.85673(9)	0.031(2)
C6	290K	1.5019(13)	0.5634(4)	0.6688(3)	0.0482(15)
	33K	1.5059(13)	0.5660(4)	0.6678(3)	0.0211(16)
	35K	1.508(5)	0.5658(19)	0.6690(14)	0.023(8)

Continued on next page

continued from previous page

		X	Y	Z	U_{iso}
	2K	1.5063(2)	0.56614(10)	0.66770(9)	0.024(2)
O1	290K	0.9953(13)	0.2752(4)	0.5917(3)	0.0440(15)
	33K	0.9962(11)	0.2742(5)	0.5899(3)	0.0131(15)
	35K	1.098(4)	0.2775(18)	0.5916(12)	0.000(8)
	2K	0.9962(2)	0.27424(10)	0.58968(9)	0.018(2)
N7	290K	1.0219(16)	0.2286(4)	0.8162(3)	0.071(2)
	33K	1.0290(9)	0.2293(4)	0.8160(3)	0.0207(14)
	35K	1.017(2)	0.2282(10)	0.8158(8)	0.016(5)
	2K	1.0290(2)	0.22959(10)	0.81585(9)	0.023(2)
H7C	290K	1.137(4)	0.239(2)	0.8269(16)	0.133(13)
	33K	1.146(4)	0.2441(16)	0.8241(12)	0.056(6)
	35K	1.1497	0.2447	0.8329	0.019
	2K	1.14652	0.24428	0.82389	0.062(8)
H7D	290K	0.940(6)	0.2689(18)	0.8413(12)	0.20(3)
	33K	0.956(3)	0.2752(13)	0.8403(11)	0.057(7)
	35K	0.9280	0.2764	0.8413	0.019
	2K	0.95631	0.27531	0.83982	0.083(16)
C7	290K	1.001(2)	0.1328(8)	0.8381(5)	0.066(3)
	33K	0.9852(13)	0.1367(5)	0.8393(4)	0.0243(18)
	35K	0.975(4)	0.1377(3)	0.8398(8)	0.027(5)
	2K	0.9854(3)	0.13685(10)	0.83919(9)	0.032(3)
H7A	290K	1.055(5)	0.1018(19)	0.8152(16)	0.110(12)
	33K	1.057(5)	0.0902(14)	0.8071(11)	0.071(8)
	35K	1.0367	0.0886	0.8047	0.033
	2K	1.05823	0.09040	0.80701	0.073(10)
H7B	290K	0.858(3)	0.115(2)	0.8236(13)	0.118(8)
	33K	0.853(3)	0.1251(19)	0.8274(14)	0.079(9)
	35K	0.8339	0.1288	0.8353	0.033
	2K	0.85386	0.12495	0.82722	0.088(13)
C10	290K	0.9993(15)	0.2105(5)	0.5504(3)	0.0560(17)
	33K	0.9955(17)	0.2070(5)	0.5520(4)	0.034(2)
	35K	0.990(4)	0.2097(19)	0.5542(12)	0.008(7)
	2K	0.9956(3)	0.20711(10)	0.55175(9)	0.041(3)
H10	290K	1.002(5)	0.1433(14)	0.5700(11)	0.136(10)
	33K	0.985(8)	0.1361(16)	0.5724(12)	0.14(2)
	35K	0.964(10)	0.141(5)	0.577(3)	0.06(2)
	2K	0.98466	0.13639	0.57225	0.110(14)
N9	290K	1.0068(10)	0.2187(5)	0.4845(3)	0.0690(16)
	33K	1.0055(8)	0.2098(3)	0.4842(3)	0.0201(12)
	35K	0.997(2)	0.2092(11)	0.4843(7)	0.006(5)
	2K	1.0060(3)	0.21000(10)	0.48405(9)	0.025(2)
C8	290K	1.0363(11)	0.1151(6)	0.9138(5)	0.058(2)
	33K	1.0280(9)	0.1114(5)	0.9113(4)	0.0163(18)
	35K	1.027(3)	0.1091(16)	0.9114(12)	0.000(7)
	2K	1.0279(2)	0.11144(10)	0.91118(9)	0.020(3)
H8	290K	1.161(4)	0.1345(17)	0.9245(13)	0.115(8)
	33K	1.163(2)	0.1330(16)	0.9213(10)	0.044(6)
	35K	1.164(4)	0.129(5)	0.914(4)	0.06(2)
	2K	1.16284	0.13318	0.92127	0.049(7)
N8	290K	0.9031(19)	0.1584(8)	0.9554(5)	0.111(4)
	33K	0.921(2)	0.1623(8)	0.9576(6)	0.103(6)
	35K	0.917(4)	0.1585(19)	0.9617(13)	0.069(11)
	2K	0.9198(3)	0.16206(10)	0.95729(9)	0.109(9)
H8A	290K	0.905(4)	0.2284(16)	0.9610(10)	0.134(10)
	33K	0.890(6)	0.223(2)	0.9587(12)	0.107(10)
	35K	0.9212	0.2326	0.9512	0.103

Continued on next page

continued from previous page

		X	Y	Z	U_{iso}
	2K	0.88914	0.22327	0.95877	0.109(13)
H8B	290K	0.918(5)	0.1369(19)	1.0075(12)	0.145(12)
	33K	0.934(7)	0.139(2)	1.0060(12)	0.134(15)
	35K	0.9666	0.1454	1.0130	0.103
	2K	0.93118	0.13807	1.00596	0.102(15)
H8C	290K	0.784(3)	0.1342(15)	0.9403(13)	0.084(7)
	33K	0.764(4)	0.1324(17)	0.9357(14)	0.060(7)
	35K	0.7814	0.1341	0.9579	0.103
	2K	0.76642	0.13271	0.93560	0.070(10)
C9	290K	1.008(4)	0.0112(9)	0.9230(9)	0.134(6)
	33K	1.001(2)	0.0084(6)	0.9238(5)	0.043(3)
	35K	0.988(3)	0.0088(18)	0.9242(10)	0.037(9)
	2K	1.00070	0.00857	0.92366	0.054(5)
H9A	290K	1.016(6)	-0.0067(14)	0.9750(17)	0.145(10)
	33K	1.028(4)	-0.0073(13)	0.9787(12)	0.071(8)
	35K	1.0138	-0.0075	0.9776	0.056
	2K	1.02878	-0.00712	0.97842	0.079(12)
H9B	290K	1.130(7)	-0.022(3)	0.891(2)	0.21(2)
	33K	1.107(4)	-0.026(2)	0.8944(16)	0.095(12)
	35K	1.0716	-0.0339	0.8917	0.056
	2K	1.10725	-0.02623	0.89420	0.119(18)
H9C	290K	0.905(5)	-0.013(2)	0.919(2)	0.158(16)
	33K	0.908(5)	-0.012(2)	0.9109(18)	0.120(14)
	35K	0.8501	-0.0051	0.9125	0.056
	2K	0.90890	-0.01267	0.91064	0.114(16)
C11	290K	0.999(4)	0.1392(13)	0.4405(9)	0.148(6)
	33K	1.006(4)	0.1283(9)	0.4444(8)	0.095(6)
	35K	0.030(3)	0.1297(17)	0.4422(10)	0.033(10)
	2K	1.0057(2)	0.12832(10)	0.44435(9)	0.113(9)
H11A	290K	1.087(6)	0.138(3)	0.4027(13)	0.185(19)
	33K	1.120(6)	0.131(3)	0.4103(19)	0.116(15)
	35K	1.1342	0.1458	0.4057	0.050
	2K	1.11956	0.13093	0.40952	0.119(12)
H11B	290K	0.867(5)	0.152(3)	0.413(2)	0.206(19)
	33K	0.895(4)	0.117(3)	0.4123(19)	0.100(12)
	35K	0.9106	0.1109	0.4148	0.050
	2K	0.89557	0.11757	0.41254	0.116(12)
H11C	290K	1.016(8)	0.0752(19)	0.472(2)	0.199(19)
	33K	1.020(9)	0.068(3)	0.4754(14)	0.139(17)
	35K	1.0717	0.0719	0.4743	0.050
	2K	1.01893	0.06813	0.47525	0.128(12)
C12	290K	0.989(3)	0.3056(12)	0.4519(7)	0.107(4)
	33K	1.000(4)	0.2925(7)	0.4496(6)	0.082(6)
	35K	1.034(2)	0.2897(15)	0.4483(9)	0.017(8)
	2K	0.9998(2)	0.29265(10)	0.44947(9)	0.088(8)
H12A	290K	1.088(5)	0.317(3)	0.4106(18)	0.174(12)
	33K	1.088(7)	0.296(3)	0.4102(17)	0.147(19)
	35K	1.1435	0.2772	0.4136	0.026
	2K	1.09032	0.29625	0.41058	0.114(16)
H12B	290K	0.930(7)	0.357(3)	0.480(2)	0.174(13)
	33K	1.003(9)	0.350(2)	0.4868(15)	0.17(2)
	35K	1.0690	0.3445	0.4841	0.026
	2K	1.00534	0.34991	0.48651	0.135(16)
H12C	290K	0.881(6)	0.293(3)	0.433(2)	0.164(13)
	33K	0.869(4)	0.292(3)	0.426(2)	0.102(13)
	35K	0.9182	0.3105	0.4191	0.026

Continued on next page

continued from previous page					
		X	Y	Z	U_{iso}
	2K	0.86855	0.29062	0.42661	0.094(13)
O2W	290K	0.999(3)	0.4610(14)	0.8786(14)	0.234(18)
	33K	0.992(2)	0.4649(9)	0.8738(8)	0.072(6)
	35K	1.015(5)	0.468(3)	0.877(2)	0.071(13)
	2K	0.9926(3)	0.46505(10)	0.87382(9)	0.059(6)
H2WA	290K	0.933(6)	0.490(3)	0.8480(15)	0.41(7)
	33K	0.904(4)	0.489(3)	0.851(2)	0.110(16)
	35K	0.942(9)	0.498(6)	0.851(4)	0.09(2)
	2K	0.90426	0.48941	0.85154	0.18(5)
H2WB	290K	1.106(5)	0.483(4)	0.867(3)	0.32(4)
	33K	1.098(5)	0.478(3)	0.859(2)	0.138(19)
	35K	1.127(6)	0.480(7)	0.866(5)	0.10(2)
	2K	1.09958	0.47706	0.85878	0.13(3)
O3W	290K	0.975(7)	0.3440(12)	0.9826(10)	0.29(3)
	33K	1.030(7)	0.3485(15)	0.9800(9)	0.23(3)
	35K	1.032(6)	0.346(3)	0.9769(14)	0.058(14)
	2K	1.0242(3)	0.34811(10)	0.98007(9)	0.23(3)
H3WA	290K	0.984(5)	0.3644(19)	1.0242(9)	0.131(12)
	33K	1.020(4)	0.3684(15)	1.0214(11)	0.074(8)
	35K	1.002(9)	0.365(4)	1.0188(16)	0.026(13)
	2K	1.01996	0.36859	1.02140	0.095(16)
H3WB	290K	0.956(6)	0.400(2)	0.9651(19)	0.37(6)
	33K	0.982(6)	0.386(3)	0.9493(18)	0.132(17)
	35K	1.040(7)	0.381(4)	0.951(3)	0.036(17)
	2K	0.98094	0.38671	0.94934	0.095(2)

Table E.2: Anisotropic thermal parameters

		U_{11}	U_{22}	U_{33}	U_{23}	U_{13}	U_{12}
N1	290K	0.029(3)	0.045(3)	0.053(4)	-0.006(2)	-0.005(2)	-0.019(2)
N2	290K	0.032(2)	0.041(3)	0.037(3)	0.001(2)	0.003(2)	0.017(2)
N3	290K	0.035(2)	0.033(3)	0.072(4)	0.014(3)	0.005(2)	-0.010(2)
N4	290K	0.032(3)	0.022(3)	0.068(4)	-0.007(2)	0.007(2)	0.002(2)
N5	290K	0.230(11)	0.078(4)	0.045(4)	0.019(3)	0.013(6)	-0.013(6)
N6	290K	0.140(6)	0.067(3)	0.056(4)	0.016(3)	0.002(5)	-0.008(5)
C1	290K	0.018(3)	0.022(3)	0.041(4)	-0.001(3)	0.005(2)	0.004(2)
C2	290K	0.027(3)	0.016(2)	0.045(4)	0.019(2)	0.000(2)	0.014(2)
C3	290K	0.016(3)	0.037(3)	0.043(4)	-0.012(3)	-0.005(2)	0.004(2)
C4	290K	0.031(3)	0.026(3)	0.057(5)	-0.010(3)	0.004(2)	0.013(2)
C5	290K	0.079(4)	0.047(3)	0.031(3)	0.004(2)	-0.014(5)	-0.010(4)
C6	290K	0.067(3)	0.042(3)	0.034(3)	0.009(2)	0.022(4)	0.018(4)
O1	290K	0.056(3)	0.040(3)	0.034(3)	0.000(2)	-0.004(5)	0.004(4)
N7	290K	0.126(6)	0.050(3)	0.036(3)	0.002(2)	-0.007(5)	0.001(5)
H7C	290K	0.13(2)	0.15(3)	0.10(2)	0.039(19)	0.02(2)	-0.09(2)
H7D	290K	0.44(7)	0.098(16)	0.052(12)	0.030(10)	0.09(2)	0.14(2)
C7	290K	0.080(7)	0.073(7)	0.045(5)	0.022(4)	-0.021(6)	-0.030(7)
H7A	290K	0.15(3)	0.078(16)	0.09(2)	0.051(13)	0.000(16)	-0.00013)
H7B	290K	0.072(11)	0.16(2)	0.111(16)	0.026(15)	-0.033(11)	-0.050(12)
C10	290K	0.076(4)	0.059(4)	0.031(4)	-0.012(3)	0.013(5)	-0.004(5)
H10	290K	0.25(3)	0.063(11)	0.093(15)	-0.024(10)	0.03(2)	0.052(18)
N9	290K	0.055(3)	0.105(5)	0.045(3)	-0.021(3)	-0.012(3)	0.001(4)
C8	290K	0.055(5)	0.064(4)	0.054(5)	0.013(3)	-0.003(4)	0.008(4)
H8	290K	0.13(2)	0.111(19)	0.097(19)	0.017(15)	0.018(17)	-0.019(15)
N8	290K	0.195(11)	0.081(7)	0.057(6)	0.024(5)	0.053(6)	0.079(7)
H8A	290K	0.28(3)	0.059(12)	0.057(13)	0.029(9)	0.042(15)	0.028(15)
H8B	290K	0.26(3)	0.106(17)	0.067(15)	0.048(12)	0.092(16)	0.054(17)
H8C	290K	0.101(14)	0.069(12)	0.081(17)	0.009(11)	0.003(12)	0.014(10)
C9	290K	0.24(2)	0.064(7)	0.088(10)	-0.022(7)	-0.020(16)	0.040(13)
H9A	290K	0.25(3)	0.062(12)	0.114(18)	0.006(12)	0.00(2)	-0.022)
H9B	290K	0.29(5)	0.14(3)	0.17(4)	0.01(2)	0.03(3)	0.12(3)
H9C	290K	0.18(3)	0.105(19)	0.18(3)	0.052(19)	-0.01(2)	-0.10(2)
C11	290K	0.209(17)	0.152(13)	0.081(11)	-0.067(10)	-0.047(15)	0.034(16)
H11A	290K	0.31(5)	0.19(3)	0.038(15)	-0.071(18)	0.03(2)	0.03(2)
H11B	290K	0.17(3)	0.23(4)	0.20(3)	-0.12(3)	-0.08(2)	-0.01(2)
H11C	290K	0.33(5)	0.069(15)	0.19(2)	-0.055(17)	0.08(3)	-0.00(2)
C12	290K	0.150(11)	0.126(10)	0.044(6)	0.030(6)	0.006(10)	0.005(12)
H12A	290K	0.19(2)	0.22(3)	0.098(19)	0.03(2)	0.02(2)	0.00(2)
H12B	290K	0.24(3)	0.12(2)	0.14(2)	0.013(19)	0.04(2)	0.06(2)
H12C	290K	0.19(2)	0.18(2)	0.11(2)	0.02(2)	-0.02(2)	0.02(2)
O2W	290K	0.19(2)	0.128(16)	0.37(5)	-0.06(2)	-0.16(3)	0.102(17)
H2WA	290K	0.82(16)	0.35(7)	0.053(19)	0.12(3)	-0.09(4)	-0.36(9)
H2WB	290K	0.28(5)	0.17(3)	0.48(9)	0.01(4)	0.28(6)	-0.09(3)
O3W	290K	0.58(7)	0.058(10)	0.24(3)	0.038(16)	-0.21(49	-0.04(2)
H3WA	290K	0.20(2)	0.13(2)	0.046(12)	-0.016(12)	0.021(18)	0.08(2)
H3WB	290K	0.39(7)	0.54(10)	0.18(3)	0.26(5)	-0.19(4)	-0.36(2)

Bibliography

[1] A. Cornia M. Mannini L. Sorace D. Gatteschi, L. Bogani and Roberta Sessoli. Molecular magnetism, status and perspectives. *Solid State Sciences*, 10:1701–1709, 2008.

[2] C. Train, M. Gruselle and M. Verdaguer. The fruitful introduction of chirality and control of absolute configuration in molecular magnets. *Chem. Soc. Rev.*, 40:3297–3312, 2011.

[3] G. L. J. A. Rikken and E. Raupach. Pure and cascaded magnetochiral anisotropy in optical absorption. *Phys. Rev. E*, 58:5081–5084, 1998.

[4] Dante Gatteschi and Roberta Sessoli. Molecular nanomagnets: the first 10 years. *Journal of Magnetism and Magnetic Materials*, 272:1030–1036, 2004.

[5] L. Bogani and W. Wernsdorfer. Molecular spintronics using single-molecule magnets. *Nat. Mater.*, 7:179–186, 2008.

[6] W. Kaneko, S. Kitagawa and M. Ohba. Chiral Cyanide-Bridged $Mn^{II}Mn^{III}$ Ferrimagnets, $[Mn^{II}(HL)(H_2O)][Mn^{III}(CN)_6] \cdot 2H_2O$ (L=S- or R-1,2-diaminopropane): Syntheses, Structures, and Magnetic Behaviors. *J. Am. Chem. Soc.*, 129:248–249, 2007.

[7] H. Imai, K. Inoue and K. Kikuchi. Crystal structures and magnetic properties of chiral and achiral cyanide-bridged bimetallic layered compounds. *Polyhedron*, 24:2808–2812, 2005.

[8] K. Inoue, K. Kikuchi, M. Ohba and H. Okawa. Structure and Magnetic properties of a chiral two-dimensional ferrimagnet with Tc of 38K. *Angew. Chem. Internat. Ed. Eng.*, 42:4810–4813, 2003.

[9] J. Rodriguez-Carvajal. Recent advances in magnetic structure determination by neutron powder diffraction. *Physica B*, 192:55, 1992.

[10] M. Murrie. Cobalt(II) single-molecule magnets. *Chem. Soc. Rev.*, 39:1986–1995, 2010.

[11] H. Miyasaka, K. Nakata, K. Sugiura, M. Yamashita and R. Clérac. A Three-Dimensional Ferrimagnet Composed of Mixed-Valence Mn4 Clusters Linked by an Mn[N(CN)2]64- Unit. *Angew. Chem. Int. Ed.*, 43:707–711, 2004.

[12] S. Yamashita, K. Hino, Y. Inoue, Y. Okada, R. Hirahara, Y. Nakazawa, H. Miyasaka and M. Yamashita. Heat Capacities Of A Networked System Of Single Molecule Magnet with Three-Dimensional Structure. *J. Therm. Anal. Cal.*, 92:439–442, 2008.

[13] A. Morello, F. L. Mettes, O. N. Bakharev, H. B. Brom, L. J. de Jongh, F. Luis, J. F. Fernández and G. Aromí. Magnetic dipolar ordering and relaxation in the high-spin molecular cluster compound Mn6. *Phys. Rev. B*, 73:134406–134423, 2006.

[14] E. Burzuri, J. Campo, L. R. Falvello, E. Forcen-Vazquez, F. Luis, I. Mayoral, F. Palacio, C. Saenz de Pipaon and M. Tomas. A Tetragonal 2D Array of Single-Molecule Magnets with Modulated Collective Behavior. *Chem. Eur. J.*, 17:2818–2822, 2011.

[15] L. R. Falvello, E. Forcen-Vazquez, I. Mayoral, M. Tomas and F. Palacio. A square two-dimensional polymer of cobalt citrate cubanes. *Acta Cryst. C*, 67:m359–m363, 2011.

[16] E. Coronado, P. Delhaes, D. Gatteschi and J. S. Miller (Eds.). *Molecular Magnetism: From Molecular Assemblies to the Devices.* Springer, 1996.

[17] D. Gatteschi, O. Khan, J. S. Miller and F. Palacio (Eds.). *Magnetic Molecular Materials.* Springer, 1991.

[18] J. S. Miller, J. C. Calabrese, H. Rommerlmann, S. R. Chittipeddi, J. H. Zhang, W. M. Reiff and A. J. Epstein. Ferromagnetic behavior of $[Fe(C_5Me_5)_2]^+[TCNE]^-$. Structural and Magnetic Characterization of Decamethylferrocenium Tetracyanoethenide, $[Fe(C_5Me_5)_2]^+[TCNE]^-{\cdot}MeCN$, and Decamethylferrocenium Pentacyanopropenide, $[Fe(C_5Me_5)_2]^+[C_3(CN)_5]^-$. *JACS*, 109:769–781, 1987.

[19] S. Ferlay, T. Mallah, R. Ouahes, P. Veillet and M. Verdaguer. A room-temperature organometallic magnet based on Prussian blue. *Nature*, 378:701–703, 1995.

[20] M. Tamura, Y. Nakazawa, D. Shiomi, K. Nozawa, Y. Hosokoshi, M. Ishikawa, M. Takahashi and M. Kinoshita. Bulk ferromagnetism in the β-phase crystal of the p-nitrophenyl nitronyl nitroxide radical. *Chem. Phys. Lett.*, 186:401–404, 1991.

[21] A. J. Banister, N. Bricklebank, I. Lavender, J. M. Rawson, C. I. Gregory, B. K. Tanner, W. Clegg, M. R. J. Elsegood and F. Palacio. Spontaneus Magnetization in a Sulfur-Nitrogen Radical at 36K. *Angew. Chem. Int. Ed. Engl.*, 35:2533–2535, 1996.

[22] F. Palacio, G. Antorrena, M. Castro, R. Burriel, J. Rawson, J. N. B. Smith, N. Bricklebank, J. Novoa and C. Ritter. High Temperature Magnetic ORdering in a New Organic Magnet. *Phys. Rev. Lett*, 11:1992–2003, 2001.

[23] F. Palacio and J. S. Miller. Molecular electronics: A dual-action material. *Nature*, 408:421–422, 2000.

[24] E. Coronado, J. R. Galán-Mascarós, C. J. Gómez-García and Vladimir Laukhin. Coexistence of ferromagnetism and metallic conductivity in a molecule-based layered compound. *Nature*, 408:447–449, 2000.

[25] J. Crassous. Chiral transfer in coordination complexes: towards molecular materials. *Chem. Soc. Rev.*, 38:830–845, 2009.

[26] *International Tables of crystallographic. Volumen A*. International union of crystallographic.

[27] G. L. J. A. Rikken and E. Raupach. Observation of magneto-chiral dichroism. *Nature*, 390:493–494, 1997.

[28] Cyrille Train, Ruxandra Gheorghe, Vojislav Krstic, Lise-Marie Chamoreau, Nikolai S. Ovanesyan, Geert L. J. A. Rikken, Michel Gruselle and Michel Verdaguer. Strong magneto-chiral dichroism in enantiopure chiral ferromagnets. *Phys. Rev. E*, 58:5081–5084, 1998.

[29] W. Eerenstein, N. D. Mathur and J. F. Scott. Multiferroic and magnetoelectric materials. *Nature*, 442:759–765, 2006.

[30] T. Kimura, Y. Sekio, H. Nakamura, T. Siegrist and A. P. Ramirez. Cupric oxide as an induced-multiferroic with high T_c. *Nature Mater.*, 7:291–294, 2008.

[31] C. González Jiménez. *Neutron diffractyion studies of the coexistence between Nuclear and Magnetic Chirality in Molecular compounds*. PhD thesis, Universidad de Zaragoza, Departamento Física de la Materia condensada, December 2006.

[32] J. Kishine, K. Inoue and Y. Yoshida. Synthesis, Structure and Magnetic Properties of Chiral Molecule-Based Magnets. *Progress of Theoretical Physics Supplement*, 159:82–95, 2005.

[33] I. V. Blokhin, A. S. Markosyan, R. B. Morgunov, K. Inoue, Y. Tanimoto and Y. Yoshida. Magnetic Resonance in a $[Cr(CN)_6Mn(S) - pnH - (H_2O)](H_2O)$ Single-Crystal Molecular Ferrimagnet. *Physics of the Solid State*, 47:2106–2113, 2005.

[34] T. Lis. Preparation, structure, and magnetic properties of a dodecanuclear mixed-valence manganese carboxylate. *Acta Crystallogr. B*, 36, 1980.

[35] D. Gatteschi and R. Sessoli. Quantum Tunneling of Magnetization and Related Phenomena in Molecular Materials. *Angew. Chem. Int. Ed.*, 42:268–297, 2003.

[36] M. N. Leuenberger and D. Loss. Quantum computing in molecular magnets. *Nature*, 410:789–793, 2001.

[37] S. Sanvito. Molecular spintronics. *Chem. Soc. Rev.*, 40:3336–3355, 2011.

[38] A. D. McNaught and A. Wilkinson. *IUPAC. Compendium of Chemical Terminology.* Blackwell Scientific Publications, 1997.

[39] Pasteur. *Researches on the molecular asymmetry of natural organic products*, volume 14. Alembic Club Reprints, facsimile reproduction by SPIE in a 1990 book, 1848.

[40] R.S. Cahn and C.K. Ingold and V. Prelog. *Angew. Chem. Internat. Ed. Eng.*, 5:385–415, 1966.

[41] V. Prelog and G. Helmchen. *Angew. Chem. Internat. Ed. Eng.*, 21:567–583, 1982.

[42] C. Giacovazzo, H. L. Monaco, D. Viterbo, F. Scordari, G. Gilli, G. Zanotti and M. Catti. *Fundamentals of Crystallography.* International union of crystallographic. Oxford University Press, 1992.

[43] J. Villain. 2-Level Systems in a Spin-Glass Model: I. General Formalism and 2-Dimensional Model. *J. Phys. C*, 10:4793–4803, 1977.

[44] S. Miyashita and H. Shiba. Nature of the Phase Transition of the Two-Dimensional Antiferromagnetic Plane Rotator Model on the Triangular Lattice. *J. Phys. Soc. Jpn.*, 53:1145–1154, 1984.

[45] H. Kawamura and H. Shiba. Phase Transition of the two-dimensional heisenberg antiferromagnet on the thiangular lattice. *J. Phys. Soc. Jpn.*, 53:4138–4154, 1984.

[46] H. Kawamura. Monte-Carlo Study of Chiral Criticality - XY and Heisenberg Stacked-Triangular Antiferromagnets. *J. Phys. Soc. Jpn.*, 61:1299–1325, 1992.

[47] V. P. Plakhty, S. V. Maleyev, J. Kulda, E.D. Visser, J. Wosnitza, E. V. Moskvin, T. Bruckel and R. K. Kremer. Spin chirality and polarised neutron scattering. *Phys. B*, 294:60–66, 2001.

[48] M. Blume. Magnetic scattering of neutrons by noncollinear Spin Densities. *Phys. Rev. Lett.*, 10:489–491, 1963.

[49] S. V Maleyev and V. G. Baryakhtar and R. A. Suris. The scattering of slow neutrons by complex magnetic structures. *Sov. Phys. Solid State*, 4:2533–2539, 1963.

[50] H. Kawamura. Universality of phase transitions of frustrated antiferromagnets. *J. Phys. Condens. Matter.*, 10:4707–4754, 1998.

[51] M.J. Harris and M.P. Zinkin. Frustration in the pyrochlore antiferromagnets. *Mod. Phys. Lett. B*, 10:417–438, 1996.

[52] G. Tatara and H. Kawamura. Chirality-Driven Anomalous Hall Effect in Weak Coupling Regime. *J. Phys. Soc. Jpn.*, 71:2613–2616, 2002.

[53] O. Khan. *Molecular Magnetism.* VCH Publishers, Inc., 1993.

[54] I. Dzyaloshinsky. A Thermodynamic Theory of Weak Ferromagnetism of Antiferromagnetics. *J. Phys. Chem. Solids*, 4:241–255, 1958.

[55] T. Moriya. Anisotropic Superexchange Interaction and Weak Ferromagnetism. *Phys. Rev.*, 120:91–98, 1960.

[56] T. Moriya. *Magnetism.* G. T. Rado, H. Shul, 1963.

[57] V. I. Sokolov. *Chirality and optical Activity in Organometallic Compounds.* Gordon and Breach Science Publishers, 1990.

[58] D. B. Amabilino. *Chirality at the Nanoscale: Nanoparticles, Surfaces, Materials and more.* Wiley-VCH, 2009.

[59] H. Amouri and M. Gruselle. *Chirality in Transition Metal Chemistry: Molecules, Supramolecular Assemblies and Materials.* John Wiley and Sons, 2008.

[60] C. Noguez and I. L. Garzón. Optically active metal nanoparticles. *Chem. Soc. Rev.*, 38:757–771, 2009.

[61] M. Faraday. . *Philos. Mag.*, 28:294, 1946.

[62] G. Wagniere and A. Meier. The influence of a static magnetic field on the absorption coefficient of a chiral molecule. *Chem. Phys. Lett.*, 93:78–81, 1982.

[63] L. D. Barron and J. Vrbancich. Magneto-chiral birefringence and dichroism. *Mol. Phys.*, 51:715–730, 1984.

[64] M. Ceolín, S. Goberna-Ferrón and J. R. Galán-Mascarós. Strong hard X-ray magnetochiral dichroism in paramagnetic enantiopure molecules. *Adv. Mater*, 24:3120–3123, 2012.

[65] P. Kleindienst and G. H. Wagniere. Interferometric detection of magnetochiral birrefringence. *Chem. Phys. Lett.*, 288:89–97, 1998.

[66] C. A. Beevers and H. Lipson. . *Z. Krist.*, 83:123–135, 1932.

[67] A. W. Schlueter, R. A. Jacobson and R. E. Rundle. Interferometric detection of magnetochiral birrefringence. *Inorg. Chem.*, 5:277–280, 1966.

[68] H. Kumagai and K. Inoue. A chiral molecular based metamagnet prepared from manganese ions and a chiral triplet organic radical as a bridging ligand. *Angew. Chem., Int. Ed.*, 38:1601–1603, 1999.

[69] M. Minguet, D. Luneau, E. Lhotel, V. Villar, C. Paulsen, D. B. Amabilino and J. Veciana. Interferometric detection of magnetochiral birefringence. *Angew. Chem., Int. Ed.*, 41:586–589, 2002.

[70] A. Beghidja, P. Rabu, G. Rogez and R. Welter. Synthesis, structure and magnetic properties of chiral and nonchiral transition-metal malates. *Chem. Eur. J.*, 12:7627–7638, 2006.

[71] E. Coronado, J. R. Galan-Mascaros, C. J. Gomez-Garcia and A. Murcia-Martinez. Chiral molecular magnets: Synthesis, structure, and magnetic behavior of the series [M(L-tart)] $M = Mn^{II}$, Fe^{II}, Co^{II}, Ni^{II} L-tart =(2R,3R)-(+)-tartrate). *Chem. Eur. J.*, 12:3484–3492, 2006.

[72] M. Pilkington and S. Decurtins. *Magnetism: Molecules to Materials II.* Wiley-VCH, 2001.

[73] R. Clement, S. Decurtins, M. Gruselle and C. Train. Polyfunctional Two-(2D) and Three-(3D) Dimensional Oxalate Bridged Bimetallic Magnets. *Monatsh. Chem.*, 134:117–135, 2003.

[74] M. Gruselle, C. Train, K. Boubekeur, P. Gredin and N. Ovanesyan. Enantioselective self-assembly of chiral bimetallic oxalate-based networks. *Coord. Chem. Rev.*, 250:2491–2500, 2006.

[75] M. Verdaguer and G. Girolami. *Magnetism : Molecules to Materials V. 9. Magnetic Prussian Blue Analogs.* WILEY-VCH Verlag GmbH and Co, 2007.

[76] J. B. Goodenough. *Magnetism and the Chemical Bond.* John Wiley And Sons., 1963.

[77] K. Inoue, H. Imai, P. S. Ghalsasi, K. Kikuchi, M. Ohba, H. Okawa and J. V. Yakhmi. A three-dimensional ferrimagnet with a high magnetic transition temperature Tc of 53 K based on a chiral molecule. *Angew. Chem. Internat. Ed. Eng.*, 40:4242–4245, 2001.

[78] H. Imai, K. Inoue, K. Kikuchi, Y. Yoshida, M. Ito, T. Sunahara and S. Onaka. Three-Dimensional Chiral Molecule-Based Ferrimagnet with Triple-Helical-Strand Structure. *Angew. Chem. Internat. Ed.*, 43:5618–5621, 2004.

[79] "H. Higashikawa, K. Okuda, J. Kishine, N. Masuhara and K. Inoue. Chiral Effects on Magnetic Properties for Chiral and Racemic W^V-Cu^{II} Prussian Blue Analogues. *Chem. Lett.*, 36:1022–1023, 2007.

[80] A. Hoshikawa, T. Kamiyama, A. Purwanto, K. Ohishi, W. Higemoto, T. Ishigaki, H. Imai and K. Inoue. Time-of-Flight Neutron Powder Diffraction Studies on a Chiral Two-dimensional Molecule-based Magnet. *Angew. Chem. Internat. Ed. Eng.*, 73:2597–2600, 2004.

[81] K. Ohishi, W. Higemoto, A. Koda, S. R. Saha, R. Kadono, K. Inoue, H. Imai and H. Higashikawa. Possible Magnetic Chirality in Optically Chiral Magnet $[Cr(CN)_6][Mn(S)-pnH(H_2O)](H_2O)$ Probed by Muon Spin Rotation and Relaxation. *Journal of the Physical Society of Japan*, 75, 2006.

[82] R. B. Morgunov, M. V. Kirman, V. L. Berdinski, K. Inoue and J. Kishine. Spin Solitons and Waves in Chiral Molecular Ferrimagnets. *Journal Of Experimental And Theoretical Physics, JEEP*, 107:74–82, 2008.

[83] M. Mito, K. Iriguchi, H. Deguchi and J. Kishine. Giant nonlinear magnetic response in a molecule-based magnet. *Phys. Rev. B*, 79, 2009.

[84] K. Inoue. Private communication.

[85] J. W. Campbell, Q. Hao, M. M. Harding, N. D. Nguti and C. Wilkinson. Laugen version 6.0 and INTLDM. *J. Appl. Cryst.*, 31:496–502, 1998.

[86] C. Wilkinson, H. W. Khamis, R. F. D. Stansfields and G. J. McIntyre. Integration of single crystal reflections using area multidetectors. *J. Appl. Cryst.*, 21:471–478, 1988.

[87] J. Campbell, J. Habash, J.R. Helliwell and K. Moffat. Determination of the Wavelength Normalisation Curve in the Laue Method. *Information Quarterly for Protein Crystallography*, 18:23–31, 1986.

[88] G. M. Sheldrick. SHELXL97, Programs for Crystal Structure Analysis. *Institüt für Anorganische Chemie der Universität, Tammanstrasse, Göttingen, Germany*, 1998.

[89] R. L. Carlin. *Magnetochemistry.* Springer-Verlag, 1986.

[90] E. Hovestreydt, M. Aroyo, S. Sattler and H. Wondratschek. KAREP, a program for calculating irreducible space-group representations. *J. Appl. Cryst.*, 25:544, 1992.

[91] P. Franz, C. Ambrus, A. Hauser, D. Chernyshov, M. Hostettler, J. Hauser, L. Keller, K. Krämer, H. Stockli-Evans,P. Pattison, H. Bürgi and S. Decurtins. Crystalline, Mixed-Valence Manganese Analogue of Prussian blue: Magnetic, Spectroscopic, X-ray and Neutron Diffraction Studies. *J. Am. Chem. Soc.*, 126:16472–16477, 2004.

[92] K. Inoue. Private communication.

[93] M. S. Lehmann, F. K. Larsen . A method for location of the peaks in step-scan measured Bragg reflexions. *Acta Cryst. Section A*, 30:580–584, 1974.

[94] P. Coppens, L. Leiserow, D. Rabinovi. Calculation of Absortion Corrections for Camera and Diffractometer Data. *Acta Cryst.*, 18:1035, 1965.

[95] R. L. Harlow. Troublesome Crystal Structures: Prevention, Detection and Resolution. *J. Res. Natl. Inst. Stand. Tachnol.*, 101:327–339, 1996.

[96] A. Pelissetto and E. Vicari. Critical Phenomena and Renormalization-Group Theory. *Phys. Rept.*, 368:2042–2046, 1980.

[97] R. Sessoli, D. Gatteschi, A. Caneschi and M. A. Novak. Magnetic bistability in a metal-ion cluster. *Nature*, 365:141–143, 1993.

[98] N. Bontemps, J. Rajchenbach, R. V. Chamberlin and R. Orbach. Dynamic scaling in the $eu_{0.4}sr_{0.6}s$ spin-glass. *Phys. Rev. B*, 30:6514–6520, 1984.

[99] E. Ruiz, J. Cirera, J. Cano, S. Alvarez, C. Loosec and J. Kortus. Can large magnetic anisotropy and high spin really coexist? *Chem. Commun.*, pages 52–54, 2008.

[100] O. Waldmann. A Criterion for the Anisotropy Barrier in Single-Molecule Magnets. *Inor. Chem.*, 46:10035–10037, 2007.

[101] A. J. Tasiopoulos, A. Vinslava, W. Wernsdorfer, K. A. Abboud and G. Christou. Giant single-molecule magnets: A Mn-84 torus and its supramolecular nanotubes. *Angew. Chem. Int. Ed.*, 43:2117–2121, 2004.

[102] C. J. Milios, A. Vinslava, W. Wernsdorfer, S. Moggach, S. Parsons, S. P. Perlepes, G. Christou and E. K. Brechin. A Record Anisotropy Barrier for a Single-Molecule Magnet. *J. Am. Chem. Soc.*, 129:2754–2755, 2007.

[103] W . Wernsdorfer and R. Sessoli. Quantum Phase Interference and Parity Effects in Magnetic Molecular Clusters. *Science*, 284:133, 1999.

[104] L. Thomas, F. Lionti, R. Ballou, D. Gatteschi, R. Sessoli and B. Barbara. Macroscopic quantum tunnelling og magnetization in a single crystal of nanomagnets. *Nature*, 383:145–147, 1996.

[105] F. Troiania and M. Affronte. Molecular spins for quantum information technologies. *Chem. Soc. Rev.*, 40:3119–3129, 2011.

[106] M.Clemente-León, H. Soyer, E. Coronado, C. Mingotaud, C. J. Gómez-García and P. Delhaés. Langmuir-Blodgett Films of Single-Molecule Nanomagnets. *Angew. Chem. Int. Ed.*, 37:2842–2845, 1998.

[107] D. Ruiz-Molina, M. Mas-Torrent, J. Gómez, A.I. Balana, N. Domingo, J. Tejada, M.T. Martínez, C. Rovira and J. Veciana. Isolated Single-Molecule Magnets on the Surface of a Polymeric Thin Film. *Adv. Mat.*, 15:42–45, 2003.

[108] F. Palacio, P. Oliete, U. Schubert, I. Mijatovic, N. Hüsing and H. Peterlik. Magnetic behavior of a hybrid polymer obtained from ethyl acrylate and the magnetic cluster $\mathrm{Mn_12O_12(acrylate)_16}$. *J. Mat. Chem.*, 14:1873–1878, 2004.

[109] A. Cornia, M. Mannini, P. Sainctavit and R. Sessoli. Chemical strategies and characterization tools for the organization of single molecule magnets on surfaces. *Chem. Soc. Rev.*, 40:3076–3091, 2011.

[110] A. Cornia, A. C. Fabretti, M. Pacchioni, L. Zobbi, D. Bonacchi, A. Caneschi, D. Gatteschi, R. Biagi, U. Del Pennino, V. De Renzi, L. Gurevich and H. S. J. Van der Zant. Direct Observation of Single-Molecule Magnets Organized on Gold Surfaces. *Angew. Chem. Int. Ed.*, 42:1645–1648, 2003.

[111] J. I. Martín, J. Nogués, K. Liu, J. L. Vicent and I. K. Schuller. Ordered magnetic nanostructures: fabrication and properties. *J. Magn. Magn. Mater.*, 256:449–501, 2003.

[112] P. Allia, M. Coisson, P. Tiberto, F. Vinai, M. Knobel, M. A. Novak and W. C. Nunes. Granular Cu-Co alloys as interacting superparamagnets. *Phys. Rev. B*, 64:144420–144432, 2001.

[113] W. Wernsdorfer, N. Aliaga-Alcalde, D. N. Hendrickson and G. Christou. Exchange-biased quantum tunnelling in a supramolecular dimer of single-molecule magnets. *Nature*, 416:406–409, 2002.

[114] P. Mahata, S. Natarajan, P. Panissod and M. Drillon. Quasi-2D XY Magnetic Properties and Slow Relaxation in a Body Centered Metal Organic Network of [Co_4] Clusters. *J. Am. Chem. Soc.*, 131:10140–10150, 2009.

[115] M. Mito, M. Ogawa, H. Deguchi, M. Yamashita and H. Miyasaka. Ac field-switchable magnetic properties of two-dimensional netwroked nano-size magnets. *J. Appl. Phys.*, 107:124316–124322, 2010.

[116] M. Evangelisti, F. Luis, F. L. Mettes, N. Aliaga, G. Aromí, J. J. Alonso, G. Christou,and L. J. de Jongh. Magnetic Long-Range Order Induced by Quantum Relaxation in Single-Molecule Magnets. *Phys. Rev. Lett.*, 93:117202–117206, 2004.

[117] O. Roubeau and R. Clérac. Rational Assembly of High-Spin Polynuclear Magnetic Complexes into Coordination Networks: the Case of a [Mn_4] Single-Molecule Magnet Building Block. *Eur. J. Inorg. Chem.*, pages 4325–4342, 2008.

[118] L. F. Jones, A. Prescimone, M. Evangelisti and E. K. Brechin. 1D chains of Mn6 single-molecule magnets. *Chem. Commun.*, pages 2023–2025, 2009.

[119] R. Ababei, Y-G. Li, O. Roubeau, M. Kalisz, N. Bréfuel, C. Coulon, E. Harté, X. Liu, C. Mathonière and R. Clérac. Bimetallic cyanido-bridged magnetic materials derived from manganese(III) Schiff-base complexes and pentacyanidonitrosylferrate(II) precursor. *New J. Chem.*, 33:1237–1248, 2009.

[120] L. A. Kushch, V. D. Sasnovskaya, E. B. Yagubskii, S. S. Khasanov, S. V. Simonov, R. P. Shibaeva, A. V. Korolev, D. V. Starichenko, A. O. Anokhin, V. Yu. Irkhin and Y. N. Shvachko. 1D chain coordination assembly of $[Mn_4(hmp)_6(NO_3)_2]^{2+}$ single-molecule magnets linked by the

photochromic $[FeNO(CN)_5]^{2-}$ precursor. *Inor. Chim. Acta*, 378:169–173, 2011.

[121] J. Yoo, A. Yamaguchi, M. Nakano, J. Krzystek, W. E. Streib, L. Brunel, H. Ishimoto, G. Christou and D. N. Hendrickson. Mixed-Valence Tetranuclear Manganese Single-Molecule Magnets. *Inorg. Chem.*, 40:4604–4616, 2001.

[122] J. Yoo, W. Wernsdorfer, E. Yang, M. Nakano, A. L. Rheingold and D. N. Hendrickson. One-Dimensional Chain of Tetranuclear Manganese Single-Molecule Magnets. *Inorg. Chem.*, 44:3377–3379, 2005.

[123] H. Miyasaka, K. Nakata, L. Lecren, C. Coulon, Y. Nakazawa, T. Fujisaki, K. Sugiura,M. Yamashita and R. Clérac. Two-Dimensional Networks Based on Mn4 Complex linked by Dicyanamide Anion: From Single-Molecule Magnet to Classical Magnet Behavior. *J. Am. Chem. Soc.*, 128:3770–3783, 2006.

[124] S. Hu, J. Liu, Z. Meng, Y. Zheng, Y. Lan,A. K. Powell and M. Tong. Pentacobalt(II) cluster based pcu network exhibits both magnetic slow-relaxation and hysteresis behaviour. *Dalton Trans.*, 40:27–30, 2011.

[125] M. Murrie, S. J. Teat, H. Stœckli-Evans and H. U. Güdel. Synthesis and Characterization of a Cobalt(II) Single-Molecule Magnet. *Angew. Chem.*, 42:4653–4656.

[126] K. W. Galloway, M. Schmidtmann, J. Sanchez-Benitez, K. V. Kamenev, W. Wernsdorferc and M. Murrie. Slow magnetic relaxation in a 3D network of cobalt(II) citrate cubanes. *Dalton Trans.*, 39:4727–4729, 2010.

[127] Z. Lin, Z. Li and H. Zhang. Syntheses, Structures, and Magnetic Properties of Two Novel Three-Dimensional Frameworks Built from M_4O_4 Cubanes and Dicyanamide Bridges. *Cryst. Growth Des.*, 7:589–591, 2007.

[128] S. Xiang, X. Wu, J. Zhang, R. Fu, S. Hu and X. Zhang. A 3D Canted Antiferromagnetic Porous Metal-Organic Framework with Anatase Topology through Assembly of an Analogue of Polyoxometalate. *J. Am. Chem. Soc.*, 127:16352–16353, 2005.

[129] J. Campo, L. R. Falvello, I. Mayoral, F. Palacio, T. Soler and M. Tomás. Reversible Single-Crystal-to-Single-Crystal Cross-Linking of a Ribbon of Cobalt Citrate Cubanes To Form a 2D Net. *J. Am. Chem. Soc.*, 130:2932–2933, 2008.

[130] D. Wu, D. Guo, Y. Song, W. Huang, C. Duan, Q. Meng and O. Sato. Co^{II} Molecular Square with Single-Molecule Magnet Properties. *Inorg. Chem.*, 48:854–860, 2009.

[131] "S. Karasawa, D. Yoshihara, N. Watanabe, M. Nakano, and N. Koga". Formation of monometallic single-molecule magnets with an s_{total} value of 3/2 in diluted frozen solution. *Dalton Trans.*, 11:1418–1420, 2008.

[132] R. Basler, C. Boskovic, G. Chaboussant, H. U. Güdel, M. Murrie,S. T. Ochsenbein and A. Sieber. Molecular Spin Clusters: New Synthetic Approaches and Neutron Scattering Studies. *Chem. Phys. Chem.*, 4:910–926, 2003.

[133] A. Palii, B. Tsukerblat, S. Klokishner, K. R. Dunbar, J. M. Clemente-Juan and E. Coronado. Beyond the spin model: exchange coupling in molecular magnets with unquenched orbital angular momenta. *Chem. Soc. Rev.*, 40:3130–3156, 2011.

[134] J. J. Borrás-Almenar, J. M. Clemente-Juan, E. Coronado and B. S. Tsukerblat. MAGPACK: A Package to Calculate the Energy Levels, Bulk Magnetic Properties, and Inelastic Neutron Scattering Spectra of High Nuclearity Spin Clusters. *J. Comput. Chem.*, 22:985–991, 2001.

[135] M.E. Lines. Orbital Angular Momentum in the Theory of Paramagnetic Clusters. *J. Chem. Phys.*, 55:2977–2984, 1971.

[136] H. Sakiyama, R. Ito, H. Kumagai, K. Inoue, M. Sakamoto, Y. Nishida and M. Yamasaki. Dinuclear Cobalt(II) Complexes of an Acyclic Phenol-Based Dinucleating Ligand with Four Methoxyethyl Chelating Arms-First Magnetic Analyses in an Axially Distorted Octahedral Field. *Eur. J. Inorg. Chem.*, 2001:2027–2032, 2001.

[137] A. V. Palii, B. S. Tsukerblat, E. Coronado, J. M. Clemente-Juan and J. J. Borrás-Almenar. Microscopic Approach to the Pseudo-Spin-1/2 Hamiltonian for Kramers Doublets in Exchange Coupled Co(II) Pairs. *Inorg. Chem.*, 42:2455–2458, 2003.

[138] A. V. Palii, B. S. Tsukerblat, E. Coronado, J. M. Clemente-Juan and J. J. Borrás-Almenar. Orbitally dependent magnetic coupling between cobalt(II) ions: The problem of the magnetic anisotropy. *J. Chem. Phys.*, 118:5566–5581, 2003.

[139] A. V. Palii, B. S. Tsukerblat, E. Coronado, J. M. Clemente-Juan and J. J. Borrás-Almenar. Orbitally dependent kinetic exchange in cobalt(II) pairs: origin of the magnetic anisotropy. *Polyhedron*, 22:2537–2544, 2003.

[140] F. Lloret, M. Julve, J. Cano, R. Ruiz-García and E. Pardo. Magnetic properties of six-coordinated high-spin cobalt(II) complexes: Theoretical background and its application. *Inor. Chem. Acta*, 361:3432–3445, 2008.

[141] A. Cornia, M. Mannini, P. Sainctavit and R. Sessoli. Chemical strategies and characterization tools for the organization of single molecule magnets on surfaces. *Chem. Soc. Rev.*, 40:3076–3091, 2011.

[142] K. Isele, F. Gigon, A.F. Williams, G. Bernardinelli, P. Franz and S. Decurtins. Synthesis, structure and properties of M_4O_4 cubanes containing nickel(II) and cobalt(II). *Dalton Trans.*, pages 332–341, 2007.

[143] C. J. Milios, R. Inglis, A. Vinslava, R. Bagai, W. Wernsdorfer, S. Parsons, S. P. Perlepes, G. Christou and E. K. Brechin. Toward a magnetostructural correlation for a family of mn_6 smms. *J. Am. Chem. Soc.*, 129:12505–12511, 2007.

[144] M. A. Halcrow, J. Sun, J. C. Huffman and G. Christou. Structural and Magnetic Properties of $[\mathrm{Ni_4}(\mu_3\text{-OMe})_4(\mathrm{dbm})_4(\mathrm{MeOH})_4]$ and $[\mathrm{Ni_4}(\eta_1,\mu_3\text{-}\mathrm{N_3})_4(\mathrm{dbm})_4(\mathrm{EtOH})_4]$. Magnetostructural Correlations for $[\mathrm{Ni_4X_4}]^4+$ Cubane Complexes. *Inorg. Chem.*, 34:4167–4177, 1995.

[145] J. M. Clemente-Juan, B. Chansou, B. Donnadieu and J. P. Tuchagues. Synthesis, Structure, and Magnetic Properties of the Low-Symmetry Tetranuclear Cubane-like Nickel Complex $[\mathrm{Ni_4}(\mathrm{pypentO})(\mathrm{pym})(\mu_3\text{-}\mathrm{OH})_2(\mu\text{-Oac})_2(\mathrm{NCS})_2(\mathrm{OH_2})]$. *Inorg. Chem.*, 39:5515–5519, 2000.

[146] J. F. Berry, F. A. Cotton, C. Y. Liu, T. Lu, C. A. Murillo, B. S. Tsukerblat, D. Villagrán and X. Wang. Modeling spin interactions in cyclic trimer and cuboidal Co_4O4 core with Co(II) in tetrahedral and octahedral environments. *J. Am. Chem. Soc*, 127:4895–4902, 2005.

[147] G. Aromí, A. S. Batsanov, P. Christin, M. Halliwell, O. Roubeau, G. A. Timco and R. E. P. Winpenny. Synthesis, structure and magnetic properties of hydroxyquinaldine-brigded cobalt and nickel cubanes. *Dalton Trans.*, pages 4466–4471, 2003.

[148] E. C. Yang, D. N. Hendrickson, W. Wernsdorfer, M. Nakano, L. N. Zakharov, R. D. Sommer, A. L. Rheingold, M. Ledezma-Gairaud and G. Christou. Cobalt single-molecule magnet. *J. of App. Phys.*, 91:7382–7384, 2002.

[149] F. Klöwer, Y. Lan, J. Nehrkorn, O. Waldmann, C. E. Anson and A. K. Powell. Modelling the Magnetic Behaviour of Square-Pyramidal $CoII^5$ Aggregates: Tuning SMM Behaviour through Variations in the Ligand Shell. *Chem. Eur. J.*, 15:7413–7422, 2009.

[150] T. A. Hudson, K. J. Berry, B. Moubaraki, K. S. Murray and R. Robson. Citrate, in collaboration with a guanidinium ion, as a generator of

cubane-like complexes with a range of metal cations: Synthesis, structures, and magnetic properties of $[c(nh_2)_3]_8[(m^{II})_4(cit)_4]\cdot 8h_2o$ (m= mg, mn, fe, co, ni, and zn; cit= citrate). *Inorg. Chem.*, 45:3549–3556, 2006.

[151] K. W. Galloway, A. M. Whyte, W. Wernsdorfer, J. Sanchez-Benitez, K. V. Kamenev, A. Parkin, R. D. Peacock and M. Murrie. Cobalt(II) Citrate Cubane Single-Molecule Magnet. *Inor. Chem.*, 47:7438–7441, 2008.

[152] B. Moubaraki, K. S. Murray, T. A. Hudson and R. Robson. Tetranuclear and Octanuclear Cobalt(II) Citrate Cluster Single Molecule Magnets. *Eur. J. Inorg. Chem.*, pages 4525–4529, 2008.

[153] *Quantum Design. URL http://www.qdusa.com/.*

[154] *Servicios de apoyo a la investigación de la Universidad de Zaragoza. Servicio de Medidas Físicas. URL http://sai.unizar.es/medidas/index.html.*

[155] A. Abragam and B. Bleaney. *Electron Paramagnetic Resonance of Transition Ions.* Dover Publications, 1970.

[156] O. Montero E. Coronado S. Cardona-Serra C. Marti-Gastaldo J. M. Clemente-Juan J. Sesé D. Drung F. Luis, M. J. Martinez-Perez and T. Schurig. Spin-lattice relaxation via quantum tunneling in an er^{3+}-polyoxometalate molecular magnet. *Phys. Rev. B*, 82:060403, 2010.

[157] Y. Imry and S. Ma. Random-field instability of the ordered state of continuous symmetry. *Phys. Rev. Lett.*, 35:1399–1401, 1975.

[158] C.A. Garanin. Extended Debye model for molecular magnets. *Phys. Rev. B*, 78:20405–20409, 2008.

[159] J. Chadwick. Possible Existence of a Neutron. *Nature*, 129:3252, 1932.

[160] A. Furrer, J. Mesot and T. Strässle. *Neutron Scattering in Condensed Matter Physics*, volume 4. World Scientific Publishing Co.Pte.Ltd., 2009.

[161] G. L. Squires. *Introduction of the theory of Thermal Neutron Scattering.* Cambridge University Press, 1978.

[162] P. J. Brown, J. B. Forsyth, E. Lelievre-Berna and F. Tasset. Determination of the magnetization distribution in Cr_2O_3 using spherical neutron polarimetry. *J. Phys. Condens. Matter.*, 14:1957–1966, 2002.

[163] E. Clementi and C. Roetti. . *Data Tables*, 14:182, 1974.

[164] G. J. McIntyre and R. G. D. Stansfield. A gerenal Lorentz correction for single-crystal diffractometers. *Acta Crystallogr.*, A44:257–262, 1988.

[165] J. A. K. Howard, O. Johnson, A. J. Schultz and A. M. Stringer. Determination of the neutron absorption cross section for hydrogen as a function of wavelength with a pulsed neutron source. *J. Appl. Cryst.*, 20:120–122, 1987.

[166] V.F. Sears. Neutron scattering lengths and cross sections. *Neutron News*, 3:26–37, 1992.

[167] P. Coppens, L. Leiserowitz and D. Rabinovich . Calculation of absorption correctios for camera and diffractometer data. *Acta Crystallogr.*, 18:1035–1038, 1965.

[168] P.J. Becker amd P. Coppens. Extinction within the Limit of Validity of the Darwin transfer Equations. II. Refinement of extinction in Spherical Crystals of SrF_2 and LiF. *Acta Crystallogr.*, A30:129–147, 1974.

[169] P. P. Ewald. Introduction to the dynamical theory of X-ray diffraction. *Acta Crystallographica Section A*, 25:103, 1969.

[170] W. R. Busing, H. A. Levy . Angle Calculations for 3- and 4- Circle X-ray and Neutron Diffractometers. *Acta Cryst.*, 22:457–464, 1967.

[171] C. Wilkinson, H. W. Khamis, R. F. D. Stansfield, G. J. McIntyre. Integration of single-crystal reflections using area multidetectors. *J. Appl. Cryst.*, 21:471–478, 1988.

[172] J. L. Amorós, M. J. Buerger, M. Canut de Amorós. *The Laue Method.* Academic Press, Inc., 1975.

[173] D. W. J. Cruickshank, J. R. Helliwell and K. Moffat. Multiplicity Distribution of Reflections in Laue Diffraction. *43*, pages 656–674, 1987.

[174] Z. Ren and K. Moffat. Deconvolution of Energy Overlaps in Laue Diffraction. *J. Appl. Cryst.*, 28:482–493, 1995.

[175] Q. Hao, J. W. Campbell, M.M. Harding, J.R. Helliwell. Evaluation of Reflection Intensities for the Components of Multiple Laue Diffraction Spots by Direct-Methods. *Acta Cryst. Sect. A*, 49:528–531, 1993.

[176] J. W. Campbell and Q. Hao. Evaluation of Reflection Intensities for the Components of Multiple Laue Diffraction Spots .II. Using the Wavelength-Normalization Curve. *Acta Cryst. Sect. A*, 49:889–893, 1993.

[177] D. W. J. Cruickshank and J. R. Helliwell. Angular-Distribution of Reflections in Laue Diffraction. *Acta Cryst. Sect. A*, 47:352, 1991.

[178] F. Cipriani, J. C. Castagna, C. Wilkinson, P. Oleinek and M. S. Lehmann. Cold neutron protein crystallography using a large position-sensitive detector based on image-plate technology. *J. Neutron Res.*, 4:79–85, 1996.

[179] C. Wilkinson, J.A. Cowan, D.A.A. Myles, F. Cipriani and G.J. McIntyre. High-speed neutron Laue diffraction comes of age. *Neutron News*, 13:37, 2002.

[180] B. Ouladdiaf, J. Archer, G. J. McIntyre, A. W. Hewat, D. Brau, S. York. OrientExpress: A new system for Laue neutron diffraction. *Physica B*, 385-386:1052–1054, 2006.

[181] B. Ouladdiaf, J. Archer, J. R. Allibon, P. Decarpentrie, M. Lemée-Cailleau, J. Rodríguez-Carvajal, A. W. Hewat, S. York, D. Brau and G. J. McIntyre. CYCLOPS: a reciprocal-space explorer based on CCD neutron detectors. *J. Appl. Cryst.*, 44:392–397, 2011.

[182] G. J. McIntyre, M. H. Lemée-Cailleau and C. Wilkinson. High-speed neutron Laue diffraction comes of age. *Physica B*, 385-386:1055–1058, 2006.

[183] J. W. Campbell. Lauegen, an X-Windows based program for the processing of Laue X-Ray diffraction data. *J. Appl. Cryst.*, 28:228–236, 1995.

[184] J. W. Campbell and I. J. Cliffton and M.M. Harding and Q. Hao. The Laue-Data-Module (LDM), a software development for Laue X-Ray diffraction data processing. *J. Appl. Cryst.*, 28:635–640, 1995.

[185] L. D. Landau. On the Theory of Phase Transitions I. *Phys. Z. Soviet*, 11:545, 1937.

[186] L. D. Landau and E. M. Lifshitz. *Statisticheskaya fizila (statistical Physics*. 1951.

[187] J. Schweizer. *Neutron and Synchrotron radiation for condensed matter studies. Chapter V: Neutron Scattering and Magnetic Structure.* Springer-Verla berlin Heidelberg and Les Editions de Physique, 1994.

[188] E. F. Bertaut. Representation Analysis of Magnetic Structures. *Acta Crystallogr. Sec. A*, 24:217, 1968.

[189] E. P. Wigner. *Group theory and its application to Quantum mechanics of atomic spectra.* New York and London, 1959.

[190] E. F. Bertaut. Magnetic Structure Analysis And Group Theory. *Journal de Physique, Colloque C1*, 32:462–470, 1971.

[191] L. P. Landau and E. M. Lifshits. *Electrodynamics of Continuous Media.* Pergamon Press: Oxford, 1960.

[192] Y. A. Izyumov and V. E. Naish. Symmetry Analysis in Neutron-Diffraction Studies of Magnetic-Structures .1. Phase-Transition Concept to Describe Magnetic-Structures in Crystals. *J. Magn. Magn. Mater.*, 12:239–248, 1979.